Chemical Tools for Protein Imaging in Live Bacterial Cells

Thesis by

Samuel Hin-Yuen Ho

In Partial Fulfillment of the Requirements for

the degree of

Doctor of Philosophy in Chemistry

CALIFORNIA INSTITUTE OF TECHNOLOGY

Pasadena, California

2019

Defended May 3, 2019

Samuel Hin-Yuen Ho
ORCID: 0000-0001-7647-0752

ACKNOWLEDGEMENTS

First and foremost, I would like to thank my advisor, Prof. David Tirrell. Dave's approach to science has taught me how to push the boundaries of scientific discovery, to appreciate the joy of understanding the natural world, and to practice humility as a scientific scholar. I most appreciate the intellectual freedom Dave fosters in his lab in terms of project conception, development, and completion. Importantly, I am proud of the work I completed during my graduate career, and I will always appreciate the scientific discussions I had with Dave. Much of my scientific grounding and the way I approach science are attributed to Dave's mentorship. Thanks, Dave, for everything.

I would like to thank members of my committee: Prof. Peter Dervan, Prof. Tom Miller, and Prof. Grant Jensen. Throughout my graduate career, I have had the opportunity to interact with each member of the committee individually and learn how to grow as a young scientist. Thanks to Peter for providing advice on next steps in my scientific career. Thanks to Tom for providing perspective on how to think about evolving scientific fields. Thanks to Grant for guiding me in thinking about grand problems in bacterial cell biology. At some point of my graduate career, I have stopped by, unannounced, to each of your offices, to ask for advice. Thanks to you all for always providing a welcoming and supportive environment.

I would like to thank past and present members of the Tirrell lab for teaching me how to think about experimental design (and for tolerating my quirky personality). Thanks to Roy Pattipeiluhu for allowing me to be your mentor. Thanks to Nathan Dalleska and Cajetan Neubauer at the Environmental Analysis Center for help with the lipid profiling experiments discussed in Chapter 2. Thanks to Cindy Cao for help with some of the work described in Chapter 3. Thanks to Mona Shahgholi at the Mass Spectrometry Laboratory and Sonja Hess and Annie Moradian at the Proteome Exploration Laboratory for help with mass spectrometry analysis. Thanks to Andres Collazo at the Biological Imaging Facility in the Beckman Institute for help with microscopy.

Lastly, thanks to all my friends and family, near and far, for countless get-togethers, endless love and support, and lasting memories.

ABSTRACT

Bacteria spatially and temporally localize their proteins to carry out fundamental cellular processes. Methods for visualizing protein subcellular localization have been critical to our understanding of prokaryotic cell biology. Fluorescent reporters have been instrumental for imaging bacterial proteins in live cells. Small-molecule fluorescent dyes, which have favorable spectral properties, including high brightness and photostability, are attractive in labeling proteins of interest. Here we present a method to site-specifically label the N-termini of bacterial protein targets *in situ* for fluorescence imaging in bacterial cells. The method uses the eukaryotic enzyme N-myristoyltransferase to ligate target proteins, bearing a nonapeptide recognition sequence, with an azide-bearing fatty acid. Subsequent strain-promoted azide–alkyne cycloaddition with fluorophores enable tagging of chemotaxis and cell division proteins in live cells. We describe using a reactive BODIPY fluorophore for visualization of the chemotaxis proteins Tar and CheA and the division proteins FtsZ and FtsA. Next we integrate a single copy of the gene encoding the protein target into the chromosome via Tn7 transposon mutagenesis and use the method to fluorescently label a bacterial chemoreceptor. Finally, we describe the preparation of photoswitchable rhodamine spirolactam dyes for super-resolution imaging in live bacterial cells. Our work highlights the utility of using photoswitchable molecules to label intracellular protein targets. The ability to tag proteins, perform super-resolution imaging, and visualize proteins in space and time will prove broadly useful.

PUBLISHED CONTENT AND CONTRIBUTIONS

(1) Ho, S. H.; Tirrell, D. A. Chemoenzymatic Labeling of Proteins for Imaging in Bacterial Cells. *Journal of the American Chemical Society* **2016**, *138*, 15098–15101. DOI: 10.1021/jacs.6b07067.

S.H.H. and D.A.T. conceived project idea. S.H.H. performed all experimental work and analyzed all associated data. S.H.H. co-wrote the manuscript with D.A.T.

(2) Ho, S. H.; Tirrell, D. A. Enzymatic Labeling of Bacterial Proteins for Super-Resolution Imaging in Live Cells. *Manuscript to be submitted*.

S.H.H. conceived project idea with input from D.A.T. S.H.H. synthesized new compounds, performed all experimental work, and analyzed all associated data. S.H.H. co-wrote the manuscript with D.A.T.

TABLE OF CONTENTS

LIST OF ILLUSTRATIONS

LIST OF TABLES

NOMENCLATURE

12-ADA. 12-azidododecanoic acid.

NMT. N-myristoyltransferase.

BODIPY. Boron-dipyrromethene.

PALM. Photoactivated localization microscopy.

STORM. Stochastic optical reconstruction microscopy.

dSTORM. Direct Stochastic optical reconstruction microscopy.

STED. Stimulated emission depletion.

ESI–MS. Electrospray ionization–mass spectrometry.

GC–MS. Gas chromatography–mass spectrometry.

LC–MS. Liquid chromatography–mass spectrometry.

NMR. Nuclear magnetic resonance.

Chapter 1

PROTEIN LOCALIZATION IN BACTERIA

1.1 Abstract

Despite their small size, bacterial cells precisely coordinate protein localization in space and time as they perform fundamental cellular processes. The compartmentalization of proteins by bacterial cells is often tightly regulated with mechanisms that guide the specific proteins to their final destinations. Advances in high-resolution imaging modalities allow researchers to visualize the ultrastructural assemblies of macromolecules with nanometer resolution. Fluorescent protein reporters have found widespread use in prokaryotic cell biology. However, some bacterial proteins cannot be expressed as the fusion, as the fusion can cause artifacts in imaging or improper localization. Therefore, the development of strategies to site-specifically and orthogonally label specific bacterial proteins with fluorescent small-molecules would provide information about subcellular bacterial localization and would elucidate the organization of protein assemblies within microbial species.

1.2 Protein Localization in Bacteria

The different length scales of all forms of life make up the wondrous biological world. Despite only being a few microns in length, bacterial cells spatially and temporally localize their proteins for both form and function. Once viewed as amorphous vessels to harbor randomly distributed proteins, decades of basic research in prokaryotic cell biology has shown these simple organisms have a great degree of control of the macromolecular topologies formed from their proteins.[1] In bacteria, the subcellular localization of many proteins have direct consequences in processes such as cell division,[2] cell motility,[3] and regulation of chromosomes.[4] The positioning of these proteins within cells is an important phenomenon to study: many of the proteins found in microbial species are homologs to eukaryotic proteins.[5–8] Understanding the localization patterns of bacterial proteins, and more importantly, the mechanisms which drive formation of these assemblies, is critical for understanding how multicellular organisms may localize their proteins.

One of the early studies in bacterial cells came from an observation in 1980 of a mutant, temperature-sensitive *Escherichia coli* strain that was unable to divide but still regulate its chromosomal DNA.[9] The gene was named filament temperature-sensitive mutant Z (*ftsZ*) and encoded the formation of a protein that was later shown to localize at the site of cell division through immunolabeling with gold nanoparticles in fixed cells and visualization by electron microscopy.[10] In 1996, researchers demonstrated the localization and formation of what is now called the "Z-ring" of FtsZ by virtue of fusing the FtsZ to the green fluorescent protein (GFP).[11] These initial key experiments, coupled with the discovery of GFP (*vide infra*) as a fluorescent reporter to tag and image proteins of interest in the early 1990s, were crucial in understanding the mechanisms of bacterial cell division, akin to cytokinesis in eukaryotes. The mechanism by which the polymerization of the FtsZ protofilaments are involved with formation of the Z-ring and how that process drives cell division is important for understanding how mother cells divide into two new daughter cells. The bacterial divisome is precisely coordinated with the self-assembly of FtsZ polymers and is mediated by the *Min* system (composed of proteins MinC, MinD, and MinE) in *E. coli*.[12] The oscillations of MinC, for example, destabilize the FtsZ polymers and regulate the

intracellular concentrations of FtsZ during formation of the Z-ring.[13,14] Other models of divisome positioning involve nucleoid occlusion mediated by the *E. coli* nucleoid occlusion factor SlmA.[15] How the FtsZ protofilaments (structurally analogous to microtubules) are coupled both in space and time to cellular division is a longstanding question in fundamental biology. Recently it was demonstrated by two independent research groups that a process called FtsZ treadmilling is directly coupled to the recruitment of peptidoglycan synthases during cell division.[16,17] Other cell division proteins in *E. coli* (e.g. FtsA)[18] and in other bacterial organisms (e.g. *Caulobacter crescentus* and *Bacillus subtilis*) have also been studied for their subcellular localization and function in cell division.[19,20]

The biogenesis and compartmentalization of bacterial proteins is noteworthy in prokaryotic cell biology: the discrete complexes formed by bacterial proteins are analogous to organelles in eukaryotic cells.[21] Importantly, the enclosure of subcellular compartments in bacteria allow them to carry out specific and defined functions. For example, the marine bacterium *Magnetospirillum sp. AMB-1* forms magnetosomes,[22] membranous compartments for formation of magnetite crystals, that are involved with aligning the bacteria to the Earth's magnetic poles for optimal oxygen concentrations.[23] The *mamABE* gene cluster is responsible for the formation of these vesicles, and it was demonstrated that the protein MamA, in particular, is responsible for the formation of the magnetite crystals inside these compartments.[24] Deletion of the *mamA* gene directly affected the ability of the cells to produce biogenetic magnetite crystals, although the cells were still able to produce the vesicles. The origins of organelles (e.g. chloroplasts, mitochondria, endoplasmic reticulum, Golgi apparatus) are longstanding questions in fundamental biology.[25,26] The fact that model prokaryotic organisms can produce magnetite-filled compartments may provide clues towards the biogenesis of other organelles in different organisms. Another example of compartmentalization in bacteria involves the formation of carboxysomes in species of cyanobacteria. The carboxysome is an intricate structure composed of a polyhedral protein shell that houses the enzyme ribulose-1,5-bisphosphate carboxylase/oxygenase (RubisCO), an enzyme that is involved in the first step in the fixation of carbon dioxide.[27] Much like chloroplasts in plants, cyanobacteria that form carboxysomes participate in steps in the

Calvin Cycle.[28] The enzymes within the carboxysomes show a striking and remarkable arrangement of these structures such that they are evenly spaced.[29] More recently, the inner and outer protein components and matrix organization in the cyanobacterium *Synechococcus elongatus* have been elucidated using three-dimensional structured illumination microscopy.[30] Key experiments revealed that the two isoforms of the protein CcmM colocalize at the site of new carboxysomes. The protein CcmM is thought to be involved in forming junctions between the RubisCO enzymes within each carboxysome. Because bacterial cells are able to form structures that are analogous to organelles, the study of protein localization within defined compartments may be key to understanding the evolutionary origins of organelles in multicellular organisms.

Proper positioning of proteins is essential for bacterial cells to perform basic cellular processes. For example, it was known that the Gram-negative marine organism *C. crescentus* exhibited an S-shaped curvature, as opposed to rod-shaped species such as *E. coli* and *B. subtilis.* The protein responsible for this shape in *C. crescentus* was identified to be crescentin (CreS) in 2003.[31] The protein provides a curvature unique to *C. crescentus* cells and forms filaments towards the inner region of the cell. Imaging was performed by virtue of expressing FLAG-tagged CreS in *C. crescentus* cells, fixing those cells, and labeling CreS with anti-FLAG antibodies conjugated to fluorophores. Construction of the fusion reporter gene *creS-gfp* was also conducted in imaging experiments to analyze the localization patterns in live cells. Formation of CreS filaments in *C. crescentus* is particularly interesting in that the protein bare similarities to intermediate filament (IF) proteins found in vertebrates. Through many years of research of examining CreS, it has been proposed that the CreS proteins and formation of the S-shape in *C. crescentus* is crucial for the cell to adhere to surfaces in its environment. The actin homolog MreB has found considerable attention in prokaryotic cell biology.[32] The positioning of MreB has been shown to provide structure within the bacterial cell, similar to cytoskeletal networks in eukaryotes.[33] Interestingly, the observed localization patterns of MreB and whether the protein forms discrete patches or a helical array have been of considerable debate in microbiology.[34,35] Nonetheless, key studies

of MreB function and localization have been invaluable in our understanding of how protein networks give rise to the individual cell's shape.

The polar assemblies of bacterial proteins have been implicated in processes such cellular division and chemotactic signaling. One example involves the polar assembly of PleC, a histidine protein kinase, in *C. crescentus*.[36] As a model organism for cell division, the bacterium exhibits a remarkable phenotype as the mother cell divides into two daughter cells. The resulting cells are asymmetric. Cell division results in formation of one motile swarmer cell and one non-motile stalked cell. The regulation of DNA separation is regulated by phosphorylation cascades and control of intracellular concentrations of proteins such as DivJ, CtrA, and PleC.[37] The subcellular localization of PleC is precisely controlled as the mother cell begins its asymmetric division into the swarmer and stalked cells. PleC initially is located at the flagellar pole of the cell but becomes delocalized during the formation of the stalked cell. It has been shown that the protein DivJ is coordinated on the opposite pole in the stalked cell. How the localization of PleC changes during the process of cell division in *C. crescentus* was elucidated in 2004 by fluorescence microscopy and single-molecule imaging.[38] The determination of its diffusion coefficient was achieved by fusion of PleC to the enhanced yellow fluorescent protein (EYFP). Using a 514-nm laser to bleach a majority of PleC–EYFP, single emissive molecules of the fusion protein could be visualized using fluorescence microscopy. Importantly, these experiments revealed that during delocalization of the PleC–EYFP molecules in cell division, the protein follows a Brownian trajectory, consistent with a diffusion and capture mechanism for localizing PleC to cellular poles, as opposed to active transport. In *E. coli*, the study of polar localization of transmembrane and cytoplasmic associated chemotaxis proteins has received attention for many decades of research in microbiology.[39–41] Examples include the cytoplasmic proteins CheA, CheW, and CheY; the clustering of these proteins is believed to enhance chemotactic signaling in bacteria.[42] The mechanism by which these proteins form clusters was studied by high-resolution imaging by means of photoactivated localization microscopy (PALM) in live cells.[43] An exponential array of clusters suggested that formation of these clusters was dependent on nucleation of the chemotaxis proteins. The transmembrane chemoreceptors

Tar, Tap, Trg, and Tsr are known to coordinate the events of chemotaxis with the cytoplasmic chemotaxis proteins.[44] The study of the topological patterns of these chemoreceptors was examined by high-resolution imaging by means of electron microscopy. These chemoreceptors adopt a hexagonal array with remarkable symmetry; it has been demonstrated that these arrays are present in many bacterial species.[45] The coupling of the transmembrane chemoreceptors to the cytoplasmic chemotaxis proteins are directly related to how the cell responds to external stimuli and changes in chemical environment.[46] Other forms of taxis (i.e. energy) that exist for other bacterial proteins, such as Aer,[47] are modulated by changes in oxygen concentration or light exposure, which directly affect the protein electron transport chain.

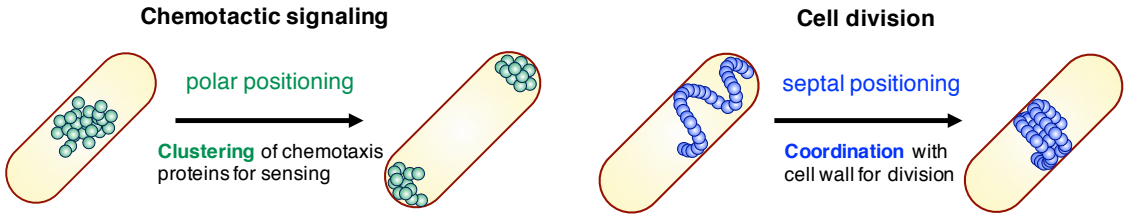

Figure 1.1. Examples of protein localization in bacterial cells. Polar clustering of chemotaxis proteins is thought to enhance chemotactic signaling. Proteins involved in cell division localize at the septum of cell.

The examples described above capture only a fraction of the exquisite spatial and temporal control bacteria have in localizing their proteins. The tools of molecular biology and chemical biology have transformed our understanding of the microbial world. Advances in microscopy are critical if scientists are to fully understand the intricate workings of bacterial cells. These tools will allow researchers to fully immerse into the world of microbiology and understand the mechanisms that drive protein localization in bacteria.

1.3 Fluorescent Protein Reporters

The ability to genetically encode the *Aequorea victoria* green fluorescent protein to proteins of interest as a fusion transformed molecular biology in the early 1990s. The protein sequence of wtGFP was reported in 1992,[48] but the utility of GFP was realized when

scientists were able to heterologously express the protein in *E. coli* and *C. elegans* in 1994.[49] The photophysical properties (e.g. quantum yield and photostability) were dramatically improved with the identification of a key S65T mutation within the chromophore in 1996.[50] Since its discovery, GFP and other fluorescent proteins[51] spanning the visible spectrum have been widely used to tag and image specific proteins in bacterial organisms.

Fluorescence imaging has been powerful in the determination of macromolecular protein assemblies, but the method is inherently diffraction-limited. The resolution achieved in such imaging experiments approach 200 nm in the radial direction and 500 nm in the axial direction.[52] Before the advent of super-resolution microscopy, key experiments revealed that single molecules of GFP immobilized within polymer gels could blink between dark-off and bright-on states through excitation with a 488-nm laser.[53] Importantly, the single molecules of GFP reached a long-lived dark state (on the timescale of seconds) that could reversed through activation with a 405-nm laser pulse. These observations would not be discernable using ensemble-averaged measurements of GFP emission. Photoactivatable GFP (PA-GFP) was reported in 2002, and its use was demonstrated to track diffusion in live cells.[54] These experiments were particularly noteworthy and set the stage that single emitters could be resolved temporally by identifying the centroid of their individual point spread functions (PSF).[52] This idea, which is the fundamental principle of super-resolution based imaging, was demonstrated in 2006 and was coined photoactivation localization microscopy, or PALM.[55] (The report was published at the same time when stochastic optical reconstruction microscopy was reported in 2006, which is described in greater detail in **1.4**). In 2009, the crystal structures of dark and bright PA-GFP were solved, and the operative mechanism by which photoactivation occurs is facilitated by loss of carbon dioxide at Glu222, forming the anionic chromophore.[56] By stochastic activation of a subset of dark-off fluorophores to their bright-on states, the localization precision from the centroid of individual PSFs could be determined, leading to construction of a high-resolution image. The imaging resolutions are dramatically improved, achieving resolutions of approximately 20 nm in the radial direction and 50 nm in the axial direction.[52] Since the discovery of PA-GFP, many other photoactivatable (e.g. PA-mCherry,[57] PA-mKate,[58] PA-CFP2[59]), photoconvertible (e.g.

mEos[60]), and photoswitchable (e.g. Dronpa[61]) have been developed, characterized, and used for acquiring high-resolution images of protein assemblies in living cells.

PALM imaging has enabled the study of complex biological phenomena in bacterial systems with unparalleled levels of spatial resolution. One example involves the study of the nanodomains formed by the polar protein PopZ in *C. crescentus*.[62] PopZ has earned considerable attention in prokaryotic cell biology; its localization to the cell poles is essential for the recruitment of other anchoring proteins during chromosomal separation and cellular division.[63] Cryo-EM sectioning of the flagellated pole of *C. crescentus* revealed a polymeric network of PopZ filaments large enough to exclude macromolecules such as ribosomes.[64] The working hypothesis generated from these studies was that the localization of *Caulobacter* PopZ is essential during the cell cycle progression and its asymmetric cell division. Using a PA-mCherry–PopZ fusion for PALM imaging, it was demonstrated that the density of individual PopZ molecules is conserved across numerous *C. crescentus* cells, suggesting that the three-dimensional polymeric network is highly conserved.[62] The fact that PopZ forms a highly polarized network to exclude large molecules suggest that this architecture is critical for partitioning of the chromosome during different stages of the cell cycle. Revisiting the early example of the cell division protein FtsZ (*vide supra*), PALM imaging has revealed key insights about the protofilaments that are coupled with peptidoglycan synthases involved during cell division. A study in 2008 in which researchers imaged a fusion of FtsZ–Dendra2 in *E. coli* demonstrated that the protein adopts two types of structures:[65] one belonging to the Z-ring previously known and a more dynamic helix with a diffusion coefficient approaching 0.1 $\mu m^2 s^{-1}$. PALM imaging of Dendra2-tagged FtsZ in *C. crescentus* showed that the FtsZ filaments are able to dissociate from the Z-ring on the timescale of subseconds,[19,66] whereas the depolymerization of FtsZ in *B. subtilis* and *E. coli* were measured to be on the order of 8–9 s.[20] Strikingly, the FtsZ thickness spans on the order of 100 nm in *C. crescentus*. Furthermore, FtsZ is present in many bacterial species (e.g. *E. coli*, *C. crescentus*, *B. subtilis*) but the proteins which interact with FtsZ are different in each type of bacteria.[67–69] Fundamentally, this raises the question of how the molecular architecture is conserved for FtsZ, if at all, among different bacteria. With more

developments in single-molecule detection, super-resolution imaging experiments will reveal a wealth of information about the organization of bacterial proteins.[70]

1.4 Small-Molecule Fluorescent Reporters

In recent years, there has been considerable interest in the use of small-molecule fluorescent dyes for super-resolution microscopy.[71] Organic dyes are known to possess favorable photophysical properties,[72] such as increased brightness,[73] photostability,[74] and photon output.[75] Furthermore, the spectral properties of such dyes can be tuned through chemical modification of the dye core.[76–78] Methods to site-specifically and covalently modify a biomolecule of interest with a synthetic molecule is a core idea in chemical biology.[79,80] (These methods are described in more detail in **1.5**). Super-resolution dyes include photoactivatable dyes, such as rhodamine spiroamides[81] and spirocyclic diazoketones,[82] and photoswitchable dyes, such as cyanine[83] and oxazine[84] dyes. Photoactivatable fluorescent dyes undergo irreversible transition between a dark-off and bright-on state and is usually facilitated through exposure to weak UV illumination.[54] Stimulated emission depletion (STED) microscopy, first reported in 2000, uses excitation to deactivate a subset of fluorophores to effectively create a defined local point to enable super-resolution imaging.[85] Photoswitchable fluorescent dyes can undergo multiple switching cycles between the dark-off and bright-on states, and this process can be facilitated by redox process or exogenous thiols added in the imaging buffer.[86] A simplified energy diagram is shown in **Figure 1.2**. Fluorophores can be excited and transition from ground (S_0) to excited (S_1) states. Relaxation back to S_0 of lower energy emits photons, and this process occurs on the timescale of nanoseconds (ns). Intersystem crossing (ISC) can occur to allow for transition from the S_1 states to triplet (T_1) states. The fluorophore can either relax back to S_0 or cross into long-lived non-fluorescent "dark" states (D); these events are usually facilitated by redox processes. UV irradiation can promote the transition between D and S_0. The cycling, which occurs on the order of milliseconds, is essential for stochastic optical reconstruction microscopy, or STORM.[87] The high-resolution image is produced by reconstructing the image from the localized centroids of each PSF. The imaging resolutions typically achieved using these dyes approach 20 nm and 50 nm in the radial and axial directions, respectively.

The improvement of the photon output of these synthetic dyes through chemical modification[77] has been noteworthy in dye development since localization precision is directly related to the number of photons emitted during each switching event.[88]

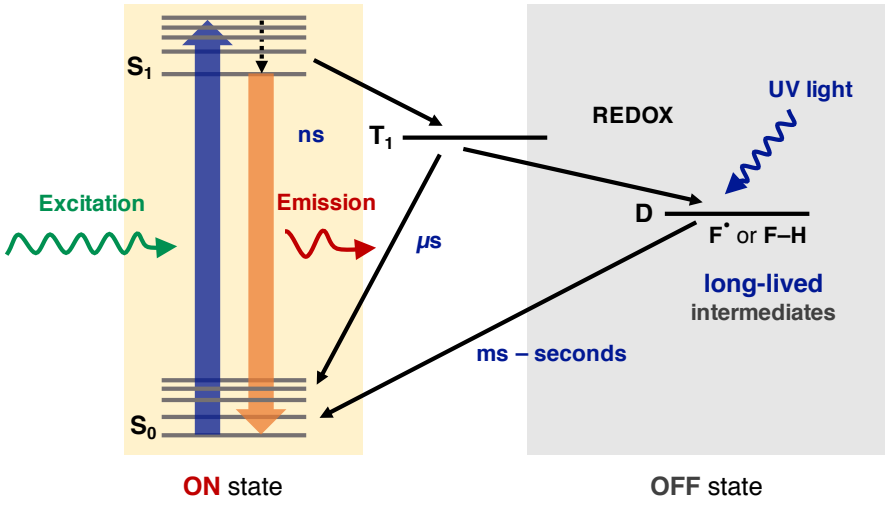

Figure 1.2. Simplified energy diagram showing dark-off and bright-on states of fluorophores. Dark states are long-lived intermediates, which can revert back to the ground state on the timescale of milliseconds to seconds. Adapted from Ref. 87.

Photoactivatable single-molecule emitters have found use in labeling specific bacterial protein targets for super-resolution imaging. The tubular stalks of *C. crescentus* were labeled by reaction of lysine residues with a Cy3–Cy5 heterodimer conjugate, resulting in a resolution of 30 nm.[89] In 2010, it was reported that photoactivatable dicyanomethylenedihydrofuran chromophore could be elaborated to the HaloTag ligand (described further in **1.5**) for site-specific modification of PopZ in live *C. crescentus* cells.[90] Photoswitchable rhodamine spiroamides were then used for three-dimensional super resolution imaging of the cell-surface of live *C. crescentus* cells in 2014.[91] It is important to note that many photoswitchable STORM dyes, such as Cy3 and Alexa Fluor 647, are not compatible for live-cell imaging. Specifically, many dyes require fixation and permeabilization of cells.[71] Moreover, a study demonstrated that many bacterial proteins in *C. crescentus* are sensitive to where the fluorescent protein fusion is placed.[92] Therefore,

there is still a need for the development of dyes that can enable site-specific covalent modification of intracellular proteins in live bacterial cells.

1.5 Site-Specific Covalent Modification of Proteins

At the apex of chemical biology is the ability to site-specifically and covalently modify a protein of interest (POI) with a probe of choice (e.g. fluorophore, affinity handle, enrichment handle).[93] Labeling proteins with fluorescent probes has allowed researchers to understand protein organization, dynamics, diffusion, and trafficking.[94] Because these probes are generally smaller than larger fusions like GFP, there is considerable interest in being able to modify proteins with small molecules. It has been shown in the case of proteins in *C. crescentus* that many proteins are sensitive to where the fluorescent protein is placed (N- or C-termini).[92] Localization artifacts have been demonstrated for the bacterial protein MreB when a fluorescent protein reporter is fused to its N-terminus.[34]

Chemoenzymatic labeling utilizes an enzyme that is not present in the host organism to mediate the ligation of a small, metabolic analog onto a POI bearing a short, genetically encoded peptide recognition sequence.[95] The metabolic handle usually contains a bioorthogonal functional group (e.g. azide, alkyne) that can further be reacted for enrichment or visualization of the protein. In 2007, it was demonstrated that the bacterial lipoic acid ligase could be re-engineered to enable site-specific modification of cell surface proteins with azide-containing fatty acid analogues.[96] The same year, it was shown that the formylglycine–generating enzyme (FGE) could recognize a short peptide sequence, known as the "sulfatase motif," to cause the oxidation of a cysteine residue into an aldehyde, which could be further modified through selective aldehyde chemistry.[97] Enzyme systems, such as sortases[98,99] and farnesyl transferases,[100] have also been used for chemoenzymatic labeling.

Pro-fluorescent probes, amber suppression, and ribosome engineering have been used to fluorescently label proteins. Tsien and co-workers first reported the design of a biarsenical fluorescein analog (FlAsH) that is weakly fluorescent when the arsenic atoms were bound to 1, 2-ethanedithiol; however, upon thiol-arsenic exchange with a genetically encoded tetracysteine motif on a protein, the probe becomes highly fluorescent.[101] Since this

discovery, a number of bis-arsenical dyes have been reported, such as ReAsH,[102] CrAsH,[103] and Cy3As.[104] Schepartz and co-workers reported the development of pro-fluorescent bis-boronic acid fluorescein derivatives[105] that would become highly fluorescent upon binding to tetraserine motifs. Amber suppression[106–108] was used to incorporate a fluorescent non-natural amino acid in the protein FtsZ in live *E. coli* cells.[109] Recently, it was shown that bacterial cells bearing modified ribosomes are able to translate fluorescent amino acids that lack an α-amino group or asymmetric center at the α-carbon.[110] The method was applied for incorporating the fluorescent dye into the bacterial protein MreB for imaging in live *E. coli* cells.

Enzymes that can be covalently modified with synthetic probes have also found use in imaging, specifically in bacterial cells. The SNAP Tag,[111] CLIP Tag,[112] and HaloTag[113] protein systems are based on proteins that have their active sites modified in such a way that allows them to be covalently modified with a synthetic protein ligand bearing the probe of choice. For example, the HaloTag is a modified bacterial haloalkane dehalogenase from *Rhodococcus* (DhaA) that can be ligated with a synthetic haloalkane ligand. The aspartic acid amino acid (Asp106) undergoes nucleophilic displacement with the synthetic ligand. For imaging applications, these proteins are expressed as a fusion to the POI, and the ligand is added to cells to enable the modification. The HaloTag system has been useful in labeling bacterial proteins; for example, the HaloTag protein was fused to PopZ to enable super-resolution imaging in live *C. crescentus* cells.[90] The HaloTag system was applied for super-resolution imaging to visualize protein subunits of the Type I Secretion System (T1SS) and a transcription factor in live *Salmonella enterica*.[114] Notably, the HaloTag is a useful system because it allows for the incorporation of synthetic dyes onto the protein of interest. Photoactivatable dyes, in particular, have been elaborated into the HaloTag ligands and used in both single-molecule and super-resolution imaging.[115]

1.6 N-Myristoyltransferase-Mediated Protein Labeling

The eukaryotic enzyme, N-myristoyltransferase (NMT), catalyzes the amide bond formation between myristic acid, a rare 14-carbon, aliphatic fatty acid, and the N-terminus of a protein

bearing a 7–9 amino acid recognition sequence as a co-translational or post-translational modification.[116–118] It has been demonstrated in the early 1990s that the enzyme tolerates fatty acid analogues of myristic acid with varying functional groups, such as terminal azides and alkynes.[119–122] Importantly, the enzyme is not present in *E. coli*.[123] Several labs have taken advantage of the orthogonality of this enzyme. Work from Ploegh and co-workers showed that NMT-mediated labeling could be used for proteomic profiling of fatty acid acylated proteins in mammalian cells.[124] Tate and co-workers reported that NMT could be used for N-terminal labeling of non-natural substrate proteins in bacteria for bioorthogonal ligations.[125,126] It was reported that engineered protein substrates could be labeled on the N-terminus with azide-containing fatty acids and used for capture on alkyne-printed microarrays.[127]

1.7 Progress Towards Achieving Higher Resolutions

Attention has been given to the development of correlated, electron cryotomography and super-resolution imaging. Cryo-electron microscopy (cryo-EM) and electron cryo-tomography (ECT) approach resolutions well below (on the order of 10 nm) those achieved in ambient temperature super-resolution microscopy.[128] These methods have been powerful in identifying ultrastructures in mammalian and bacterial organisms. Correlative light and cryo-EM (cryo-CLEM) has been useful for the identification of novel macromolecular assemblies, but the inherent diffraction limit (approximately 200 nm in the lateral direction and 500 nm in the axial direction) obscures correlation between the fluorescence image and the electron micrograph. Due to the lack of optimized optical setups (e.g. requirement of using long-working-distance air objectives with approximately 0.7 numerical aperture) for cryo-fluorescence microscopy, the resolutions only approach 400–500 nm.[129] ECT relies on structures with previously known organization within a cell,[130] but correlative ECT and super-resolution microscopy would allow for discovery of uncharacterized and novel structures within the cell.

In 2014, the first report of combining PALM imaging and ECT was published. Importantly, this method allowed for the identification of ultrastructures involved in the Type 6 Secretion

System (T6SS) of *Myxococcus xanthus*.[131] Importantly, of the different photoactivatable or photoswitchable fluorescent proteins imaged at cryogenic temperature (i.e. 80 K), PA-GFP was the only one to show blinking events. It is currently unclear of the mechanisms that are allowed for photoactivation or photoswitching at low temperatures. Structural rearrangements, such as trans–cis isomerization, have been shown to occur at 100 K for the photoswitchable fluorescent protein Padron.[132] However, many photoswitchable fluorescent proteins (e.g. Dronpa) do not respond under cryogenic temperatures.[131] At cryogenic temperatures, the transition between the triplet (T_1) state back to the ground (S_0) state is nearly suppressed, a large fraction of molecules does not transition back to the ground state, and a major population of fluorophores exist in the T_1 or dark states.[133] The lack of oxygen diffusion decreases the rate at which these long-lived dark states transition to the ground state. In 2018, it was demonstrated that photoactivatable mKate (PA-mKate) could photoactivate at 77 K.[134] The localization precision was 1.4 nm, and a small fraction (8%) of PA-mKate molecules emitted 10^5 photons. However, the long on-times of the activated fluorescent protein proved challenging, as multiple PSFs from overlapping emitters obscured the resolution. Nonetheless, the fact that PA-GFP and PA-mKate and others respond at cryogenic temperatures suggest that cryonanoscopy may be a future direction in super-resolution based imaging.

1.8 Overview of Thesis Chapters

In this Thesis, the NMT method was adapted for site-specific modification of bacterial proteins *in situ* for fluorescence imaging. Chapter 2 describes the development of the method and its application to image four bacterial proteins in *E. coli* cells (Tar, CheA, FtsZ, and FtsA). Chapter 3 then describes the adaptation of the method to image proteins that are expressed from a chromosomal copy integrated within the *E. coli* genome. Chapter 4 then describes the synthesis of cell-permeant, photoswitchable dyes and their use with the NMT-mediated labeling method to enable super-resolution imaging in live bacterial cells.

1.9 References

(1) Rudner, D. Z.; Losick, R. Protein Subcellular Localization in Bacteria. *Cold Spring Harb Perspect Biol* **2010**, *2* (4), a000307. https://doi.org/10.1101/cshperspect.a000307.

(2) Loose, M.; Mitchison, T. J. The Bacterial Cell Division Proteins FtsA and FtsZ Self-Organize into Dynamic Cytoskeletal Patterns. *Nature Cell Biology* **2014**, *16* (1), 38–46. https://doi.org/10.1038/ncb2885.

(3) Rajagopala, S. V.; Titz, B.; Goll, J.; Parrish, J. R.; Wohlbold, K.; McKevitt, M. T.; Palzkill, T.; Mori, H.; Finley, R. L.; Uetz, P. The Protein Network of Bacterial Motility. *Mol Syst Biol* **2007**, *3*. https://doi.org/10.1038/msb4100166.

(4) Renzette, N.; Gumlaw, N.; Nordman, J. T.; Krieger, M.; Yeh, S.-P.; Long, E.; Centore, R.; Boonsombat, R.; Sandler, S. J. Localization of RecA in Escherichia Coli K-12 Using RecA-GFP. *Mol. Microbiol.* **2005**, *57* (4), 1074–1085. https://doi.org/10.1111/j.1365-2958.2005.04755.x.

(5) Derman, A. I.; Becker, E. C.; Truong, B. D.; Fujioka, A.; Tucey, T. M.; Erb, M. L.; Patterson, P. C.; Pogliano, J. Phylogenetic Analysis Identifies Many Uncharacterized Actin-like Proteins (Alps) in Bacteria: Regulated Polymerization, Dynamic Instability and Treadmilling in Alp7A. *Mol. Microbiol.* **2009**, *73* (4), 534–552. https://doi.org/10.1111/j.1365-2958.2009.06771.x.

(6) Daniel, R. A.; Errington, J. Control of Cell Morphogenesis in Bacteria: Two Distinct Ways to Make a Rod-Shaped Cell. *Cell* **2003**, *113* (6), 767–776.

(7) Jensen, R. B.; Gerdes, K. Partitioning of Plasmid R1. The ParM Protein Exhibits ATPase Activity and Interacts with the Centromere-like ParR-ParC Complex. *J. Mol. Biol.* **1997**, *269* (4), 505–513. https://doi.org/10.1006/jmbi.1997.1061.

(8) Jones, L. J.; Carballido-López, R.; Errington, J. Control of Cell Shape in Bacteria: Helical, Actin-like Filaments in Bacillus Subtilis. *Cell* **2001**, *104* (6), 913–922.

(9) Lutkenhaus, J. F.; Wolf-Watz, H.; Donachie, W. D. Organization of Genes in the FtsA-EnvA Region of the Escherichia Coli Genetic Map and Identification of a New Fts Locus (FtsZ). *J. Bacteriol.* **1980**, *142* (2), 615–620.

(10) Bi, E. F.; Lutkenhaus, J. FtsZ Ring Structure Associated with Division in Escherichia Coli. *Nature* **1991**, *354* (6349), 161–164. https://doi.org/10.1038/354161a0.

(11) Ma, X.; Ehrhardt, D. W.; Margolin, W. Colocalization of Cell Division Proteins FtsZ and FtsA to Cytoskeletal Structures in Living Escherichia Coli Cells by Using Green Fluorescent Protein. *Proc. Natl. Acad. Sci. U.S.A.* **1996**, *93* (23), 12998–13003.

(12) de Boer, P. A.; Crossley, R. E.; Rothfield, L. I. A Division Inhibitor and a Topological Specificity Factor Coded for by the Minicell Locus Determine Proper Placement of the Division Septum in E. Coli. *Cell* **1989**, *56* (4), 641–649.

(13) Hale, C. A.; Meinhardt, H.; de Boer, P. A. Dynamic Localization Cycle of the Cell Division Regulator MinE in Escherichia Coli. *EMBO J.* **2001**, *20* (7), 1563–1572. https://doi.org/10.1093/emboj/20.7.1563.

(14) Raskin, D. M.; de Boer, P. A. MinDE-Dependent Pole-to-Pole Oscillation of Division Inhibitor MinC in Escherichia Coli. *J. Bacteriol.* **1999**, *181* (20), 6419–6424.

(15) Bernhardt, T. G.; de Boer, P. A. J. SlmA, a Nucleoid-Associated, FtsZ Binding Protein Required for Blocking Septal Ring Assembly over Chromosomes in E. Coli. *Mol. Cell* **2005**, *18* (5), 555–564. https://doi.org/10.1016/j.molcel.2005.04.012.

(16) Yang, X.; Lyu, Z.; Miguel, A.; McQuillen, R.; Huang, K. C.; Xiao, J. GTPase Activity-Coupled Treadmilling of the Bacterial Tubulin FtsZ Organizes Septal Cell Wall Synthesis. *Science* **2017**, *355* (6326), 744–747. https://doi.org/10.1126/science.aak9995.

(17) Bisson-Filho, A. W.; Hsu, Y.-P.; Squyres, G. R.; Kuru, E.; Wu, F.; Jukes, C.; Sun, Y.; Dekker, C.; Holden, S.; VanNieuwenhze, M. S.; et al. Treadmilling by FtsZ Filaments Drives Peptidoglycan Synthesis and Bacterial Cell Division. *Science* **2017**, *355* (6326), 739–743. https://doi.org/10.1126/science.aak9973.

(18) Addinall, S. G.; Lutkenhaus, J. FtsA Is Localized to the Septum in an FtsZ-Dependent Manner. *Journal of Bacteriology* **1996**, *178* (24), 7167–7172. https://doi.org/10.1128/jb.178.24.7167-7172.1996.

(19) Holden, S. J.; Pengo, T.; Meibom, K. L.; Fernandez, C. F.; Collier, J.; Manley, S. High Throughput 3D Super-Resolution Microscopy Reveals Caulobacter Crescentus in Vivo Z-Ring Organization. *PNAS* **2014**, *111* (12), 4566–4571. https://doi.org/10.1073/pnas.1313368111.

(20) Anderson, D. E.; Gueiros-Filho, F. J.; Erickson, H. P. Assembly Dynamics of FtsZ Rings in Bacillus Subtilis and Escherichia Coli and Effects of FtsZ-Regulating Proteins. *Journal of Bacteriology* **2004**, *186* (17), 5775–5781. https://doi.org/10.1128/JB.186.17.5775-5781.2004.

(21) Yeates, T. O.; Crowley, C. S.; Tanaka, S. Bacterial Microcompartment Organelles: Protein Shell Structure and Evolution. *Annu Rev Biophys* **2010**, *39*, 185–205. https://doi.org/10.1146/annurev.biophys.093008.131418.

(22) Komeili, A. Molecular Mechanisms of Magnetosome Formation. *Annu. Rev. Biochem.* **2007**, *76*, 351–366. https://doi.org/10.1146/annurev.biochem.74.082803.133444.

(23) Lefèvre, C. T.; Bennet, M.; Landau, L.; Vach, P.; Pignol, D.; Bazylinski, D. A.; Frankel, R. B.; Klumpp, S.; Faivre, D. Diversity of Magneto-Aerotactic Behaviors and Oxygen Sensing Mechanisms in Cultured Magnetotactic Bacteria. *Biophys J* **2014**, *107* (2), 527–538. https://doi.org/10.1016/j.bpj.2014.05.043.

(24) Komeili, A.; Vali, H.; Beveridge, T. J.; Newman, D. K. Magnetosome Vesicles Are Present before Magnetite Formation, and MamA Is Required for Their Activation. *Proc. Natl. Acad. Sci. U.S.A.* **2004**, *101* (11), 3839–3844. https://doi.org/10.1073/pnas.0400391101.

(25) Gray, M. W. The Evolutionary Origins of Organelles. *Trends Genet.* **1989**, *5* (9), 294–299.

(26) Cooper, G. M. The Origin and Evolution of Cells. *The Cell: A Molecular Approach. 2nd edition* **2000**.

(27) Yeates, T. O.; Kerfeld, C. A.; Heinhorst, S.; Cannon, G. C.; Shively, J. M. Protein-Based Organelles in Bacteria: Carboxysomes and Related Microcompartments. *Nat. Rev. Microbiol.* **2008**, *6* (9), 681–691. https://doi.org/10.1038/nrmicro1913.

(28) Cameron, J. C.; Wilson, S. C.; Bernstein, S. L.; Kerfeld, C. A. Biogenesis of a Bacterial Organelle: The Carboxysome Assembly Pathway. *Cell* **2013**, *155* (5), 1131–1140. https://doi.org/10.1016/j.cell.2013.10.044.

(29) Kerfeld, C. A.; Sawaya, M. R.; Tanaka, S.; Nguyen, C. V.; Phillips, M.; Beeby, M.; Yeates, T. O. Protein Structures Forming the Shell of Primitive Bacterial Organelles. *Science* **2005**, *309* (5736), 936–938. https://doi.org/10.1126/science.1113397.

(30) Niederhuber, M. J.; Lambert, T. J.; Yapp, C.; Silver, P. A.; Polka, J. K. Superresolution Microscopy of the β-Carboxysome Reveals a Homogeneous Matrix. *Mol Biol Cell* **2017**, *28* (20), 2734–2745. https://doi.org/10.1091/mbc.E17-01-0069.

(31) Ausmees, N.; Kuhn, J. R.; Jacobs-Wagner, C. The Bacterial Cytoskeleton: An Intermediate Filament-like Function in Cell Shape. *Cell* **2003**, *115* (6), 705–713.

(32) Errington, J. Bacterial Morphogenesis and the Enigmatic MreB Helix. *Nat. Rev. Microbiol.* **2015**, *13* (4), 241–248. https://doi.org/10.1038/nrmicro3398.

(33) Carballido-López, R. The Bacterial Actin-Like Cytoskeleton. *Microbiol Mol Biol Rev* **2006**, *70* (4), 888–909. https://doi.org/10.1128/MMBR.00014-06.

(34) Swulius, M. T.; Jensen, G. J. The Helical MreB Cytoskeleton in Escherichia Coli MC1000/PLE7 Is an Artifact of the N-Terminal Yellow Fluorescent Protein Tag. *Journal of Bacteriology* **2012**, *194* (23), 6382–6386. https://doi.org/10.1128/JB.00505-12.

(35) Margolin, W. The Price of Tags in Protein Localization Studies. *J Bacteriol* **2012**, *194* (23), 6369–6371. https://doi.org/10.1128/JB.01640-12.

(36) Fumeaux, C.; Radhakrishnan, S. K.; Ardissone, S.; Théraulaz, L.; Frandi, A.; Martins, D.; Nesper, J.; Abel, S.; Jenal, U.; Viollier, P. H. Cell Cycle Transition from S-Phase to G1 in *Caulobacter* Is Mediated by Ancestral Virulence Regulators. *Nature Communications* **2014**, *5*, 4081. https://doi.org/10.1038/ncomms5081.

(37) Hinz, A. J.; Larson, D. E.; Smith, C. S.; Brun, Y. V. The Caulobacter Crescentus Polar Organelle Development Protein PodJ Is Differentially Localized and Is Required for Polar Targeting of the PleC Development Regulator. *Molecular Microbiology* **2003**, *47* (4), 929–941. https://doi.org/10.1046/j.1365-2958.2003.03349.x.

(38) Deich, J.; Judd, E. M.; McAdams, H. H.; Moerner, W. E. Visualization of the Movement of Single Histidine Kinase Molecules in Live Caulobacter Cells. *Proceedings of the National Academy of Sciences* **2004**, *101* (45), 15921–15926. https://doi.org/10.1073/pnas.0404200101.

(39) Sourjik, V.; Armitage, J. P. Spatial Organization in Bacterial Chemotaxis. *EMBO J* **2010**, *29* (16), 2724–2733. https://doi.org/10.1038/emboj.2010.178.

(40) Bren, A.; Eisenbach, M. How Signals Are Heard during Bacterial Chemotaxis: Protein-Protein Interactions in Sensory Signal Propagation. *J Bacteriol* **2000**, *182* (24), 6865–6873.

(41) Sourjik, V.; Wingreen, N. S. Responding to Chemical Gradients: Bacterial Chemotaxis. *Curr Opin Cell Biol* **2012**, *24* (2), 262–268. https://doi.org/10.1016/j.ceb.2011.11.008.

(42) Maddock, J. R.; Shapiro, L. Polar Location of the Chemoreceptor Complex in the Escherichia Coli Cell. *Science* **1993**, *259* (5102), 1717–1723.

(43) Greenfield, D.; McEvoy, A. L.; Shroff, H.; Crooks, G. E.; Wingreen, N. S.; Betzig, E.; Liphardt, J. Self-Organization of the Escherichia Coli Chemotaxis Network Imaged with Super-Resolution Light Microscopy. *PLoS Biol.* **2009**, *7* (6), e1000137. https://doi.org/10.1371/journal.pbio.1000137.

(44) Weerasuriya, S.; Schneider, B. M.; Manson, M. D. Chimeric Chemoreceptors in Escherichia Coli: Signaling Properties of Tar-Tap and Tap-Tar Hybrids. *J. Bacteriol.* **1998**, *180* (4), 914–920.

(45) Briegel, A.; Ortega, D. R.; Tocheva, E. I.; Wuichet, K.; Li, Z.; Chen, S.; Müller, A.; Iancu, C. V.; Murphy, G. E.; Dobro, M. J.; et al. Universal Architecture of Bacterial Chemoreceptor Arrays. *PNAS* **2009**, *106* (40), 17181–17186. https://doi.org/10.1073/pnas.0905181106.

(46) Van Haastert, P. J. M.; Devreotes, P. N. Chemotaxis: Signalling the Way Forward. *Nat. Rev. Mol. Cell Biol.* **2004**, *5* (8), 626–634. https://doi.org/10.1038/nrm1435.

(47) Taylor, B. L.; Zhulin, I. B.; Johnson, M. S. Aerotaxis and Other Energy-Sensing Behavior in Bacteria. *Annu. Rev. Microbiol.* **1999**, *53*, 103–128. https://doi.org/10.1146/annurev.micro.53.1.103.

(48) Prasher, D. C.; Eckenrode, V. K.; Ward, W. W.; Prendergast, F. G.; Cormier, M. J. Primary Structure of the Aequorea Victoria Green-Fluorescent Protein. *Gene* **1992**, *111* (2), 229–233. https://doi.org/10.1016/0378-1119(92)90691-H.

(49) Chalfie, M.; Tu, Y.; Euskirchen, G.; Ward, W. W.; Prasher, D. C. Green Fluorescent Protein as a Marker for Gene Expression. *Science* **1994**, *263* (5148), 802–805.

(50) Ormö, M.; Cubitt, A. B.; Kallio, K.; Gross, L. A.; Tsien, R. Y.; Remington, S. J. Crystal Structure of the Aequorea Victoria Green Fluorescent Protein. *Science* **1996**, *273* (5280), 1392–1395.

(51) Shaner, N. C.; Steinbach, P. A.; Tsien, R. Y. A Guide to Choosing Fluorescent Proteins. *Nature Methods* **2005**, *2* (12), 905–909. https://doi.org/10.1038/nmeth819.

(52) Huang, B.; Babcock, H.; Zhuang, X. Breaking the Diffraction Barrier: Super-Resolution Imaging of Cells. *Cell* **2010**, *143* (7), 1047–1058. https://doi.org/10.1016/j.cell.2010.12.002.

(53) Dickson, R. M.; Cubitt, A. B.; Tsien, R. Y.; Moerner, W. E. On/off Blinking and Switching Behaviour of Single Molecules of Green Fluorescent Protein. *Nature* **1997**, *388* (6640), 355–358. https://doi.org/10.1038/41048.

(54) Patterson, G. H.; Lippincott-Schwartz, J. A Photoactivatable GFP for Selective Photolabeling of Proteins and Cells. *Science* **2002**, *297* (5588), 1873–1877. https://doi.org/10.1126/science.1074952.

(55) Betzig, E.; Patterson, G. H.; Sougrat, R.; Lindwasser, O. W.; Olenych, S.; Bonifacino, J. S.; Davidson, M. W.; Lippincott-Schwartz, J.; Hess, H. F. Imaging Intracellular Fluorescent Proteins at Nanometer Resolution. *Science* **2006**, *313* (5793), 1642–1645. https://doi.org/10.1126/science.1127344.

(56) Henderson, J. N.; Gepshtein, R.; Heenan, J. R.; Kallio, K.; Huppert, D.; Remington, S. J. Structure and Mechanism of the Photoactivatable Green Fluorescent Protein. *J. Am. Chem. Soc.* **2009**, *131* (12), 4176–4177. https://doi.org/10.1021/ja808851n.

(57) Subach, F. V.; Patterson, G. H.; Manley, S.; Gillette, J. M.; Lippincott-Schwartz, J.; Verkhusha, V. V. Photoactivatable MCherry for High-Resolution Two-Color Fluorescence Microscopy. *Nature Methods* **2009**, *6* (2), 153–159. https://doi.org/10.1038/nmeth.1298.

(58) Subach, F. V.; Patterson, G. H.; Renz, M.; Lippincott-Schwartz, J.; Verkhusha, V. V. Bright Monomeric Photoactivatable Red Fluorescent Protein for Two-Color Super-Resolution SptPALM of Live Cells. *J Am Chem Soc* **2010**, *132* (18), 6481–6491. https://doi.org/10.1021/ja100906g.

(59) Chudakov, D. M.; Verkhusha, V. V.; Staroverov, D. B.; Souslova, E. A.; Lukyanov, S.; Lukyanov, K. A. Photoswitchable Cyan Fluorescent Protein for Protein Tracking. *Nat. Biotechnol.* **2004**, *22* (11), 1435–1439. https://doi.org/10.1038/nbt1025.

(60) McKinney, S. A.; Murphy, C. S.; Hazelwood, K. L.; Davidson, M. W.; Looger, L. L. A Bright and Photostable Photoconvertible Fluorescent Protein. *Nat. Methods* **2009**, *6* (2), 131–133. https://doi.org/10.1038/nmeth.1296.

(61) Habuchi, S.; Ando, R.; Dedecker, P.; Verheijen, W.; Mizuno, H.; Miyawaki, A.; Hofkens, J. Reversible Single-Molecule Photoswitching in the GFP-like Fluorescent Protein Dronpa. *Proc. Natl. Acad. Sci. U.S.A.* **2005**, *102* (27), 9511–9516. https://doi.org/10.1073/pnas.0500489102.

(62) Gahlmann, A.; Ptacin, J. L.; Grover, G.; Quirin, S.; von Diezmann, A. R. S.; Lee, M. K.; Backlund, M. P.; Shapiro, L.; Piestun, R.; Moerner, W. E. Quantitative Multicolor Subdiffraction Imaging of Bacterial Protein Ultrastructures in Three Dimensions. *Nano Lett.* **2013**, *13* (3), 987–993. https://doi.org/10.1021/nl304071h.

(63) Laloux, G.; Jacobs-Wagner, C. Spatiotemporal Control of PopZ Localization through Cell Cycle–Coupled Multimerization. *J Cell Biol* **2013**, *201* (6), 827–841. https://doi.org/10.1083/jcb.201303036.

(64) Bowman, G. R.; Comolli, L. R.; Gaietta, G. M.; Fero, M.; Hong, S.-H.; Jones, Y.; Lee, J. H.; Downing, K. H.; Ellisman, M. H.; McAdams, H. H.; et al. Caulobacter PopZ Forms a Polar Subdomain Dictating Sequential Changes in Pole Composition and Function. *Mol Microbiol* **2010**, *76* (1), 173–189. https://doi.org/10.1111/j.1365-2958.2010.07088.x.

(65) Niu, L.; Yu, J. Investigating Intracellular Dynamics of FtsZ Cytoskeleton with Photoactivation Single-Molecule Tracking. *Biophys J* **2008**, *95* (4), 2009–2016. https://doi.org/10.1529/biophysj.108.128751.

(66) Biteen, J. S.; Goley, E. D.; Shapiro, L.; Moerner, W. E. Three-Dimensional Super-Resolution Imaging of the Midplane Protein FtsZ in Live Caulobacter Crescentus Cells Using Astigmatism. *Chemphyschem* **2012**, *13* (4), 1007–1012. https://doi.org/10.1002/cphc.201100686.

(67) Margolin, W. FtsZ and the Division of Prokaryotic Cells and Organelles. *Nat Rev Mol Cell Biol* **2005**, *6* (11), 862–871. https://doi.org/10.1038/nrm1745.

(68) Robson, S. A.; Michie, K. A.; Mackay, J. P.; Harry, E.; King, G. F. The Bacillus Subtilis Cell Division Proteins FtsL and DivIC Are Intrinsically Unstable and Do Not Interact with One Another in the Absence of Other Septasomal Components. *Mol. Microbiol.* **2002**, *44* (3), 663–674.

(69) Martin, M. E.; Trimble, M. J.; Brun, Y. V. Cell Cycle-Dependent Abundance, Stability and Localization of FtsA and FtsQ in Caulobacter Crescentus. *Mol. Microbiol.* **2004**, *54* (1), 60–74. https://doi.org/10.1111/j.1365-2958.2004.04251.x.

(70) Gahlmann, A.; Moerner, W. E. Exploring Bacterial Cell Biology with Single-Molecule Tracking and Super-Resolution Imaging. *Nat. Rev. Microbiol.* **2014**, *12* (1), 9–22. https://doi.org/10.1038/nrmicro3154.

(71) Wang, L.; Frei, M. S.; Salim, A.; Johnsson, K. Small-Molecule Fluorescent Probes for Live-Cell Super-Resolution Microscopy. *J. Am. Chem. Soc.* **2019**, *141* (7), 2770–2781. https://doi.org/10.1021/jacs.8b11134.

(72) Lavis, L. D.; Raines, R. T. Bright Ideas for Chemical Biology. *ACS Chem. Biol.* **2008**, *3* (3), 142–155. https://doi.org/10.1021/cb700248m.

(73) Ulrich, G.; Ziessel, R.; Harriman, A. The Chemistry of Fluorescent Bodipy Dyes: Versatility Unsurpassed. *Angewandte Chemie International Edition* **2008**, *47* (7), 1184–1201. https://doi.org/10.1002/anie.200702070.

(74) Altman, R. B.; Zheng, Q.; Zhou, Z.; Terry, D. S.; Warren, J. D.; Blanchard, S. C. Enhanced Photostability of Cyanine Fluorophores across the Visible Spectrum. *Nat. Methods* **2012**, *9* (5), 428–429. https://doi.org/10.1038/nmeth.1988.

(75) Dempsey, G. T.; Vaughan, J. C.; Chen, K. H.; Bates, M.; Zhuang, X. Evaluation of Fluorophores for Optimal Performance in Localization-Based Super-Resolution Imaging. *Nature Methods* **2011**, *8* (12), 1027–1036. https://doi.org/10.1038/nmeth.1768.

(76) Butkevich, A. N.; Bossi, M. L.; Lukinavicius, G.; Hell, S. W. Triarylmethane Fluorophores Resistant to Oxidative Photobluing. *J. Am. Chem. Soc.* **2018**. https://doi.org/10.1021/jacs.8b11036.

(77) Grimm, J. B.; English, B. P.; Chen, J.; Slaughter, J. P.; Zhang, Z.; Revyakin, A.; Patel, R.; Macklin, J. J.; Normanno, D.; Singer, R. H.; et al. A General Method to Improve Fluorophores for Live-Cell and Single-Molecule Microscopy. *Nat Methods* **2015**, *12* (3), 244–250. https://doi.org/10.1038/nmeth.3256.

(78) Grimm, J. B.; Muthusamy, A. K.; Liang, Y.; Brown, T. A.; Lemon, W. C.; Patel, R.; Lu, R.; Macklin, J. J.; Keller, P. J.; Ji, N.; et al. A General Method to Fine-Tune Fluorophores for Live-Cell and in Vivo Imaging. *Nat. Methods* **2017**, *14* (10), 987–994. https://doi.org/10.1038/nmeth.4403.

(79) MacDonald, J. I.; Munch, H. K.; Moore, T.; Francis, M. B. One-Step Site-Specific Modification of Native Proteins with 2-Pyridinecarboxyaldehydes. *Nature Chemical Biology* **2015**, *11* (5), 326–331. https://doi.org/10.1038/nchembio.1792.

(80) Uttamapinant, C.; White, K. A.; Baruah, H.; Thompson, S.; Fernández-Suárez, M.; Puthenveetil, S.; Ting, A. Y. A Fluorophore Ligase for Site-Specific Protein Labeling inside Living Cells. *PNAS* **2010**, *107* (24), 10914–10919. https://doi.org/10.1073/pnas.0914067107.

(81) Bossi, M.; Fölling, J.; Belov, V. N.; Boyarskiy, V. P.; Medda, R.; Egner, A.; Eggeling, C.; Schönle, A.; Hell, S. W. Multicolor Far-Field Fluorescence Nanoscopy through Isolated Detection of Distinct Molecular Species. *Nano Lett.* **2008**, *8* (8), 2463–2468. https://doi.org/10.1021/nl801471d.

(82) Belov, V. N.; Wurm, C. A.; Boyarskiy, V. P.; Jakobs, S.; Hell, S. W. Rhodamines NN: A Novel Class of Caged Fluorescent Dyes. *Angewandte Chemie International Edition* **2010**, *49* (20), 3520–3523. https://doi.org/10.1002/anie.201000150.

(83) Heilemann, M.; Margeat, E.; Kasper, R.; Sauer, M.; Tinnefeld, P. Carbocyanine Dyes as Efficient Reversible Single-Molecule Optical Switch. *J. Am. Chem. Soc.* **2005**, *127* (11), 3801–3806. https://doi.org/10.1021/ja044686x.

(84) Deniz, E.; Tomasulo, M.; Cusido, J.; Yildiz, I.; Petriella, M.; Bossi, M. L.; Sortino, S.; Raymo, F. M. Photoactivatable Fluorophores for Super-Resolution Imaging Based on Oxazine Auxochromes. *The Journal of Physical Chemistry C* **2012**, *116* (10), 6058–6068. https://doi.org/10.1021/jp211796p.

(85) Klar, T. A.; Jakobs, S.; Dyba, M.; Egner, A.; Hell, S. W. Fluorescence Microscopy with Diffraction Resolution Barrier Broken by Stimulated Emission. *Proc. Natl. Acad. Sci. U.S.A.* **2000**, *97* (15), 8206–8210.

(86) Whelan, D. R.; Bell, T. D. M. Image Artifacts in Single Molecule Localization Microscopy: Why Optimization of Sample Preparation Protocols Matters. *Sci Rep* **2015**, *5*, 7924. https://doi.org/10.1038/srep07924.

(87) Nahidiazar, L.; Agronskaia, A. V.; Broertjes, J.; van den Broek, B.; Jalink, K. Optimizing Imaging Conditions for Demanding Multi-Color Super Resolution Localization Microscopy. *PLoS ONE* **2016**, *11* (7), e0158884. https://doi.org/10.1371/journal.pone.0158884.

(88) Thompson, R. E.; Larson, D. R.; Webb, W. W. Precise Nanometer Localization Analysis for Individual Fluorescent Probes. *Biophys. J.* **2002**, *82* (5), 2775–2783. https://doi.org/10.1016/S0006-3495(02)75618-X.

(89) Conley, N. R.; Biteen, J. S.; Moerner, W. E. Cy3-Cy5 Covalent Heterodimers for Single-Molecule Photoswitching. *J Phys Chem B* **2008**, *112* (38), 11878–11880. https://doi.org/10.1021/jp806698p.

(90) Lee, H. D.; Lord, S. J.; Iwanaga, S.; Zhan, K.; Xie, H.; Williams, J. C.; Wang, H.; Bowman, G. R.; Goley, E. D.; Shapiro, L.; et al. Superresolution Imaging of Targeted Proteins in Fixed and Living Cells Using Photoactivatable Organic Fluorophores. *J Am Chem Soc* **2010**, *132* (43), 15099–15101. https://doi.org/10.1021/ja1044192.

(91) Lee, M. K.; Rai, P.; Williams, J.; Twieg, R. J.; Moerner, W. E. Small-Molecule Labeling of Live Cell Surfaces for Three-Dimensional Super-Resolution Microscopy. *Journal of the American Chemical Society* **2014**, *136* (40), 14003–14006. https://doi.org/10.1021/ja508028h.

(92) Werner, J. N.; Chen, E. Y.; Guberman, J. M.; Zippilli, A. R.; Irgon, J. J.; Gitai, Z. Quantitative Genome-Scale Analysis of Protein Localization in an Asymmetric Bacterium. *Proceedings of the National Academy of Sciences* **2009**, *106* (19), 7858–7863. https://doi.org/10.1073/pnas.0901781106.

(93) Chen, I.; Howarth, M.; Lin, W.; Ting, A. Y. Site-Specific Labeling of Cell Surface Proteins with Biophysical Probes Using Biotin Ligase. *Nature Methods* **2005**, *2* (2), 99–104. https://doi.org/10.1038/nmeth735.

(94) Giepmans, B. N. G.; Adams, S. R.; Ellisman, M. H.; Tsien, R. Y. The Fluorescent Toolbox for Assessing Protein Location and Function. *Science* **2006**, *312* (5771), 217–224. https://doi.org/10.1126/science.1124618.

(95) Rabuka, D. Chemoenzymatic Methods for Site-Specific Protein Modification. *Curr Opin Chem Biol* **2010**, *14* (6), 790–796. https://doi.org/10.1016/j.cbpa.2010.09.020.

(96) Fernández-Suárez, M.; Baruah, H.; Martínez-Hernández, L.; Xie, K. T.; Baskin, J. M.; Bertozzi, C. R.; Ting, A. Y. Redirecting Lipoic Acid Ligase for Cell Surface Protein Labeling with Small-Molecule Probes. *Nat. Biotechnol.* **2007**, *25* (12), 1483–1487. https://doi.org/10.1038/nbt1355.

(97) Carrico, I. S.; Carlson, B. L.; Bertozzi, C. R. Introducing Genetically Encoded Aldehydes into Proteins. *Nature Chemical Biology* **2007**, *3* (6), 321–322. https://doi.org/10.1038/nchembio878.

(98) Mao, H.; Hart, S. A.; Schink, A.; Pollok, B. A. Sortase-Mediated Protein Ligation: A New Method for Protein Engineering. *J. Am. Chem. Soc.* **2004**, *126* (9), 2670–2671. https://doi.org/10.1021/ja039915e.

(99) Glasgow, J. E.; Salit, M. L.; Cochran, J. R. In Vivo Site-Specific Protein Tagging with Diverse Amines Using an Engineered Sortase Variant. *Journal of the American Chemical Society* **2016**, *138* (24), 7496–7499. https://doi.org/10.1021/jacs.6b03836.

(100) Dozier, J. K.; Khatwani, S. L.; Wollack, J. W.; Wang, Y.-C.; Schmidt-Dannert, C.; Distefano, M. D. Engineering Protein Farnesyltransferase for Enzymatic Protein Labeling Applications. *Bioconjug Chem* **2014**, *25* (7), 1203–1212. https://doi.org/10.1021/bc500240p.

(101) Griffin, B. A.; Adams, S. R.; Tsien, R. Y. Specific Covalent Labeling of Recombinant Protein Molecules inside Live Cells. *Science* **1998**, *281* (5374), 269–272.

(102) Adams, S. R.; Campbell, R. E.; Gross, L. A.; Martin, B. R.; Walkup, G. K.; Yao, Y.; Llopis, J.; Tsien, R. Y. New Biarsenical Ligands and Tetracysteine Motifs for Protein Labeling in Vitro and in Vivo: Synthesis and Biological Applications. *J. Am. Chem. Soc.* **2002**, *124* (21), 6063–6076.

(103) Cao, H.; Chen, B.; Squier, T. C.; Mayer, M. U. CrAsH: A Biarsenical Multi-Use Affinity Probe with Low Non-Specific Fluorescence. *Chem. Commun. (Camb.)* **2006**, No. 24, 2601–2603. https://doi.org/10.1039/b602699k.

(104) Cao, H.; Xiong, Y.; Wang, T.; Chen, B.; Squier, T. C.; Mayer, M. U. A Red Cy3-Based Biarsenical Fluorescent Probe Targeted to a Complementary Binding Peptide. *J. Am. Chem. Soc.* **2007**, *129* (28), 8672–8673. https://doi.org/10.1021/ja070003c.

(105) Halo, T. L.; Appelbaum, J.; Hobert, E. M.; Balkin, D. M.; Schepartz, A. Selective Recognition of Protein Tetraserine Motifs with a Cell-Permeable, pro-Fluorescent Bis-Boronic Acid. *J. Am. Chem. Soc.* **2009**, *131* (2), 438–439. https://doi.org/10.1021/ja807872s.

(106) Wang, L.; Brock, A.; Herberich, B.; Schultz, P. G. Expanding the Genetic Code of Escherichia Coli. *Science* **2001**, *292* (5516), 498–500. https://doi.org/10.1126/science.1060077.

(107) Bianco, A.; Townsley, F. M.; Greiss, S.; Lang, K.; Chin, J. W. Expanding the Genetic Code of Drosophila Melanogaster. *Nat. Chem. Biol.* **2012**, *8* (9), 748–750. https://doi.org/10.1038/nchembio.1043.

(108) Noren, C. J.; Anthony-Cahill, S. J.; Griffith, M. C.; Schultz, P. G. A General Method for Site-Specific Incorporation of Unnatural Amino Acids into Proteins. *Science* **1989**, *244* (4901), 182–188.

(109) Charbon, G.; Brustad, E.; Scott, K. A.; Wang, J.; Løbner-Olesen, A.; Schultz, P. G.; Jacobs-Wagner, C.; Chapman, E. Subcellular Protein Localization by Using a Genetically Encoded Fluorescent Amino Acid. *ChemBioChem* **2011**, *12* (12), 1818–1821. https://doi.org/10.1002/cbic.201100282.

(110) Chen, S.; Ji, X.; Gao, M.; Dedkova, L. M.; Hecht, S. M. In Cellulo Synthesis of Proteins Containing a Fluorescent Oxazole Amino Acid. *J. Am. Chem. Soc.* **2019**, *141* (14), 5597–5601. https://doi.org/10.1021/jacs.8b12767.

(111) Keppler, A.; Gendreizig, S.; Gronemeyer, T.; Pick, H.; Vogel, H.; Johnsson, K. A General Method for the Covalent Labeling of Fusion Proteins with Small Molecules in Vivo. *Nat. Biotechnol.* **2003**, *21* (1), 86–89. https://doi.org/10.1038/nbt765.

(112) Gautier, A.; Juillerat, A.; Heinis, C.; Corrêa, I. R.; Kindermann, M.; Beaufils, F.; Johnsson, K. An Engineered Protein Tag for Multiprotein Labeling in Living Cells. *Chem. Biol.* **2008**, *15* (2), 128–136. https://doi.org/10.1016/j.chembiol.2008.01.007.

(113) Los, G. V.; Encell, L. P.; McDougall, M. G.; Hartzell, D. D.; Karassina, N.; Zimprich, C.; Wood, M. G.; Learish, R.; Ohana, R. F.; Urh, M.; et al. HaloTag: A Novel Protein Labeling Technology for Cell Imaging and Protein Analysis. *ACS Chem. Biol.* **2008**, *3* (6), 373–382. https://doi.org/10.1021/cb800025k.

(114) Barlag, B.; Beutel, O.; Janning, D.; Czarniak, F.; Richter, C. P.; Kommnick, C.; Göser, V.; Kurre, R.; Fabiani, F.; Erhardt, M.; et al. Single Molecule Super-Resolution Imaging of Proteins in Living Salmonella Enterica Using Self-Labelling Enzymes. *Sci Rep* **2016**, *6*. https://doi.org/10.1038/srep31601.

(115) Grimm, J. B.; English, B. P.; Choi, H.; Muthusamy, A. K.; Mehl, B. P.; Dong, P.; Brown, T. A.; Lippincott-Schwartz, J.; Liu, Z.; Lionnet, T.; et al. Bright Photoactivatable Fluorophores for Single-Molecule Imaging. *Nature Methods* **2016**, *13* (12), 985–988. https://doi.org/10.1038/nmeth.4034.

(116) Nimchuk, Z.; Marois, E.; Kjemtrup, S.; Leister, R. T.; Katagiri, F.; Dangl, J. L. Eukaryotic Fatty Acylation Drives Plasma Membrane Targeting and Enhances Function of Several Type III Effector Proteins from Pseudomonas Syringae. *Cell* **2000**, *101* (4), 353–363.

(117) Boutin, J. A. Myristoylation. *Cell. Signal.* **1997**, *9* (1), 15–35.

(118) Boisson, B.; Giglione, C.; Meinnel, T. Unexpected Protein Families Including Cell Defense Components Feature in the N-Myristoylome of a Higher Eukaryote. *J. Biol. Chem.* **2003**, *278* (44), 43418–43429. https://doi.org/10.1074/jbc.M307321200.

(119) Lu, T.; Li, Q.; Katoh, A.; Hernandez, J.; Duffin, K.; Jackson-Machelski, E.; Knoll, L. J.; Gokel, G. W.; Gordon, J. I. The Substrate Specificity of Saccharomyces Cerevisiae Myristoyl-CoA: Protein N-Myristoyltransferase. Polar Probes of the Enzyme's Myristoyl-CoA Recognition Site. *J. Biol. Chem.* **1994**, *269* (7), 5346–5357.

(120) Kishore, N. S.; Wood, D. C.; Mehta, P. P.; Wade, A. C.; Lu, T.; Gokel, G. W.; Gordon, J. I. Comparison of the Acyl Chain Specificities of Human Myristoyl-CoA Synthetase and Human Myristoyl-CoA:Protein N-Myristoyltransferase. *J. Biol. Chem.* **1993**, *268* (7), 4889–4902.

(121) Kishore, N. S.; Lu, T. B.; Knoll, L. J.; Katoh, A.; Rudnick, D. A.; Mehta, P. P.; Devadas, B.; Huhn, M.; Atwood, J. L.; Adams, S. P. The Substrate Specificity of Saccharomyces Cerevisiae Myristoyl-CoA:Protein N-Myristoyltransferase. Analysis of Myristic Acid Analogs Containing Oxygen, Sulfur, Double Bonds, Triple Bonds, and/or an Aromatic Residue. *J. Biol. Chem.* **1991**, *266* (14), 8835–8855.

(122) Devadas, B.; Lu, T.; Katoh, A.; Kishore, N. S.; Wade, A. C.; Mehta, P. P.; Rudnick, D. A.; Bryant, M. L.; Adams, S. P.; Li, Q. Substrate Specificity of Saccharomyces Cerevisiae Myristoyl-CoA: Protein N-Myristoyltransferase. Analysis of Fatty Acid Analogs Containing Carbonyl Groups, Nitrogen Heteroatoms, and Nitrogen Heterocycles in an in Vitro Enzyme Assay and Subsequent Identification of Inhibitors of Human Immunodeficiency Virus I Replication. *J. Biol. Chem.* **1992**, *267* (11), 7224–7239.

(123) Duronio, R. J.; Jackson-Machelski, E.; Heuckeroth, R. O.; Olins, P. O.; Devine, C. S.; Yonemoto, W.; Slice, L. W.; Taylor, S. S.; Gordon, J. I. Protein N-Myristoylation in Escherichia Coli: Reconstitution of a Eukaryotic Protein Modification in Bacteria. *Proceedings of the National Academy of Sciences* **1990**, *87* (4), 1506–1510. https://doi.org/10.1073/pnas.87.4.1506.

(124) Hang, H. C.; Geutjes, E.-J.; Grotenbreg, G.; Pollington, A. M.; Bijlmakers, M. J.; Ploegh, H. L. Chemical Probes for the Rapid Detection of Fatty-Acylated Proteins in Mammalian Cells. *J. Am. Chem. Soc.* **2007**, *129* (10), 2744–2745. https://doi.org/10.1021/ja0685001.

(125) Heal, W. P.; Wickramasinghe, S. R.; Leatherbarrow, R. J.; Tate, E. W. N-Myristoyl Transferase-Mediated Protein Labelling in Vivo. *Organic & Biomolecular Chemistry* **2008**, *6* (13), 2308. https://doi.org/10.1039/b803258k.

(126) Heal, W. P.; Wright, M. H.; Thinon, E.; Tate, E. W. Multifunctional Protein Labeling via Enzymatic N-Terminal Tagging and Elaboration by Click Chemistry. *Nature Protocols* **2012**, *7* (1), 105–117. https://doi.org/10.1038/nprot.2011.425.

(127) Kulkarni, C.; Kinzer-Ursem, T. L.; Tirrell, D. A. Selective Functionalization of the Protein N Terminus with N-Myristoyl Transferase for Bioconjugation in Cell Lysate. *ChemBioChem* **2013**, *14* (15), 1958–1962. https://doi.org/10.1002/cbic.201300453.

(128) Tocheva, E. I.; Li, Z.; Jensen, G. J. Electron Cryotomography. *Cold Spring Harb Perspect Biol* **2010**, *2* (6), a003442. https://doi.org/10.1101/cshperspect.a003442.

(129) Wolff, G.; Hagen, C.; Grünewald, K.; Kaufmann, R. Towards Correlative Super-Resolution Fluorescence and Electron Cryo-Microscopy. *Biol. Cell* **2016**, *108* (9), 245–258. https://doi.org/10.1111/boc.201600008.

(130) Nickell, S.; Kofler, C.; Leis, A. P.; Baumeister, W. A Visual Approach to Proteomics. *Nat. Rev. Mol. Cell Biol.* **2006**, *7* (3), 225–230. https://doi.org/10.1038/nrm1861.

(131) Chang, Y.-W.; Chen, S.; Tocheva, E. I.; Treuner-Lange, A.; Löbach, S.; Søgaard-Andersen, L.; Jensen, G. J. Correlated Cryogenic Photoactivated Localization Microscopy and Cryo-Electron Tomography. *Nature Methods* **2014**, *11* (7), 737–739. https://doi.org/10.1038/nmeth.2961.

(132) Faro, A. R.; Carpentier, P.; Jonasson, G.; Pompidor, G.; Arcizet, D.; Demachy, I.; Bourgeois, D. Low-Temperature Chromophore Isomerization Reveals the Photoswitching Mechanism of the Fluorescent Protein Padron. *J. Am. Chem. Soc.* **2011**, *133* (41), 16362–16365. https://doi.org/10.1021/ja207001y.

(133) Kaufmann, R.; Hagen, C.; Grünewald, K. Fluorescence Cryo-Microscopy: Current Challenges and Prospects. *Curr Opin Chem Biol* **2014**, *20*, 86–91. https://doi.org/10.1016/j.cbpa.2014.05.007.

(134) Dahlberg, P. D.; Sartor, A. M.; Wang, J.; Saurabh, S.; Shapiro, L.; Moerner, W. E. Identification of PAmKate as a Red Photoactivatable Fluorescent Protein for Cryogenic Super-Resolution Imaging. *Journal of the American Chemical Society* **2018**, *140* (39), 12310–12313. https://doi.org/10.1021/jacs.8b05960.

Chapter 2

CHEMOENZYMATIC LABELING OF PROTEINS FOR IMAGING IN BACTERIAL CELLS

Content from this chapter is adapted with permission from:

Ho, S. H.; Tirrell, D. A. Chemoenzymatic Labeling of Proteins for Imaging in Bacterial Cells. *Journal of the American Chemical Society* **2016**, *138*, 15098–15101. DOI: 10.1021/jacs.6b07067.

2.1 Abstract

Reliable methods to determine the subcellular localization of bacterial proteins are needed for the study of prokaryotic cell biology. We describe here a simple and general technique for imaging bacterial proteins *in situ* by fluorescence microscopy. The method uses the eukaryotic enzyme *N*-myristoyltransferase to modify the *N*-terminus of the protein of interest with an azido-fatty acid. Subsequent strain-promoted azide–alkyne cycloaddition allows conjugation of dyes and imaging of tagged proteins by confocal fluorescence microscopy. We demonstrate the method by labeling the chemotaxis proteins Tar and CheA and the cell division proteins FtsZ and FtsA in *Escherichia coli*. We observe distinct spatial patterns for each of these proteins in both fixed and live cells. The method should prove broadly useful for protein imaging in bacteria.

2.2 Main Text

Bacteria exercise exquisite control of protein localization as they orchestrate processes such as cell division, chromosome segregation, and environmental sensing.[1] Recent advances in super-resolution microscopy, including stochastic optical reconstruction microscopy (STORM)[2] and photo-activated localization microscopy (PALM),[3] along with new techniques in electron microscopy (e.g., correlated, cryogenic-PALM)[4] allow researchers to visualize molecular ultrastructures in bacterial cells with nanometer-scale resolution. Although fluorescent proteins (FPs) have found widespread use in labeling of proteins for imaging studies,[5] the large size of the FP can perturb protein localization.[6] Because organic fluorophores are smaller and generally brighter than FPs,[7] site-specific protein modification with biophysical probes remains an active area of research.[8–11]

Building on prior studies from the Gordon laboratory and others[12–14] including our own,[15] we report here a simple and general method for imaging bacterial proteins in fixed and live cells. By co-expressing human *N*-myristoyltransferase (NMT) and a target bacterial protein outfitted with a short NMT recognition sequence,[16] we append azido-fatty acids **1** or **3** to the N-terminus of the target (**Figure 2.1**). The azide-labeled protein is then tagged with a fluorophore (**2**) via strain-promoted azide–alkyne cycloaddition.[17,18]

Several features of the NMT system make it an effective tool for labeling recombinant proteins in bacterial cells and specifically in *Escherichia coli*. Neither azido fatty acids nor NMT are normally present in *E. coli* cells;[19] the azido functionality provides a site for facile bioorthogonal ligation; and the fatty acyl-coenzyme A synthetase (FACS) machinery of *E. coli* is known to convert **1** into an active substrate for NMT.[20] To the best of our knowledge, however, there has been no prior report on use of the NMT labeling system for protein imaging in bacteria.

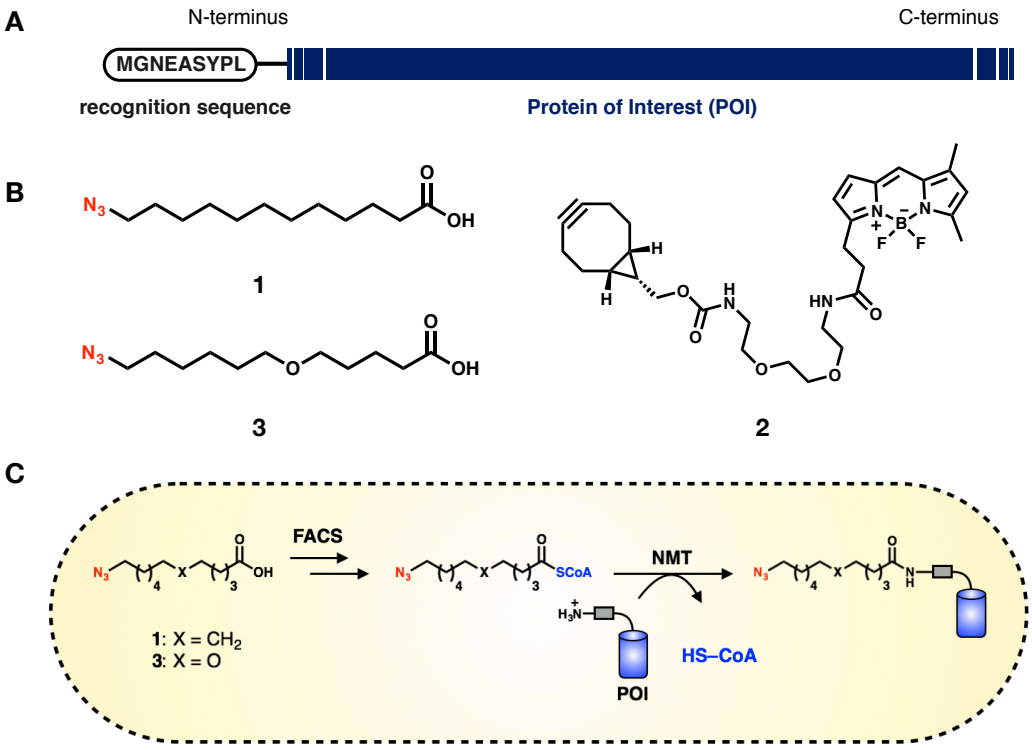

Figure 2.1. Site-specific labeling strategy in bacterial cells. (**A**) A genetically encoded N-terminal amino acid sequence serves as the recognition element for NMT on the protein of interest (POI). (**B**) Structures of fatty acid probes **1** and **3** and BODIPY fluorophore **2**. (**C**) Metabolic incorporation of fatty acid surrogate **1** or **3** allows site-specific labeling with NMT. Probe **1** or **3** is added directly to bacterial cultures and is converted into an active thioester for NMT recognition. FACS = Fatty acyl-coenzyme A synthetase, NMT = N-myristoyltransferase, HS–CoA: Coenzyme A.

We chose the bacterial chemotaxis proteins Tar and CheA and the cell division proteins FtsZ and FtsA as test substrates for NMT labeling and fluorescence imaging. The transmembrane protein Tar and cytoplasmic protein CheA localize at the poles of *E. coli* in clusters believed to enhance chemotactic signaling.[21,22] FtsZ and FtsA have been shown to localize at the septum and to play important roles in cell division.[23,24] To label these proteins, we introduced at each N-terminus the nonapeptide sequence MGNEASYPL derived from calcineurin B, a protein that is naturally myristoylated in mammalian cells.[25] NMT appends fatty acid substrates to the N-terminal glycine residue of the recognition sequence, following cleavage

of the initiator methionine by methionyl aminopeptidase.[26] Target proteins were expressed from modified pQE80-L plasmids under control of the bacteriophage T5 promoter[27] (**Table S2.1**). Cells were outfitted with a dual-plasmid expression system, with one plasmid (pHV738-NMT-MetAP)[28] directing expression of NMT and methionyl aminopeptidase and a second coding for inducible expression of one of the four bacterial protein targets (**Figure S2.1**). *E. coli* cultures were grown at 37 °C to an optical density at 600 nm (OD_{600}) of 0.5. Protein expression was then induced by addition of 1 mM isopropyl-β-D-thiogalactopyranoside (IPTG) and N-terminal labeling was accomplished by addition of 500 μM **1**. After 4 h, cells were harvested by centrifugation, washed twice with phosphate-buffered saline (PBS), and lysed. Crude lysates were alkylated with 1 mM iodoacetamide and subsequently treated with 2 μM BODIPY conjugate **2**, which carries a reactive bicyclononyne unit,[29] at 37 °C for 0.5 h.

We verified by gel electrophoresis that protein labeling occurred selectively. For each of the bacterial proteins, in-gel fluorescence detection (488 nm excitation, 520 nm emission) showed a distinct band with apparent molecular corresponding to that of the intended target (**Figure 2.2**). To provide a measure of the sensitivity of the method, we compared the intensity of this band in the inverted grayscale image to the background grayscale intensity associated with the same region of a gel prepared from uninduced cells treated with **1** and **2** (**Figure S2.2**). For cells expressing Tar, CheA, FtsZ, and FtsA, we found band intensities 2.4-, 6.6-, 6.7-, and 5.7-fold above background, respectively. We verified conjugation of a single copy of 1 to each protein of interest by mass spectrometry (**Figures S2.3−S2.6 and Tables S2.4−S2.7**). In cells labeled with **1**, we observed complete modification of each target protein; the unmodified forms were not observed. CheA was found in its phosphorylated form[30] in the absence of **1**. In cells expressing NMT and FtsZ or FtsA but not treated with **1**, we observed modification by endogenous myristic acid;[31] endogenous myristoylation was not detected for Tar or CheA.

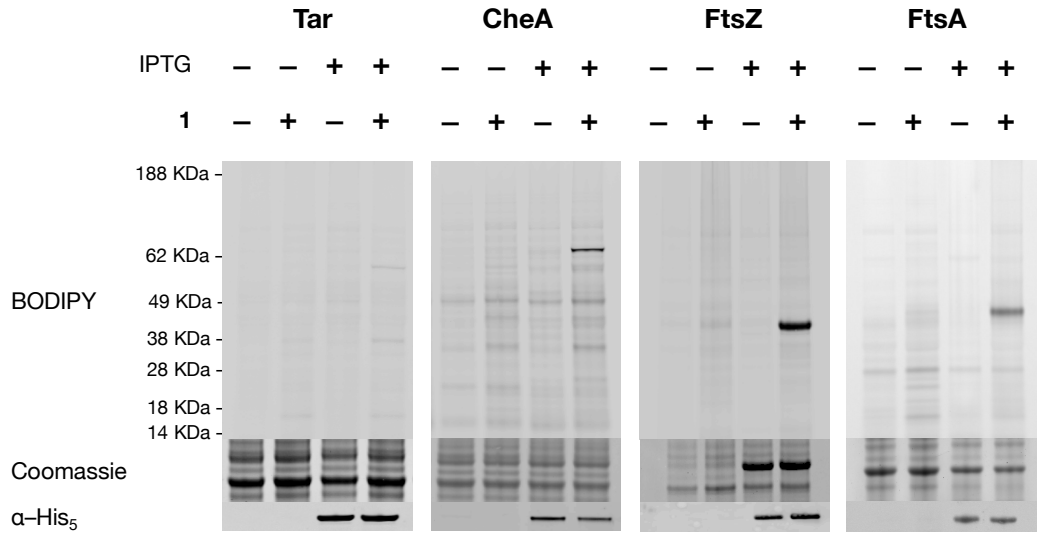

Figure 2.2. SDS–PAGE analysis of *E. coli* lysates prepared from cells expressing target proteins encoded on modified pQE80-L plasmids (**Table S2.1**). Protein expression was achieved by addition of 1 mM IPTG. Cultures were labeled with **1** at the time of induction. Cells were lysed and lysates were treated with **2**. Western blot analysis against a C-terminal His_5 epitope tag with a primary antibody conjugated to Alexa Fluor 647 confirms protein expression.

We screened a range of concentrations of **1** and **2** in cellular labeling experiments (**Figure S2.7**); concentrations of 250 μM **1** and 20 μM **2** were found to be sufficient. At these concentrations, we observed no effect on cell growth (**Figure S2.8**). We found no chain length redistribution of **1** in cells (**Figure S2.9**), but we did find evidence for incorporation of **1** into the phosphatidylethanolamine fraction of cellular lipids (Figures S10−S12). Although reaction of **2** with modified membrane lipids might be expected to contribute to diffuse background labeling in imaging experiments, we did not encounter problems of this kind.

For *in situ* imaging experiments, target proteins were outfitted with C-terminal myc tags for immunofluorescence labeling and expressed from modified pBAD24 plasmids (**Table S2.2**) under control of the tightly regulated P_{BAD} promoter[32] (**Figure S2.13**). Cells were treated with 0.2% (w/v) arabinose and 250 μM **1** at 37 °C for 2 h, fixed with 4% paraformaldehyde, and permeabilized with 0.3% (v/v) Triton X-100. Permeabilized cells were incubated with 20 μM **2** and an anti-myc antibody conjugated to Alexa Fluor 647 for two-color fluorescence

labeling. In fluorescence confocal microscopy, cells were excited at 488 nm and the emission was monitored from 505 to 550 nm for detection of the BODIPY fluorophore. The same cells were excited at 633 nm and monitored at 650 nm for immunofluorescence detection. We found clear evidence of polar localization for the bacterial chemotaxis proteins Tar and CheA and septal localization for the cell division proteins FtsZ and FtsA (**Figure 2.3**). Control experiments confirmed that addition of the hydrophobic fatty acid **1** did not interfere with localization of the target proteins, nor was there significant interference from labeling of **1** in the absence of induction of the target protein (**Figures S2.14 and S2.15**).

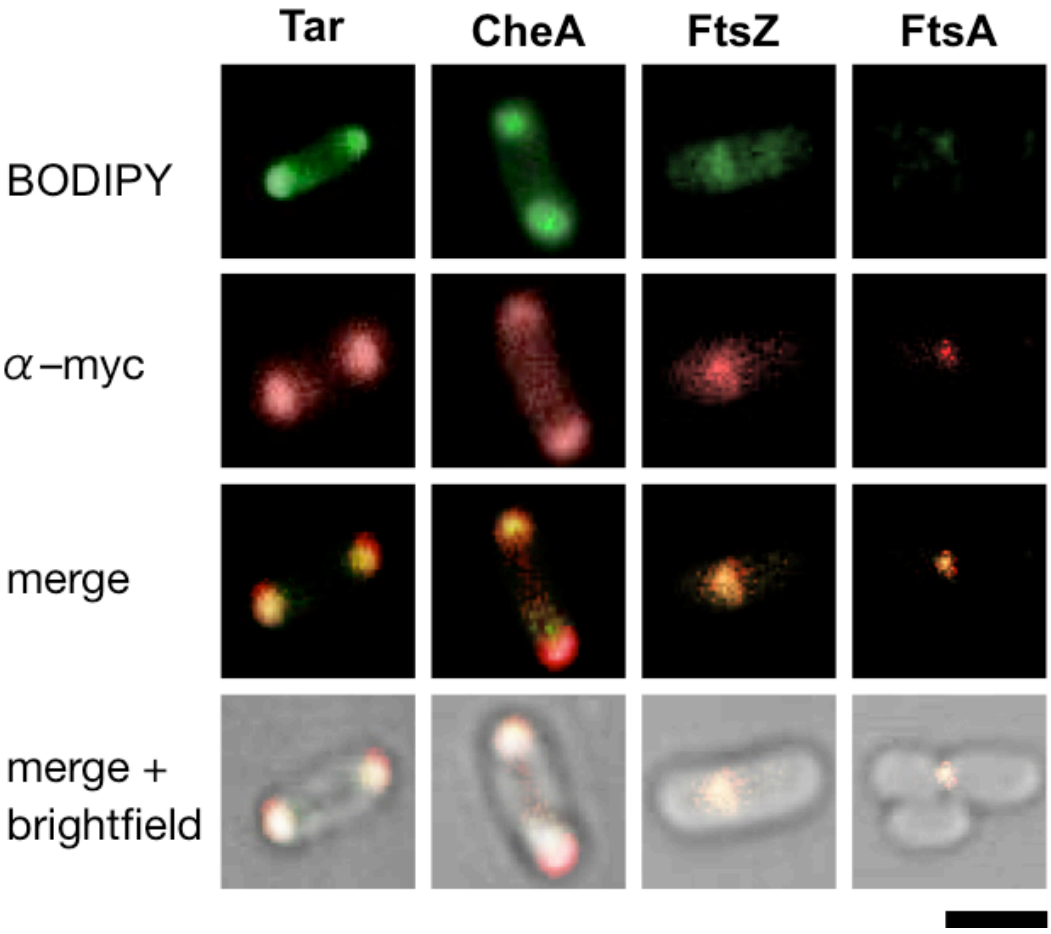

Figure 2.3. Imaging of proteins in fixed cells. Polar localization of Tar and CheA can be visualized by *N*-terminal fluorescence labeling with **2** and by immunofluorescence. Septal localization of FtsZ and FtsA can be visualized in similar fashion (scale bar = 1 μm).

We then asked whether the methods introduced here could be used for protein imaging in live cells. Cells harboring both pHV738-NMT-MetAP and one of the modified pBAD24 plasmids for inducible expression of target proteins (**Table S2.2**) were treated with 250 μM **1** at the time of induction and then grown at 37 °C for 2 h. Cells were collected by centrifugation, resuspended to an OD_{600} of 2, and rinsed three times with PBS. A 100 μL aliquot of the cell suspension was treated with 20 μM **2** at 37 °C for 30 min in the dark, and the cells were washed three times with PBS and mounted on agarose slides for imaging. When we labeled cells with **2** without fixation or permeabilization, we again found clear evidence of polar localization of each of the chemotaxis proteins and septal localization of each of the cell division proteins (**Figure 2.4**). Analysis of fluorescence from cells expressing Tar, CheA, FtsZ, and FtsA showed labeling 2.7-, 9.8-, 10.8-, and 7.1 fold above background, respectively (**Figure S2.16**). Labeling of FtsZ was also observed at lower concentrations of arabinose (**Figure S2.17**). In control experiments, cells did not show significant fluorescence in the absence of expression of the target protein or treatment with **1** (**Figure S2.18**). These results suggest that the NMT labeling system and fluorophore **2** should be broadly useful for live-cell imaging.

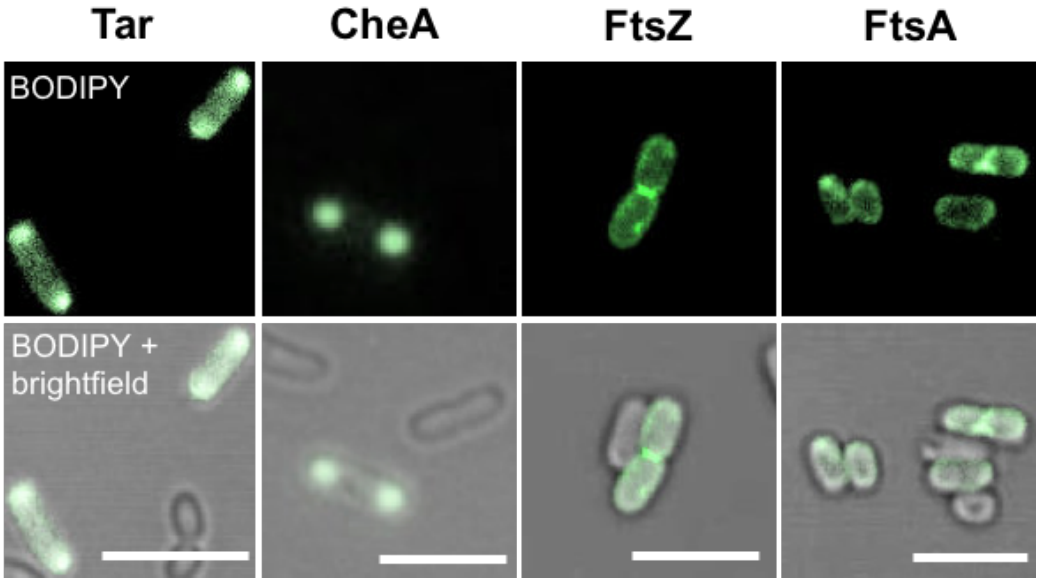

Figure 2.4. Live-cell images for chemotaxis and cell division proteins labeled with **1** and **2** (scale bar = 2 μm).

Finally, we asked whether both the *E. coli* FACS[33] and NMT could process other fatty acid substrates and expand the toolbox of probes for protein imaging. To demonstrate the feasibility of using alternative fatty acids, we prepared the more hydrophilic fatty acid **3**. Analysis of crude bacterial lysates prepared from cells treated with **2** and **3** confirmed selective modification of Tar, CheA, FtsZ, and FtsA (**Figures S2.19−S2.21**). The extent of modification by **3** was determined by mass spectrometry (**Figures S2.22−S2.25 and Tables S2.4−S2.7**). Addition of **3** did not affect cell growth (**Figure S2.8**). Degradation of **3** in cells was not observed (**Figure S2.9**), and 3 did not perturb the lipidome (**Figure S2.26**).

Live cells labeled with **3** yielded clear evidence of polar localization for Tar and CheA as well as septal localization for FtsZ and FtsA (**Figure S2.27**); the extent of labeling above background was similar to that observed with **1** (**Figure S2.16**). These results, along with the known promiscuity of NMT, suggest that other fatty acids bearing bioorthogonal functionality might be useful for protein labeling and imaging in live bacterial cells.

The results reported here demonstrate the feasibility of using NMT to modify membrane-associated and cytosolic bacterial proteins for fluorescence imaging. Although the method is unlikely to be applicable to proteins that bear N-terminal localization signals (roughly 10% of the *E. coli* proteome),[34] it may be especially useful in experiments in which fusion to a fluorescent protein disrupts localization of the protein of interest. With the advent of super-resolution imaging in bacterial systems,[35,36] we anticipate that the methods described here may be useful for conjugation of bright, photoswitchable fluorophores to bacterial proteins. We are currently working to combine the NMT labeling system with super-resolution techniques for live-cell protein imaging in bacteria.

2.3 Acknowledgments

The authors thank B. M. Babin, S. E. Stone, L. J. Dooling, K. P. Yuet, K. S. Burke, J. D. Bagert, and C. Kulkarni for insightful discussions. S. H. H. would like to thank D. K. Romney, S. Brinkmann-Chen, A. Collazo, S. Hess, A. Moridan, M. Shahgholi, C. Neubauer, and N. Dalleska for advice. S. H. H. is supported in part by a National Science Foundation Graduate Research Fellowship. This work was supported by the Caltech Center for Environmental Microbial Interactions, the Jacobs Institute for Molecular Engineering for Medicine, and the Institute for Collaborative Biotechnologies through grant W911NF-09-0001 from the U.S. Army Research Office.

2.4 Experimental Procedures

Materials and Methods. Unless otherwise stated, all synthetic reactions were performed using oven-dried glassware and under an atmosphere of argon. Anhydrous solvents (*N,N*-dimethylformamide and dichloromethane) were purchased from Sigma-Aldrich and kept under argon. All other chemicals and reagents for chemical reactions were purchased from commercial vendors (Sigma-Aldrich, Oakwood Chemical, Life Technologies) and used without further purification. Reactions were monitored with thin layer chromatography (EMD/Merck silica gel 60 F254 pre-coated plates) and UV light for visualization, with an acidic mixture of phosphomolybdic acid, cerium ammonium molybdate, or basic aqueous KMnO4 as developing agents. Flash chromatography purifications were carried out using EMD/Merck silica gel 60 (230–400 mesh). ^{1}H and ^{13}C NMR spectra were measured on either a Bruker Prodigy 400 (400 MHz and 101 MHz, respectively) or a Varian Inova 500 (500 MHz and 126 MHz, respectively), as noted. ^{1}H and ^{13}C NMR chemical shifts are reported as δ in units of parts per million (ppm) relative to tetramethylsilane (TMS, δ = 0) and calibrated using the residual solvent peak in chloroform (δ 7.26, singlet and δ 77.16, respectively). Data for ^{1}H NMR are reported as follows: chemical shift (δ ppm), multiplicity (s = singlet, d = doublet, t = triplet, q = quartet, m = multiplet, br = broad), coupling constant (Hz), and integration. High-resolution mass spectrometry (HRMS) was performed with either a JEOL JMS-600H High Resolution Mass Spectrometer with fast atom bombardment (FAB) at the California Institute of Technology Mass Spectrometry Facility in the Division of Chemistry and Chemical Engineering or with an Agilent 6200 Series TOF with an Agilent G1978A Multimode source in electrospray ionization (ESI), atmospheric pressure chemical ionization (APCI), or mixed (MM) ionization mode at the Caltech Beckman Institute Center for Catalysis and Chemical Synthesis. Low-resolution mass spectrometry (LRMS) was performed using an Agilent 1290 UHPLC–MS in positive or negative mode at the Center for Catalysis and Chemical Synthesis.

Lysogeny broth (LB) contained 10 g casein hydrolysate, 5 g yeast extract, and 10 g NaCl per liter. Super optimal broth (SOB) was composed of 20 g casein hydrolysate, 5 g yeast extract, 0.58 g NaCl, 0.19 g KCl, 10 mL 1 M MgCl2, and 10 mL 1M MgSO4 per liter. Super optimal

broth with catabolite repression (SOC) was comprised of SOB with the addition of 0.1 mL 2 M glucose to 1 L of SOB medium. Hyper Broth (AthenaESTM, USA) was purchased and prepared according to the manufacturer's instructions. Ampicillin sodium salt (BioPioneer, USA) and kanamycin sulfate (BioPioneer, USA) were used at working concentrations of 200 μg/mL and 35 μg/mL, respectively. Phosphate-buffered saline (PBS) was purchased from Thermo Fisher Scientific (USA) and maintained at pH 7.4. PBST was a solution comprising PBS and 0.1% v/v Tween-20. Q5 Hot Start High-Fidelity DNA Polymerase, restriction endonucleases, Instant Sticky-End Master Mix, Antarctic phosphatase, and Blunt Ligase Master Mix were all purchased from New England Biolabs (USA) and used according to the manufacturer's instructions. DNA constructs were sequenced by Retrogen (USA).

Cells were made chemically competent by using the Mix & Go *E. coli* Transformation Kit (Zymo Research, USA) according to the manufacturer's instructions. Electrocompetent cells were freshly prepared as follows: 8 mL of overnight cultures were washed extensively with 300 mM sucrose on ice. The culture was then concentrated to a final volume of 60 μL cells, after which 20 μL cells were mixed with 50 ng plasmid DNA. Electroporation was carried out using the Gene Pulse XCell (BioRad, USA) according to the recommended manufacturer's protocol. Cells were immediately rescued in 500 μL SOC at 37 °C for 1 h, and plated on LB agar plates carrying the appropriate antibiotic supplements. Plates containing colonies were always used within one week for further experiments.

The plasmid encoding N-myristoyltransferase (NMT) and methionyl aminopeptidase (pHV738-NMT-MetAP) was a generous gift from the Kahn laboratory (Emory University, USA). The plasmid confers resistance against kanamycin and contains the p15A origin of replication.

Plasmid construction in pQE80-L. The pQE80-L vector (Qiagen, USA) confers resistance to ampicillin and carries a 6xHis tag following the T5 promoter sequence, lac operon and ribosomal binding site (RBS). To remove the 6xHis tag and RBS, pQE80-L was linearized with EcoRI and HindIII. The gene fragment encoding the N-terminal nonapeptide sequence from eukaryotic calcineurin B (hCaNB) was 5'– ATG GGT AAC GAA GCG TCT TAC

CCG CTG – 3' (encoding the peptide sequence MGNEASYPL for NMT recognition). The gene encoding the chemoreceptor Tar was amplified from genomic DH10B *E. coli* DNA using primers such that the final PCR product read EcoRI::RBS:: hCaNB::BamHI::tar::SacI::6xHis::HindIII. This PCR product was digested with EcoRI/HindIII and ligated into pQE80-L to yield plasmid pQE80-hCaNB-Tar-6xHis. For the remaining bacterial proteins (CheA, FtsZ, and FtsA) amplification was carried out using genomic DH10B *E. coli* DNA as the template. Primers were designed such that the PCR products read BamHI::gene of interest::SacI. The PCR products were digested with BamHI/SacI and ligated into pQE80-hCaNB-Tar-6xHis, which was also digested with BamHI/SacI to yield plasmids pQE80-hCaNB-CheA-6xHis, pQE80-hCaNB-FtsZ-6xHis, and pQE80-hCaNB-FtsA-6xHis. These plasmids were transformed via electroporation into BL21 cells that already harbored plasmid pHV738-NMT-MetAP, generating strains SHH001–004 (**Table S2.3**). Colonies were selected against ampicillin and kanamycin. The primers used in this study are summarized in **Table S2.1**.

Plasmid construction in pBAD24. The pBAD24 vector contains an arabinose-inducible promoter and confers resistance against ampicillin. The gene encoding the methyl aspartate chemoreceptor Tar was amplified from genomic DH10B *E. coli* DNA using primers such that the final PCR product read EcoRI::hCaNB::SpeI::tar::SacI::6xHis::HindIII. Both the PCR product and pBAD24 were digested with EcoRI/HindIII and the resulting DNA fragments were ligated to make pBAD24-hCaNB-Tar-6xHis. For the remaining bacterial proteins (CheA, FtsZ, and FtsA, also amplified from genomic DH10B *E. coli* DNA), primers were designed such that the final PCR products read SpeI::gene of interest::SacI. The PCR products were digested with SpeI/SacI and ligated into pBAD24-hCaNB-Tar-6xHis, which was also digested with SpeI/SacI to make the plasmids pBAD24-hCaNB-CheA-6xHis, pBAD24-hCaNB-FtsZ-6xHis, and pBAD24-hCaNB-FtsA-6xHis. To encode the C-terminal myc epitope tag and remove the C-terminal His tag, phosphorylated primers were used for amplification, with the pBAD24-hCaNB-gene of interest-6xHis as the template. The forward primers for these four constructs are the same and contain the sequence encoding the myc epitope tag, whereas each reverse primer corresponds to a unique bacterial protein.

The template was then digested with DpnI, after which blunt-end ligation was performed to make the plasmids pBAD24-hCaNB-Tar-cmyc, pBAD24-hCaNB-CheA-cmyc, pBAD24-hCaNB-FtsZ-cmyc, and pBAD24-hCaNB-FtsA-cmyc. These plasmids were transformed via electroporation into BL21 cells that already harbored plasmid pHV738-NMT-MetAP, generating strains SHH005–012 (**Table S2.3**). Colonies were selected against both ampicillin and kanamycin. The primers used to design these constructs are summarized in **Table S2.2**.

Gel analyses. Sodium dodecyl sulfate–poly(acrylamide) gel electrophoresis (SDS–PAGE) was accomplished on a FB3000Q protein gel electrophoresis apparatus from Fisher Scientific (USA) using NuPAGE Novex 4–12% Bis-Tris protein gels (1.0 mm, 10-well) from Thermo Fisher (USA). Protein samples were mixed with an SDS loading buffer consisting of 0.05% w/v bromophenol blue, 0.1 M dithiothreitol (DTT), 10% w/v glycerol, 2% w/v sodium dodecyl sulfate, and 8 M urea in 50 mM Tris, pH 8.0. Samples were heated at 95 °C for 10 min to ensure denaturation and reduction of disulfide bonds. SeeBlue Plus 2 (Thermo Fisher, USA) was used as a molecular weight marker for all SDS–PAGE experiments. Total protein loading was visualized by using InstantBlue (Expedeon, Carlsbad, USA) as a coomassie blue stain, following the manufacturer's instructions.

Protein expression and labeling with ω-azido fatty acids. Individual colonies were used to inoculate LB medium supplemented with 200 μg/mL ampicillin and 35 μg/mL kanamycin, and cultures were grown overnight at 37 °C with mild agitation (250 rpm). Cultures were diluted 1:50 in 10 mL LB medium (also supplemented with 200 μg/mL ampicillin and 35 μg/mL kanamycin) and grown until the optical density at 600 nm (OD_{600}) reached 0.5. Protein expression was induced with either 1 mM isopropyl-β-D-1-thiogalactopyrannoside (IPTG) or 0.2% w/v L-(+)-arabinose (for pQE80-L or pBAD24 vectors, respectively). At the time of induction, 500 μM of either **1** or **3** was added to the culture; growth was continued for an additional 4 h (37 °C, 250 rpm). Cultures were harvested, washed twice with PBS, and resuspended in a solution containing 1% w/v sodium dodecyl sulfate (SDS) in Tris pH 8.4. Lysis was accomplished by boiling cells at 90 °C for

5 min, after which the solution was cooled on ice. Benzonase nuclease (Sigma-Aldrich, USA) and protease inhibitor (cOmplete, EDTA-free, Roche, USA) were added to the lysate to degrade chromosomal DNA and to prevent protein proteolysis, respectively. The lysate was allowed to incubate at 37 °C for 1 h, after which the lysates were centrifuged at 13,000 rpm at 4 °C for 30 min. The supernatant was collected, and protein quantification was performed using the bicinchoninic acid (BCA) assay kit (Thermo Fisher, USA). Lysates were separated into aliquots and stored at -80 °C until further use. Protein expression and labeling with fatty acids were performed in three independent replicate experiments.

Cell viability with compounds 1–3. Individual colonies were used to inoculate LB medium supplemented with 200 μg/mL ampicillin and 35 μg/mL kanamycin, and cultures were grown overnight at 37 °C with mild agitation (250 rpm). Cultures were diluted to an OD_{600} of 0.1 in LB medium (also supplemented with 200 μg/mL ampicillin and 35 μg/mL kanamycin). To each culture was added 250 μM **1** or **3**, or 20 μM fluorophore **2**. Cultures were allowed to continue to grow in the presence of each compound, and OD_{600} was monitored every 10 min for 800 min using a Varioskan LUX microplate reader (Thermo Fisher, USA). The OD_{600} of cultures grown without the presence of **1**–**3** were also measured as a control.

Preparation of fatty acid methyl esters (FAMEs) and mass analysis. Individual colonies were used to inoculate LB medium supplemented with 200 μg/mL ampicillin and 35 μg/mL kanamycin, and cultures were grown overnight at 37 °C with mild agitation (250 rpm). Cultures were diluted 1:50 in 10 mL LB medium (also supplemented with 200 μg/mL ampicillin and 35 μg/mL kanamycin) and grown until OD_{600} reached 0.5. To each culture was added 250 μM **1** or **3**, or no fatty acid mimic as a control. Growth was continued (37 °C, 250 rpm) until OD_{600} reached approximately 1.0. Cultures were harvested, washed twice with 0.5X PBS, and once with ddH_2O before being lyophilized. Fatty acids were extracted and methylated in a single acidic methylation step. Briefly, freeze-dried cell pellets (approximately 8.0 mg) were resuspended in a 20: 1 v/v methanol: acetyl chloride solution and heated at 100 °C for 10 min. The solutions were allowed to cool to room temperature,

after which 1 mL hexane and 1 mL water were added, and FAMEs were extracted twice with hexane (2 x 1 mL). The organic layers were combined and concentrated to a final volume of 200 μL for mass analysis. GC–MS analysis of FAMEs was accomplished using a ThermoFinnigan Trace GC equipped with a HP-5MS column (30 m x 0.250 mm x 0.25 μm), with the column effluent split between a flame ionization detector (FID) and ThermoFinnigan DSQ mass spectrometer. The GC oven was held at 90 °C for 1 min, ramped at 3 °C / min to 140 °C, ramped at 3 °C / min to 250 °C, and finally ramped at 20 °C / min to a final temperature of 310 °C. Known FAMEs present in *E. coli* were identified using the NIST MS Search 2.0 program and quantified against an internal standard (methyl behenate). GC traces of FAME extracts of cells not treated with fatty acids were compared with GC traces of FAME extracts of cells treated with fatty acids to identify new peaks.

Lipid extraction from cells grown with 1 or 3 and mass analysis. Individual colonies were used to inoculate LB medium supplemented with 200 μg/mL ampicillin and 35 μg/mL kanamycin, and cultures were grown overnight at 37 °C with mild agitation (250 rpm). Cultures were diluted 1:50 in 10 mL LB medium (also supplemented with 200 μg/mL ampicillin and 35 μg/mL kanamycin) and grown until OD_{600} reached 0.5. To each culture was added 250 μM **1** or **3**, or no fatty acid mimic as a control. Growth was continued (37 °C, 250 rpm) until OD_{600} reached approximately 1.0. Cultures were harvested and washed twice with 0.5X PBS. Lipid extraction was performed following literature protocols. Briefly, cell pellets were resuspended in 120 μL 0.1% wt/v ammonium acetate (dissolved in ddH_2O). To the solution was added 300 μL methanol and 1 mL methyl-*tert*-butyl ether (MTBE). Solutions were briefly vortexed and then sonicated for 1 hour at room temperature using a sonicator bath. 8 μg of internal standard (di17:0 phosphatidylcholine, phosphatidylethanolamine, and phosphatidylglycerol) (Avanti Polar Lipids, Alabaster, USA) was added at this time. Internal standards were prepared as 0.1 g/L solutions in methanol/dichloromethane (9:1) Lipids were extracted by addition of 260 μL of water, forming a biphasic solution, with lipids in the top (MTBE/methanol) layer. The MTBE/methanol layer was separated from the water layer and dried under a gentle stream of nitrogen. Dried samples were dissolved in 1 mL 9:1 methanol/dichloromethane for

analysis using LC–MS. Fatty acids **1** and **3** were also dissolved to a final concentration of 10 μM in 9:1 methanol/dichloromethane as standards for mass spectrometry. Samples were submitted to the Caltech Environmental Analysis Center of the Beckman Institute. Mass spectrometry (UPLC–MS) analysis was accomplished using an Acquity I-Class UPLC coupled to a Xevo G2-S TOF mass spectrometer (Waters, USA). Lipid samples (injection volume, 5 μL) were separated on an Acquity UPLC CSH C18 column (2.1 μm x 100 mm, 1.7 μm, Waters, USA). UPLC–TOF–MS^E data were collected in positive and negative mode using electrospray ionization (ESI). Indiscriminate fragmentation of all parent ions was performed with the capillary voltage set to 2.0 KV, the cone voltage set to 30 V, and the acquisition range set for data collection between 100 to 2000 m/z. MS^E data consists of two channels acquired simultaneously. Extracted ion chromatograms were performed using m/z searches based on fragment ions with a mass window of 10 mDa. Lipids were identified from their fragmentation patterns in both negative and positive mode.

Fluorescence labeling in cell lysates. To 100 μg protein in cell lysate diluted to 250 μL with PBS, was added iodoacetamide to a final concentration of 1 mM. Lysates were incubated at 37 °C for 1 h in the dark. Then, **2** was added to each solution to a final concentration of 2 μM. Reactions were performed at room temperature for 10 min in the dark. Proteins were then precipitated by addition of chloroform and methanol. Pellets were resuspended in SDS loading buffer. Samples were boiled for 10 min at 95 °C, after which 20 μg lysate were subjected to SDS–PAGE. Protein gels were washed with a solution containing 10% acetic acid, 20% methanol, and 70% water, with mild agitation (2 x 30 min). Fluorescence labeling was visualized using a Typhoon Trio (GE Healthcare, USA) with excitation at 488 nm, the photomultiplier tube (PMT) voltage set to 400 V, and emission monitored using a 520 nm band pass filter. Protein bands corresponding to the fluorescently labeled protein of interest were quantified using ImageQuant TL (GE Healthcare, USA), and normalized against the intensity of that particular band in the coomassie lane. Fluorescence labeling was quantified for each biological replicate. Plots representing the average fluorescence intensities from independent experiments were prepared using IGOR Pro (Wavemetrics, Oregon, USA).

Immunoblotting. Protein lysates were separated by SDS–PAGE and transferred to a 0.2 μm nitrocellulose membrane using an iBlot 2 gel transfer apparatus from Life Technologies (USA), following the manufacturer's protocol. Membranes were blocked with 5% w/v non-fat dry milk in PBST at room temperature for 1 h, and washed three times with PBST before incubating with either 1:5000 PentaHis–Alexa Fluor 647 (Qiagen, USA), or 1:2000 c–myc Alexa Fluor 647 conjugate (Cell Signaling Technologies, USA) at 4 °C overnight. Membranes (covered from light) were then washed five times with PBST at room temperature (10 min each wash). Fluorescence was visualized using a Typhoon Trio (GE Healthcare, USA) with excitation at 633 nm, the photomultiplier tube (PMT) voltage set to 300 V, and emission monitored using a 670 nm band pass filter.

Expression, purification and mass spectrometry of Tar. An overnight culture of *E. coli* strain SHH001 bearing plasmids pQE80-hCaNB-Tar-6xHis and pHV738-NMT-MetAP was diluted 1:50 in 100 mL Hyper Broth supplemented with 200 μg/mL ampicillin and 35 μg/mL kanamycin and grown at 37 °C with mild agitation (180 rpm). When OD_{600} reached approximately 0.5, the culture was cooled on ice for 20 min, after which 500 μM of either **1** or **3** and 0.025 mM IPTG were added to induce protein expression and to initiate *N*-terminal labeling. Cells were grown for an additional 20 h at reduced temperature and agitation speed (20 °C, 140 rpm), harvested, and stored at -80 °C until use. Cell pellets were thawed and resuspended in a solution (4 mL/g cell mass) containing 50 mM NaH_2PO_4, 300 mM NaCl, 1 mg/mL lysozyme, pH 8.0, and incubated on ice for 30 min. Lysis was achieved using a Q500 Sonicator (QSonica, USA), operating at a power of 500 watts and frequency of 20 kHz, with 5 s on and 25 s off bursts at 40% amplitude (1 min total for on cycle). The lysates were centrifuged at 13,000 rpm at 4 °C for 30 min, and the supernatant was discarded. To the insoluble fraction was added a solution (10 mL) containing 100 mM NaH_2PO_4, 10 mM Tris, 8 M urea, 1% w/v n-dodecyl β-D-maltoside (DDM), pH 8.0, and incubated at 4 °C with mild agitation for 30 min. Lysates were centrifuged at 13,000 rpm at 4 °C for 30 min, after which the protein was purified from lysate using Ni–NTA agarose (Qiagen, USA) under denaturing conditions. Briefly, 10 mL lysate was incubated with 250 μL Ni–NTA agarose at room temperature for 30 min and loaded onto the column. The column was washed with 10

column volumes of Buffer A (100 mM NaH_2PO_4, 10 mM Tris, 8 M urea, 0.2% w/v DDM, pH 8.0) and 10 column volumes of Buffer B (100 mM NaH_2PO_4, 10 mM Tris, 8 M urea, 0.2% w/v DDM, pH 6.3). The protein was eluted in 4 column volumes of Buffer C (100 mM NaH_2PO_4, 10 mM Tris, 8 M urea, 0.2% w/v DDM, pH 5.9) and 5 column volumes of Buffer D (100 mM NaH_2PO_4, 10 mM Tris, 8 M urea, 0.2% w/v DDM, pH 4.5). Fractions containing purified Tar were pooled and dialyzed against 25 mM Tris, 50 mM NaCl, 0.2% w/v DDM, pH 8.0 for 24 h. The protein was diluted in a solution of 0.2% v/v formic acid in 95% ddH_2O and 5% acetonitrile to a final concentration of 20 μM. Protein samples were submitted for LC–MS analysis using an Agilent 1100 MSD equipped with a quadrupole detector (Agilent Technologies, USA) at the Proteome Exploration Laboratory of the Beckman Institute at Caltech.

Expression, purification, and mass spectrometry of CheA. An overnight culture of *E. coli* strain SHH002 bearing plasmids pQE80-hCaNB-CheA-6xHis and pHV738-NMT-MetAP was diluted 1:50 in 100 mL Hyper Broth supplemented with 200 μg/mL ampicillin and 35 μg/mL kanamycin and grown at 37 °C with mild agitation (180 rpm). When OD_{600} reached approximately 0.5, the culture was cooled on ice for 20 min, after which 500 μM of either **1** or **3** and 0.025 mM IPTG were added to induce protein expression and to initiate *N*-terminal labeling. Cells were grown for an additional 20 h at reduced temperature and agitation speed (20 °C, 140 rpm), harvested, and stored at -80 °C until use. Pellets were thawed and resuspended in a solution (4 mL/g cell mass) containing 50 mM NaH_2PO_4, 300 mM NaCl, 10 mM imidazole, 1 mg/mL lysozyme, pH 8.0, and incubated on ice for 30 min. Lysis was achieved using a Q500 Sonicator (QSonica, USA), operating at a power of 500 watts and frequency of 20 kHz, with 5 s on and 25 s off bursts at 40% amplitude (1 min total for on cycle). The lysates were centrifuged at 13,000 rpm at 4 °C for 30 min. Clarified lysates were loaded onto Ni–NTA columns (1 mL size, HP resin, GE Healthcare) using an ÄKTA purifier FPLC system (GE Healthcare, USA). CheA was eluted from the column using a linear gradient from 100% Buffer A' (50 mM NaH_2PO_4, 300 mM NaCl, 10 mM imidazole, pH 8.0), 0% Buffer B' (50 mM NaH_2PO_4, 300 mM NaCl, 500 mM imidazole, pH 8.0) to 100% Buffer B' over 20 column volumes. Fractions containing CheA were pooled and

buffer exchanged into an anion exchange buffer (25 mM Tris, 10 mM NaCl, pH 8.0) and loaded onto an anion exchange Q-Sepharose column (HiTrapTM Q HP, GE Healthcare) using an ÄKTA purifier FPLC system (GE Healthcare, USA). CheA was eluted from the Q-column by running a linear gradient from 10 mM NaCl to 1 M NaCl over 20 column volumes. The protein was diluted in a solution of 0.2% v/v formic acid in 95% ddH_2O and 5% acetonitrile to a final concentration of 20 μM. Protein samples were submitted for LC–MS analysis using an Agilent 1100 MSD equipped with a quadrupole detector (Agilent Technologies, USA) at the Proteome Exploration Laboratory of the Beckman Institute at Caltech.

Expression, purification, and mass spectrometry of FtsZ. An overnight culture of *E. coli* strain SHH003 bearing plasmids pQE80-hCaNB-FtsZ-6xHis and pHV738-NMT-MetAP was diluted 1:50 in 10 mL LB medium supplemented with 200 μg/mL ampicillin and 35 μg/mL kanamycin and grown at 37 °C with mild agitation (250 rpm). When OD_{600} reached approximately 0.5, 500 μM of either **1** or **3** and 1 mM IPTG were added to the culture to induce protein expression and to initiate *N*-terminal labeling. Cells were grown for an additional 4 h (37 °C, 250 rpm) and harvested. Cell pellets were resuspended in a solution containing 50 mM NaH_2PO_4, 300 mM NaCl, 5 mM imidazole, 1 mg/mL lysozyme, and incubated on ice for 30 min. Lysis was achieved using a Q500 Sonicator (QSonica, USA), operating at a power of 500 watts and frequency of 20 kHz, with 5 s on and 25 s off bursts at 30% amplitude (1 min total for on cycle). The lysates were centrifuged at 13,000 rpm at 4 °C for 30 min, after which the protein was purified from lysate using Ni–NTA agarose spin columns (Qiagen, USA) according to the manufacturer's instructions. The purified protein was eluted in a buffer solution containing 50 mM NaH_2PO_4, 300 mM NaCl, and 500 mM imidazole. The purified protein was further concentrated using 30 kDa MWCO spin filters (Millipore, USA) and the buffer was exchanged into a solution containing 50 mM NH_4HCO_3. The protein was diluted in a solution of 0.2% v/v formic acid in 95% ddH_2O and 5% acetonitrile to a final concentration of 20 μM. ESI–TOF mass spectrometry was performed using an LCT Premier XE mass spectrometer (Waters, USA) at the Mass Spectrometry Facility in the Division of Chemistry and Chemical Engineering at Caltech. Mass spectra

were deconvoluted using MassLynx V 4.1 (Waters, USA) and spectra were plotted using IGOR Pro (Wavemetrics, Oregon, USA).

Expression, purification, and mass spectrometry of FtsA. An overnight culture of *E. coli* strain SHH004 bearing plasmids pQE80-hCaNB-FtsA-6xHis and pHV738-NMT-MetAP was diluted 1:50 in 100 mL Hyper Broth supplemented with 200 μg/mL ampicillin and 35 μg/mL kanamycin and grown at 37 °C with mild agitation (180 rpm). When OD_{600} reached approximately 0.5, the culture was cooled on ice for 20 min, after which 500 μM of either **1** or **3** and 0.025 mM IPTG were added to induce protein expression and to initiate *N*-terminal labeling. Cells were grown for an additional 20 h at reduced temperature and agitation speed (20 °C, 140 rpm), harvested, and stored at -80 °C until use. Cell pellets were resuspended in a solution (4 mL/g cell mass) containing 100 mM NaH_2PO_4, 10 mM Tris, 8 M urea, pH 8.0, and were lysed at 4 °C with mild agitation for 60 min. Lysates were clarified with centrifugation (13,000 rpm, 4 °C, 30 min). Clarified lysate was incubated with 250 μL Ni–NTA agarose (Qiagen, USA) at room temperature for 30 min before being loaded onto the column. The column was washed with 10 column volumes of 100 mM NaH_2PO_4, 10 mM Tris, 8 M urea, pH 8.0 and 15 column volumes of 100 mM NaH_2PO_4, 10 mM Tris, 8 M urea, pH 6.3. FtsA was eluted from the column with 5 column volumes of 100 mM NaH_2PO_4, 10 mM Tris, 8 M urea, pH 5.9, and 5 column volumes of 100 mM NaH_2PO_4, 10 mM Tris, 8 M urea, pH 4.5. Fractions containing FtsA were pooled and dialyzed against 25 mM Tris, 50 mM NaCl, pH 8.0 overnight. The protein was diluted in a solution of 0.2% v/v formic acid in 95% ddH_2O and 5% acetonitrile to a final concentration of 20 μM. Protein samples were submitted for LC–MS analysis using an Agilent 1100 MSD equipped with a quadrupole detector (Agilent Technologies, USA) at the Proteome Exploration Laboratory of the Beckman Institute at Caltech.

Mass calibration for the Agilent 1100 MSD was performed with an internal standard of myoglobin in positive mode. Mass calibration for the LCT Premier XE mass spectrometer was performed with an internal standard consisting of sodium iodide clusters.

Calculated and observed masses are summarized in **Tables S2.4–S2.7**. Protein masses were calculated using http://www.expasy.org. Masses for proteins modified with **1** or **3** take into account for the following: the loss of the starting Met, the addition of the fatty acid, and the loss of a water molecule due to amide bond formation between the fatty acid and the Gly residue. In cells that were not labeled with fatty acids, we observed that proteins of interest were labeled with endogenous myristic acid. Additionally, we observed the mass addition of a phosphoryl group on unmodified CheA. CheA has been reported to be autophosphorylated in bacterial cells.

Labeling bacterial proteins with ω-azido fatty acids in fixed cells. Overnight cultures were diluted 1:50 in LB medium supplemented with 200 μg/mL ampicillin and 35 μg/mL kanamycin and grown at 37°C with mild agitation (250 rpm). Cells (harboring pBAD24-derived and pHV738-NMT-MetAP plasmids) expressing Tar or CheA were grown to an OD_{600} of 0.5, and cells expressing FtsZ and FtsA were grown to an OD_{600} of 0.9, after which 0.2% w/v arabinose and 250 μM **1** were added to the cultures. Cells were allowed to grow for an additional 2 h, after which aliquots of cells were concentrated to an OD_{600} of approximately 2. Cells were fixed by addition of 4% paraformaldehyde in PBS for 10 min at room temperature, and permeabilized with 0.3% v/v Triton X-100 for 15 min at room temperature. Proteins were alkylated by addition of 100 mM iodoacetamide at room temperature for 1 h in the dark. *N*-terminal fluorescence labeling was carried out by incubating the cells with 20 μM **2** at room temperature for 30 min. Cells were rinsed four times with PBS and blocked with 3% w/v BSA in PBS at room temperature for 1 h, after which c-myc Alexa Fluor 647 antibody (Cell Signaling Technologies, USA) was added to the solution at a 1:100 dilution. Cells were allowed to incubate with the antibody solution overnight at 4 °C, and washed five times with PBS the following day. Cells were then mounted on 5% w/v agarose (in PBS) slides for imaging.

Labeling bacterial proteins with ω-azido fatty acids in live cells. Overnight cultures (harboring modified pBAD24 and pH738-NMT-MetAP plasmids) were diluted 1:50 in LB medium supplemented with 200 μg/mL ampicillin and 35 μg/mL kanamycin and grown at

37°C with mild agitation (250 rpm). Cells expressing Tar or CheA were grown to an OD_{600} of 0.5, and cells expressing FtsZ and FtsA were grown to an OD_{600} of 0.9, after which 0.2% w/v arabinose and 250 μM **1** or **3** were added to the cultures. Cells were allowed to grow for an additional 2 h, after which aliquots of cells were concentrated to an OD_{600} of approximately 2. Cells were rinsed three times with PBS, after which **2** was added to a 100 μL aliquot of cell suspension to a final concentration of 20 μM. The cells were incubated with **2** at 37°C for 30 min, after which the solution was washed three times with PBS to remove excess fluorophore. Cells were then mounted onto a 5% w/v agarose slide in PBS for imaging.

Fluorescence microscopy. Protein localization in cells was detected using an inverted Zeiss LSM 5 Exciter laser scanning confocal microscope at the Biological Imaging Facility of the Beckman Institute at Caltech. A 488 nm laser line (25 mW argon laser, 1–2 %) and 505–550 nm band pass filter were used in the detection of proteins labeled by **2**. Excitation at 633 nm (5 mW neon laser, 1–5 %) and emission at 650 nm (long pass) were used for immunofluorescence detection. Images were taken as 15 Z-stacks, with 0.2 μm per stack. ImageJ (NIH) was used to sum each Z-stack to form the projections represented in the figures. Cell Profiler was used to quantify the integrated fluorescence per cell for approximately 100–150 cells per sample.

Discussion on fatty acid probes 1 and 3. Gordon and coworkers previously showed that heteroatom-containing myristic acid analogues are well-tolerated by NMT, and that replacement of a methylene group by an ether oxygen atom is roughly equivalent to deletion of four methylene groups in terms of reduction in the hydrophobic character of the acid. Estimated logP values for **1** and **3** were calculated using Molinspiration Chemoinformatics (www.molinspiration.com), resulting in logP values of 4.84 and 2.86, respectively. The software uses group contribution values to determine estimated partition coefficients.

Discussion on fatty acid pool and intact lipids in *E. coli*. We analyzed the free fatty acid pool of bacterial cells that were treated with the azide-containing fatty acids (**Figure S2.9**) by GC–MS. Cells treated with **1** showed a peak in the GC trace that matched that of the

methyl ester of **1**; otherwise, the GC trace was identical to that of untreated cells. We looked at the intact phospholipids by LC–MS (**Figures S2.10–S2.12**). In cells treated with **1**, we observed a single new peak that was not present in untreated cells. On the basis of extracted ions in negative mode, we conclude that the phospholipid contained palmitic acid and **1**. Fragmentation in positive mode showed a m/z loss of 141 Da, corresponding to a phosphorylethanolamine molecule. This would suggest that *E. coli* incorporates **1** into a PE molecule. Treatment of cells with **3** did not significantly alter the intact lipid profile (**Figure S2.26**).

Table S2.1. Primers used in construction of pQE80-L-based vectors.

Plasmid name	Forward (5' to 3')	Reverse (3' to 5')
pQE80-hCaNB-Tar-6xHis	ATATGAATTCGAGGAGAAATTAACTATGGGTAACGAAGCGTCTTACCCGCTGGGATCCATGATTAACCGTATCCGC	TATAAGCTTCTAGTGATGGTGATGGTGATGGAGCTCAAATGTTTCCCAGTTTGGATC
pQE80-hCaNB-CheA-6xHis	ATATATGGATCCGTGAGCATGGATATAAGCGATTTTTATCAGACATTTTTTGATGAA	ATATATGAGCTCGGCGGCGGTGTTCGCCAT
pQE80-hCaNB-FtsZ-6xHis	ATATATGGATCCATGTTTGAACCAATGGAACTT	ATATATGAGCTCATCAGCTTGCTTACGCAG
pQE80-hCaNB-FtsA-6xHis	ATATATGGATCCATGATCAAGGCGACGGAC	ATATATGAGCTCAAACTCTTTTCGCAGCCAACT

Table S2.2. Primers used in construction of pBAD24-based vectors.

Plasmid name	Forward (5' to 3')	Reverse (3' to 5')
pBAD24-hCaNB-Tar-6xHis	ATATATGAATTCACCATGGGTAACGAAGCGTCTTACCCGCTGACTAGTATGATTAACCGTATCCGC	TATAAGCTTCTAGTGATGGTGATGGTGATGGAGCTCAAATGTTTCCCAGTTTGGATC
pBAD24-hCaNB-CheA-6xHis	ATATATACTAGTGTGAGCATGGATATAAGCGATTTTTATCAGACATTTTTTGATGAA	ATATATGAGCTCGGCGGCGGTGTTCGCCAT
pBAD24-hCaNB-FtsZ-6xHis	ATATATACTAGTATGTTTGAACCAATGGAACTT	ATATATGAGCTCATCAGCTTGCTTACGCAG
pBAD24-hCaNB-FtsA-6xHis	ATATATACTAGTATGATCAAGGCGACGGAC	ATATATGAGCTCAAACTCTTTTCGCAGCCAACT
pBAD24-hCaNB-Tar-cmyc	GAGCTCGAACAAAAACTTATTTCTGAAGAAGATCTGTAGAAGCTTGGCTGTTTTGG	AAATGTTTCCCAGTTTGGATC
pBAD24-hCaNB-CheA-cmyc	GAGCTCGAACAAAAACTTATTTCTGAAGAAGATCTGTAGAAGCTTGGCTGTTTTGG	GGCGGCGGTGTTCGCCATA
pBAD24-hCaNB-FtsZ-cmyc	GAGCTCGAACAAAAACTTATTTCTGAAGAAGATCTGTAGAAGCTTGGCTGTTTTGG	ATCAGCTTGCTTACGCAGG
pBAD24-hCaNB-FtsA-cmyc	GAGCTCGAACAAAAACTTATTTCTGAAGAAGATCTGTAGAAGCTTGGCTGTTTTGG	AAACTCTTTTCGCAGCCAAC

Table S2.3. *E. coli* strains constructed in this study.

Name	Strain	Genotype
SHH001	BL21	AmpR, KanR pQE80-hCaNB-Tar-6xHis pHV738-NMT-MetAP
SHH002	BL21	AmpR, KanR pQE80-hCaNB-CheA-6xHis pHV738-NMT-MetAP
SHH003	BL21	AmpR, KanR pQE80-hCaNB-FtsZ-6xHis pHV738-NMT-MetAP
SHH004	BL21	AmpR, KanR pQE80-hCaNB-FtsA-6xHis pHV738-NMT-MetAP
SHH005	BL21	AmpR, KanR pBAD24-hCaNB-Tar-6xHis pHV738-NMT-MetAP
SHH006	BL21	AmpR, KanR pBAD24-hCaNB-CheA-6xHis pHV738-NMT-MetAP
SHH007	BL21	AmpR, KanR pBAD24-hCaNB-FtsZ-6xHis pHV738-NMT-MetAP
SHH008	BL21	AmpR, KanR pBAD24-hCaNB-FtsA-6xHis pHV738-NMT-MetAP
SHH009	BL21	AmpR, KanR pBAD24-hCaNB-Tar-myc pHV738-NMT-MetAP
SHH010	BL21	AmpR, KanR pBAD24-hCaNB-CheA-myc pHV738-NMT-MetAP
SHH011	BL21	AmpR, KanR pBAD24-hCaNB-FtsZ-myc pHV738-NMT-MetAP
SHH012	BL21	AmpR, KanR pBAD24-hCaNB-FtsA-myc pHV738-NMT-MetAP

Table S2.4. Calculated and observed masses for modification of Tar.

Calculated mass (Da)	Observed mass (Da)	+/- (Da)	Notes
61984.8	61984.9	4.5	Unmodified Tar (–Met)
62208.0	Not observed		Tar modified with **1**
62229.8	62226.9	4.1	Tar modified with **1** (sodium adduct)
62210.0	62210.2	4.6	Tar modified with **3**

Table S2.5. Calculated and observed masses for modification of CheA.

Calculated mass (Da)	Observed mass (Da)	+/- (Da)	Notes
73391.5	73391.2	5.2	Unmodified CheA (–Met)
73470.5	73471.8	4.6	CheA modified by phosphorylation
73614.7	Not observed		CheA modified with **1**
73636.7	73635.9	5.1	CheA modified with **1** (sodium adduct)
73616.7	Not observed	4.9	CheA modified with **3**
73638.7	73638.7	5.1	CheA modified with **3** (sodium adduct)

Table S2.6. Calculated and observed masses for modification of FtsZ.

Calculated mass (Da)	Observed mass (Da)	+/- (Da)	Notes
42365.1	42364.8	1.1	Unmodified FtsZ (–Met)
42575.5	42575.1	1.0	FtsZ modified with endogenous myristic acid
42588.3	42588.2	1.0	FtsZ modified with **1**
42562.3	42562.2	1.0	FtsZ modified with **1** (reduction of azide to amine)
42590.3	42590.1	1.2	FtsZ modified with **3**

Table S2.7. Calculated and observed masses for modification of FtsA.

Calculated mass (Da)	Observed mass (Da)	+/- (Da)	Notes
47371.1	Not observed		Unmodified FtsA (–Met)
47581.5	47582.6	3.1	FtsA modified with endogenous myristic acid
47594.3	47594.6	3.5	FtsA modified with **1**
47596.3	47595.8	2.4	FtsA modified with **3**

2.5 Protein Sequences used in this Study

The NMT recognition sequence is highlighted in blue. *C*-terminal epitope tags (either 6xHis or myc) are highlighted in red.

pQE80-hCaNB-Tar-6xHis

MGNEASYPLGSMINRIRVVTLLVMVLGVFALLQLISGSLFFSSLHHSQKSFVVSNQLREQQGELTS
TWDLMLQTRINLSRSAVRMMMDSSNQQSNAKVELLDSARKTLAQAATHYKKFKSMAPLPEMVAT
SRNIDEKYKNYYTALTELIDYLDYGNTGAYFAQPTQGMQNAMGEAFAQYALSSEKLYRDIVTDNAD
DYRFAQWQLAVIALVVVLILLVAWYGIRRMLLTPLAKIIAHIREIAGGNLANTLTIDGRSEMGDLAQSV
SHMQRSLTDTVTHVREGSDAIYAGTREIAAGNTDLSSRTEQQASALEETAASMEQLTATVKQNAD
NARQASQLAQSASDTAQHGGKVVDGVVKTMHEIADSSKKIADIISVIDGIAFQTNILALNAAVEAAR
AGEQGRGFAVVAGEVRNLASRSAQAAKEIKALIEDSVSRVDTGSVLVESAGETMNNIVNAVTRVT
DIMGEIASASDEQSRGIDQVALAVSEMDRVTQQNASLVQESAAAAAALEEQASRLTQAVSAFRLA
ASPLTNKPQTPSRPASEQPPAQPRLRIAEQDPNWETFELHHHHHH

pQE80-hCaNB-CheA-6xHis

MGNEASYPLGSVSMDISDFYQTFFDEADELLADMEQHLLVLQPEAPDAEQLNAIFRAAHSIKGGA
GTFGFSVLQETTHLMENLLDEARRGEMQLNTDIINLFLETKDIMQEQLDAYKQSQEPDAASFDYIC
QALRQLALEAKGETPSAVTRLSVVAKSEPQDEQSRSQSPRRIILSRLKAGEVDLLEEELGHLTTLTD
VVKGADSLSAILPGDIAEDDITAVLCFVIEADQITFETVEVSPKISTPPVLKLAAEQAPTGRVEREKTT
RSNESTSIRVAVEKVDQLINLVGELVITQSMLAQRSSELDPVNHGDLITSMGQLQRNARDLQESVM
SIRMMPMEYVFSRYPRLVRDLAGKLGKQVELTLVGSSTELDKSLIERIIDPLTHLVRNSLDHGIELPE
KRLAAGKNSVGNLILSAEHQGGNICIEVTDDGAGLNRERILAKAASQGLTVSENMSDDEVAMLIFA
PGFSTAEQVTDVSGRGVGMDVVKRNIQKMGGHVEIQSKQGTGTTIRILLPLTLAILDGMSVRVADE
VFILPLNAVMESLQPREADLHPLAGGERVLEVRGEYLPIVELWKVFNVAGAKTEATQGIVVILQSGG
RRYALLVDQLIGQHQVVVKNLESNYRKVPGISAATILGDGSVALIVDVSALQAINREQRMANTAAEL
HHHHHH

pQE80-hCaNB-FtsZ-6xHis

MGNEASYPLGSMFEPMELTNDAVIKVIGVGGGGGNAVEHMVRERIEGVEFFAVNTDAQALRKTA
VGQTIQIGSGITKGLGAGANPEVGRNAADEDRDALRAALEGADMVFIAAGMGGGTGTGAAPVVAE
VAKDLGILTVAVVTKPFNFEGKKRMAFAEQGITELSKHVDSLITIPNDKLLKVLGRGISLLDAFGAAN
DVLKGAVQGIAELITRPGLMNVDFADVRTVMSEMGYAMMGSGVASGEDRAEEAAEMAISSPLLED
IDLSGARGVLVNITAGFDLRLDEFETVGNTIRAFASDNATVVIGTSLDPDMNDELRVTVVATGIGMD
KRPEITLVTNKQVQQPVMDRYQQHGMAPLTQEQKPVAKVVNDNAPQTAKEPDYLDIPAFLRKQA
DELHHHHHH

pQE80-hCaNB-FtsA-6xHis

MGNEASYPLGSMIKATDRKLVVGLEIGTAKVAALVGEVLPDGMVNIIGVGSCPSRGMDKGGVNDL
ESVVKCVQRAIDQAELMADCQISSVYLALSGKHISCQNEIGMVPISEEEVTQEDVENVVHTAKSVR
VRDEHRVLHVIPQEYAIDYQEGIKNPVGLSGVRMQAKVHLITCHNDMAKNIVKAVERCGLKVDQLIF
AGLASSYSVLTEDERELGVCVVDIGGGTMDIAVYTGGALRHTKVIPYAGNVVTSDIAYAFGTPPSD
AEAIKVRHGCALGSIVGKDESVEVPSVGGRPPRSLQRQTLAEVIEPRYTELLNLVNEEILQLQEKLR
QQGVKHHLAAGIVLTGGAAQIEGLAACAQRVFHTQVRIGAPLNITGLTDYAQEPYYSTAVGLLHYG
KESHLNGEAEVEKRVTASVGSWIKRLNSWLRKEFELHHHHHH

pBAD24-hCaNB-Tar-cmyc

MGNEASYPLTSMINRIRVVTLLVMVLGVFALLQLISGSLFFSSLHHSQKSFVVSNQLREQQGELTS
TWDLMLQTRINLSRSAVRMMMDSSNQQSNAKVELLDSARKTLAQAATHYKKFKSMAPLPEMVAT
SRNIDEKYKNYYTALTELIDYLDYGNTGAYFAQPTQGMQNAMGEAFAQYALSSEKLYRDIVTDNAD
DYRFAQWQLAVIALVVVLILLVAWYGIRRMLLTPLAKIIAHIREIAGGNLANTLTIDGRSEMGDLAQSV
SHMQRSLTDTVTHVREGSDAIYAGTREIAAGNTDLSSRTEQQASALEETAASMEQLTATVKQNAD
NARQASQLAQSASDTAQHGGKVVDGVVKTMHEIADSSKKIADIISVIDGIAFQTNILALNAAVEAAR
AGEQGRGFAVVAGEVRNLASRSAQAAKEIKALIEDSVSRVDTGSVLVESAGETMNNIVNAVTRVT
DIMGEIASASDEQSRGIDQVALAVSEMDRVTQQNASLVQESAAAAAALEEQASRLTQAVSAFRLA
ASPLTNKPQTPSRPASEQPPAQPRLRIAEQDPNWETFELEQKLISEEDL

pBAD24-hCaNB-CheA-cmyc

MGNEASYPLGSVSMDISDFYQTFFDEADELLADMEQHLLVLQPEAPDAEQLNAIFRAAHSIKGGA
GTFGFSVLQETTHLMENLLDEARRGEMQLNTDIINLFLETKDIMQEQLDAYKQSQEPDAASFDYIC
QALRQLALEAKGETPSAVTRLSVVAKSEPQDEQSRSQSPRRIILSRLKAGEVDLLEEELGHLTTLTD
VVKGADSLSAILPGDIAEDDITAVLCFVIEADQITFETVEVSPKISTPPVLKLAAEQAPTGRVEREKTT
RSNESTSIRVAVEKVDQLINLVGELVITQSMLAQRSSELDPVNHGDLITSMGQLQRNARDLQESVM
SIRMMPMEYVFSRYPRLVRDLAGKLGKQVELTLVGSSTELDKSLIERIIDPLTHLVRNSLDHGIELPE
KRLAAGKNSVGNLILSAEHQGGNICIEVTDDGAGLNRERILAKAASQGLTVSENMSDDEVAMLIFA
PGFSTAEQVTDVSGRGVGMDVVKRNIQKMGGHVEIQSKQGTGTTIRILLPLTLAILDGMSVRVADE
VFILPLNAVMESLQPREADLHPLAGGERVLEVRGEYLPIVELWKVFNVAGAKTEATQGIVVILQSGG
RRYALLVDQLIGQHQVVVKNLESNYRKVPGISAATILGDGSVALIVDVSALQAINREQRMANTAAEL
EQKLISEEDL

pBAD24-hCaNB-FtsZ-cmyc

MGNEASYPLGSMFEPMELTNDAVIKVIGVGGGGGNAVEHMVRERIEGVEFFAVNTDAQALRKTA
VGQTIQIGSGITKGLGAGANPEVGRNAADEDRDALRAALEGADMVFIAAGMGGGTGTGAAPVVAE
VAKDLGILTVAVVTKPFNFEGKKRMAFAEQGITELSKHVDSLITIPNDKLLKVLGRGISLLDAFGAAN
DVLKGAVQGIAELITRPGLMNVDFADVRTVMSEMGYAMMGSGVASGEDRAEEAAEMAISSPLLED
IDLSGARGVLVNITAGFDLRLDEFETVGNTIRAFASDNATVVIGTSLDPDMNDELRVTVVATGIGMD
KRPEITLVTNKQVQQPVMDRYQQHGMAPLTQEQKPVAKVVNDNAPQTAKEPDYLDIPAFLRKQA
DELEQKLISEEDL

pBAD24-hCaNB-FtsA-cmyc

MGNEASYPLGSMIKATDRKLVVGLEIGTAKVAALVGEVLPDGMVNIIGVGSCPSRGMDKGGVNDL
ESVVKCVQRAIDQAELMADCQISSVYLALSGKHISCQNEIGMVPISEEEVTQEDVENVVHTAKSVR
VRDEHRVLHVIPQEYAIDYQEGIKNPVGLSGVRMQAKVHLITCHNDMAKNIVKAVERCGLKVDQLIF
AGLASSYSVLTEDERELGVCVVDIGGGTMDIAVYTGGALRHTKVIPYAGNVVTSDIAYAFGTPPSD
AEAIKVRHGCALGSIVGKDESVEVPSVGGRPPRSLQRQTLAEVIEPRYTELLNLVNEEILQLQEKLR
QQGVKHHLAAGIVLTGGAAQIEGLAACAQRVFHTQVRIGAPLNITGLTDYAQEPYYSTAVGLLHYG
KESHLNGEAEVEKRVTASVGSWIKRLNSWLRKEFELEQKLISEEDL

2.6 Synthesis and Characterization of Compounds

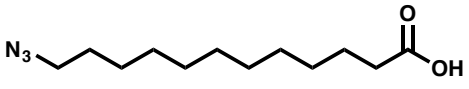

12-azidododecanoic acid (**1**). To a flamed-dried 100 mL round bottom flask, was added 20 mL DMF, 419.1 mg sodium azide (6.45 mmol, 1.80 equiv), and 53.7 mg sodium iodide (0.36 mmol, 0.1 equiv). The mixture was stirred to form a heterogeneous suspension, after which 12-bromododecanoic acid (1.0 g, 3.58 mmol, 1.0 equiv) was added. The reaction mixture was allowed to stir at room temperature for 24 h, after which 20 mL ethyl acetate was added, and the solution was cooled on ice. To the resultant solution, 1 M HCl was added dropwise until the suspension became clear. The reaction mixture was extracted twice with ethyl acetate (2 x 20 mL). The organic layer was washed three times with saturated LiCl (3 x 20 mL), dried over $MgSO_4$, and concentrated in vacuo, resulting in a slightly yellow solid. The crude product was washed extensively with ice-cold ether and ice-cold water before being filtered. The white solid was collected and dried overnight under high vacuum to afford 785.6 mg of **1** as a brilliant, white solid (91%). ^{1}H NMR (400 MHz, $CDCl_3$): δ 3.25 (t, 2H, J = 6.8 Hz), 2.35 (t, 2H, J = 7.6 Hz), 1.58 – 1.65 (m, 4H), 1.30 – 1.36 (m, 6H), 1.25 – 1.30 (m, 8H). ^{13}C NMR (101 MHz, $CDCl_3$): δ 179.67, 77.36, 51.63, 34.08, 29.58, 29.50, 29.35, 29.28, 29.17, 28.98, 26.85, 24.80. HRMS (FAB) calculated for $C_{12}H_{24}N_3O_2$ ($[M+H]^+$) 242.1868, found 242.1853.

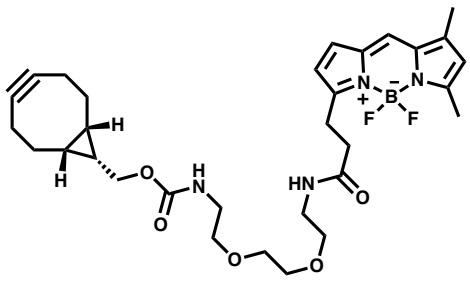

BCN–BODIPY conjugate (**2**). An oven-dried 20 mL scintillation vial was charged with 4,4-difluoro-5,7-dimethyl-4-bora-3a,4a-diaza-*s*-indacene-3-propionic acid (5 mg, 17 μmol, 1.0 equiv), *O*-(6-chlorobenzotriazol-1-yl)-*N,N,N',N'*-tetramethyluronium hexafluorophosphate (HCTU) (7 mg, 17 μmol, 1.0 equiv), and *N*-(1*R*,8*S*,9*s*)-bicyclo[6.1.0]non-4-yn-9-ylmethyloxycarbonyl]-1,8-diamino-3,6-dioxaoctane (10 mg, 31 μmol, 1.8 equiv). *N,N*-dimethylformamide (2 mL) was then added to the vial. To the solution, *N,N*-diisopropylethylamine (DIPEA) (6.7 μL, 39 μmol, 2.3 equiv) was added, and the reaction mixture was allowed to stir at room temperature for 4 h, after which the solvent was removed *in vacuo*. The residue was taken up in 10 mL ethyl acetate and

extracted twice with 1 M HCl (2 x 20 mL), washed once with deionized water (10 mL), and washed three times with saturated LiCl (3 x 30 mL). The organic layer was dried over Na_2SO_4 and concentrated under reduced pressure to give a lustrous brown oil as the crude product. Flash chromatography (1–2% methanol in dichloromethane) afforded 9.2 mg of **2** as a brilliant, red solid (90%). ^{1}H NMR (400 MHz, $CDCl_3$): δ, 7.08 (s, 1H), 6.89 (d, 1H, J = 4.0 Hz), 6.30 (d, 1H, J = 4.0 Hz), 6.12 (br s, 1H), 5.22 (br s, 1H), 4.14 (br s, 1H), 4.12 (br s, 1H), 3.57 (br s, 1H), 3.54 – 3.50 (m, 4H), 3.46 – 3.42 (m, 2H), 3.37 – 3.33 (m, 2H), 3.30 – 3.25 (m, 2H), 2.63 (t, 2H, J = 8.0 Hz), 2.56 (s, 3H), 2.25 (s, 3H), 2.23 – 2.21 (m, 2H), 1.61 – 1.50 (m, 7H), 1.33 (t, 2H, J = 8.8 Hz), 0.91 (t, 2H, J = 9.6 Hz). ^{13}C NMR (101 MHz, $CDCl_3$): δ, 171.89, 160.27, 157.71, 156.90, 143.92, 135.20, 133.49, 128.37, 123.88, 120.52, 117.63, 98.96, 70.39, 70.33, 70.24, 70.04, 62.90, 40.88, 39.39, 36.11, 29.16, 24.99, 21.57, 20.22, 17.90, 15.09, 11.48. HRMS (FAB) calculated for $C_{31}H_{42}O_5N_4BF_2$ ($[M+H]^+$) 599.3216, found 599.3219.

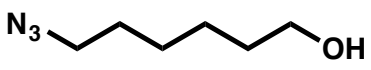

6-azidohexan-1-ol (**S1**). To a flamed-dried 100 mL round bottom flask was added sodium azide (968.9 mg, 14.9 mmol, 1.8 equiv), sodium iodide (123.4 mg, 0.83 mmol, 0.1 equiv), and 10 mL DMF to form a heterogeneous suspension. To this mixture was added 6-bromohexan-1-ol (1.5 g, 8.28 mmol, 1.0 equiv) dropwise over the course of 2 min. The reaction mixture was allowed to stir at room temperature for 18 h, after which the solution was diluted with 30 mL ethyl acetate and cooled on ice. To the solution, 10 mL 1 M HCl was slowly added to quench the reaction. The solution was extracted twice with 1 M HCl (2 x 10 mL), twice with deionized water (2 x 10 mL), twice with saturated LiCl (2 x 10 mL), dried over $MgSO_4$, and concentrated *in vacuo*. Flash chromatography (10% ethyl acetate: 90% hexanes) afforded 1.07 g of **S1** as a colorless oil (90%). ^{1}H NMR (500 MHz, $CDCl_3$): δ, 3.66 (t, 2H, J = 6.5 Hz), 3.28 (t, 2H, J = 7.0 Hz), 1.61 (m, 4H), 1.41 (m, 4H). ^{13}C NMR (126 MHz, $CDCl_3$): δ, 62.93, 51.51, 32.69, 28.95, 26.66, 25.47. LRMS (ESI) calculated for $C_6H_{14}N_3O$ ($[M+H]^+$) 144, found 144.

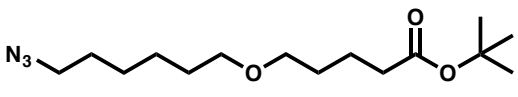

tert-butyl 5-((6-azidohexyl)oxyl)pentanoate (**S2**). A flame-dried 50 mL flask was charged with **S1** (276 mg, 1.93 mmol, 1.1 equiv), followed by anhydrous DMF (10 mL), and cooled

to 0°C on ice. To the solution was slowly added NaH (84.1 mg 60% wt dispersion in mineral oil, 2.10 mmol, 1.2 equiv), and the resulting suspension was allowed to stir on ice for 0.5 h. The solution was warmed to room temperature and allowed to stir for an additional 0.5 h, after which the reaction mixture was cooled on ice. To the reaction mixture was added *tert*-butyl 5-bromopentanoate (415.5 mg, 1.75 mmol, 1.0 equiv) dropwise over the course of 10 min. The reaction mixture was allowed to warm to room temperature and stirred for an additional 5 h, after which the solution was cooled on ice and quenched by addition of aqueous, saturated LiCl (20 mL). The solution was extracted twice with ethyl acetate, dried over $MgSO_4$, and concentrated in vacuo. The residue was suspended in dichloromethane and purified by flash chromatography (1–5% ethyl acetate in hexanes) to afford 146.7 mg of **S2** as a colorless oil (28%). ^{1}H NMR (500 MHz, $CDCl_3$): δ, 3.40 (t, 2H, J = 6.0 Hz), 3.39 (t, 2H, J = 6.5 Hz), 2.23 (t, 2H, J = 7.0 Hz), 1.62 (m, 4H), 1.59 (m, 4H), 1.43 (s, 9H), 1.38 (m, 4H). ^{13}C NMR (126 MHz, $CDCl_3$): δ, 173.15, 80.16, 70.83, 70.58 51.53, 35.44, 29.74, 29.27, 28.94, 28.25, 26.71, 25.93, 21.99. HRMS (FAB) calculated for $C_{15}H_{30}N_3O_3$ ($[M+H]^+$) 300.2287, found 300.2283.

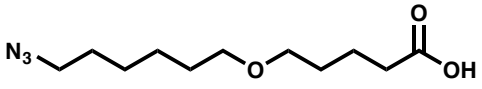

5-((6-azidohexyl)oxy)pentanoic acid (**3**). A 20 mL scintillation vial was charged with **S2** (140 mg, 0.47 mmol, 1 equiv) and 2 mL dichloromethane. The reaction mixture was allowed to stir to form a homogenous solution, after which 2 mL trifluoroacetic acid was added dropwise over the course of 5 min. The reaction mixture continued to stir at room temperature for 1 h, after which the trifluoroacetic acid was evaporated using a gentle stream of nitrogen. Remaining trifluoroacetic acid was removed by azeotropic evaporation with toluene (5 x 5 mL) under reduced pressure to afford **3** as a faint yellow oil (quantitative). The material was used without further purification. ^{1}H NMR (500 MHz, $CDCl_3$): δ, 3.43 (t, 2H, J = 6.0 Hz), 3.40 (t, 2H, J = 6.0 Hz), 3.26 (t, 2H, J = 7.0 Hz), 2.39 (t, 2H, J = 7.0 Hz), 1.72 (m, 2H), 1.61 (m, 6H), 1.38 (m, 4H). ^{13}C NMR (126 MHz, $CDCl_3$): δ, 179.08, 70.92, 70.46, 51.53, 33.81, 29.68, 29.09, 28.93, 26.70, 25.92, 21.72. HRMS (MM) calculated for $C_{11}H_{20}N_3O_3$ $[M-H]^-$ 242.1510, found 242.1507.

2.7 Supplementary Figures

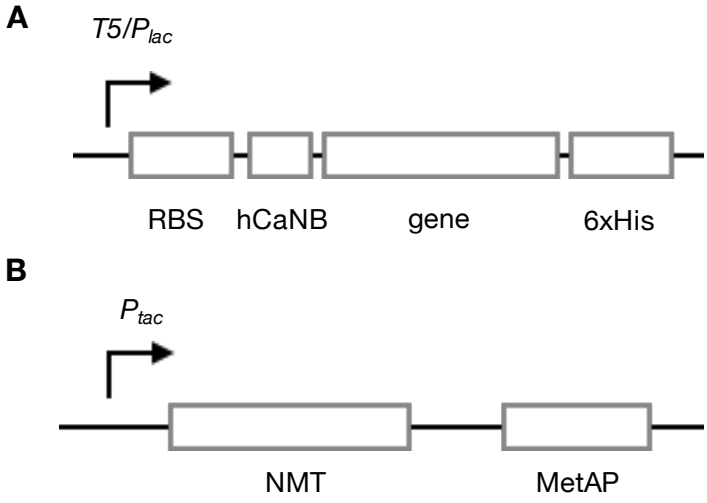

Figure S2.1. Schematic of vector construction in pQE80-L and pHV738-NMT-MetAP plasmids. (**A**) The gene encoding the protein of interest is placed under control of the bacteriophage T5 promoter in the pQE80-L vector. The protein is outfitted with the N-terminal nonapeptide sequence from calcineurin B (hCaNB) for NMT recognition and a C-terminal hexahistidine tag for purification. RBS = ribosome binding site. (**B**) Simplified vector schematic for pHV738-NMT-MetAP. Expression of NMT is placed under control of the Ptac promoter whereas methionyl aminopeptidase (MetAP) expression is placed under control of its own promoter. The plasmid harboring the genes encoding NMT and MetAP contains a p15A origin of replication.

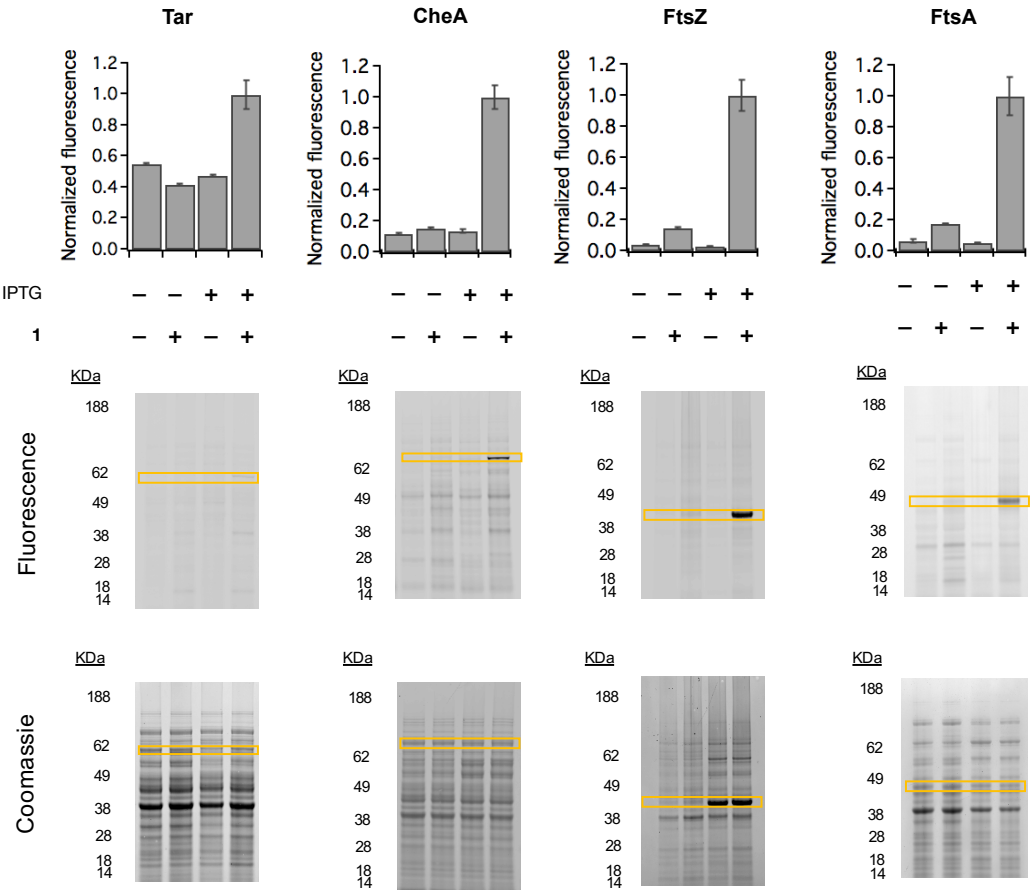

Figure S2.2. Fluorescence emission from labeled proteins expressed from pQE80-L plasmids. Crude lysates from cells (labeled with **1**) expressing NMT and one of the four bacterial proteins (Tar, CheA, FtsZ, or FtsA) from pQE80-L plasmids were treated with **2** and separated using SDS–PAGE. Fluorescence measurements (from gels corresponding to **Figure 2.2**) were normalized to the band corresponding to the labeled protein in the coomassie lane. Error bars denote standard deviations from three independent experiments. Shown below the bar graphs are the fluorescence and coomassie gels in inverted grayscale. The regions boxed in yellow denote the band regions which were used in quantifying fluorescence emission. Fluorescence emission was normalized against the intensity from the associated coomassie gels.

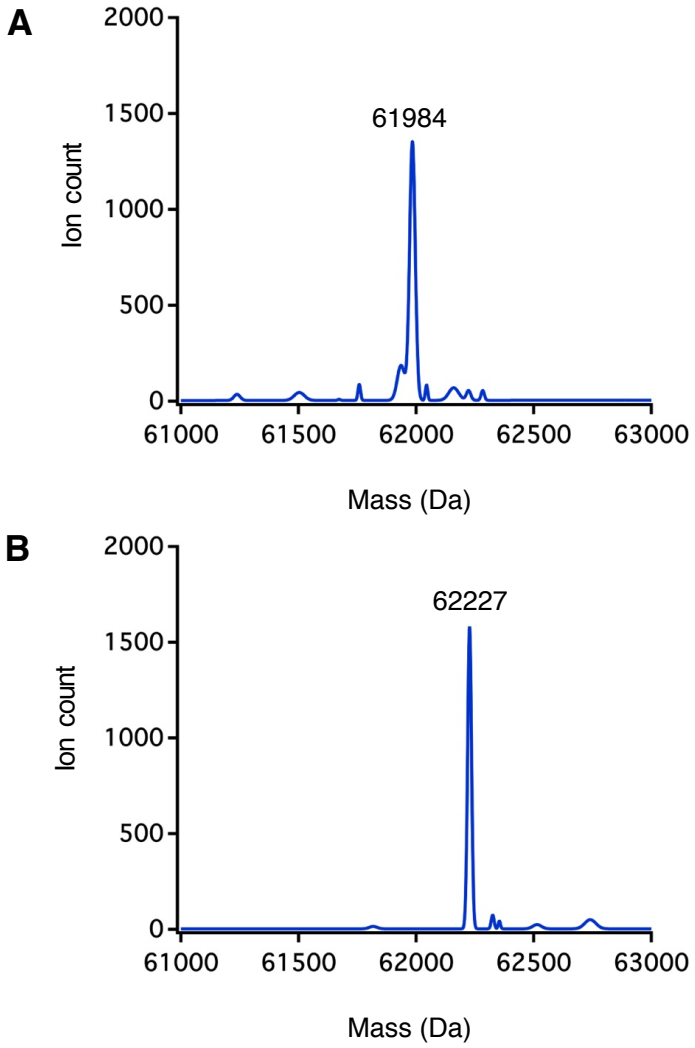

Figure S2.3. Deconvoluted mass spectra of Tar. (**A**) Tar isolated from cells expressing both NMT and Tar but not labeled with **1**. The mass at 61984 Da corresponds to unmodified Tar. (**B**) Tar isolated from cells labeled with **1**. The mass at 62227 Da corresponds to Tar modified with **1** (sodium adduct). Calculated and observed masses for modification of Tar are listed in **Table S2.4**.

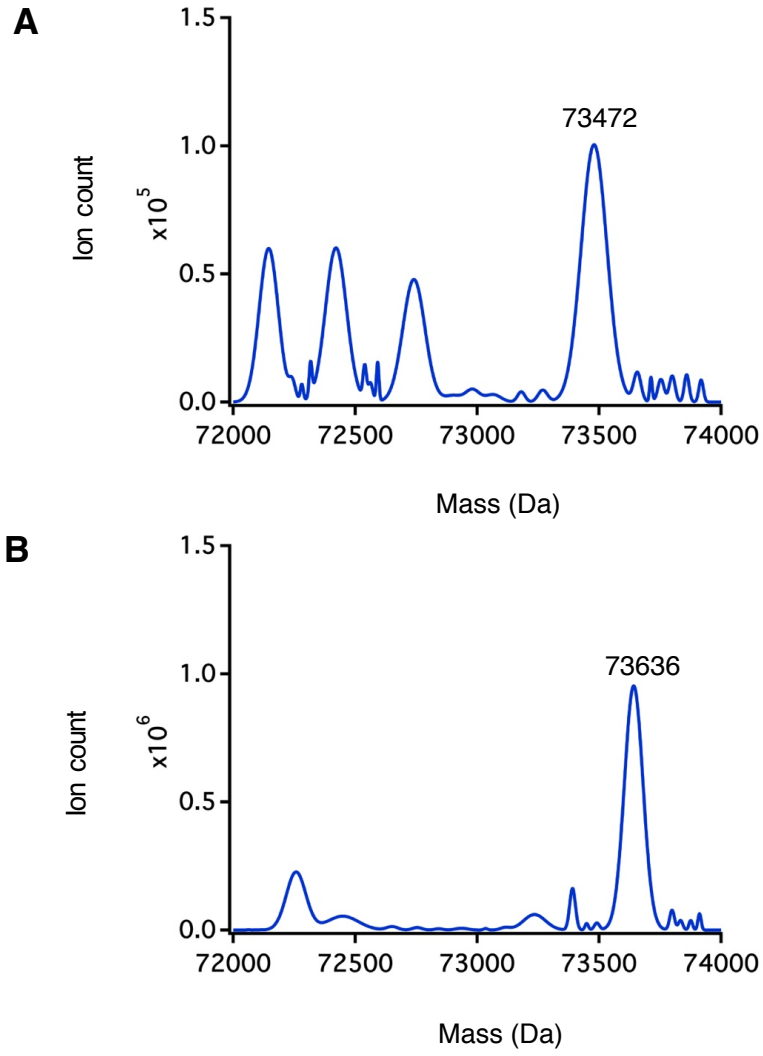

Figure S2.4. Deconvoluted mass spectra of CheA. (**A**) CheA isolated from cells expressing both NMT and CheA but not labeled with **1**. The mass at 73472 Da corresponds to the phosphorylated form of CheA. (**B**) CheA isolated from cells labeled with **1**. The mass at 73636 Da corresponds to CheA modified with **1** (sodium adduct). Calculated and observed masses for modification of CheA are listed in **Table S2.5**.

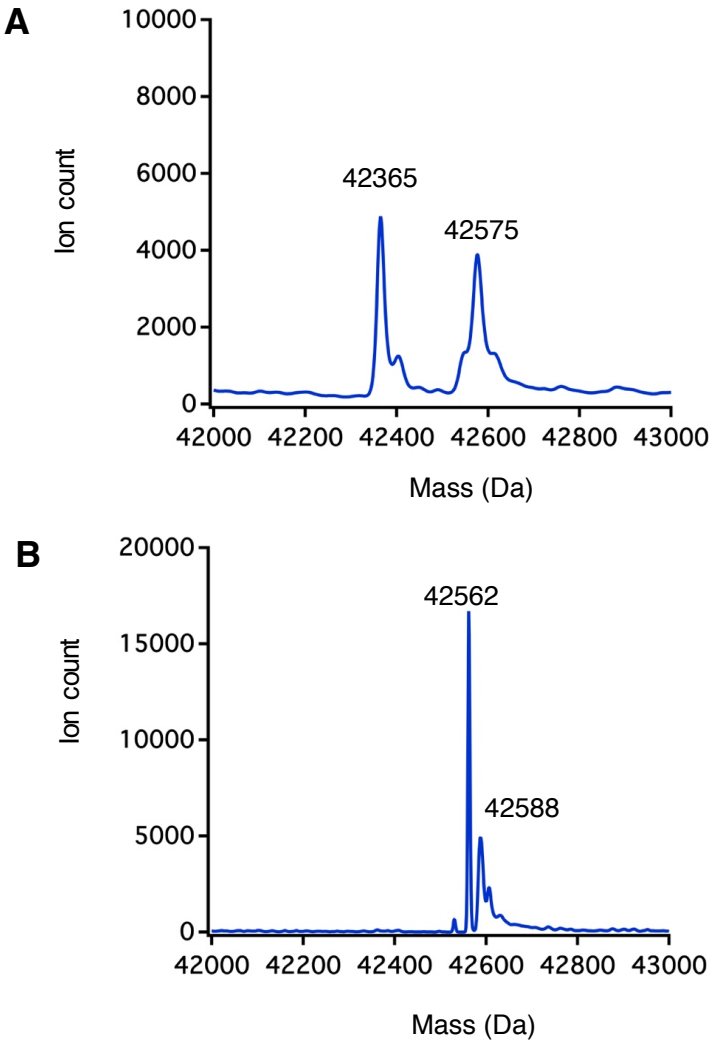

Figure S2.5. Deconvoluted mass spectra of FtsZ. (**A**) FtsZ isolated from cells expressing both NMT and FtsZ but not labeled with **1**. The mass at 42365 Da corresponds to unmodified FtsZ, and the mass at 42575 Da corresponds to FtsZ modified from endogenous myristic acid. (**B**) FtsZ isolated from cells labeled with **1**. The mass at 42588 Da corresponds to FtsZ modified with **1**. The mass at 42562 Da corresponds to FtsZ modified with **1**, with reduction of the terminal azide to an amine. Calculated and observed masses for modification of FtsZ are listed in **Table S2.6**.

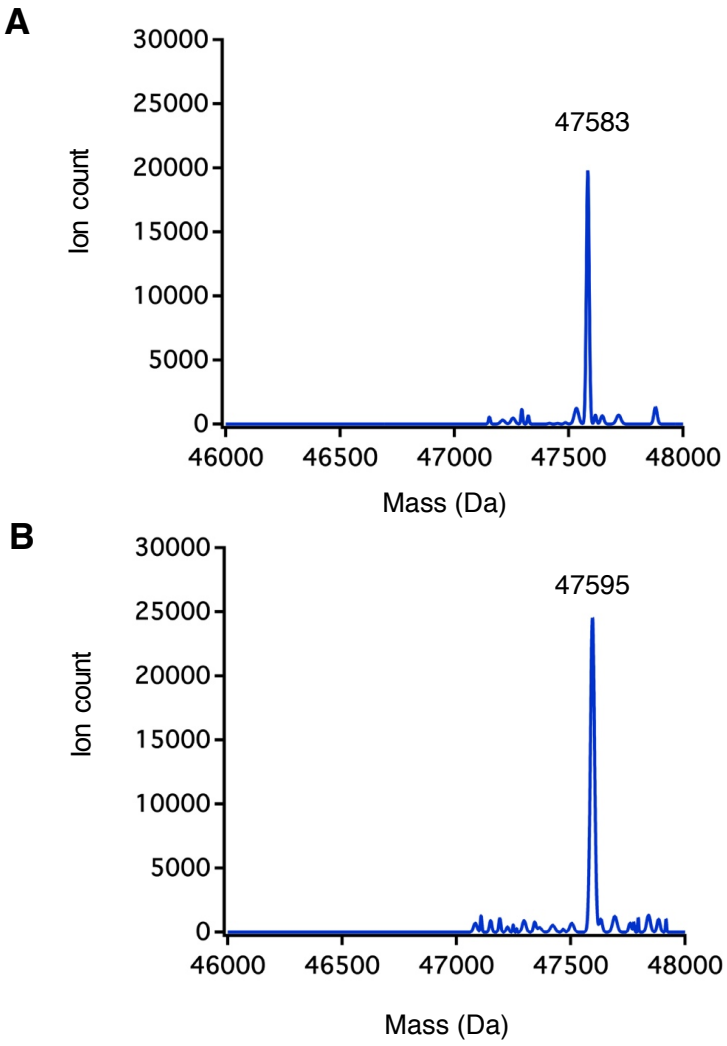

Figure S2.6. Deconvoluted mass spectra of FtsA. (**A**) FtsA isolated from cells expressing both NMT and FtsA but not labeled with **1**. The mass at 47583 Da corresponds to FtsA modified from endogenous myristic acid. (**B**) FtsA isolated from cells labeled with **1**. The mass at 47595 Da corresponds to FtsA modified with **1**. Calculated and observed masses for modification of FtsA are listed in **Table S2.7**.

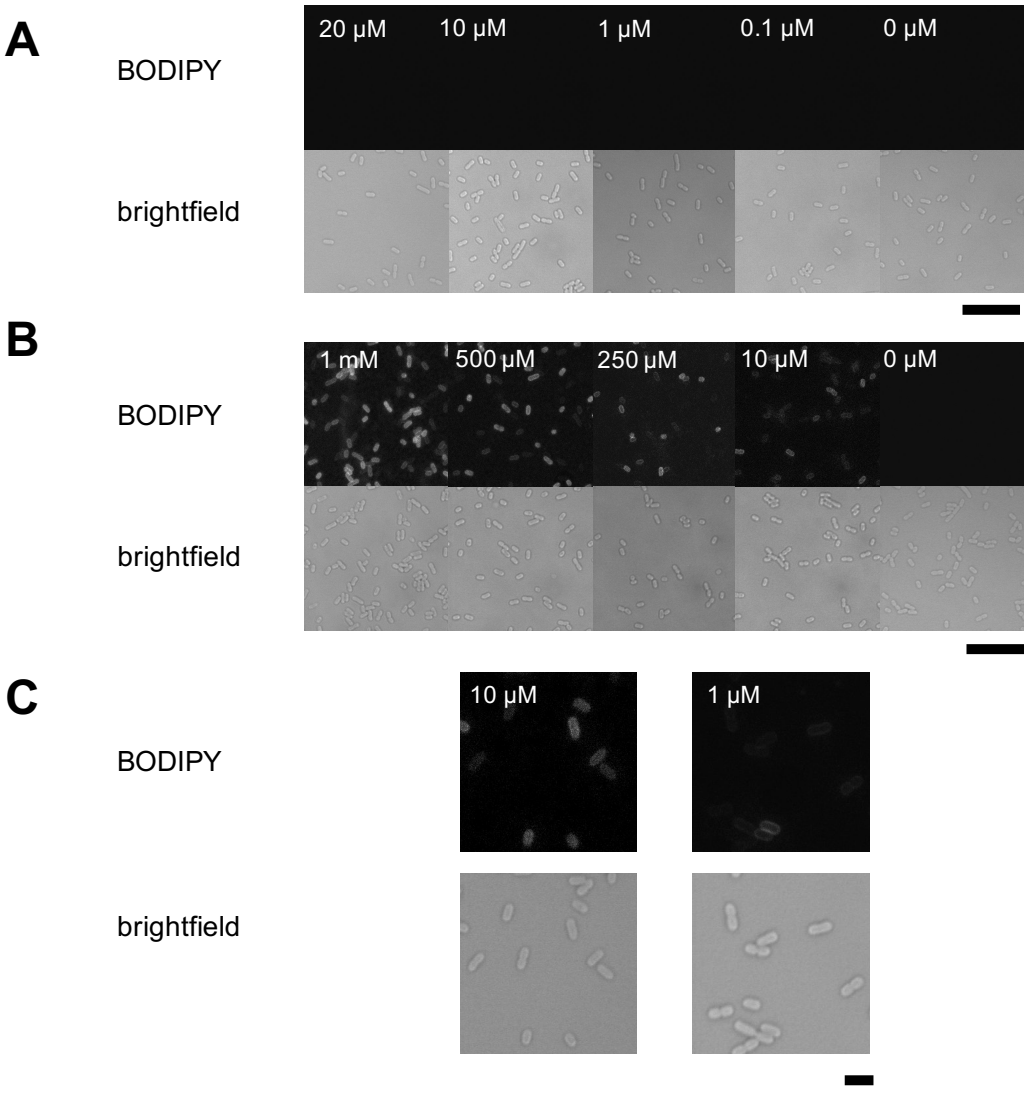

Figure S2.7. Screening fatty acid and fluorophore concentration ranges. Cells not expressing a target protein were grown at 37 °C to OD_{600} = 0.5 and treated as described in (**A**) – (**C**). After treatment, cells were washed three times with PBS and imaged by confocal fluorescence microscopy. (**A**) Cells that were not treated with **1** were labeled with different concentrations of **2** for 30 min at 37 °C. Scale bar = 10 µm. (**B**) Cells that were treated for 2 h with different concentrations of **1** were labeled with 20 µM **2**. Scale bar = 10 µm. (**C**) Cells that were treated for 2 h with 250 µM **1** and labeled for 30 min with different concentrations of **2**. Fluorescence can be observed for 10 µM **2** and low fluorescence is observed for 1 µM **2**. Scale bar = 2 µm.

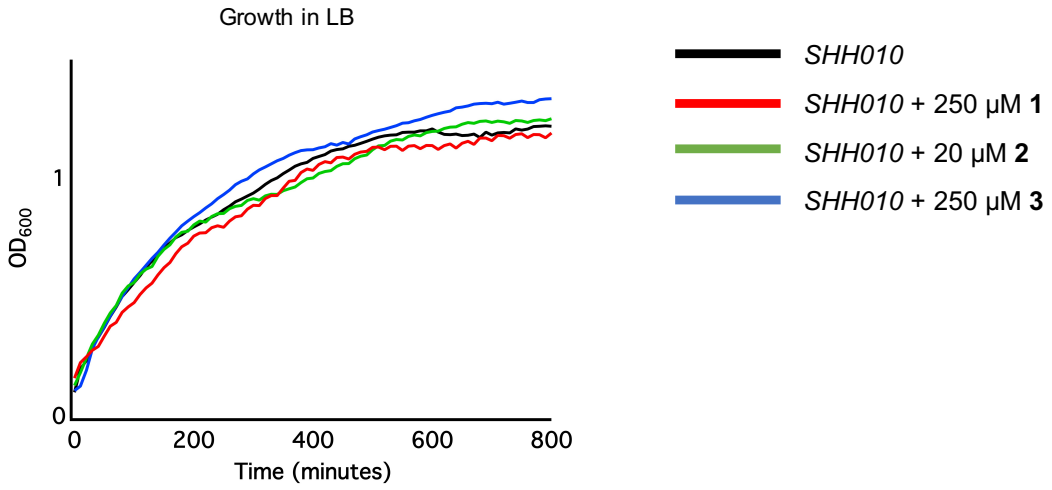

Figure S2.8. Addition of **1**, **2**, or **3** does not affect cell growth. Cells were diluted from an overnight culture to an OD_{600} = 0.1. Cells were then treated with either **1, 2,** or **3,** and continued to grow through the course of 800 min. OD_{600} was monitored every 10 min for each culture. *E. coli* strain SHH010 (culture bearing plasmids pBAD24-hCaNB-CheA-myc and pHV738-NMT-MetAP) was used in this experiment.

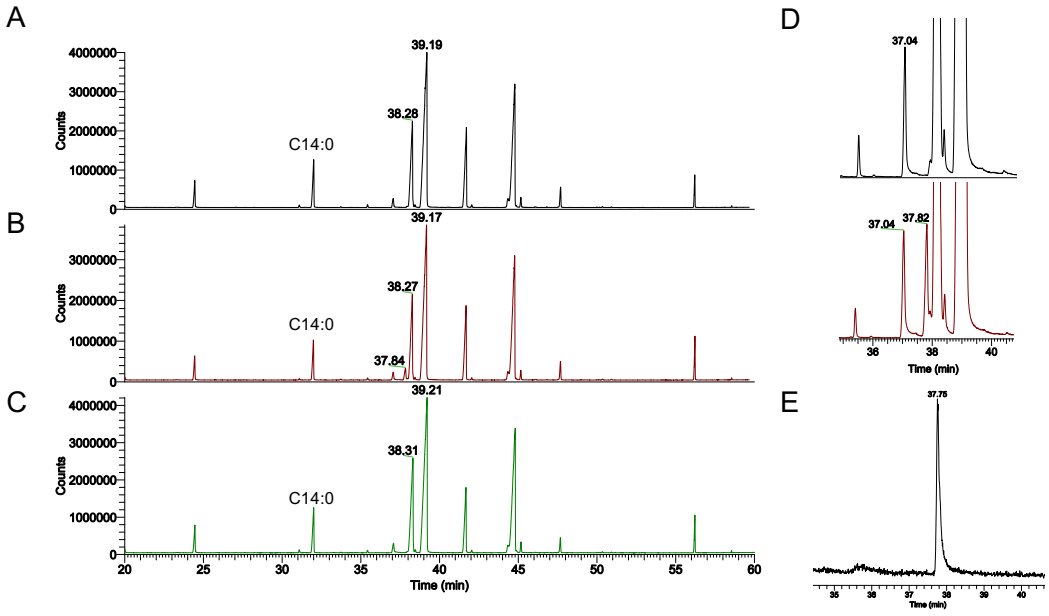

Figure S2.9. GC traces of fatty acid methyl esters (FAMEs) extracted from *E. coli*. FAMEs were extracted from cells that were (**A**) untreated with fatty acids, (**B**) treated with **1**, or (**C**) treated with **3**. The methyl ester derivative of **1** is found in (**B**) at t = 37.84 min. (**D**) Zoomed image comparing FAMEs from untreated cells (top) and cells treated with **1** (bottom). For cells treated with **3**, the fatty acid pool is essentially identical to that of cells that were not treated with any azido-fatty acids. (**E**) Compound **1** was subjected to esterification and injected for GC–MS analysis. The elution time (t = 37.75 min) matches that of the peak in trace (**B**) at t = 37.84 min. The methyl ester of endogenous myristic acid (C14:0) is labeled in traces **A–C**. FAME analysis yields no evidence that probes **1** and **3** undergo chain-length redistribution.

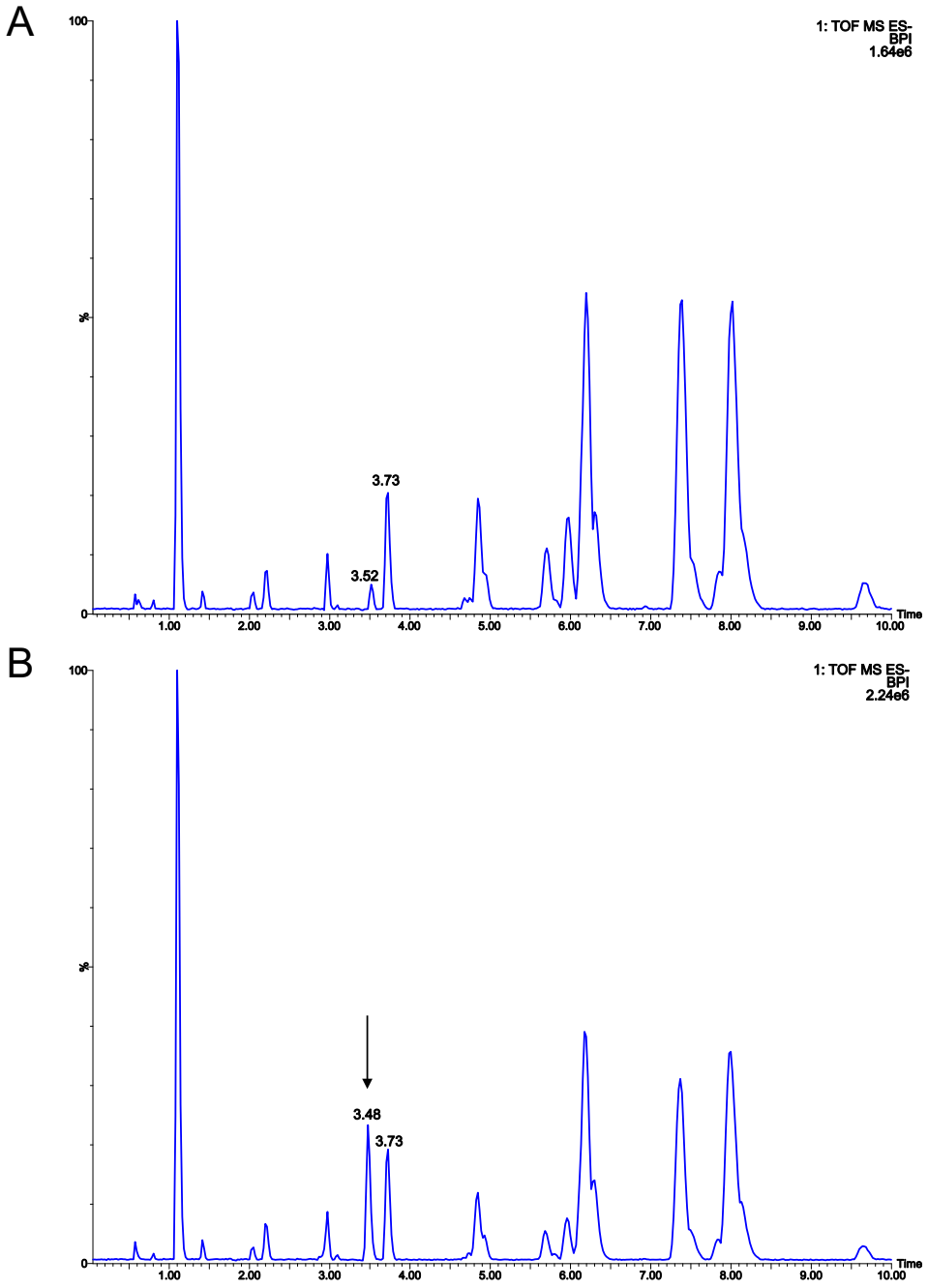

Figure S2.10. LC traces of intact lipids from *E. coli*. Intact lipids were extracted from cells (**A**) untreated with azide-containing fatty acids or (**B**) treated with **1**. (**B**) Fatty acid probe **1** is incorporated into a phosphatidylethanolamine with a C_{16} acyl chain (t = 3.48 min). Identification of PE molecule eluting at t = 3.48 min was performed by analysis of fragmentation patterns in both negative (**Figure S2.11**) and positive (**Figure S2.12**) mode. BPI = Base peak intensity.

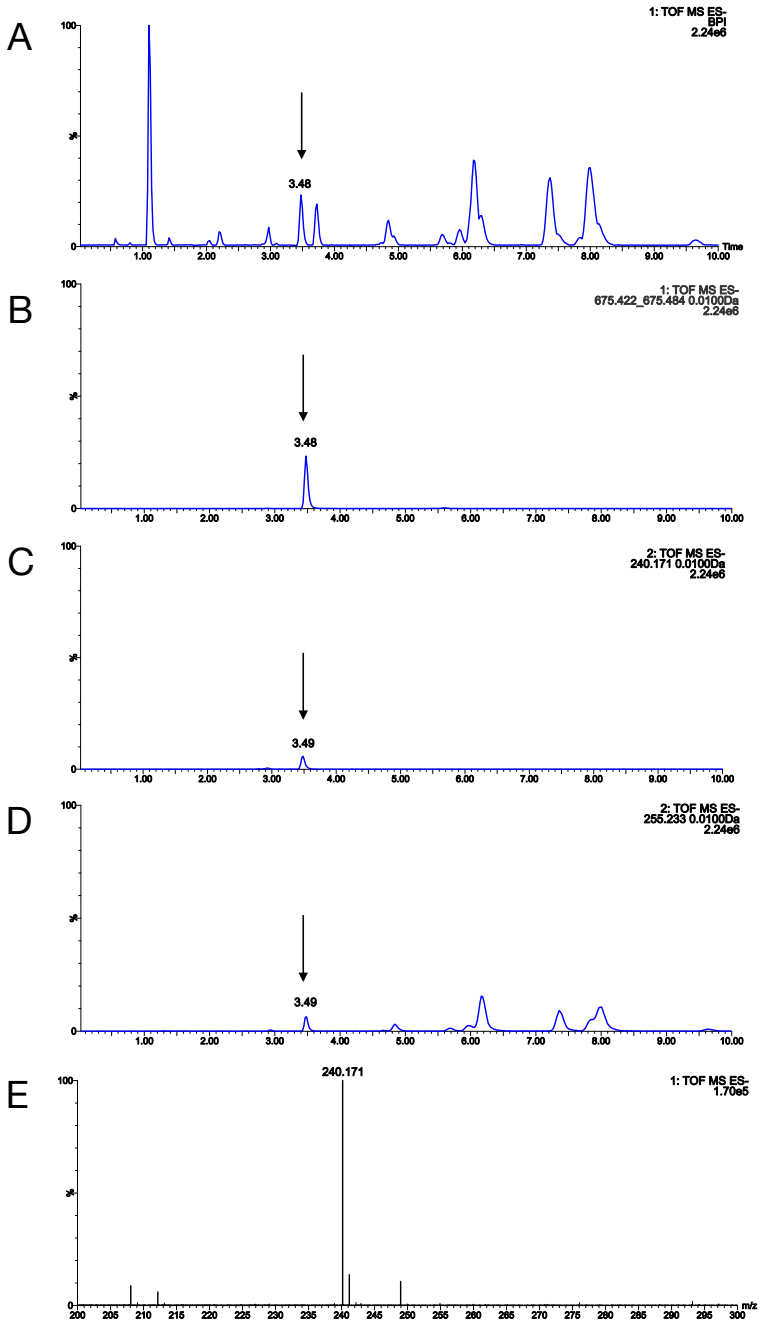

Figure S2.11. Identification of fatty acids from phospholipids (negative mode). (**A**) Base peak ion (BPI) chromatogram of cells treated with **1**. (**B**) Extracted ion chromatogram (EIC) for phospholipid (parent ion), using m/z value search from MS1 channel (m/z = 675.422 – 675.484 ± 0.010 Da). Elution peak occurs at t = 3.48 min. (**C and D**) Identification of individual chain components of phospholipid eluting at t = 3.48 min. EICs were generated

using m/z values from MS2 channel (fragment ions). (**C**) EIC for m/z value corresponding to **1** (m/z = 240.171 ± 0.010 Da). (**D**) EIC for m/z value corresponding to palmitic acid (m/z = 255.233 ± 0.010 Da). The fragment ions (traces **C** and **D**) show an elution peak at t = 3.48 min, matching that of the peak corresponding to the parent ion (trace **B**) and indicating that **1** is incorporated into a cellular lipid bearing a palmitic acid chain. Max ion count for traces A–D: 2.24×10^6. (**E**) Probe **1** was run to confirm production of the expected ion at the expected m/z.

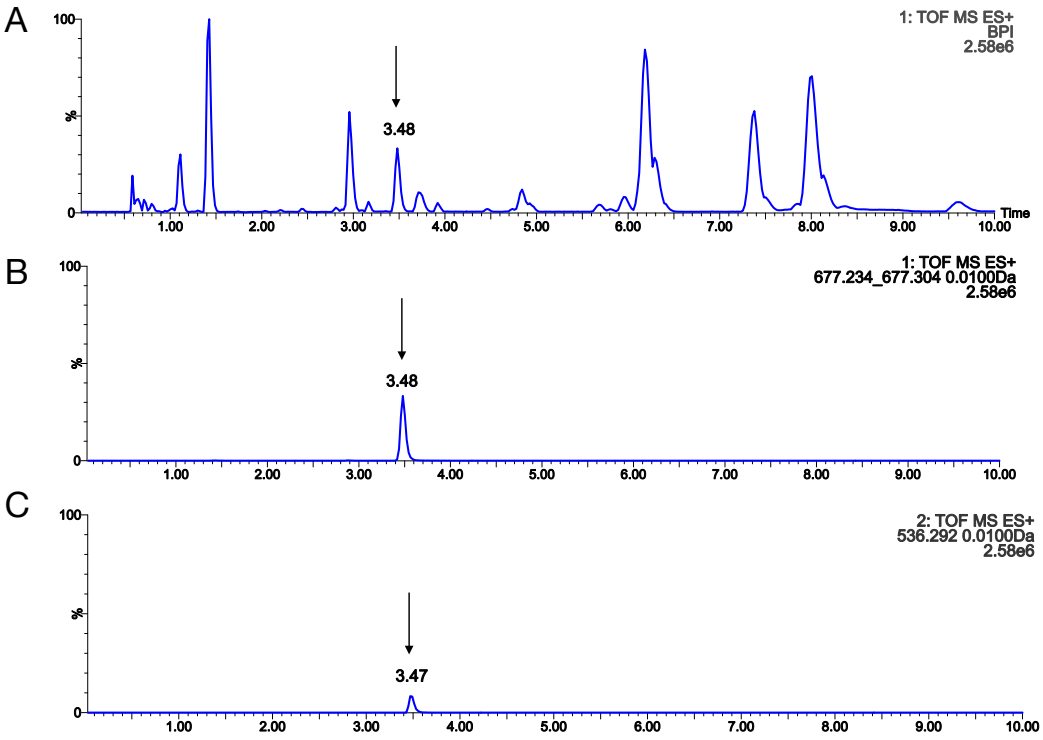

Figure S2.12. Identification of fatty acids from phospholipids (positive mode). (**A**) Base peak ion (BPI) chromatogram of cells treated with **1**. (**B**) Extracted ion chromatogram (EIC) for phospholipid (parent ion), using m/z value search from MS1 channel (m/z = 677.234 – 677.304 ± 0.010 Da). (**C**) EIC for the fragment ion (MS2 channel; m/z = 536.292 ± 0.010 Da) shows an elution peak at t = 3.48 min. The difference in m/z between the parent ion in (**B**) and fragment ion in (**C**) suggests the loss of phosphorylethanolamine (calculated m/z: 141.019 Da), consistent with formation of a phosphatidylethanolamine bearing acyl chains derived from **1** and palmitic acid. Max ion count for traces **A–C**: 2.58 x 10^6.

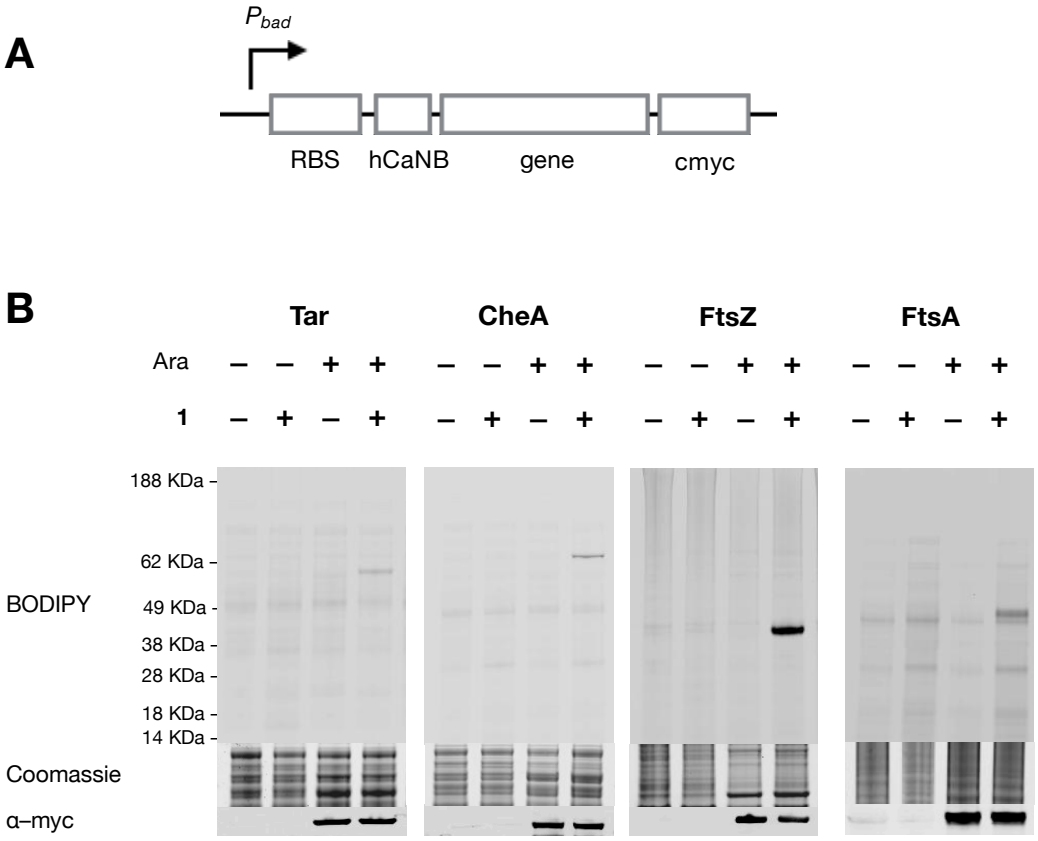

Figure S2.13. In-gel fluorescence detection of proteins expressed from pBAD24 plasmids and labeled with **1**. (**A**) The gene encoding the protein of interest is placed under control of the P_{BAD} promoter in the modified pBAD24 plasmid. The protein is outfitted with the *N*-terminal nonapeptide sequence from calcineurin B (hCaNB) for NMT recognition and a *C*-terminal myc-tag (cmyc) for immunoblotting and immunofluorescence imaging. RBS = ribosome binding site. (**B**) In-gel fluorescence analysis shows NMT can achieve site-specific labeling of *E. coli* proteins expressed under control of the arabinose-inducible promoter. SDS–PAGE analysis of *E. coli* lysates. Protein expression was achieved by addition of 0.2% w/v L-arabinose (Ara). Cultures were labeled with **1** when protein expression was induced. Cells were lysed and lysates were treated with **2**. Western blot analysis against a *C*-terminal myc tag with a primary antibody conjugated to Alexa Fluor 647 confirms protein expression.

The T5 promoter can exhibit basal expression in the absence of an inducer. The pBAD promoter is more tightly regulated with reduced basal expression. In cells outfitted with pBAD24 plasmids, NMT is constitutively expressed under control of the *tac* promoter. We found sufficient labeling for imaging with basal NMT expression.

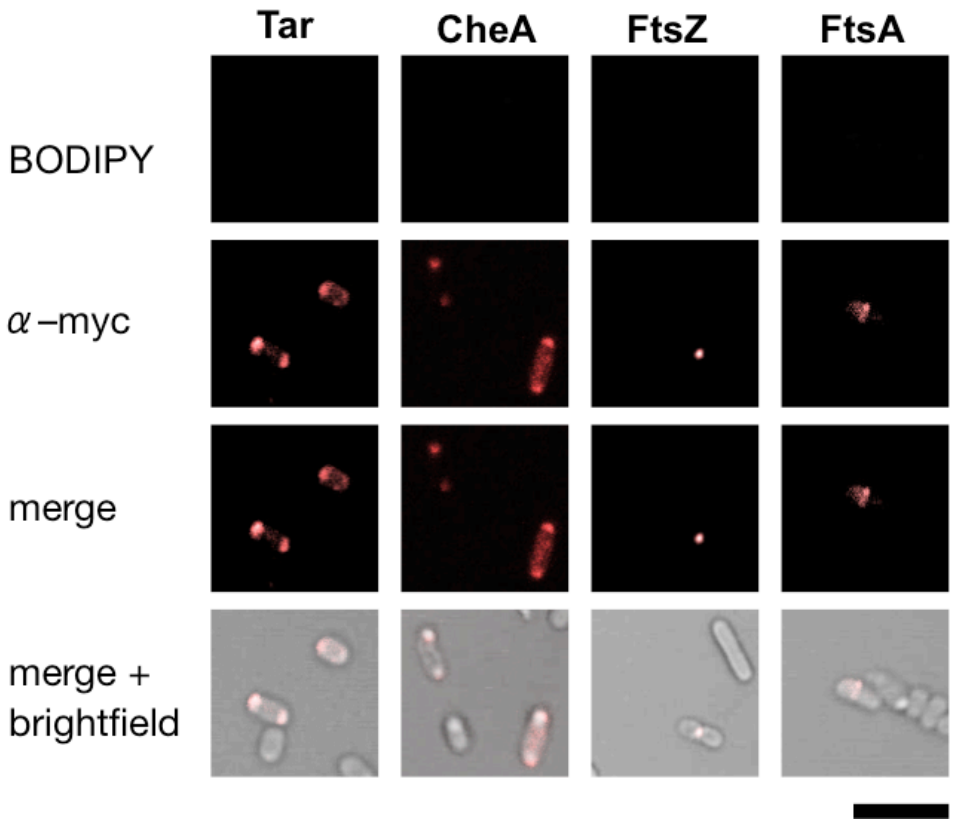

Figure S2.14. Immunofluorescence labeling of bacterial proteins. Bacterial proteins that are not labeled with **1** show localization patterns indistinguishable from those treated with **1**. Polar localization is observed for Tar and CheA; septal localization for FtsZ and FtsA. After protein expression was induced, cells were fixed, permeabilized, and treated with **2** and an anti–myc antibody conjugated to Alexa Fluor 647 (scale bar = 2 μm).

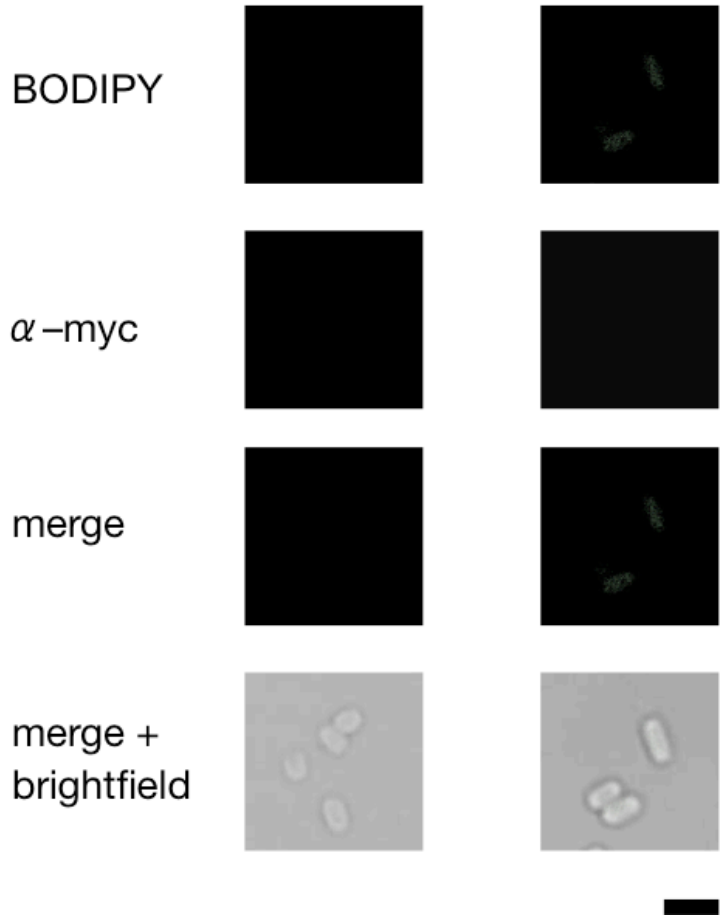

Figure S2.15. Immunofluorescence labeling of uninduced cells or uninduced cells treated with **1**. Control experiments where cells do not express a target protein but are treated with **1, 2**, and antibody (following fixation and permeabilization) show no observable, distinct localization patterns (for all four proteins Tar, CheA, FtsZ, and FtsA), confirming that there is little interference from labeling of free **1** or of **1** incorporated into membrane lipids (scale bar = 1 μm).

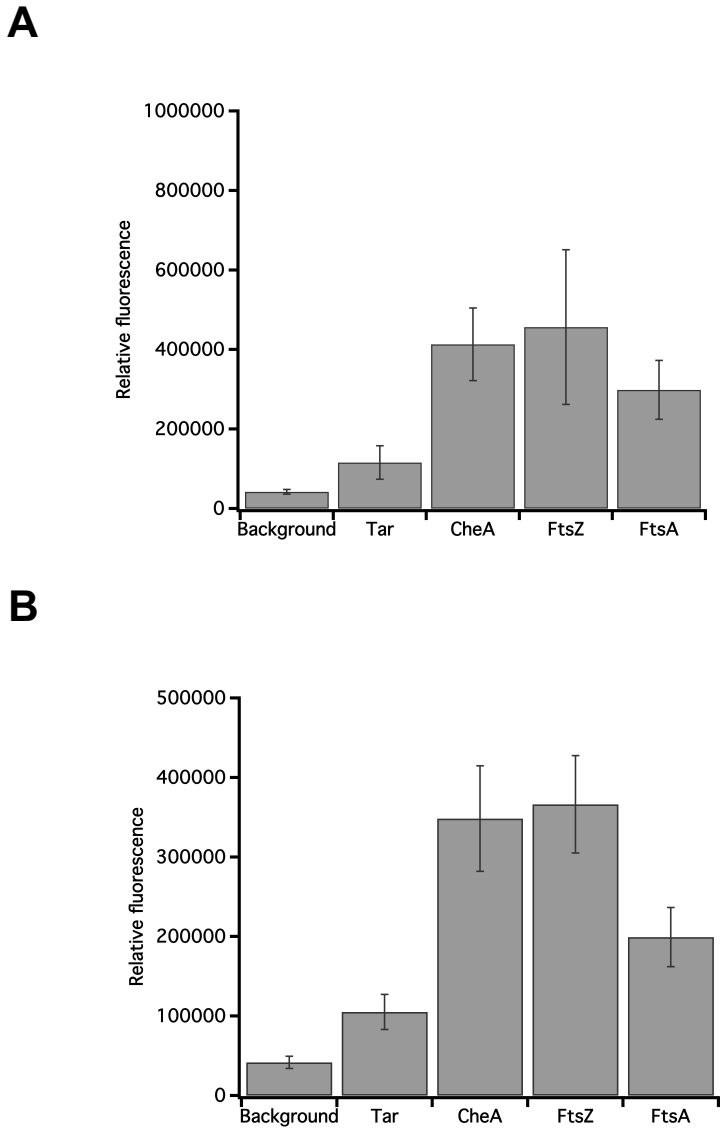

Figure S2.16. Relative fluorescence intensities for live cells labeled with **1** or **3** and **2**. Fluorescence signal from cells was quantified using Cell Profiler. Background signal was measured from cells that were not expressing protein targets but were treated with 250 μM of either (**A**) **1** or (**B**) **3**, and labeled with 20 μM **2**. The fold changes above background for Tar, CheA, FtsZ, and FtsA are (**A**) 2.7, 9.8, 10.8, and 7.1 and (**B**) 2.5, 8.4, 8.8, and 4.8, respectively. Error bars denote standard deviation from fluorescence quantification for 100–150 cells for each of the cells expressing one of the four protein targets or cells used for quantifying background signal.

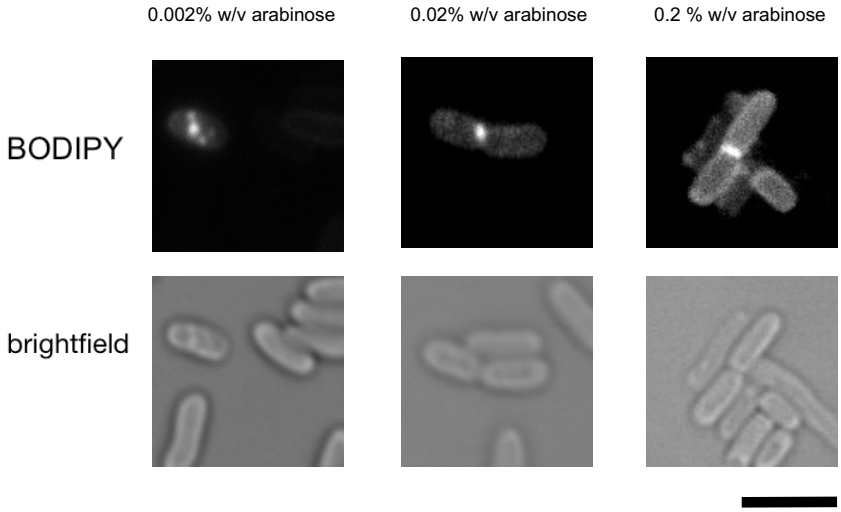

Figure S2.17. Cells can be labeled with lower concentrations of arabinose. We were able to achieve similar labeling when protein targets were induced with lower concentrations of arabinose. Shown here is a representative example of FtsZ expressing cells labeled with 250 μM **1** and 20 μM **2**. Scale bar is 2 μm.

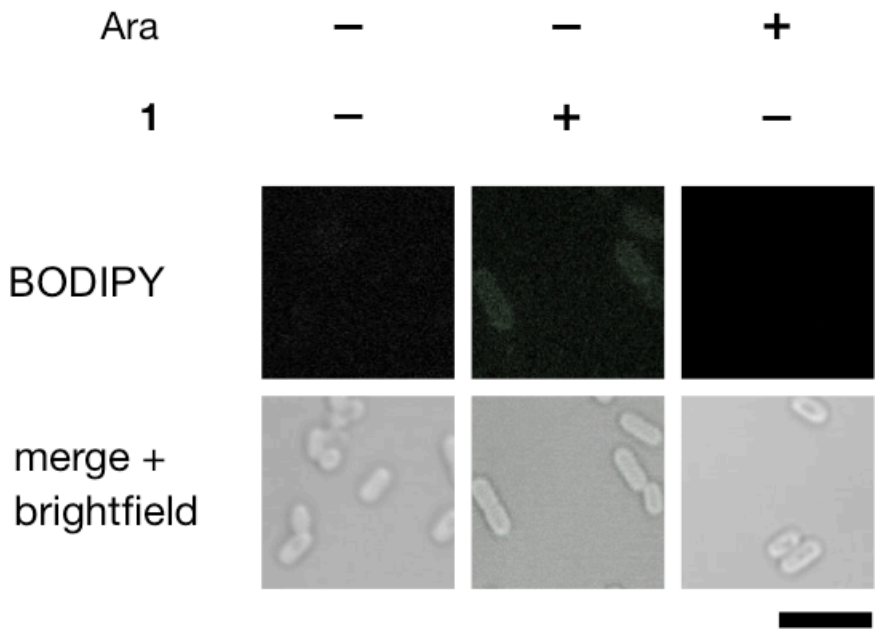

Figure S2.18. Live-cell fluorescence imaging of uninduced cells. Representative live-cell imaging for control experiments. Cells that do not express the protein of interest, but that have been treated with **1** and **2**, do not show distinct localization patterns (scale bar = 1 μm).

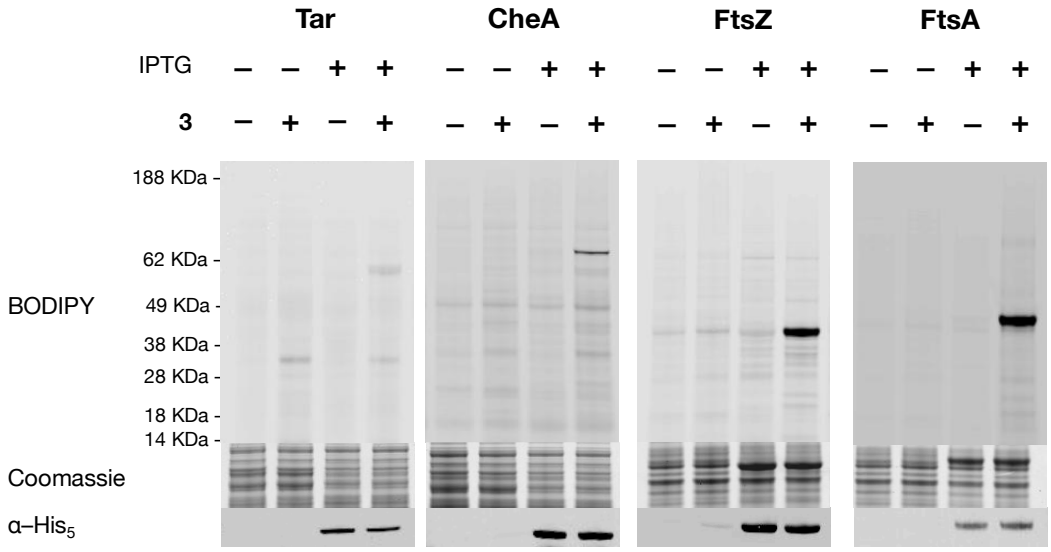

Figure S2.19. In-gel fluorescence detection of proteins expressed from pQE80-L plasmids and labeled with **3**. SDS–PAGE analysis of *E. coli* lysates. Protein expression was achieved by addition of 1 mM IPTG. Cultures were labeled with **3** when protein expression was induced. Cells were lysed and lysates were treated with **2**. Western blot analysis against a *C*-terminal His_5 tag with a primary antibody conjugated to Alexa Fluor 647 confirms protein expression.

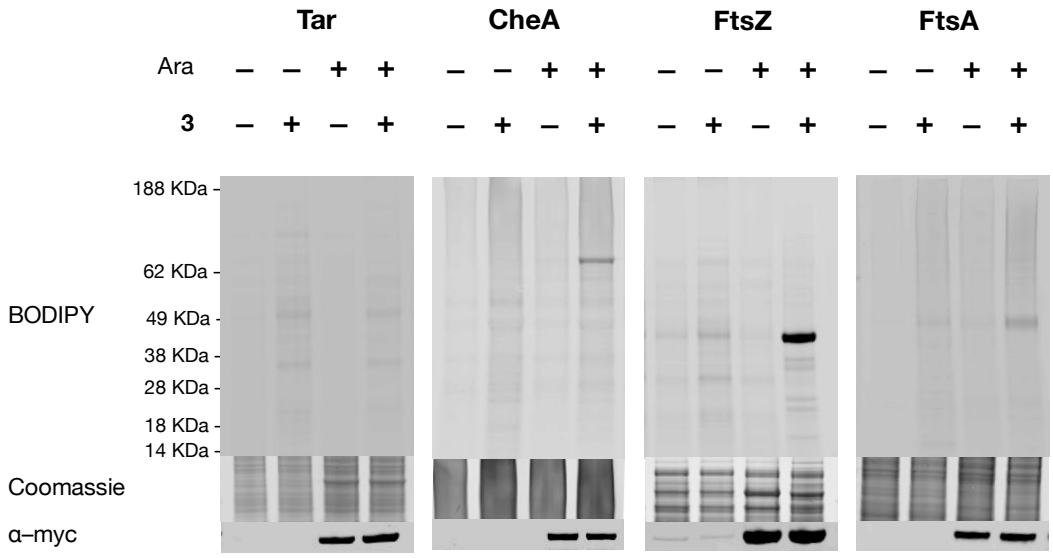

Figure S2.20. In-gel fluorescence detection of proteins expressed from pBAD24 plasmids and labeled with **3**. SDS–PAGE analysis of *E. coli* lysates. Protein expression was achieved by addition of 0.2% w/v L-arabinose (Ara). Cultures were labeled with **3** when protein expression was induced. Cells were lysed and lysates were treated with **2**. Western blot analysis against a *C*-terminal myc tag with a primary antibody conjugated to Alexa Fluor 647 confirms protein expression. With hydrophilic fatty acid **3**, we were unable to observe fluorescence labeling for the transmembrane protein, Tar.

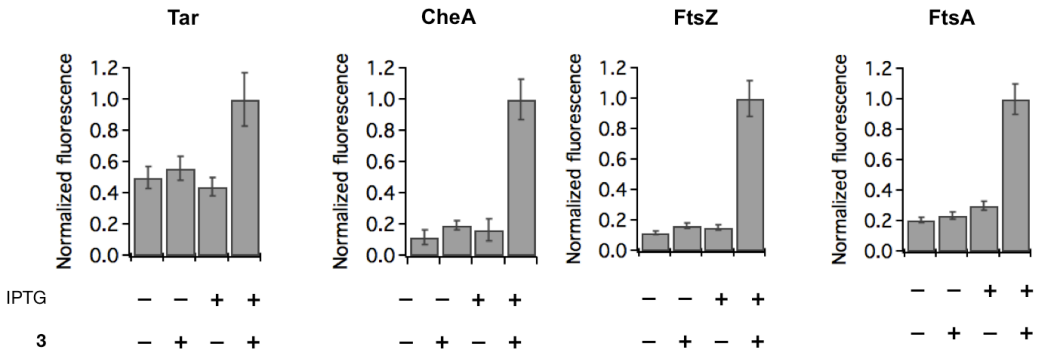

Figure S2.21. Fluorescence emission of proteins expressed from pQE80-L plasmids and labeled with **3**. Crude lysates from cells (labeled with **3**) expressing one of the four bacterial proteins (Tar, CheA, FtsZ, or FtsA) were treated with **2** and separated using SDS–PAGE. Fluorescence measurements (from gels corresponding to **Figure S2.19**) were normalized to the bands corresponding to the labeled proteins in the coomassie gels. The extent of fluorescence enhancement above background measured by gel electrophoresis was 1.8-, 5.1-, 6.2-, and 4.3-fold, respectively. Error bars denote standard deviations from three independent experiments.

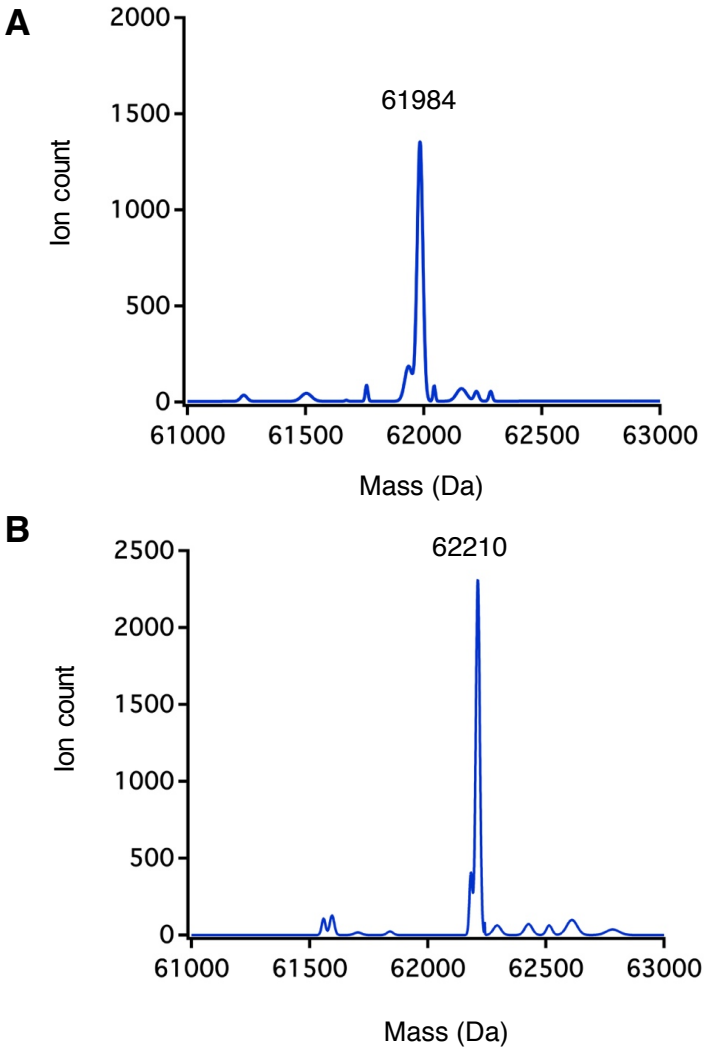

Figure S2.22. Deconvoluted mass spectra of Tar. (**A**) Tar isolated from cells expressing both NMT and Tar but not labeled with **3**. The mass at 61984 Da corresponds to unmodified Tar. (**B**) Tar isolated from cells labeled with **3**. The mass at 62210 Da corresponds to Tar modified with **3**. Calculated and observed masses for modification of Tar are listed in **Table S2.4**.

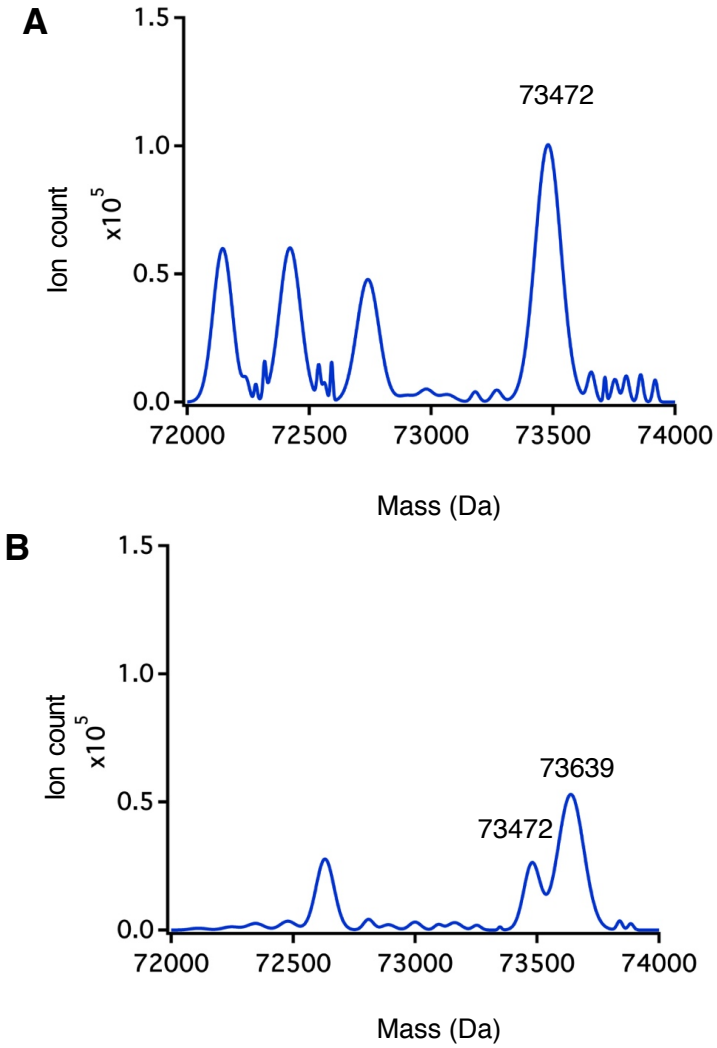

Figure S2.23. Deconvoluted mass spectra of CheA. (**A**) CheA isolated from cells expressing both NMT and CheA but not labeled with **3**. The mass at 73472 Da corresponds to the phosphorylated form of CheA. (**B**) CheA isolated from cells labeled with **3**. The mass at 73639 Da corresponds to CheA modified with **3** (sodium adduct). Calculated and observed masses for modification of CheA are listed in **Table S2.5**.

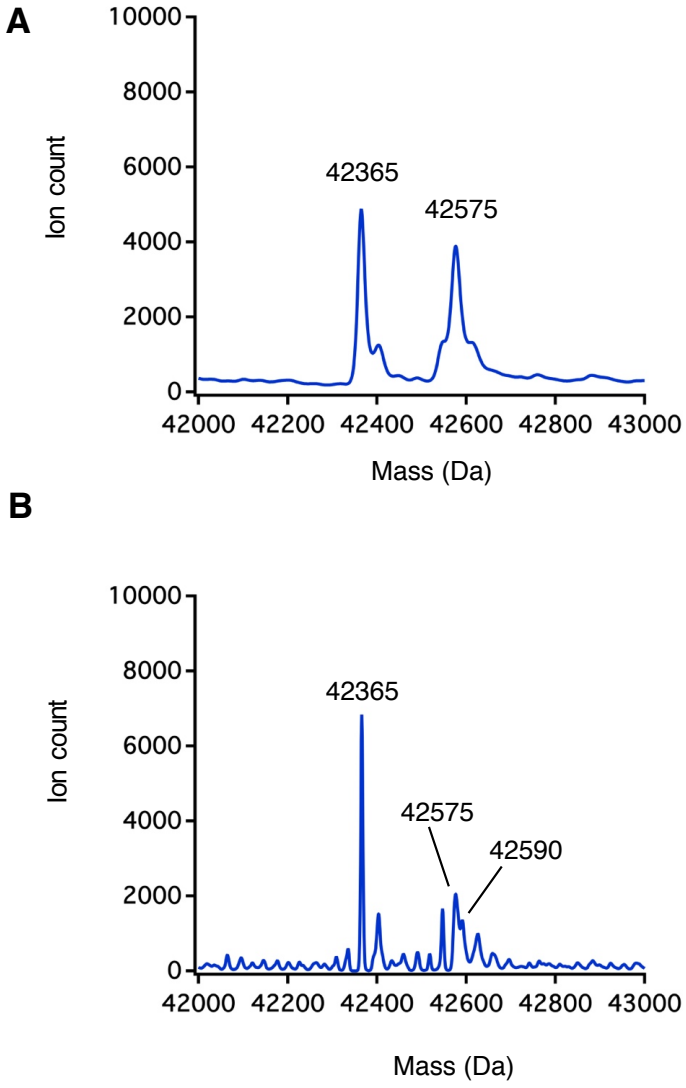

Figure S2.24. Deconvoluted mass spectra of FtsZ. (**A**) FtsZ isolated from cells expressing both NMT and FtsZ but not labeled with **3**. The mass at 42365 Da corresponds to unmodified FtsZ, and the mass at 42575 Da corresponds to FtsZ modified from endogenous myristic acid. (**B**) FtsZ isolated from cells labeled with **3**. The mass at 42590 Da corresponds to FtsZ modified with **3**. Calculated and observed masses for modification of FtsZ are listed in **Table S2.6**.

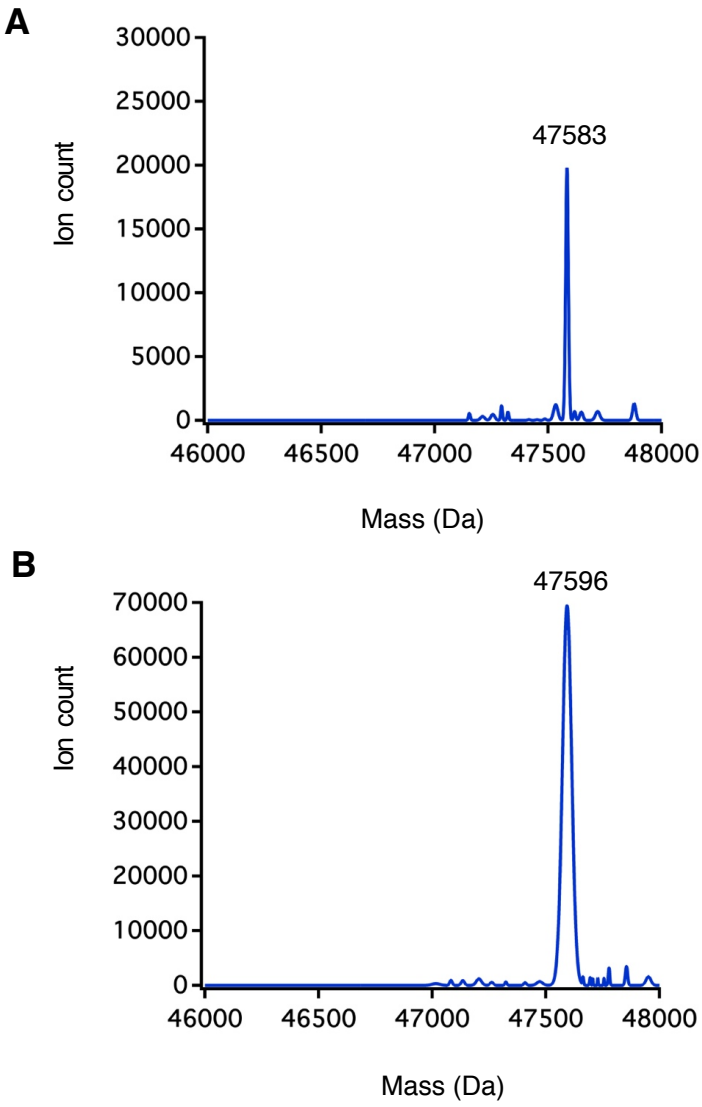

Figure S2.25. Deconvoluted mass spectra of FtsA. (**A**) FtsA isolated from cells expressing both NMT and FtsA but not labeled with **3**. The mass at 47583 Da corresponds to FtsA modified from endogenous myristic acid. (**B**) FtsA isolated from cells labeled with **3**. The mass at 47596 Da corresponds to FtsA modified with **3**. Calculated and observed masses for modification of FtsA are listed in **Table S2.7**.

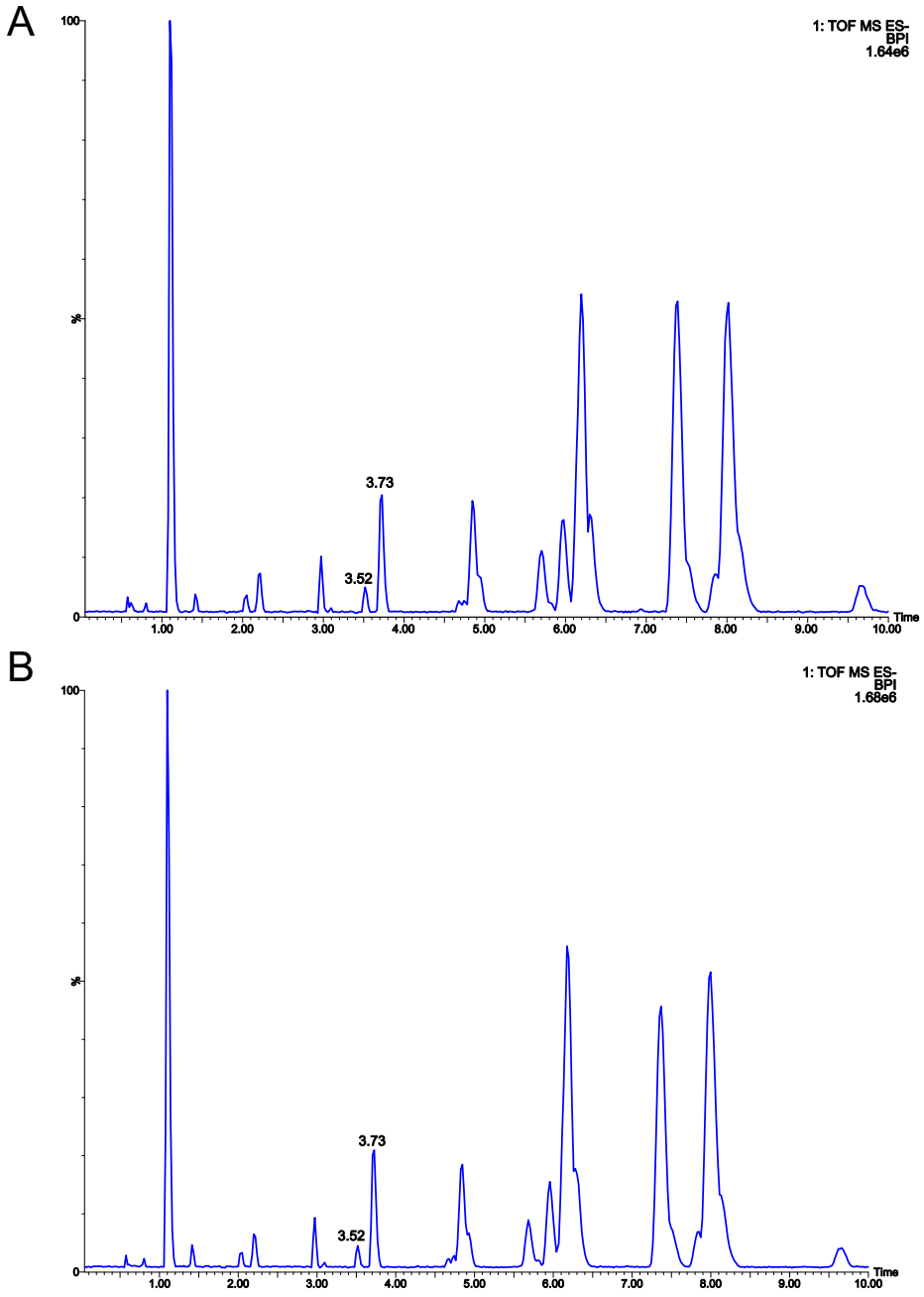

Figure S2.26. The lipidome of cells treated with **3** does not differ from that of untreated cells. LC trace of intact lipids extracted from cells (**A**) untreated with azide fatty acids, or (**B**) treated with **3**. The profile of (**B**) does not differ significantly from the LC trace of untreated cells in (**A**), suggesting that **3** is not incorporated into cellular lipids.

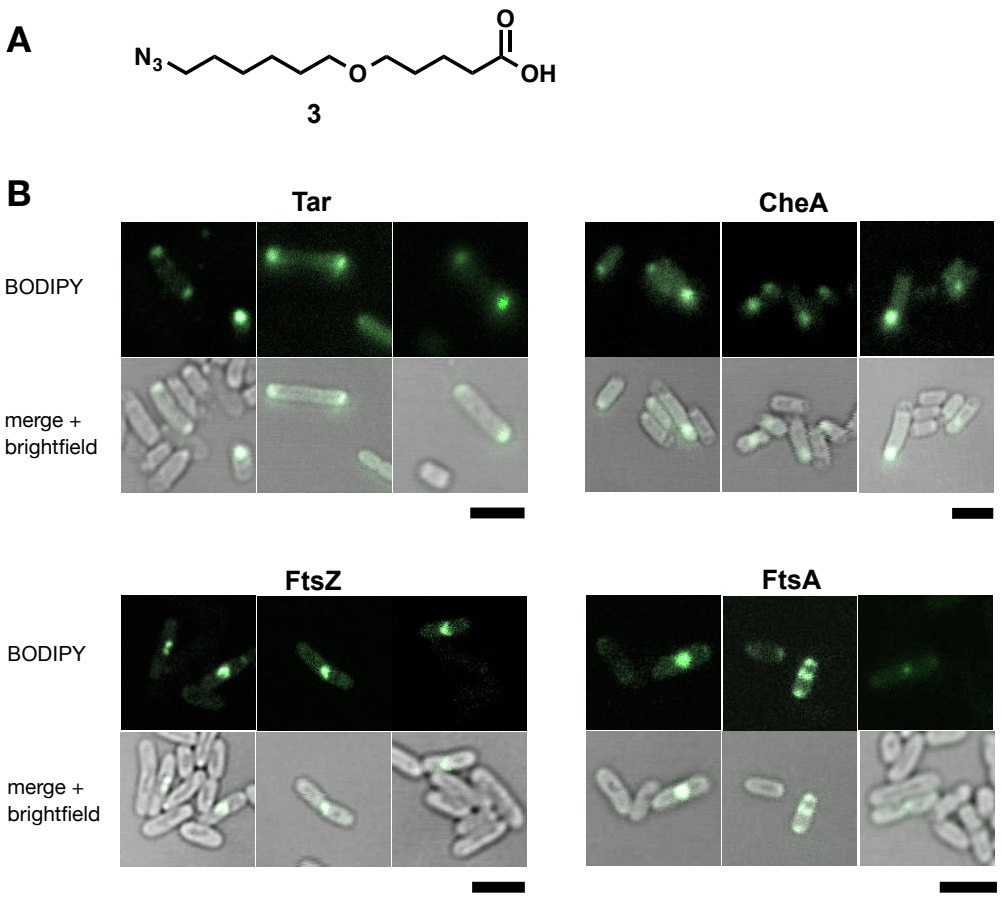

Figure S2.27. Representative live-cell images for chemotaxis and cell division proteins labeled with **2** and **3**. (**A**) Structure of fatty acid analogue **3** used for live-cell labeling. (**B**) *N*-terminal fluorescence labeling shows polar localization for Tar and CheA and septal localization for FtsZ and FtsA (scale bar = 1 μm).

2.8 NMR Spectra

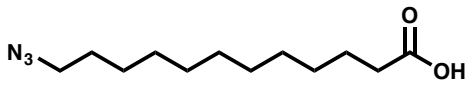

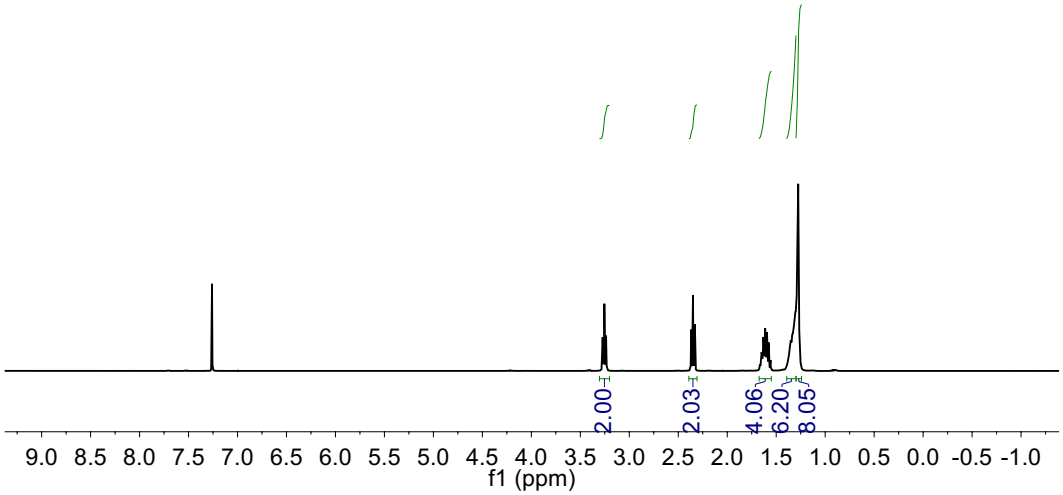

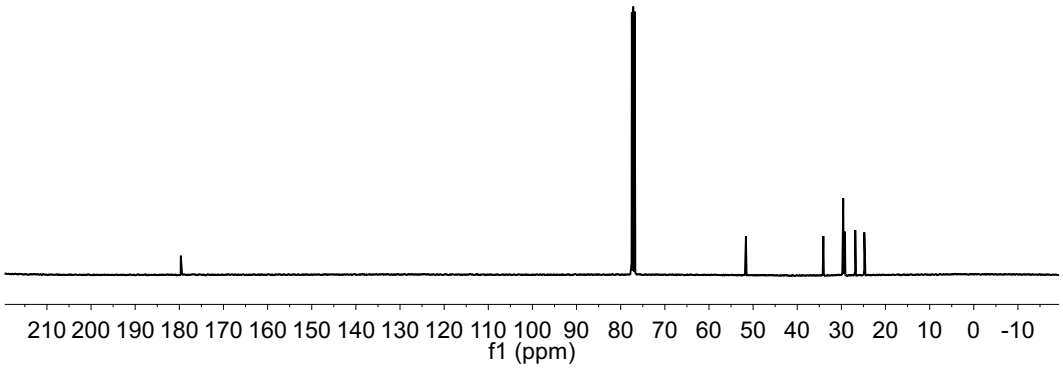

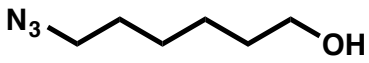
N3
OH

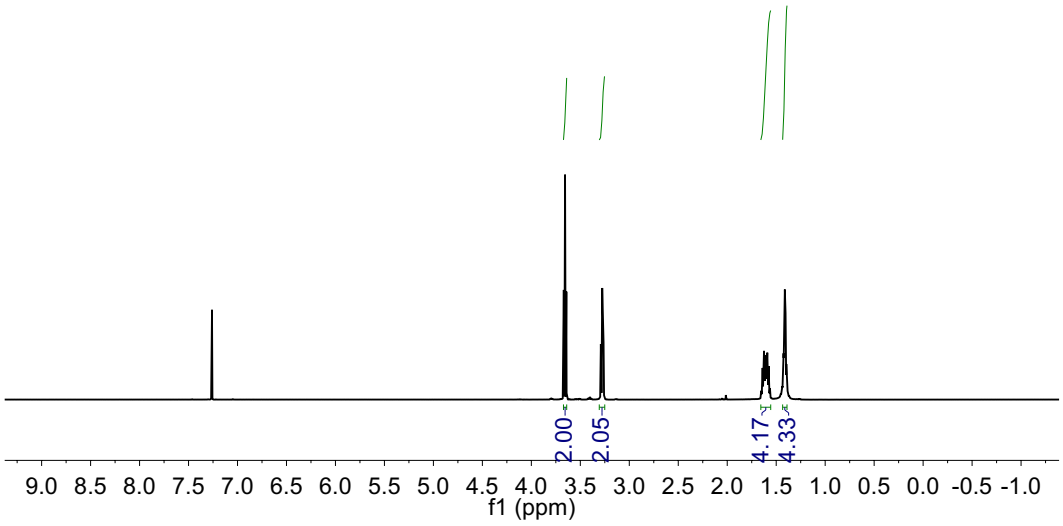
2.00
2.05
4.17
4.33
9.0 8.5 8.0 7.5 7.0 6.5 6.0 5.5 5.0 4.5 4.0 3.5 3.0 2.5 2.0 1.5 1.0 0.5 0.0 -0.5 -1.0
f1 (ppm)

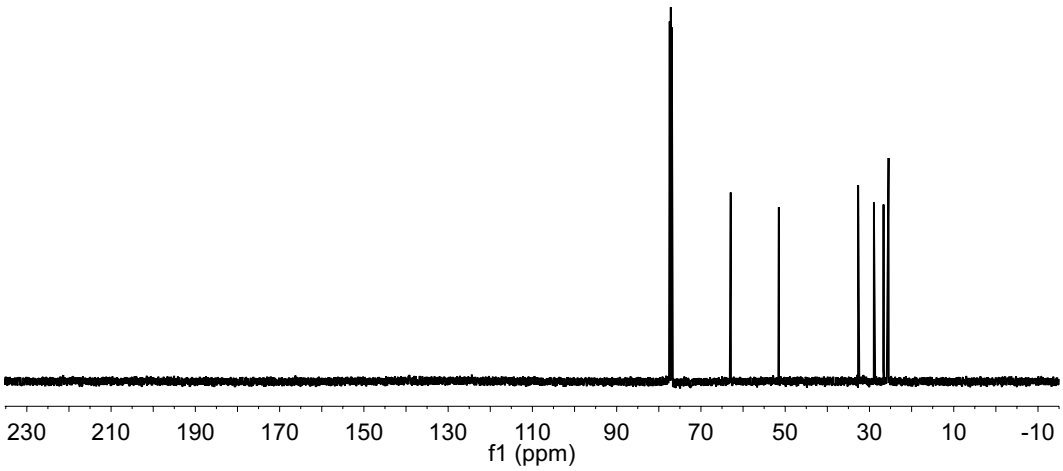
230 210 190 170 150 130 110 90 70 50 30 10 -10
f1 (ppm)

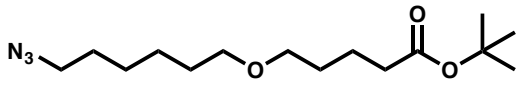
N3
O
O
O

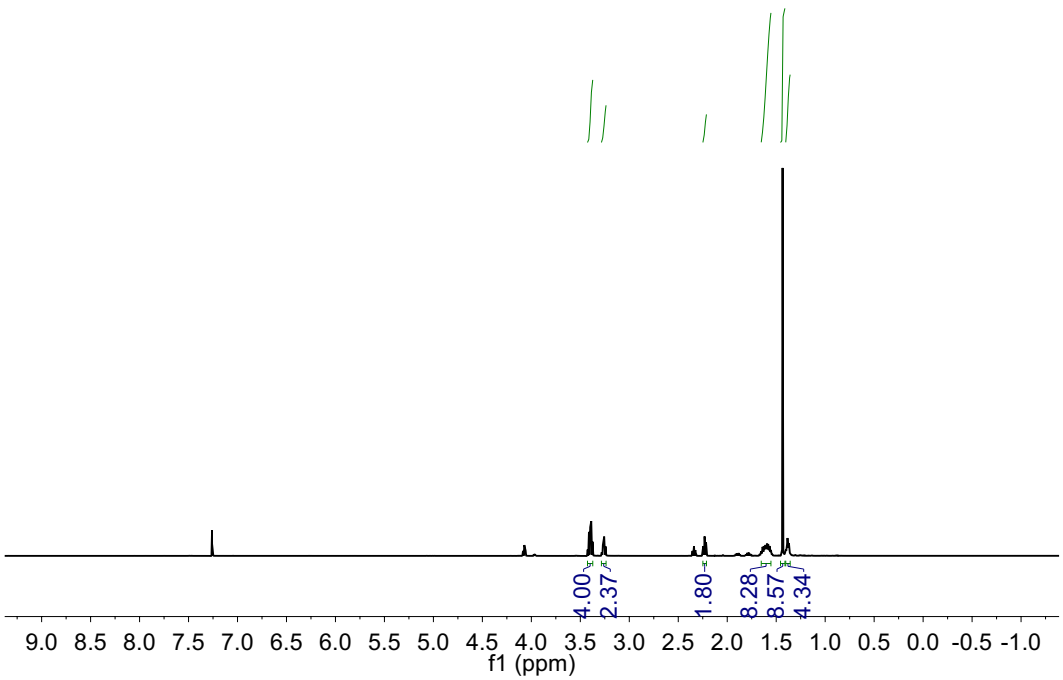
4.00
2.37
1.80
8.28
8.57
4.34
9.0 8.5 8.0 7.5 7.0 6.5 6.0 5.5 5.0 4.5 4.0 3.5 3.0 2.5 2.0 1.5 1.0 0.5 0.0 -0.5 -1.0
f1 (ppm)

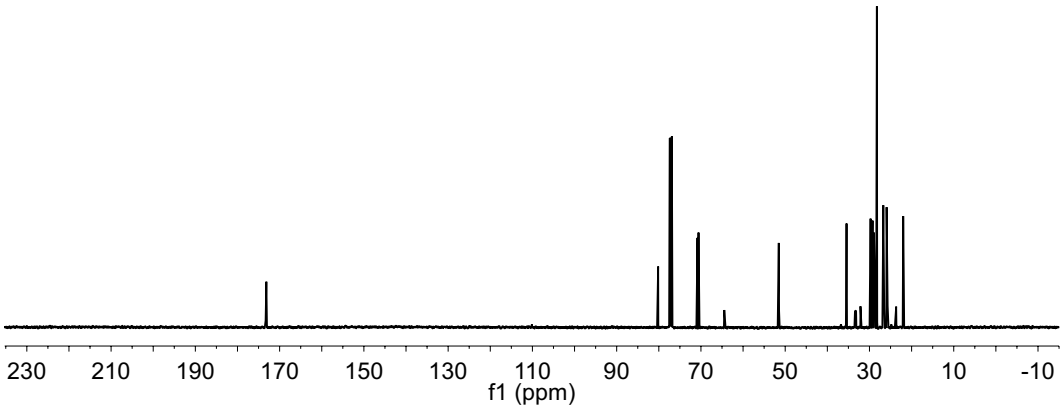
230 210 190 170 150 130 110 90 70 50 30 10 -10
f1 (ppm)

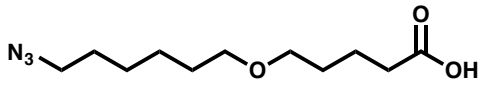
N3
O
O
OH

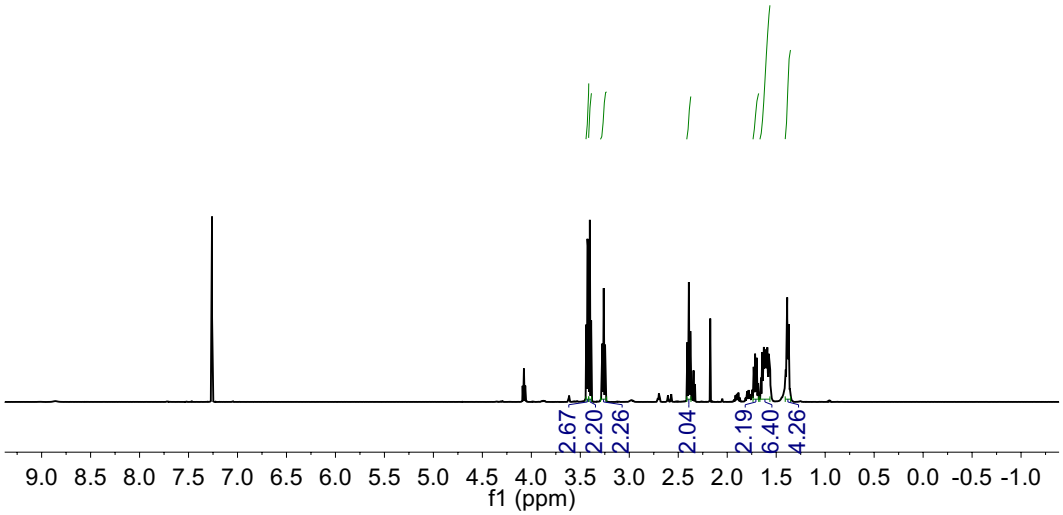
2.67
2.20
2.26
2.04
2.19
6.40
4.26
9.0 8.5 8.0 7.5 7.0 6.5 6.0 5.5 5.0 4.5 4.0 3.5 3.0 2.5 2.0 1.5 1.0 0.5 0.0 -0.5 -1.0
f1 (ppm)

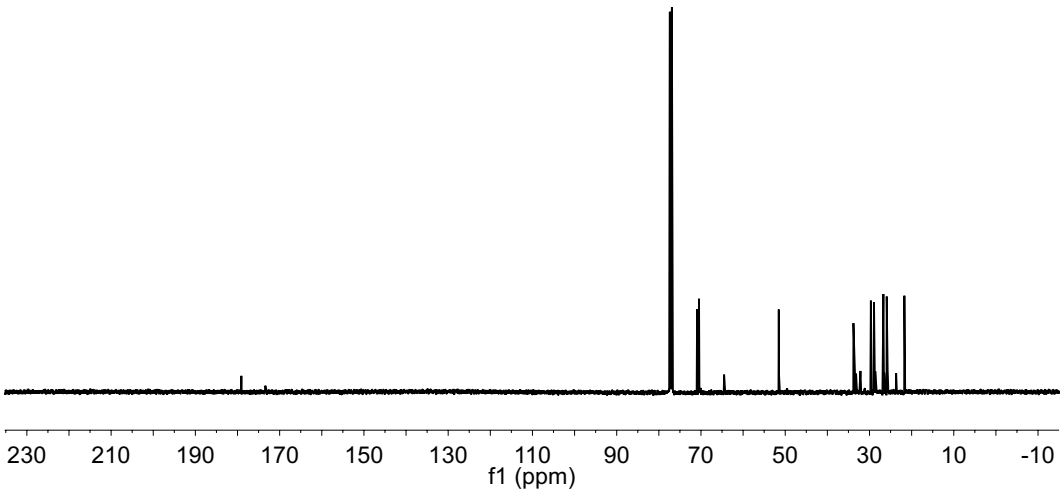
230 210 190 170 150 130 110 90 70 50 30 10 -10
f1 (ppm)

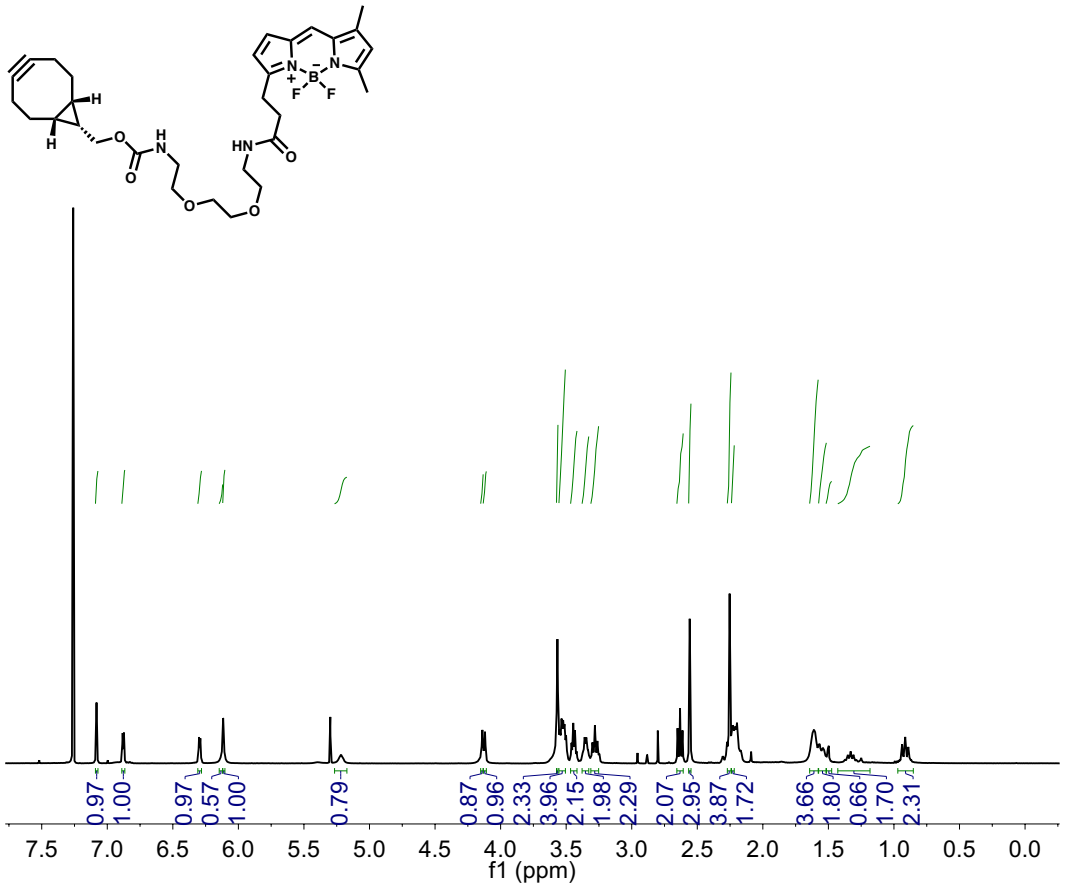
0.97
1.00
0.97
0.57
1.00
0.79
0.87
0.96
2.33
3.96
2.15
1.98
2.29
2.07
2.95
3.87
1.72
3.66
1.80
0.66
1.70
2.31
7.5 7.0 6.5 6.0 5.5 5.0 4.5 4.0 3.5 3.0 2.5 2.0 1.5 1.0 0.5 0.0
f1 (ppm)

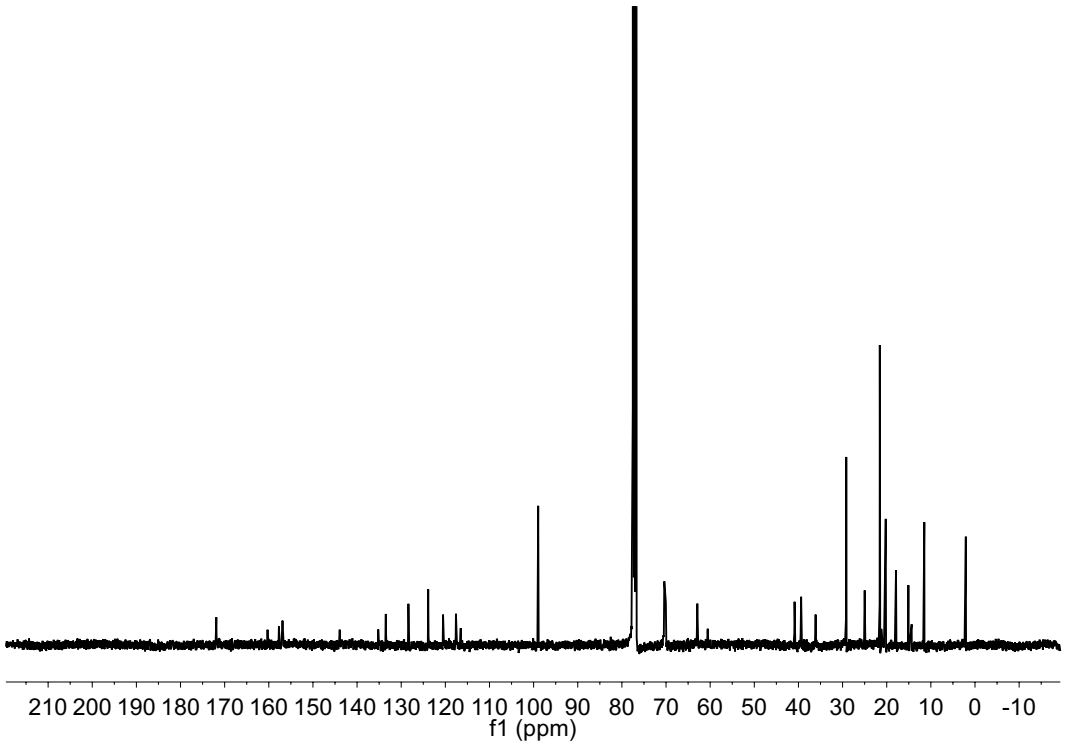
210 200 190 180 170 160 150 140 130 120 110 100 90 80 70 60 50 40 30 20 10 0 -10
f1 (ppm)

2.9 References

(1) Shapiro, L.; McAdams, H. H.; Losick, R. Why and How Bacteria Localize Proteins. *Science* **2009**, *326* (5957), 1225–1228. https://doi.org/10.1126/science.1175685.

(2) Rust, M. J.; Bates, M.; Zhuang, X. Sub-Diffraction-Limit Imaging by Stochastic Optical Reconstruction Microscopy (STORM). *Nature Methods* **2006**, *3* (10), 793–796. https://doi.org/10.1038/nmeth929.

(3) Betzig, E.; Patterson, G. H.; Sougrat, R.; Lindwasser, O. W.; Olenych, S.; Bonifacino, J. S.; Davidson, M. W.; Lippincott-Schwartz, J.; Hess, H. F. Imaging Intracellular Fluorescent Proteins at Nanometer Resolution. *Science* **2006**, *313* (5793), 1642–1645. https://doi.org/10.1126/science.1127344.

(4) Chang, Y.-W.; Chen, S.; Tocheva, E. I.; Treuner-Lange, A.; Löbach, S.; Søgaard-Andersen, L.; Jensen, G. J. Correlated Cryogenic Photoactivated Localization Microscopy and Cryo-Electron Tomography. *Nature Methods* **2014**, *11* (7), 737–739. https://doi.org/10.1038/nmeth.2961.

(5) Shaner, N. C.; Steinbach, P. A.; Tsien, R. Y. A Guide to Choosing Fluorescent Proteins. *Nature Methods* **2005**, *2* (12), 905–909. https://doi.org/10.1038/nmeth819.

(6) Werner, J. N.; Chen, E. Y.; Guberman, J. M.; Zippilli, A. R.; Irgon, J. J.; Gitai, Z. Quantitative Genome-Scale Analysis of Protein Localization in an Asymmetric Bacterium. *Proceedings of the National Academy of Sciences* **2009**, *106* (19), 7858–7863. https://doi.org/10.1073/pnas.0901781106.

(7) Ulrich, G.; Ziessel, R.; Harriman, A. The Chemistry of Fluorescent Bodipy Dyes: Versatility Unsurpassed. *Angewandte Chemie International Edition* **2008**, *47* (7), 1184–1201. https://doi.org/10.1002/anie.200702070.

(8) Chen, I.; Howarth, M.; Lin, W.; Ting, A. Y. Site-Specific Labeling of Cell Surface Proteins with Biophysical Probes Using Biotin Ligase. *Nature Methods* **2005**, *2* (2), 99–104. https://doi.org/10.1038/nmeth735.

(9) Carrico, I. S.; Carlson, B. L.; Bertozzi, C. R. Introducing Genetically Encoded Aldehydes into Proteins. *Nature Chemical Biology* **2007**, *3* (6), 321–322. https://doi.org/10.1038/nchembio878.

(10) Glasgow, J. E.; Salit, M. L.; Cochran, J. R. In Vivo Site-Specific Protein Tagging with Diverse Amines Using an Engineered Sortase Variant. *Journal of the American Chemical Society* **2016**, *138* (24), 7496–7499. https://doi.org/10.1021/jacs.6b03836.

(11) Charbon, G.; Brustad, E.; Scott, K. A.; Wang, J.; Løbner-Olesen, A.; Schultz, P. G.; Jacobs-Wagner, C.; Chapman, E. Subcellular Protein Localization by Using a Genetically Encoded Fluorescent Amino Acid. *ChemBioChem* **2011**, *12* (12), 1818–1821. https://doi.org/10.1002/cbic.201100282.

(12) Devadas, B.; Lu, T.; Katoh, A.; Kishore, N. S.; Wade, A. C.; Mehta, P. P.; Rudnick, D. A.; Bryant, M. L.; Adams, S. P.; Li, Q. Substrate Specificity of Saccharomyces Cerevisiae Myristoyl-CoA: Protein N-Myristoyltransferase. Analysis of Fatty Acid Analogs Containing Carbonyl Groups, Nitrogen Heteroatoms, and Nitrogen Heterocycles in an in Vitro Enzyme Assay and Subsequent Identification of Inhibitors of Human Immunodeficiency Virus I Replication. *J. Biol. Chem.* **1992**, *267* (11), 7224–7239.

(13) Rangan, K. J.; Yang, Y.-Y.; Charron, G.; Hang, H. C. Rapid Visualization and Large-Scale Profiling of Bacterial Lipoproteins with Chemical Reporters. *Journal of the American Chemical Society* **2010**, *132* (31), 10628–10629. https://doi.org/10.1021/ja101387b.

(14) Charlton, T. M.; Kovacs-Simon, A.; Michell, S. L.; Fairweather, N. F.; Tate, E. W. Quantitative Lipoproteomics in Clostridium Difficile Reveals a Role for Lipoproteins in Sporulation. *Chemistry & Biology* **2015**, *22* (11), 1562–1573. https://doi.org/10.1016/j.chembiol.2015.10.006.

(15) Kulkarni, C.; Kinzer-Ursem, T. L.; Tirrell, D. A. Selective Functionalization of the Protein N Terminus with N-Myristoyl Transferase for Bioconjugation in Cell Lysate. *ChemBioChem* **2013**, *14* (15), 1958–1962. https://doi.org/10.1002/cbic.201300453.

(16) Duronio, R. J.; Jackson-Machelski, E.; Heuckeroth, R. O.; Olins, P. O.; Devine, C. S.; Yonemoto, W.; Slice, L. W.; Taylor, S. S.; Gordon, J. I. Protein N-Myristoylation in Escherichia Coli: Reconstitution of a Eukaryotic Protein Modification in Bacteria. *Proceedings of the National Academy of Sciences* **1990**, *87* (4), 1506–1510. https://doi.org/10.1073/pnas.87.4.1506.

(17) Agard, N. J.; Prescher, J. A.; Bertozzi, C. R. A Strain-Promoted [3 + 2] Azide−Alkyne Cycloaddition for Covalent Modification of Biomolecules in Living Systems. *Journal of the American Chemical Society* **2004**, *126* (46), 15046–15047. https://doi.org/10.1021/ja044996f.

(18) Beatty, K. E.; Fisk, J. D.; Smart, B. P.; Lu, Y. Y.; Szychowski, J.; Hangauer, M. J.; Baskin, J. M.; Bertozzi, C. R.; Tirrell, D. A. Live-Cell Imaging of Cellular Proteins by a Strain-Promoted Azide-Alkyne Cycloaddition. *ChemBioChem* **2010**, *11* (15), 2092–2095. https://doi.org/10.1002/cbic.201000419.

(19) Heal, W. P.; Wright, M. H.; Thinon, E.; Tate, E. W. Multifunctional Protein Labeling via Enzymatic N-Terminal Tagging and Elaboration by Click Chemistry. *Nature Protocols* **2012**, *7* (1), 105–117. https://doi.org/10.1038/nprot.2011.425.

(20) Heal, W. P.; Wickramasinghe, S. R.; Leatherbarrow, R. J.; Tate, E. W. N-Myristoyl Transferase-Mediated Protein Labelling in Vivo. *Organic & Biomolecular Chemistry* **2008**, *6* (13), 2308. https://doi.org/10.1039/b803258k.

(21) Maddock, J. R.; Shapiro, L. Polar Location of the Chemoreceptor Complex in the Escherichia Coli Cell. *Science* **1993**, *259* (5102), 1717–1723.

(22) Shiomi, D.; Banno, S.; Homma, M.; Kawagishi, I. Stabilization of Polar Localization of a Chemoreceptor via Its Covalent Modifications and Its Communication with a Different Chemoreceptor. *Journal of Bacteriology* **2005**, *187* (22), 7647–7654. https://doi.org/10.1128/JB.187.22.7647-7654.2005.

(23) Sun, Q.; Margolin, W. FtsZ Dynamics during the Division Cycle of Live Escherichia Coli Cells. *J. BACTERIOL.* **1998**, *180*, 7.

(24) Addinall, S. G.; Lutkenhaus, J. FtsA Is Localized to the Septum in an FtsZ-Dependent Manner. *Journal of Bacteriology* **1996**, *178* (24), 7167–7172. https://doi.org/10.1128/jb.178.24.7167-7172.1996.

(25) Aitken, A.; Cohen, P.; Santikarn, S.; Williams, D. H.; Calder, A. G.; Smith, A.; Klee, C. B. Identification of the NH_2 -Terminal Blocking Group of Calcineurin B as Myristic Acid. *FEBS Letters* **1982**, *150* (2), 314–318. https://doi.org/10.1016/0014-5793(82)80759-X.

(26) Towler, D. A.; Adams, S. P.; Eubanks, S. R.; Towery, D. S.; Jackson-Machelski, E.; Glaser, L.; Gordon, J. I. Purification and Characterization of Yeast Myristoyl CoA:Protein N-Myristoyltransferase. *Proceedings of the National Academy of Sciences* **1987**, *84* (9), 2708–2712. https://doi.org/10.1073/pnas.84.9.2708.

(27) Gentz, R.; Bujard, H. Promoters Recognized by Escherichia Coli RNA Polymerase Selected by Function: Highly Efficient Promoters from Bacteriophage T5. *J. Bacteriol.* **1985**, *164* (1), 70–77.

(28) Van Valkenburgh, H. A.; Kahn, R. A. Coexpression of Proteins with Methionine Aminopeptidase/or N-Myristoyltransferase in Escherichia Coli to Increase Acylation Homogeneity of Protein Preparations. In *Methods in Enzymology*; Elsevier, 2002; Vol. 344, pp 186–193. https://doi.org/10.1016/S0076-6879(02)44715-5.

(29) Dommerholt, J.; Schmidt, S.; Temming, R.; Hendriks, L. J. A.; Rutjes, F. P. J. T.; van Hest, J. C. M.; Lefeber, D. J.; Friedl, P.; van Delft, F. L. Readily Accessible Bicyclononynes for Bioorthogonal Labeling and Three-Dimensional Imaging of Living Cells. *Angewandte Chemie International Edition* **2010**, *49* (49), 9422–9425. https://doi.org/10.1002/anie.201003761.

(30) Wind, M.; Wegener, A.; Kellner, R.; Lehmann, W. D. Analysis of CheA Histidine Phosphorylation and Its Influence on Protein Stability by High-Resolution Element and Electrospray Mass Spectrometry. *Analytical Chemistry* **2005**, *77* (7), 1957–1962. https://doi.org/10.1021/ac040140h.

(31) Marr, A. G.; Ingraham, J. L. Effect of Temperature on the Composition of Fatty Acids in Escherichia Coli. *J. Bacteriol.* **1962**, *84* (6), 1260–1267.

(32) Guzman, L. M.; Belin, D.; Carson, M. J.; Beckwith, J. Tight Regulation, Modulation, and High-Level Expression by Vectors Containing the Arabinose PBAD Promoter. *Journal of Bacteriology* **1995**, *177* (14), 4121–4130. https://doi.org/10.1128/jb.177.14.4121-4130.1995.

(33) Weimar, J. D.; DiRusso, C. C.; Delio, R.; Black, P. N. Functional Role of Fatty Acyl-Coenzyme A Synthetase in the Transmembrane Movement and Activation of Exogenous Long-Chain Fatty Acids: Amino Acid Residues within the ATP/AMP Signature Motif of *Escherichia coli* FadD are Required for Enzyme Activity and Fatty Acid Transport. *Journal of Biological Chemistry* **2002**, *277* (33), 29369–29376. https://doi.org/10.1074/jbc.M107022200.

(34) Ivankov, D. N.; Payne, S. H.; Galperin, M. Y.; Bonissone, S.; Pevzner, P. A.; Frishman, D. How Many Signal Peptides Are There in Bacteria? *Environmental Microbiology* **2013**, *15* (4), 983–990. https://doi.org/10.1111/1462-2920.12105.

(35) Kocaoglu, O.; Carlson, E. E. Progress and Prospects for Small-Molecule Probes of Bacterial Imaging. *Nature Chemical Biology* **2016**, *12* (7), 472–478. https://doi.org/10.1038/nchembio.2109.

(36) Lee, M. K.; Rai, P.; Williams, J.; Twieg, R. J.; Moerner, W. E. Small-Molecule Labeling of Live Cell Surfaces for Three-Dimensional Super-Resolution Microscopy. *Journal of the American Chemical Society* **2014**, *136* (40), 14003–14006. https://doi.org/10.1021/ja508028h.

Chapter 3

LABELING THE BACTERIAL CHEMORECEPTOR TSR

3.1 Abstract

Site-specific modification of bacterial proteins mediated by N-myristoyltransferase (NMT) presents an attractive method for attaching fluorescent dyes to protein targets. Protein targets are expressed using a plasmid-based expression system. We wished to see whether proteins expressed from a single copy in the bacterial chromosome could be labeled by NMT. To this end, we integrated a single copy of the methyl-accepting chemotaxis protein Tsr into the *E. coli* chromosome using site-specific Tn7 transposon mutagenesis. Protein expression was verified through means of immunoblotting. Live-cell imaging was performed using NMT-mediated labeling and confocal fluorescence microscopy. We observed polar localization of the chemoreceptor in live cells. The method demonstrates the feasibility of labeling bacterial proteins that are expressed from a single copy of the gene on the bacterial chromosome.

3.2 Introduction

Bacterial chemoreceptors are remarkable protein assemblies that dictate how prokaryotic organisms respond to attractants or repellents.[1] The histidine–aspartate-phosphorelay signaling pathway consists of the cytoplasmic chemotaxis proteins, CheA, a histidine kinase, and CheB and CheY, regulator proteins that control adaptation and flagellar motor switching, respectively.[2,3] These cytoplasmic chemotaxis proteins interact with the periplasmic domain of bacterial methyl-accepting chemotaxis proteins (MCPs).[4] The transmembrane MCPs form a dimer consisting of a four-helix bundle. These MCPs can bind to different ligands, and these interactions results in changes in the interactions with the periplasmic domain and between the four-helix bundles. Importantly, it is thought that these changes could be important for signal propagation.[5] The bacterial chemoreceptor Tsr has been shown to adopt a hexagonal array with a spacing of 12 nm in *E. coli*.[6] Across many bacterial organisms, the hexagonal array of the chemoreceptors is present at the cellular poles, suggesting that this architecture is a conserved structural motif. The clustering of this protein and other chemotaxis proteins is thought to enhance signaling.[7] Fluorescence labeling of Tsr and its polar localization has been demonstrated by means of protein fusion to YFP on the C-terminus of the protein.[8]

We sought to label the N-terminus of Tsr using NMT-mediated protein labeling. In our previous report,[9] we expressed the bacterial proteins Tar, CheA,[10] FtsZ, and FtsA[11] bearing the NMT recognition sequence from plasmids for site-specific modification. We asked whether the method would be amenable to proteins expressed from a single copy of the gene in the bacterial chromosome. Expression of the protein target from a single genomic copy may be useful in cases where heterogeneity in plasmid copy number poses significant challenges.[12]

3.3 Results and Discussion

We utilized the Tn7 transposon machinery[13,14] to site-specifically insert a single copy of a gene encoding Tsr bearing the N-terminal nonapeptide NMT recognition sequence (MGNEASYPL) and C-terminal $(Gly\text{-}Gly\text{-}Ser\text{-}Gly)_2$ spacer sequence and 3xFLAG epitope.

We placed expression of the protein under control of the bacteriophage T5 promoter. The gene was inserted into the pGRG25 plasmid and transformed into MG1655 *E. coli* cells. The pGRG25 plasmid bears a temperature-sensitive origin of replication that allows for propagation at lower temperatures (32 °C) and plasmid curing at elevated temperatures (42 °C). The plasmid places control of the Tn7 transposon machinery (TnsA, TnsB, TnsC, and TnsD) under the araBAD promoter.[15] The transposon machinery allows for binding and insertion in the region of attTn7 site in *E. coli* between the *phoS* and *glmS* genes. Overnight cultures of MG1655 *E. coli* cells were grown in the presence of 0.1% w/v arabinose at 32 °C to induce expression of the transposon machinery and insert the modified Tsr into the *E. coli* chromosome. Plasmid curing was performed by means of temperature elevation to 42 °C, and a single copy of the inserted gene was verified through polymerase chain reaction on genomic DNA from single colonies (**Figure S3.1**).

Insertion of the modified gene did not have a noticeable impact on cell growth (**Figure S3.2**) when compared to unmodified MG1655 *E. coli* cells. Next, we induced expression of the modified chemoreceptor and analyzed expression through means of immunoblotting against the C-terminal FLAG epitope. *E. coli* cells harboring the genomic insert of the modified Tsr protein and pHV738-NMT-MetAP plasmid[16] were grown at 37 °C to an optical density at 600 nm (OD_{600}) of 0.5. We induced protein expression by addition of 1 mM isopropyl β-D-thiogalactopyranoside (IPTG), and cells continued to grow for an additional 4 h. Cells were collected by centrifugation, rinsed with phosphate-buffered saline (PBS, pH 7.4), and lysed by treatment with 1% w/v sodium dodecyl sulfate (SDS) at 95 °C. Proteins were separated by gel electrophoresis, and immunoblotting was performed with a primary antibody targeted to the FLAG epitope and secondary antibody conjugated to Alexa Fluor 647. In-gel fluorescence detection (633 nm excitation, 670 nm emission) revealed a band corresponding to the apparent molecular weight of the chemoreceptor Tsr bearing the C-terminal 3xFLAG epitope (**Figure S3.3**).

To prepare cells for NMT-mediated labeling, we transformed to the MG1655 *E. coli* cells containing the genomic insert of Tsr the plasmid (pHV738-NMT-MetAP) encoding

constitutive expression of NMT and methionyl aminopeptidase. Cells harboring the pHV738-NMT-MetAP plasmid and the modified *tsr* gene in the chromosome were grown at 37 °C until OD_{600} = 0.5. Protein expression was performed by induction with 1 mM IPTG, and N-terminal labeling was achieved by addition of 250 μM **1**. Cells continued to grow for another 2 h, after which cells were collected by centrifugation, washed with PBS, and resuspended to an OD_{600} = 4.0. Protein labeling was accomplished by treating the cells with 20 μM **2** at 37 °C for 45 min. Cells were washed with PBS three times before being mounted onto a 1.5% w/v agarose pad for imaging with confocal fluorescence microscopy. Detection of the BODIPY fluorophore was achieved by excitation at 488 nm and emission from 505 to 550 nm. In live cells, we saw clear polar localization of the protein Tsr (**Figure 3.1**).

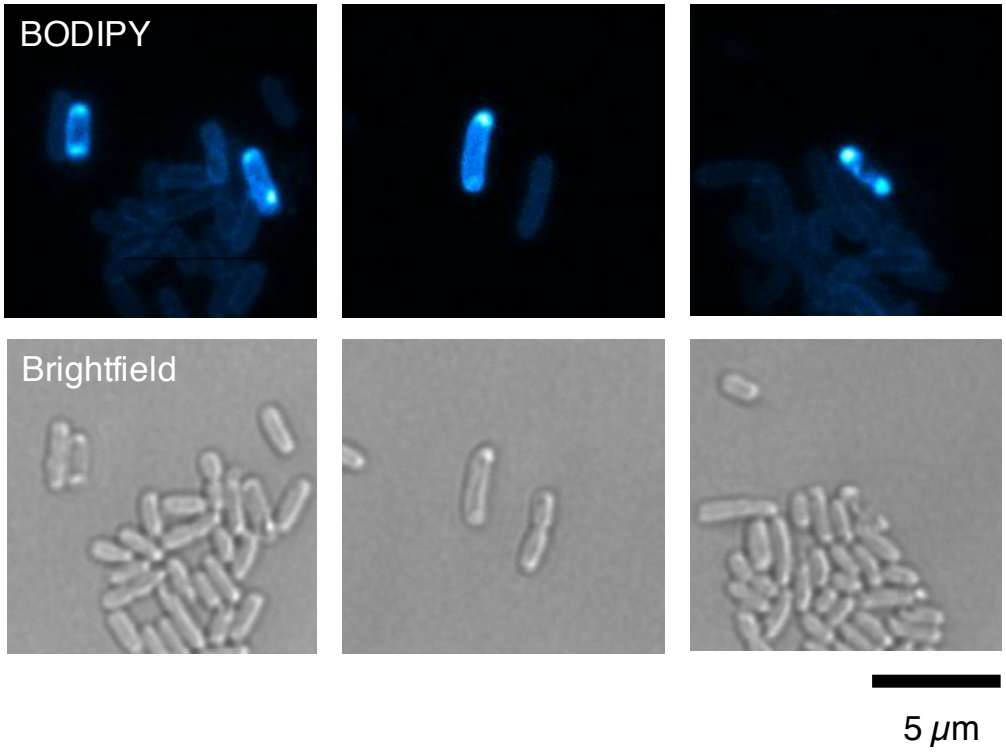

Figure 3.1. Polar localization of the bacterial chemoreceptor Tsr in live *E. coli* cells. The single copy of the gene encoding the protein Tsr bearing the N-terminal NMT recognition sequence was integrated into the *E. coli* chromosome using Tn7 transposon mutagenesis.

When we performed control imaging experiments with unmodified MG1655 *E. coli* cells, we saw diffuse labeling throughout the cell (**Figure 3.2**). The diffuse labeling pattern is

suggestive of modified cell wall lipids (from the azide-bearing fatty acid) reacting with our dye.[9]

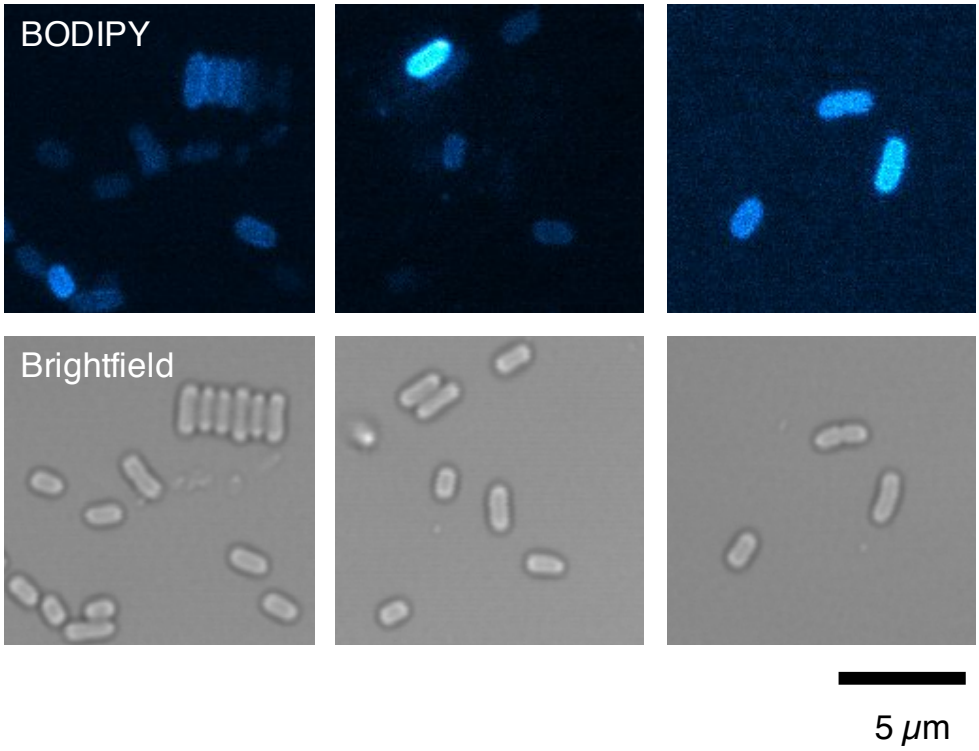

Figure 3.2. Control imaging experiments. Unmodified MG1655 *E. coli* cells were treated with azide-containing fatty acid **1** and bicyclononyne–BODIPY conjugate **2**.

3.4 Conclusions

The NMT method for labeling and imaging bacterial proteins has been adapted for labeling the bacterial protein Tsr expressed from a single genomic copy in the *E. coli* genome. The method provides a general framework for labeling bacterial proteins that are not expressed from plasmid-based expression systems, and may prove useful when overexpression from plasmid-based vectors is problematic.

3.5 Experimental Procedures

Synthetic Compounds. Azide-bearing fatty acid **1** and bicyclononyne–BODIPY **2** were synthesized and characterized as described previously.[9]

Materials and Methods. Lysogeny broth (LB) contained 10 g casein hydrolysate, 5 g yeast extract, and 10 g NaCl per liter. Super optimal broth (SOB) was composed of 20 g casein hydrolysate, 5 g yeast extract, 0.58 g NaCl, 0.19 g KCl, 10 mL 1 M $MgCl_2$, and 10 mL 1M $MgSO_4$ per liter. Super optimal broth with catabolite repression (SOC) was comprised of SOB with the addition of 0.1 mL 2 M glucose to 1 L of SOB medium. Ampicillin sodium salt (BioPioneer, USA) and kanamycin sulfate (BioPioneer, USA) were used at working concentrations of 200 μg/mL and 35 μg/mL, respectively. Phosphate-buffered saline (PBS) was purchased from Thermo Fisher Scientific (USA) and maintained at pH 7.4. PBST was a solution comprising PBS and 0.1% v/v Tween-20. Q5 Hot Start High-Fidelity DNA Polymerase, restriction endonucleases, Instant Sticky-End Master Mix, Antarctic phosphatase, and Blunt Ligase Master Mix were all purchased from New England Biolabs (USA) and used according to the manufacturer's instructions. DNA constructs were sequenced by Retrogen (USA).

pGRG25 was a gift from Nancy Craig (Addgene plasmid #16665; http://n2t.net/addgene:16665 ; RRID:Addgene_16665).

The plasmid encoding N-myristoyltransferase (NMT) and methionyl aminopeptidase (pHV738-NMT-MetAP) was a generous gift from the Kahn laboratory (Emory University, USA). The plasmid confers resistance against kanamycin and contains the p15A origin of replication.

Plasmid Construction in pGRG25. The pGRG25 vector contains an arabinose-inducible promoter for expression of the Tn7 transposon machinery and confers resistance against ampicillin. The gene encoding the methyl-accepting serine chemoreceptor Tsr was amplified from genomic MG1655 *E. coli* DNA using primers 2_hCaNB_Tsr_F and 3_Tsr_GGSG2_R such that the final PCR product read *hCaNB::tsr::$(GGSG)_2$*. The synthetic sequences

encoding the bacteriophage T5 promoter followed by ribosome binding site and 3xFLAG epitope followed by transcription terminator were ordered as linear DNA fragments (IDT, USA). Gibson assembly was performed with the DNA fragments 4_T5_RBS_hCaNB_gblock, 5_GGSG2_3xFLAG_TT_gblock, and PCR product *hCaNB::tsr::(GGSG)$_2$,* such that the final DNA product read *T5::RBS::hCaNB::tsr::(GGSG)$_2$::3xFLAG::TT*. The restriction sites PacI and NotI were introduced at the flanking regions of the DNA strand, and the DNA product was digested and ligated into the PacI/NotI site of the pGRG25.

Integration of Modified *tsr*. Modified pGRG25 plasmids bearing *T5::RBS::hCaNB::tsr::(GGSG)$_2$::3xFLAG::TT* were transformed into chemically competent NEB 10β *E. coli* cells (New England Biolabs, USA). DNA was isolated from cells, and transformed to MG1655 *E. coli* cells via electroporation. Integration of the desired gene was performed by inoculating a single colony in LB with addition of 0.1% w/v arabinose. Cells were grown overnight at 32 °C. The overnight culture was plated on LB agarose plates containing no ampicillin and grown at 42 °C to facilitate removal of the pGRG25 plasmid. Insertion events were confirmed by colony PCR.

Monitoring Growth of Modified Strains. Individual colonies bearing the gene insert of the modified *tsr* (strain SHH013) were used to inoculate LB medium, and cultures were grown overnight at 37 °C with mild agitation (250 rpm). Cultures were diluted to an OD_{600} of 0.1 in LB medium, and OD_{600} was monitored every 20 min for 800 min using a Varioskan LUX microplate reader (Thermo Fisher, USA). The OD_{600} of unmodified MG1655 *E. coli* cells were monitored as a control experiment.

Immunoblotting. Protein lysates were separated by SDS–PAGE and transferred to a 0.2 μm nitrocellulose membrane using an iBlot 2 gel transfer apparatus from Life Technologies (USA), following the manufacturer's protocol. Membranes were blocked with 5% w/v non-fat dry milk in PBST at room temperature for 1 h, and washed three times with PBST before incubating with 1:5000 monoclonal mouse anti-FLAG antibody (Sigma Aldrich) at 4 °C overnight. Membranes (covered from light) were then washed five times with PBST at room

temperature (10 min each wash). To the membrane was added 1:10000 goat anti-mouse antibody conjugated to Alexa Fluor 647 (Invitrogen) in PBST. The membrane was incubated with the secondary antibody at room temperature for 1 h. Membranes (covered from light) were then washed five times with PBST at room temperature (10 min each wash). Fluorescence was visualized using a Typhoon Trio (GE Healthcare, USA) with excitation at 633 nm, the photomultiplier tube (PMT) voltage set to 300 V, and emission monitored using a 670 nm band pass filter.

Labeling of the Bacterial Chemoreceptor Tsr for Fluorescence Imaging. An overnight culture of *E. coli* strain SHH013 (harboring modified Tsr gene and pH738-NMT-MetAP plasmid) were diluted 1:50 in LB medium supplemented with 35 μg/mL kanamycin and grown at 37°C with mild agitation (250 rpm). Cells were grown to an OD_{600} of 0.5, after which 1 mM IPTG and 250 μM **1** was added to the culture. Cells were allowed to grow for an additional 2 h and washed with PBS, after which aliquots of cells were concentrated to an OD_{600} of approximately 4. Cells were rinsed three times with PBS, after which **2** was added to a 100 μL aliquot of cell suspension to a final concentration of 20 μM. The cells were incubated with **2** at 37°C for 45 min, after which the solution was washed three times with PBS to remove excess fluorophore. Cells were then mounted onto a 1.5% w/v agarose slide in PBS for imaging.

Fluorescence microscopy. Protein localization in cells was detected using an inverted Zeiss LSM 880 Exciter laser scanning confocal microscope at the Biological Imaging Facility of the Beckman Institute at Caltech. A 488 nm laser line (25 mW argon laser, 1–2 %) and 505–550 nm band pass filter were used in the detection of proteins labeled by **2**. Images were taken as 15 Z-stacks, with 0.2 μm per stack. ImageJ (NIH) was used to sum each Z-stack to form the projections represented in the figures.

Table S3.1. Primers used in construction of pGRG25-based vector bearing the *T5::RBS::hCaNB::tsr::(GGSG)$_2$::3xFLAG::TT* insert (plasmid name: pGRG25-T5-hCaNB-Tsr-(GGSG)$_2$-3xFLAG).

Primer Name	Sequence (5' to 3')
2_hCaNB_Tsr_F	GGTAACGAAGCGTCTTACCCGCTGG GATCCATGTTAAAACGTATCAAAATT GTGACCAG
3_Tsr_GGSG2_R	ACCAGAACCACCACCAGAACCACCA AATGTTTCCCAGTTCTCCTCG
4_T5_RBS_hCaNB_gblock	ATCGGATCCTAGTAAGCCACGTTTTA ATTAATACCTAAATCATAAAAAATTTA TTTGCTTTGTGAGCGGATAACAATTA TAATAGATTCAATTGTGAGCGGATAA CAATTTCACACAGAATTCATTAAAGA GGAGAAATTAACTATGGGTAACGAAG CGTCTTACCCGCTGGGATCC
5_GGSG2_3xFLAG_TT_gblock	ATTTGGTGGTTCTGGTGGTGGTTCTG GTGACTACAAAGACCATGACGGTGA TTATAAAGATCATGACATCGACTACA AGGATGACGATGACAAGTGAAAGCT TTTTTTACCAGGCATCAAATAAAACG AAAGGCTCAGTCGAAAGACTGGGCC TTTCGTTTTATCTGTTGTTTGTCGGTG AACGCTCTCTACTAGAGTCACACTGG CTCACCTTCGGGTGGGCCTTTCTGC GTTTATAGCGGCCGCCACTCGAGCA CCTAGGA

Table S3.2. *E. coli* strains constructed in this study.

Name	Strain	Genotype
SHH013	MG1655	KanR phoS:T5:hCaNB:tsr:GGSG:3xFLAG:glmS pHV738-NMT-MetAP
SHH014	DH5αα	AmpR pGRG25-T5-hCaNB-Tsr-(GGSG)$_2$-3xFLAG

3.6 Supplementary Figures

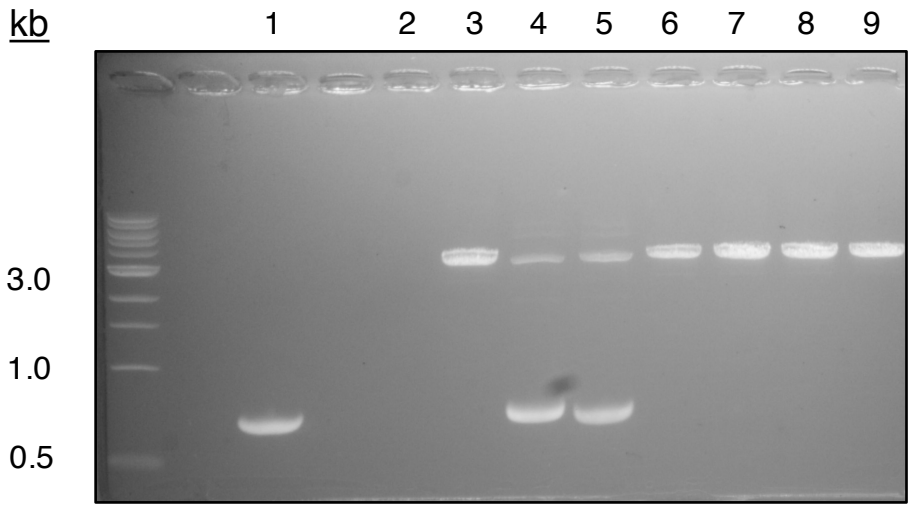

Figure S3.1. Chromosomal integration of T5::hCaNB::Tsr:$(GGSG)_2$:3xFLAG into attTn7 site in MG1655 *E. coli*. Lane 1 corresponds to amplification from unmodified cells with primers flanking the attTn7 site. Band size is approximately 600 bp for Lane 1. Lanes 2–9: Colony PCR to verify insertion event with primers flanking the attTn7 site. If insertion event occurs, the expected band size is approximately 3.0 kb.

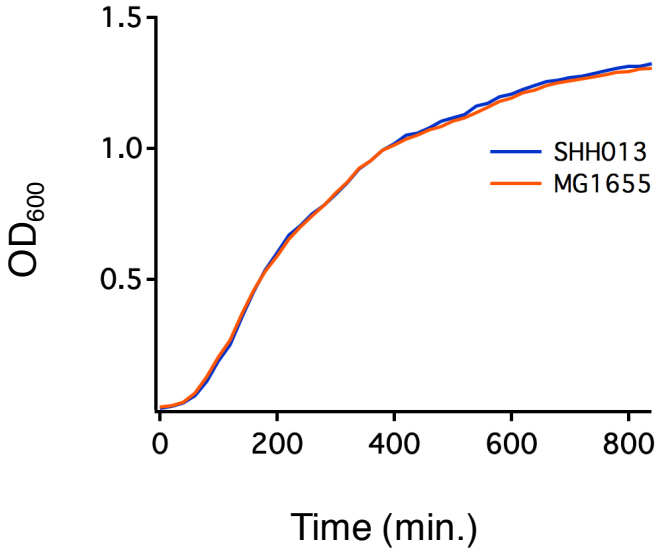

Figure S3.2. Insertion of gene does not affect cell growth. Cells were grown at 37 °C with 250 rpm for 800 min. The optical density at 600 nm (OD_{600}) was monitored every 20 min.

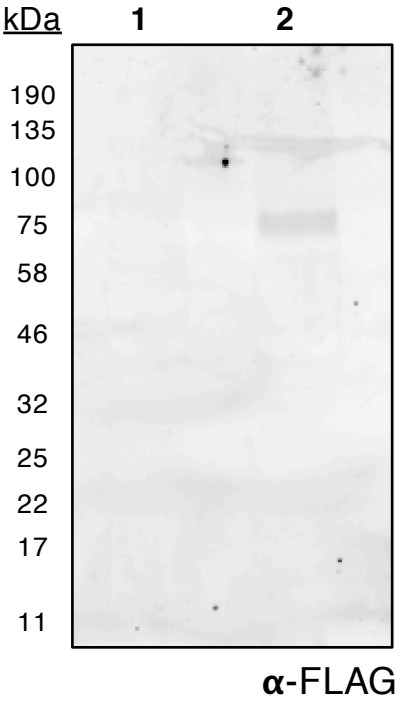

Figure S3.3. Immunoblotting against 3xFLAG epitope on Tsr to verify protein expression. Cells were lysed and proteins were resolved by SDS–PAGE. Immunoblotting was performed with a primary anti-FLAG antibody and secondary antibody conjugated to Alexa Fluor 647. The band in Lane 2 appears at the apparent molecular weight of the protein Tsr. Lane 1 = unmodified MG1655 *E. coli* cell lysate. Lane 2 = Strain SHH013 *E. coli* cell lysate.

3.7 References

(1) Sourjik, V.; Wingreen, N. S. Responding to Chemical Gradients: Bacterial Chemotaxis. *Curr Opin Cell Biol* **2012**, *24* (2), 262–268. https://doi.org/10.1016/j.ceb.2011.11.008.

(2) Khursigara, C. M.; Wu, X.; Zhang, P.; Lefman, J.; Subramaniam, S. Role of HAMP Domains in Chemotaxis Signaling by Bacterial Chemoreceptors. *PNAS* **2008**, *105* (43), 16555–16560. https://doi.org/10.1073/pnas.0806401105.

(3) Parkinson, J. S. Signaling Mechanisms of HAMP Domains in Chemoreceptors and Sensor Kinases. *Annu. Rev. Microbiol.* **2010**, *64*, 101–122. https://doi.org/10.1146/annurev.micro.112408.134215.

(4) Bren, A.; Eisenbach, M. How Signals Are Heard during Bacterial Chemotaxis: Protein-Protein Interactions in Sensory Signal Propagation. *J Bacteriol* **2000**, *182* (24), 6865–6873.

(5) Kim, K. K.; Yokota, H.; Kim, S. H. Four-Helical-Bundle Structure of the Cytoplasmic Domain of a Serine Chemotaxis Receptor. *Nature* **1999**, *400* (6746), 787–792. https://doi.org/10.1038/23512.

(6) Briegel, A.; Ortega, D. R.; Tocheva, E. I.; Wuichet, K.; Li, Z.; Chen, S.; Müller, A.; Iancu, C. V.; Murphy, G. E.; Dobro, M. J.; et al. Universal Architecture of Bacterial Chemoreceptor Arrays. *PNAS* **2009**, *106* (40), 17181–17186. https://doi.org/10.1073/pnas.0905181106.

(7) Sourjik, V.; Armitage, J. P. Spatial Organization in Bacterial Chemotaxis. *EMBO J* **2010**, *29* (16), 2724–2733. https://doi.org/10.1038/emboj.2010.178.

(8) Yu, J.; Xiao, J.; Ren, X.; Lao, K.; Xie, X. S. Probing Gene Expression in Live Cells, One Protein Molecule at a Time. *Science* **2006**, *311* (5767), 1600–1603. https://doi.org/10.1126/science.1119623.

(9) Ho, S. H.; Tirrell, D. A. Chemoenzymatic Labeling of Proteins for Imaging in Bacterial Cells. *Journal of the American Chemical Society* **2016**, *138* (46), 15098–15101. https://doi.org/10.1021/jacs.6b07067.

(10) Maddock, J. R.; Shapiro, L. Polar Location of the Chemoreceptor Complex in the Escherichia Coli Cell. *Science* **1993**, *259* (5102), 1717–1723.

(11) Loose, M.; Mitchison, T. J. The Bacterial Cell Division Proteins FtsA and FtsZ Self-Organize into Dynamic Cytoskeletal Patterns. *Nature Cell Biology* **2014**, *16* (1), 38–46. https://doi.org/10.1038/ncb2885.

(12) Jahn, M.; Vorpahl, C.; Hübschmann, T.; Harms, H.; Müller, S. Copy Number Variability of Expression Plasmids Determined by Cell Sorting and Droplet Digital PCR. *Microb Cell Fact* **2016**, *15*. https://doi.org/10.1186/s12934-016-0610-8.

(13) Waddell, C. S.; Craig, N. L. Tn7 Transposition: Recognition of the AttTn7 Target Sequence. *Proc Natl Acad Sci U S A* **1989**, *86* (11), 3958–3962.

(14) Parks, A. R.; Peters, J. E. Transposon Tn7 Is Widespread in Diverse Bacteria and Forms Genomic Islands. *Journal of Bacteriology* **2007**, *189* (5), 2170–2173. https://doi.org/10.1128/JB.01536-06.

(15) McKenzie, G. J.; Craig, N. L. Fast, Easy and Efficient: Site-Specific Insertion of Transgenes into Enterobacterial Chromosomes Using Tn7 without Need for Selection of the Insertion Event. *BMC Microbiol* **2006**, *6*, 39. https://doi.org/10.1186/1471-2180-6-39.

(16) Van Valkenburgh, H. A.; Kahn, R. A. Coexpression of Proteins with Methionine Aminopeptidase/or N-Myristoyltransferase in Escherichia Coli to Increase Acylation Homogeneity of Protein Preparations. In *Methods in Enzymology*; Elsevier, 2002; Vol. 344, pp 186–193. https://doi.org/10.1016/S0076-6879(02)44715-5.

Chapter 4

ENZYMATIC LABELING OF BACTERIAL PROTEINS FOR SUPER-RESOLUTION IMAGING IN LIVE CELLS

Content from this chapter is adapted from a manuscript in preparation:

Ho, S. H.; Tirrell, D. A. Enzymatic Labeling of Bacterial Proteins for Super-Resolution Imaging in Live Cells. *Manuscript to be submitted.*

4.1 Abstract

Methods that enable super-resolution imaging of intracellular proteins in live bacterial cells provide powerful tools for the study of prokaryotic cell biology. Photoswitchable organic dyes exhibit many of the photophysical properties needed for super-resolution imaging, including high brightness, photostability, and photon output, but most such dyes require organisms to be fixed and permeabilized if intracellular targets are to be labeled. We recently reported a general strategy for chemoenzymatic labeling of bacterial proteins with azide-bearing fatty acids in live cells using the eukaryotic enzyme N-myristoyltransferase. Here we demonstrate labeling of proteins in live *Escherichia coli* using cell-permeant bicyclononyne-functionalized photoswitchable rhodamine spirolactams. Single-molecule fluorescence measurements on model rhodamine spirolactam salts show that these dyes emit hundreds of photons per switching event. Super-resolution imaging was performed on the bacterial chemotaxis proteins Tar and CheA and cell division proteins FtsZ and FtsA. High-resolution imaging of Tar revealed a helical pattern; super-resolution imaging of FtsZ yielded banded patterns dispersed throughout the cell. The precision of radial and axial localization in reconstructed images approaches 15 nm and 30 nm, respectively. The simplicity of the method, which does not require redox imaging buffers, should make this approach broadly useful for imaging intracellular bacterial proteins in live cells with nanometer resolution.

4.2 Introduction

Imaging modalities that provide resolution beyond the diffraction limit have enabled new approaches to the exploration of complex biological phenomena.[1,2] Super-resolution and single-molecule imaging methods have revealed key elements of the structures of biological macromolecules and macromolecular assemblies with nanometer resolution.[3] Examples include the three-dimensional architectures of microtubules and clathrin-coated pits in BS-C-1 cells,[4,5] the periodicity of actin organization in neuronal cells,[6] and the localization of mitochondrial proteins enriched at cristae junctions in human skin fibroblast cells.[7] Methods such as Photoactivated Localization Microscopy (PALM),[8] Stochastic Optical Reconstruction Microscopy (STORM),[9] and direct Stochastic Optical Reconstruction Microscopy (dSTORM)[10] overcome the Abbe diffraction limit[11] by exploiting fluorophores that switch between dark ("off") and fluorescent ("on") states.[12] Conventional small-molecule dyes, which may undergo reversible photoswitching upon excitation, include those bearing carbo-rhodamine,[13] cyanine,[14] and oxazine[15] cores. Photoswitchable fluorescent proteins, such as EYFP[16] and Dronpa,[17] undergo structural rearrangements that enable transitioning between "off" and "on" states. Fluorophores may also undergo irreversible conversion through means of photoactivation with weak UV illumination.[18] This behavior is characteristic of azido push-pull chromophores,[19] rhodamine spiroamides[20] and spirocyclic diazoketones;[21] photoactivatable fluorescent proteins, such as PA-CFP2[22] and PA-mCherry;[23] and photoconvertible fluorescent proteins, such as mEos[24] and Dendra2.[25] Development of fluorescence methods that resolve molecules in space and time with high precision remains an active area of research.[26]

Resolution of adjacent emitters based on their individual point spread functions (PSF) is dependent on the individual fluorophores' photon output, duty cycle, survival fraction, and number of switching cycles.[27] Organic fluorophores offer important advantages that make them attractive for use in super-resolution microscopy, including photostability, brightness,[28] and high photon outputs.[27] Many of the conventional STORM dyes (e.g. Cy5, Alexa 647) require the use of oxygen scavenging buffers and addition of exogenous reducing agents to facilitate photoswitching.[29] Targets are typically labeled by means of immunofluorescence

staining in fixed cells with antibodies conjugated to dyes.[30] The size of antibodies used in such labeling experiments is typically on the scale of 10–15 nm, which may negate the localization precision of the single-molecule imaging experiment.[31] The reagents needed for fixation and permeabilization of cells require careful optimization to ensure that image quality is not affected.[32] For live-cell imaging, fusion of target proteins to the HaloTag[33] has found use in achieving covalent modification with photoactivatable fluorophores in live bacterial[34] and eukaryotic cells,[35] although the size of the tag is on the same order as fluorescent proteins. Improved methods for selective introduction of photoswitchable organic fluorophores into target proteins in live cells are needed to advance the field of super-resolution microscopy.

We recently reported a strategy for introducing azido fatty acids to the N-termini of intracellular proteins in *E. coli* for imaging with cell-permeant fluorophores (**Figure 4.1A**).[36] The method uses the eukaryotic enzyme N-myristoyltransferase (NMT) to ligate the myristic acid surrogate 12-azidodocanoic acid (12-ADA, **1**) to the proteins of interest.[37] Target proteins are outfitted with the nonapeptide sequence MGNEASYPL, an N-terminal NMT recognition sequence derived from the mammalian protein calcineurin B.[38] In this work, we demonstrate labeling of chemotaxis and cell division proteins in live *E. coli* cells with the cell-permeant photoswitchable rhodamine spirolactam dyes **4** and **5** (**Figure 4.1B**). Rhodamine spirolactams have been used as probes for super-resolution imaging of cell-surface targets in live *Caulobacter crescentus*.[39] Upon activation at 405 nm, the fluorophore converts from a non-fluorescent state to a fluorescent state.[40] The open rhodamine isomers thermally re-cyclize on the order of milliseconds in polar solvents,[41] allowing the molecule to undergo photoswitching. Oxygen-scavenging buffer systems and exogenous reducing agents, commonly used to facilitate activation of STORM dyes, are not required for photoswitching of these molecules. To the best of our knowledge, these scaffolds have not been used for labeling and imaging specific intracellular proteins in live bacterial cells.

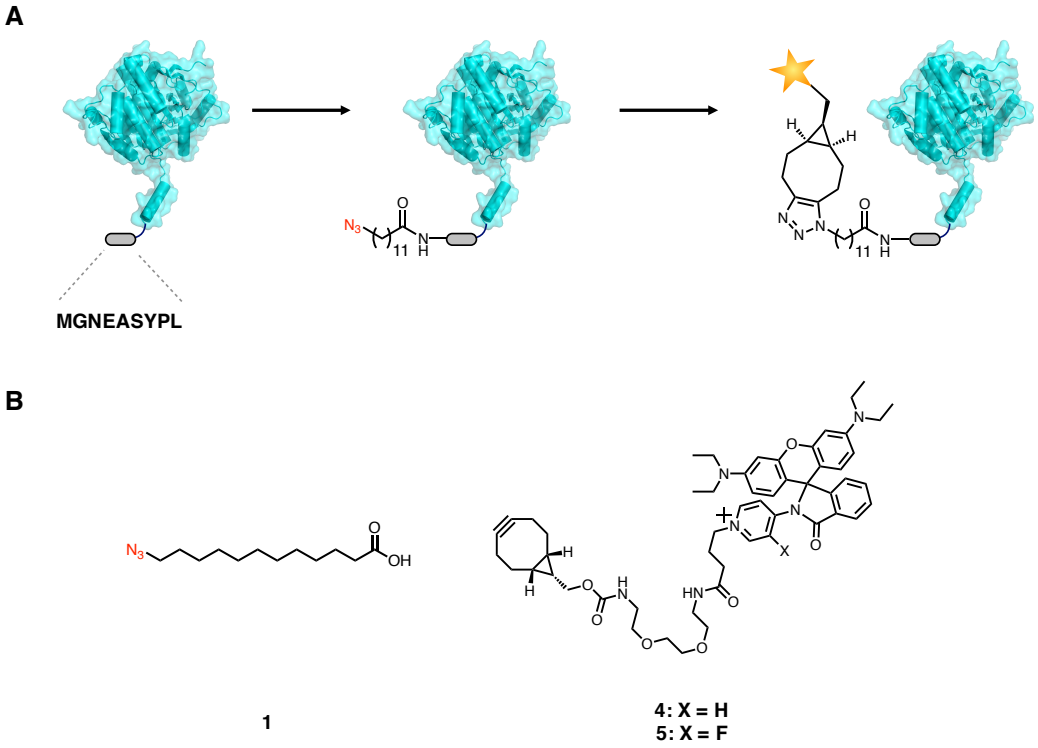

Figure 4.1. Strategy for super-resolution imaging in live cells. (**A**) A bacterial protein of interest is outfitted with a short N-terminal nonapeptide NMT recognition sequence (MGNEASYPL). Treatment of cells with **1** during expression of the target protein results in the azide-labeled protein. Subsequent strain-promoted azide–alkyne cycloaddition with cell-permeant photoswitchable dyes such as **4** and **5** tag the protein of interest for super-resolution imaging. (**B**) Structures of fatty acid **1** and rhodamines **4** and **5**.

Inspired by the potential application of these fluorophores in live-cell imaging experiments, we examined rhodamine spirolactam salts **6** and **7** as model compounds. Bulk spectroscopic characterization was performed on these dyes in aqueous and organic solvents, and we determined each fluorophore's photon output, duty cycle, survival fraction, and number of switching events at the single-molecule level. Finally, we used the reactive dyes **4** and **5** to accomplish live-cell super-resolution imaging of the chemotaxis proteins Tar and CheA[42,43] and cell division proteins FtsZ and FtsA[44,45] in live *E. coli* cells.

4.3 Results and Discussion

Rhodamines **6** and **7** were prepared as iodide salts from commercially available Rhodamine B (**Scheme S4.1** and **S4.2**). Activation of Rhodamine B with phosphorus oxychloride in

refluxing acetonitrile afforded the acid chloride, which was directly condensed with an aminopyridine at room temperature. Formation of the secondary amide induces spontaneous cyclization to form the lactam. Methylation was accomplished by treatment of the lactam with methyl iodide in refluxing acetonitrile and afforded **6** and **7** in 48% and 43% overall yields, respectively.

We characterized the spectral properties of **6** and **7** in a variety of aqueous solutions (**Figure 4.2** and **Figures S4.1–S4.6**). Rhodamine **6** showed no evidence of absorption beyond 500 nm, which is typically observed in yellow-absorbing xanthene dyes, in a 1:1 v/v mixture of water and acetonitrile (**Figure 4.2B, blue solid line**). Addition of acid resulted in a characteristic peak beyond 500 nm (**Figure 4.2B, blue dashed line**, λ_{max} = 561 nm) suggesting a shift in the position of the equilibrium between the closed and open isomers. In contrast, rhodamine **7** showed a small peak at λ_{max} = 553 nm in a 1:1 v/v mixture of water and acetonitrile (**Figure 4.2E, blue solid line**). Acidification of the solvent resulted in a strong absorption peak (λ_{max} = 563 nm) with an intensity roughly 40-fold higher than that of the 553 nm peak in the non-acidic solvent (**Figure 4.2E, blue dashed line**). To determine the spectral properties of the open isomers of **6** and **7**, we determined the molar absorptivity, quantum yield, and fluorescence emission of each compound in acidic-buffered solvents. Interestingly, rhodamine **7** had higher molar absorptivity ($\varepsilon_{563\ nm}$ = 55200 M^{-1} cm^{-1}) and quantum yield (ϕ = 0.69) when compared to **6** ($\varepsilon_{561\ nm}$ = 10200 M^{-1} cm^{-1} and ϕ = 0.54). Both **6** and **7** showed emission profiles commonly found for orange-emitting dyes (**Figure 4.2B, E**, **orange solid lines**). No significant shifts in emission maxima were observed for **7** when compared to **6** (λ_{em} = 578 nm and λ_{em} = 577 nm, respectively). The absorption spectra of rhodamine spirolactams have been shown to respond to changes in pH.[46] To test the pH-sensitivity of **6** and **7**, we prepared solutions in bis-tris propane at different pH values and measured both fluorescence emission and absorption. Analysis of fluorescence emission from **6** showed a 50-fold reduction in intensity as pH increased from 3 to 9.5 (**Figure 2C, D**). In contrast, emission from **7** decreased only 1.6-fold over the same range of pH (**Figure 2F, G**).

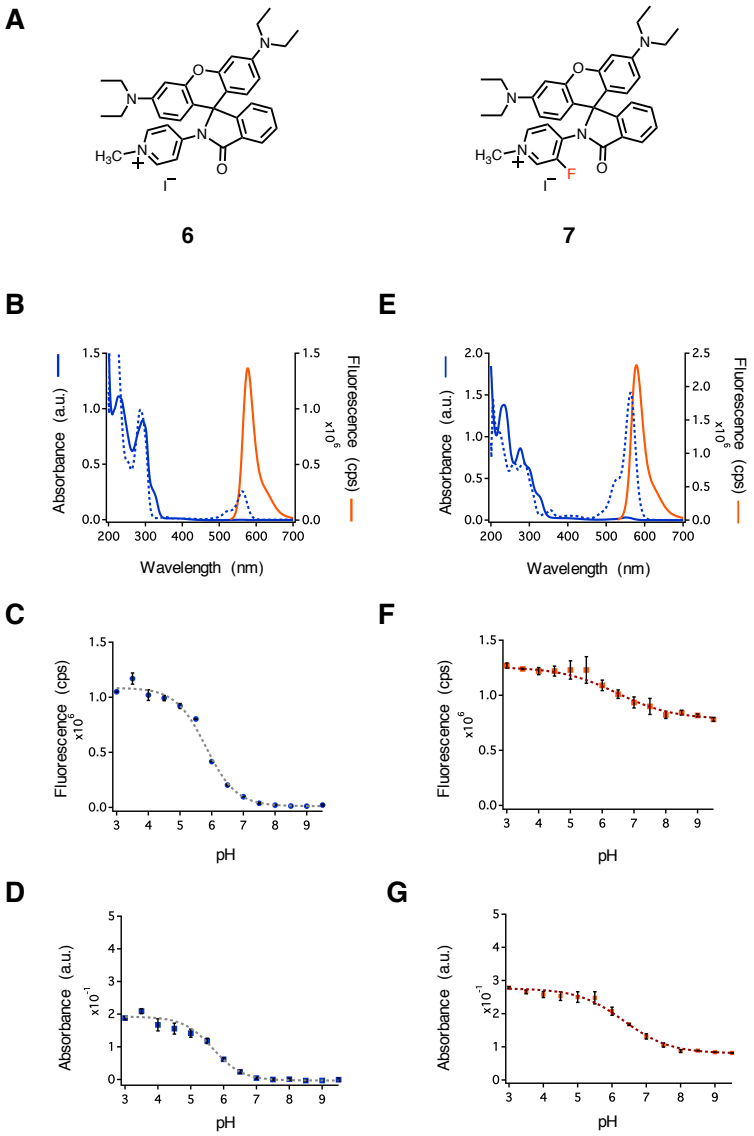

Figure 4.2. Spectroscopic characterization of rhodamines **6** and **7**. (**A**) Structures of rhodamines **6** and **7**. (**B**) Absorption and fluorescence emission spectra of **6**. (**C**) Fluorescence emission values of **6** at λ_{em} = 577 nm as a function of pH. (**D**) Absorption values of **6** at λ_{abs} = 561 nm as a function of pH. (**E**) Absorption and fluorescence emission of **7**. (**F**) Fluorescence emission values of **7** at λ_{em} = 578 nm as a function of pH. (**G**) Absorption values of **7** at λ_{abs} = 563 nm as a function of pH. Error bars donate the standard deviation from three independent experiments. cps = counts per second.

In order for dyes to be useful in super-resolution imaging experiments, they must exhibit photoswitching behavior on the millisecond timescale.[27] To investigate the blinking behavior of **6** and **7**, we analyzed their spectral properties at the single-molecule level. We

determined the photon output, duty cycle, survival fraction, and number of switching cycles for each fluorophore. Dyes were prepared as 200 nM solutions in 1% w/v polyvinyl alcohol (PVA) and cast as films on pre-cleaned glass slides. Immobilizing fluorescent molecules in polymeric films has been used to characterize blinking properties of single molecules.[47] We imaged the cast PVA films by total internal reflection fluorescence (TIRF) microscopy using a Nikon N-STORM Ti2-E inverted microscope. Samples of **6** and **7** were subjected to continuous activation at 405 nm (5% from a 30 mW laser source). Excitation was accomplished at 561 nm (25% from a 70 mW laser source) and emission was collected from 580 nm to 625 nm for 5 min at an integration time of 30 ms. Photon output profiles were plotted as a function of time (**Figure 4.3A, E**). Rhodamine **6** exhibited many photoswitching events, with a mean of 44 switching cycles during the 5 min of acquisition (**Figure 4.3A**) and an average of 661 photons per switching event (**Figure 4.3B**). Next, we calculated the duty cycle (τ)[27] (i.e. the fraction of time the fluorophore spends in the "on" state) and the survival fraction (i.e. the number of molecules that are in the "on" state versus a dark or photobleached state) as a function of time (**Figure 4.3C**). The average duty cycle was calculated to be 0.0036 for the last 100 s of acquisition (**Figure 4.3C, orange squares, gray box**), while the survival fraction declined by roughly 60% over the course of 5 min of acquisition. The behavior of **7** was similar**;** we observed an average of 603 photons per switching event (**Figure 4.3F**), 56 switching events per 5-min acquisition, a duty cycle of 0.0048, and a survival fraction of approximately 40% (**Figure 4.3G**). The photon counts of **6** and **7** are comparable to those of other STORM dyes and photoactivatable fluorescent proteins,[27,48] and suggest that these and similar fluorophores should be applicable in super-resolution imaging.

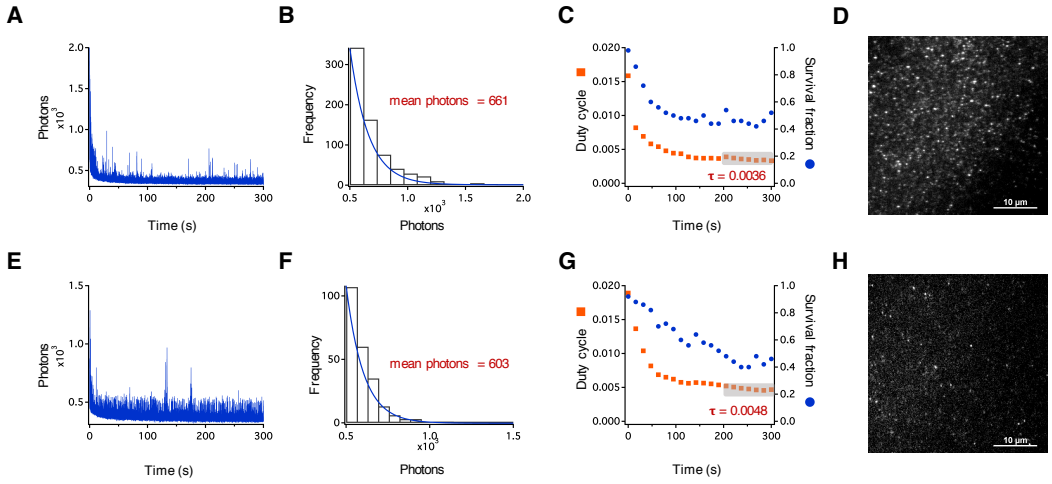

Figure 4.3. Single-molecule characterization of rhodamines **6** and **7**. (**A**) Representative single-molecule fluorescence time traces showing the number of detected photons from single molecules of **6**. (**B**) Histogram showing the distribution of photons. The mean number of photons for **6** was calculated using a single exponential fit (blue line). (**C**) The on/off duty cycle was calculated for **6** and plotted as a function of time (orange squares). The average duty cycle was calculated for the last 100 s of acquisition where the switching events reach a quasi-equilibrium state (gray box). This duty cycle was used to determine the survival fraction during image acquisition and is plotted against time (blue dots). (**D**) Image showing single molecules of **6** in 1% w/v PVA on glass. (**E**) Representative single-molecule fluorescence time traces showing the number of detected photons from single molecules of **7**. (**F**) The mean number of photons for **7** was calculated using a single exponential fit (blue line). (**G**) The on/off duty cycle was calculated for **7** and plotted as a function of time (orange squares). The average duty cycle was calculated for the last 100 s of acquisition where the switching events reach a quasi-equilibrium state (gray box). This duty cycle was used to determine the survival fraction of **7** during image acquisition and is plotted against time (blue dots). (**H**) Image showing single molecules of **7** in 1% w/v PVA on a glass surface.

To enable super-resolution imaging of bacterial proteins, we elaborated the rhodamine spirolactam scaffolds to generate **4** and **5** (**Scheme S4.3**) and employed the NMT labeling strategy illustrated in **Figure 4.1**. The *E. coli* chemotaxis proteins Tar and CheA and cell division proteins FtsZ and FtsA were chosen as test substrates. Cells harboring both the pHV738-NMT1-MetAP plasmid[49] for constitutive expression of NMT and a modified pBAD24 plasmid[50] for inducible expression of the target protein downstream of the araBAD promoter, were grown at 37 ˚C to an optical density at 600 nm (OD_{600}) of 0.5. Expression of each target protein was accomplished by addition of 0.2 % w/v L-arabinose for 1 h and N-terminal labeling was achieved by addition of 250 µM **1**. Cells were collected by

centrifugation, rinsed with PBS, and re-suspended to an OD_{600} of 2 in PBS. A 100 μL aliquot of cells was labeled with 200 nM **4** at 37 ˚C for 1 h in the dark and then washed five times with PBS. A 10 μL aliquot of cells was pipetted onto a 1.5% w/v agarose pad and imaged using the laser conditions described previously for characterization of single molecules of **6** and **7**.

We observed photoswitching of **4** in live cells and reconstructed super-resolution images (**Figure 4.4**). The chemotaxis proteins Tar and CheA predominantly clustered at the cellular poles, a phenomenon believed to enhance chemotactic signaling.[42] The reconstructed image of Tar revealed a helical array throughout the cell. The insertion of Tar into the polar membrane has been reported to be associated with the Sec protein–translocation pathway.[51] The Sec machinery has been shown to form helical patterns which colocalize with expression of Tar. The apparent coil-like structure is thought to arise from distribution of Sec translocases involved in the insertion of proteins into the membrane. Our data are consistent with an additional report detailing the observed helical nature of Tar fused to a photoswitchable fluorescent protein in live bacterial cells.[52] For cell division proteins FtsZ and FtsA, localization near the septum of the cell in diffraction-limited fluorescence images was observed. Cellular division in bacteria involves synthesis of peptidoglycan from synthases that are recruited by FtsZ and FtsA filaments. How the filaments are directionally coupled to peptidoglycan synthases during bacterial cell division in space and time is crucial to the mechanism of bacterial cytokinesis. Recent studies have demonstrated that FtsZ treadmilling both recruits peptidoglycan synthases to the division plane and distributes these enzymes along the cell in the form of concentric rings.[53,54] Our high-resolution image of FtsZ reveals banded patterning throughout the cell and may capture the many FtsZ protofilaments involved in formation of the Z-ring during cell division, consistent with other reports on FtsZ.[55,56] The mean photon output of **4** measured in these live-cell imaging experiments (**Figure 4.4B**) was 864 photons, with a mean localization precision of 13 nm in the radial direction (**Figure 4.4C**) and 27 nm in the axial direction (**Figure S4.7**). Live cells labeled with **5** yielded similar results, with similar photon output and localization precisions, in both radial and axial directions (**Figure S4.8** and **S4.9**). Control experiments, in which

cells did not express the target protein or were treated only with **1**, did not show significant fluorescence (**Figure S4.10 and S4.11**). These results demonstrate that **4** and **5** should be broadly useful for resolving azide-tagged macromolecules in live bacterial cells.

There is considerable interest in the development of methods to label macromolecular targets with small-molecule fluorescent probes for super-resolution fluorescence microscopy, specifically in live cells.[57] Fusion of targets to either the SNAP-Tag or the HaloTag has been successful in achieving site-specific modification of proteins with small-molecule fluorescent probes, but both tags are large relative to the appended fluorophores. As the field progresses towards achieving molecular resolution of new biological architectures, smaller labels will be needed. Bright organic dyes will be critical for pushing imaging modalities forward. Rhodamines **4** and **5** have photon budgets comparable to those of fluorescein, Atto 655, and Alexa 750.[27] Although **4** and **5** emit fewer photons than some yellow- and red-absorbing dyes, such as Cy3 and Cy5,[27] Lavis and co-workers have shown that replacement of the diethylamino groups on rhodamines with azetidine substituents substantially improves the photon output.[58] Furthermore, **4** and **5** can be used directly in live-cell imaging of intracellular targets without the need for fixation and permeabilization. Notably, **4** and **5** do not require inclusion of reducing agents and oxygen scavenging buffers; careful optimization of the concentrations of these reagents is usually needed to facilitate photoswitching of dyes.[59] Although the method is limited to N-terminal labeling and is unlikely to be used on bacterial proteins bearing signal peptides,[60] NMT-mediated labeling provides a simple strategy to append small, bright, photoswitchable dyes to specific target proteins. As dyes continue to be developed with chemical modifications to modulate spectral stability,[61] labeling technologies that enable site-specific covalent modification with small molecules will prove even more broadly useful.

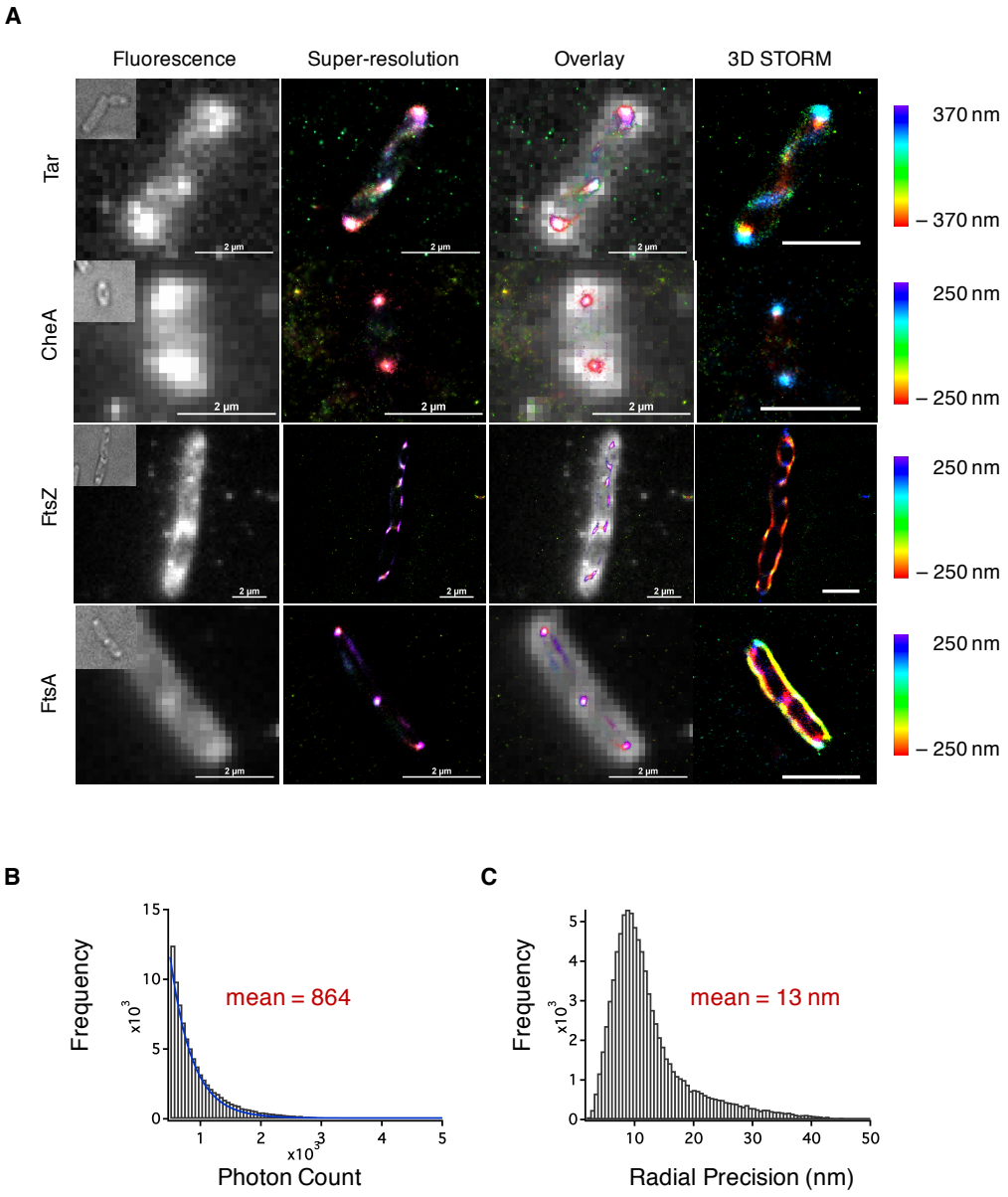

Figure 4.4. Super-resolution imaging of bacterial proteins in live cells. Cells expressing one of four bacterial proteins and are labeled with **1** and **4**. (**A**) STORM images of bacterial proteins with polar localization (Tar and CheA) or septal localization (FtsZ and FtsA) expressed in *E. coli*. Brightfield images of cells are shown in the top left corner of fluorescence images. Scale bar = 2 µm. (**B**) Histogram indicating number of detected photons during image acquisition with fit to single exponential (blue curve). The mean number of photons is calculated from the single exponential fit. (**C**) Mean radial precision for imaging in live bacterial cells.

4.4 Conclusions

The advent of super-resolution imaging methods has transformed our understanding of how prokaryotic organisms orchestrate fundamental cellular processes. Here we report a new class of reactive rhodamine spirolactam dyes and demonstrate their use as cell-permeant fluorescent probes for super-resolution imaging in live bacterial cells. Super-resolution images of the bacterial chemotaxis protein Tar and the cell division protein FtsZ capture features of protein assembly that are not discernable by diffraction-limited fluorescence microscopy. New methods that continue to push the boundaries of light microscopy (e.g. cryogenic PALM) will be particularly informative for elucidating new structures with high precision.[62,63] We anticipate the results described here will expand the palette of methods for super-resolution imaging of proteins in live cells and aid discovery of new biological ultrastructures.

4.5 Experimental Procedures

General Synthetic Procedures. Unless otherwise stated, all synthetic reactions were performed using oven-dried glassware and PTFE stir bars under an atmosphere of argon. Anhydrous solvents were purchased from Sigma-Aldrich and kept under argon. Other chemicals and reagents for chemical reactions were purchased from Sigma Aldrich and used without further purification. Reactions were monitored with thin layer chromatography (EMD/Merck silica gel 60 F254 pre-coated plates) and UV light for visualization. Flash chromatography purifications were carried out using a Biotage Isolera One purification system with pre-packed SNAP Ultra (silica) or SNAP KP-NH (amine-functionalized silica) columns. The gradient of the eluent is given as a percentage of strong solvent per column volume (CV). ^{1}H and ^{13}C NMR spectra were measured on a Bruker Prodigy 400 spectrometer (at 400 MHz and 101 MHz, respectively) equipped with a cryogenic probe. ^{19}F NMR spectra were recorded on either a Varian 300 (282 MHz) or a Bruker 400 (376 MHz) instrument. ^{1}H, ^{13}C, and ^{19}F chemical shifts are reported as δ in units of parts per million (ppm) relative to tetramethylsilane (TMS, δ = 0) and calibrated using the residual solvent peak in chloroform (δ 7.26, singlet for ^{1}H; δ 77.16 for ^{13}C; and δ 0 for ^{19}F, respectively) or dimethylsulfoxide (δ 2.50, quintet for ^{1}H; δ 39.52 for ^{13}C; and δ 0 for ^{19}F, respectively). Data for ^{1}H NMR are reported as follows: chemical shift (δ ppm), multiplicity (s = singlet, d = doublet, t = triplet, q = quartet, p = pentet, m = multiplet, br = broad, dd= doublet of doublets, td = triplet of doublets, dt = doublet of triplets), coupling constant (Hz), and integration. High-resolution mass spectrometry (HRMS) was performed with either a JEOL JMS-600H High Resolution Mass Spectrometer with fast atom bombardment (FAB) or an LCT Premier XE Electrospray TOF Mass Spectrometer with electrospray ionization (ESI) at the California Institute of Technology Mass Spectrometry Facility in the Division of Chemistry and Chemical Engineering. HMRS data are reported as follows: calculated mass, observed mass, error in ppm. Liquid chromatography (LC) coupled with low-resolution mass spectrometry (LRMS) was performed using an Agilent 1290 UHPLC–MS in positive mode at the Center for Catalysis and Chemical Synthesis in the Caltech Beckman Institute.

General Molecular Biology. Lysogeny broth (LB) contained 10 g casein hydrolysate, 5 g yeast extract, and 10 g NaCl per liter of double-distilled water (ddH_2O). Ampicillin sodium salt (BioPioneer, USA) and kanamycin sulfate (BioPioneer, USA) were used at working concentrations of 200 μg/mL and 35 μg/mL, respectively. Phosphate-buffered saline (PBS) was purchased as a 10X stock solution from Thermo Fisher Scientific (USA) and diluted to 1X (pH 7.4) in ddH_2O as needed. Colonies were grown on LB agar plates carrying the appropriate antibiotic supplements. Plates containing colonies were always used within one week or discarded.

Plasmid and Strain Construction. Construction of modified pBAD24 plasmids encoding target bacterial proteins with the NMT recognition sequence has been described previously.[36] Briefly, the gene encoding a bacterial protein of interest was amplified from DH10B *Escherichia coli* using a forward primer that contained the oligonucleotide sequence 5' – ATG GGT AAC GAA GCG TCT TAC CCG CTC – 3' to encode the NMT recognition sequence (MGNEASYPL). The amplified gene was inserted between the EcoRI and HindIII sites in pBAD24 using standard restriction enzyme digestion and ligation protocols. The modified pBAD24 plasmid and pHV738-NMT1-MetAP plasmid[49] were transformed into BL21 *E. coli* and selected against ampicillin (200 μg/mL) and kanamycin (35 μg/mL).

Characterization of Spectral Properties. Spectroscopic measurements were performed in 1-cm, 3.5 mL quartz cuvettes (Starna Cells, Atascadero, CA) at ambient temperature (23 ˚C). Absorption spectra of rhodamine salts were carried out using a Cary 50 UV–visible spectrophotometer (Varian, Palo Alto, CA). Rhodamines were diluted to concentrations ranging from 0 μM to 40 μM in different solvents (e.g. 1:1 v/v acetonitrile/water, acetonitrile, toluene, methanol, and 10 mM HEPES pH 7.3). Extinction coefficients (ε) at 561 nm for **6** and at 563 nm for **7** were calculated by applying the Beer–Lambert law to the absorption spectra of diluted samples in 1:1 v/v water/acetonitrile with addition of 1 M HCl. Measurements were made in triplicate. Fluorescence measurements were performed on a PTI QuantaMaster fluorescence spectrofluorometer (Photon Technology International, Birmingham, NJ). For quantum yield determination, rhodamine salts were diluted in acidic

ethanol (containing 1% v/v 1 M HCl) and adjusted to $A_{510} < 0.1$. Excitation was carried out at 510 nm and emission was collected from 530 nm to 700 nm at a scan rate of 1 nm/s. The quantum yields of the rhodamine salts were calculated using the integrated fluorescence intensities at $\lambda_{em, max}$ and rhodamine B as a standard with known quantum yield (0.70).[64] The reported values for ϕ are averages (n = 3). For pH studies, solutions of rhodamine salts were prepared at a concentration of 5 μM in 10 mM bis-tris propane at different pH values, such that $A_{510} < 0.1$. Fluorescence emission spectra were collected using an excitation wavelength of 510 nm and emission from 530 nm to 700 nm with a scan rate of 1 nm/s.

Single-Molecule Fluorescence Measurements. Rhodamine salts were dissolved at a concentration of 200 nM in 1 % w/v polyvinyl alcohol (31–50 KDa, Sigma Aldrich, St. Louis, MO) and solutions were cast onto 75 mm x 25 mm quartz microscope slides (Electron Microscopy Sciences, Hatfield, PA). Quartz microscope slides were cleaned extensively with acetone, methanol and double-distilled water (ddH_2O), sonication with 1 M KOH for 60 min, and another acetone wash before being dried under a stream of argon. Quartz coverslips (25 mm x 25 mm, Electron Microscopy Sciences, PA) were used to seal the films. Time series were recorded using a Nikon N-STORM Ti2-E inverted microscope (equipped with 405, 488, 561, and 647 nm fiber-coupled excitation lasers) with total reflection internal fluorescence (TIRF) illumination using an Apochromat TIRF 100X/1.49 NA oil immersion objective lens, a sCMOS detector (Andor Technology, South Windsor, CT) for PSF detection, and Perfect Focus System (PFS4) for axial stabilization. The filter cube set (TRF89902-EM-ET 405/488/561/647nm Laser Band Set, Chroma Technology, VT) was equipped with a quad-band pass ZET 405/488/561/647x excitation filter, quad-band ZT405/488/561/647rpc dichroic mirror, and ZET405/488/561/647m emission filters. The excitation wavelengths were 405 nm (5 % from 30 mW laser source) and 561 nm (25 % from 70 mW laser source) and emission was collected from 580 to 625 nm. Single molecules of the rhodamine salts were identified by drawing 7 x 7 pixels around areas that had integrated fluorescence intensities that were at least 5 times the standard deviation of the background fluorescence intensity. Molecules were selected such that the 7 x 7 pixel areas were at least 5 pixels away from each other to ensure molecules were not overlapping. Time series were

performed using an integration time of 30 ms for 5 min, resulting in 10000 frames per acquisition. The duty cycle (D.C.) for each single molecule was calculated as reported by Zhuang and co-workers.[27] Briefly, peaks from the photon output profiles were identified as switching events if the photon count was at least 5 times above the standard deviation of the background fluctuations. A sliding window of 100 s was used in calculating the duty cycle with the following equation:

$$\text{Duty cycle} = \left\langle \frac{\sum_i \tau_{on,\,i}}{100\ \text{s}} \right\rangle$$

where $\tau_{on,\,i}$ denotes the time for which the i^{th} fluorophore is in the 'on' state. The duty cycle is plotted against time in **Figure 4.3** for n = 50 single molecules. The last 100 s were used to assign the D.C. value for determining the survival fraction.

Labeling Proteins with ω-Azido Fatty Acid and Conjugation to Fluorophore in Live Cells. Overnight cultures of *E. coli* strain BL21 harboring modified pBAD24 and pHV738-NMT1-MetAP plasmids were diluted 1:50 in LB medium supplied with 200 μg/mL ampicillin and 35 μg/mL kanamycin and labeled with azido fatty acids as previously described.[36] Protein expression was carried out at 37 °C for 1 h, and cells were harvested by centrifugation, rinsed with PBS, and concentrated to OD_{600} = 2 in PBS. Fluorophore **4** or **5** (2 mM in DMSO) was then added to the cells to a concentration of 200 nM and incubation proceeded at 37 °C for 1 h, after which cells were rinsed five times with PBS to remove excess fluorophore. Cells (in 10 μL aliquots) were mounted onto 1.5 % w/v agarose pads in PBS for imaging.

Super-Resolution Imaging (STORM) in Live Bacterial Cells. Bacterial cells labeled with **1** and either **4** or **5** were mounted onto 1.5 % w/v agarose pads in PBS. Imaging was performed using the Nikon N-STORM 5.0 system on an Ti2-E inverted microscope with TIRF illumination equipped with an Apochromat 100X/1.49 NA oil immersion objective lens and sCMOS detector for PSF detection. Perfect Focus System (PFS4) was used to stabilize and detect the axial position of the agarose pad for imaging. The filter cube set

(TRF89902-EM-ET 405/488/561/647nm Laser Band Set, Chroma Technology, VT) was equipped with a quad-band pass ZET 405/488/561/647x excitation filter, quad-band ZT405/488/561/647rpc dichroic mirror, and ZET405/488/561/647m emission filters. The angle of the incidence wave was adjusted to match the angle of the evanescence wave as close as possible to maximize signal-to-noise. Samples were continuously excited with 405 nm and 561 nm (5 % from 30 mW laser source and 25 % from 70 mW laser source, respectively) and images were recorded at a frame rate of 33 Hz for 10000 frames. Drift correction was automatically implemented by NIS-Elements during image acquisition. STORM images were reconstructed using Nikon Advanced Research (AR) NIS-Elements where each voxel represents a three-dimensional Gaussian representing the localized centroid of each PSF. Histograms of photon counts and localization precisions were determined in NIS-Elements and plotted in IGOR Pro (WaveMetrics, Portland, OR).

4.6 Synthesis of Compounds

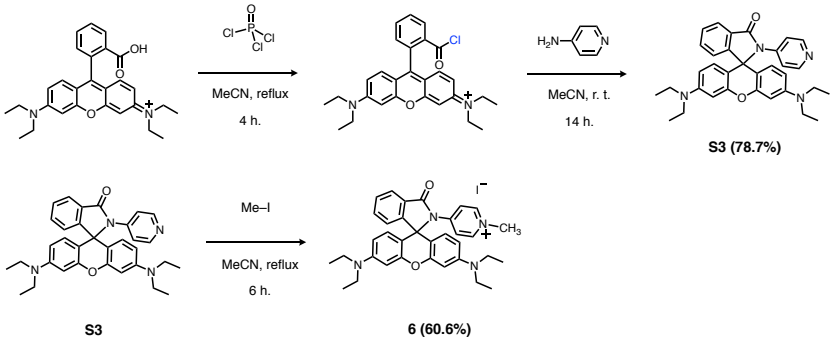

Scheme S4.1. Synthesis of rhodamines **S3** and **6**.

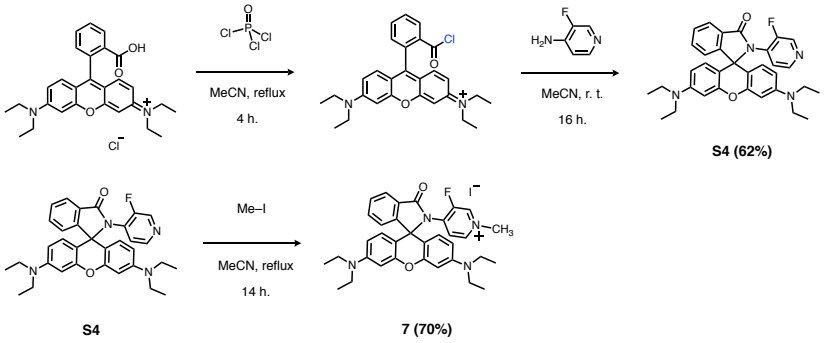

Scheme S4.2. Synthesis of rhodamines **S4** and **7**.

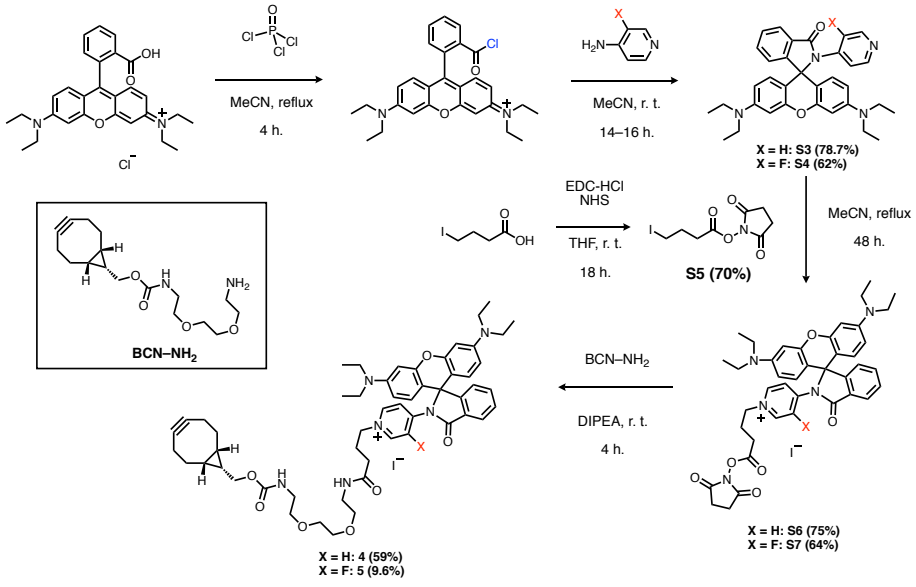

Scheme S4.3. Synthesis of rhodamine spirolactams **4** and **5**.

4.7 Synthesis and Characterization of Compounds

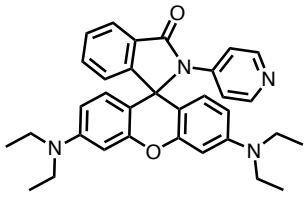

Rhodamine intermediate (**S3**): To a flame-dried 100 mL round bottom flask, was added Rhodamine B (1.5 g, 3.13 mmol, 1.0 eq), PTFE stir bar, and 20 mL acetonitrile at room temperature. Phosphorus(V) oxychloride (0.875 mL, 9.39 mmol, 3.0 eq) was added all at once to the reaction mixture, and the flask was quickly attached to a reflux condenser (14/20 neck size). The solution was heated to 92 °C and allowed to reflux for 4 h, after which the solution was cooled to room temperature and concentrated *in vacuo* to give a purple solid bearing the acid chloride. In a separate 100 mL round bottom flask, 4-aminopyridine (884.1 mg, 9.39 mmol, 3.0 eq) was dissolved in 30 mL acetonitrile. Triethylamine (1.309 mL, 9.39 mmol, 3.0 eq) was added to the solution containing 4-aminopyridine. This pre-mixed solution was then added to the acid chloride via syringe (5 mL per min over the course of 6 min) at room temperature. Gas evolution occurred upon addition of the solution to the acid chloride. The solution was allowed to stir at room temperature for 14 h, after which the solution was concentrated *in vacuo*. Ethyl acetate (50 mL) was added to the resultant solid, and the mixture was transferred to a 1 L separatory funnel. Saturated $NaHCO_3$ (30 mL) was added to wash the organic layer. The organic layer was collected and washed two more times with saturated $NaHCO_3$ (2 x 30 mL). The organic layer was washed three times with saturated NaCl (3 x 50 mL), dried over $MgSO_4$, and concentrated *in vacuo*, resulting in a purple and white solid. Flash chromatography (Biotage SNAP KP-NH, 6–60% ethyl acetate/hexanes over 15 CVs) afforded 1.28 g (78.7%) of **S3** as white solid. ^{1}H NMR (400 MHz, chloroform-d) δ 8.35 – 8.30 (m, 2H), 8.00 – 7.95 (m, 1H), 7.51 – 7.42 (m, 2H), 7.39 – 7.36 (m, 2H), 7.09 – 7.06 (m, 1H), 6.55 (d, J = 8.9 Hz, 2H), 6.37 (d, J = 2.5 Hz, 2H), 6.23 (dd, J = 8.9, 2.6 Hz, 2H), 3.31 (q, J = 7.1 Hz, 8H), 1.15 (t, J = 7.0 Hz, 12H). ^{13}C NMR (101 MHz, chloroform-d) δ 168.96, 154.37, 152.50, 150.05, 149.05, 145.18, 134.00, 128.56, 128.37, 128.05, 123.85, 123.68, 116.92, 108.42, 106.06, 98.01, 66.95, 44.45, 12.73. HRMS (FAB) calculated for $C_{33}H_{35}O_2N_4$ ($[M+H]^+$) 519.2760, found 519.2761 (Δ = 0.2 ppm).

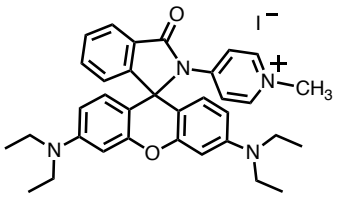

Rhodamine spirolactam (**6**): To a flame-dried 2-neck (14/20) 25 mL round bottom flask, was added rhodamine **S3** (200 mg, 0.386 mmol, 1.0 eq), PTFE stir bar, and 10 mL acetonitrile. Methyl iodide (48 µL, 0.771 mmol, 2.0 eq) was quickly added to the solution all at once and the flask was attached to a reflux condenser. The solution was allowed to reflux at 92 °C for 4 h. TLC was performed to monitor the reaction progress using a solvent system of 2% v/v methanol in methylene chloride. TLC showed that the starting material had not all been consumed. Additional methyl iodide (24 µL, 0.386 mmol, 1.0 eq) was added to the refluxing solution, and the reaction continued to reflux for an additional 2 h. TLC (2% v/v methanol in methylene chloride) indicated the presence of starting material, so additional methyl iodide (12 µL, 0.193 mmol, 0.5 eq) was added to the reaction mixture. The reaction mixture was allowed to reflux for an additional 1 h, after which TLC indicated complete consumption of starting material (total 6 h of reflux with total 3.5 eq of electrophile). Solvent from the reaction mixture was removed *in vacuo* and the resultant brown oil was dissolved in a minimal amount of methylene chloride (2 mL). A mixture of hexanes was added to triturate **6** as a solid. The solid was collected by filtration, washed with hexanes (3 x 5 mL), and dried under vacuum to afford 154.5 mg (60.6%) of rhodamine spirolactam **6** (iodide salt) as a tan solid. ^{1}H NMR (400 MHz, DMSO-d_6) δ 8.68 – 8.64 (m, 2H), 8.08 – 8.04 (m, 2H), 8.01 (dt, J = 7.5, 1.0 Hz, 1H), 7.67 (td, J = 7.5, 1.2 Hz, 1H), 7.59 (td, J = 7.5, 1.0 Hz, 1H), 7.06 (dt, J = 7.7, 0.8 Hz, 1H), 6.57 (d, J = 8.9 Hz, 2H), 6.47 (d, J = 2.7 Hz, 2H), 6.30 (dd, J = 9.0, 2.6 Hz, 2H), 4.04 (s, 3H), 3.30 (m, 8H), 1.07 (t, J = 6.9 Hz, 12H). ^{13}C NMR (101 MHz, DMSO-d_6) δ 169.11, 154.01, 151.58, 149.34, 148.89, 145.63, 136.00, 129.23, 127.28, 125.53, 124.05, 123.67, 114.70, 108.58, 104.03, 97.43, 66.74, 46.44, 43.63, 12.39. HRMS (FAB) calculated for $C_{34}H_{37}O_2N_4$ ($[M]^+$) 533.2916, found 533.2929 (Δ = 2.4 ppm).

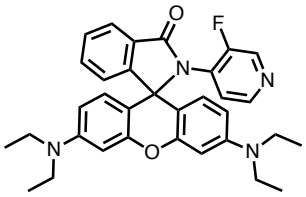

Rhodamine intermediate (**S4**): To a flame-dried 100 mL round bottom flask was added Rhodamine B, (1.5 g, 3.13 mmol, 1.0 eq), PTFE stir bar, and 10 mL acetonitrile. Phosphorus(V) oxychloride (0.875 mL, 9.39 mmol, 3.0 eq) was added all at once to the reaction mixture and the flask was quickly attached to a reflux condenser (14/20 neck size). The solution was heated to 92 °C and allowed to reflux for 4 h, after which the solution was cooled to room temperature and concentrated *in vacuo* to give a purple solid bearing the acid chloride. In a separate 100 mL round bottom flask, 4-amino-3-fluoropyridine (1.053 g, 9.39 mmol, 3.0 eq) was dissolved in 30 mL acetonitrile and triethylamine (1.309 mL, 9.39 mmol, 3.0 eq) was added. The resulting solution was added to the acid chloride (5 mL per min over the course of 6 min) at room temperature. Gas evolution occurred upon addition of the solution containing 4-amino-3-fluoropyridine to the acid chloride. The solution was allowed to stir at room temperature for 16 h, after which the solution was concentrated *in vacuo*. Ethyl acetate (50 mL) was added to the resultant solid, and the mixture was transferred to a 1 L separatory funnel. Saturated $NaHCO_3$ (30 mL) was added to wash the organic layer. The organic layer was collected and washed two more times with saturated $NaHCO_3$ (2 x 30 mL). The organic layer was washed three times with saturated NaCl (3 x 30 mL), dried over $MgSO_4$, and concentrated *in vacuo*, resulting in a purple and white solid. Flash chromatography (Biotage SNAP KP-NH, 6–60% ethyl acetate/hexanes over 15 CVs) afforded 1.04 g (62%) of **S4** as white solid. ^{1}H NMR (400 MHz, chloroform-*d*) δ 8.35 (d, *J* = 2.2 Hz, 1H), 8.10 (d, *J* = 5.2 Hz, 1H), 8.05 – 7.99 (m, 1H), 7.56 – 7.47 (m, 2H), 7.17 – 7.11 (m, 1H), 6.67 (d, *J* = 8.8 Hz, 2H), 6.39 – 6.35 (m, 1H), 6.31 (dd, *J* = 8.9, 2.7 Hz, 2H), 6.27 (d, *J* = 2.6 Hz, 2H), 3.32 (q, *J* = 7.1 Hz, 8H), 1.15 (t, *J* = 7.1 Hz, 12H). ^{13}C NMR (101 MHz, chloroform-*d*) δ 166.77, 156.59, 154.10, 153.98, 153.04, 149.06, 146.03, 145.98, 139.57, 139.34, 133.54, 132.47, 132.37, 129.69, 128.99, 128.49, 124.24, 123.69, 121.79, 108.30, 105.24, 97.65, 67.87, 44.42, 12.66. ^{19}F NMR (282 MHz, chloroform-*d*) δ -128.72. HRMS (ESI) calculated for $C_{33}H_{34}N_4O_2F$ ($[M+H]^+$) 537.2666, found 537.2642 (Δ = -4.5 ppm).

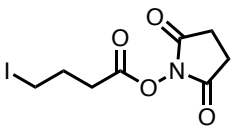

2,5-dioxopyrrolidin-1-yl-4-iodobutanoate (**S5**): To a flame-dried 100 mL round bottom flask was added 4-iodobutyric acid (100 mg, 0.467 mmol, 1.0 eq), N'-ethylcarbodiimide hydrochloride (EDC-HCl) (450 mg, 2.34 mmol, 5.0 eq) N-hydroxysuccinimide (270 mg, 2.34 mmol, 5.0 eq), and PTFE stir bar. The flask was cooled to 0 °C using an ice bath and 15 mL tetrahydrofuran was added. The reaction mixture was allowed to stir and warm to room temperature over the course of 0.5 h. The mixture was stirred for an additional 18 h, after which the solution was diluted with ethyl acetate (20 mL) and extracted with 10% w/v citric acid (20 mL). The organic layer was collected and washed with 10% w/v citric acid (2 x 30 mL) and saturated NaCl (2 x 20 mL), dried over $MgSO_4$ and concentrated *in vacuo* to yield a brown oil. The oil was dissolved in a minimal amount of methylene chloride and loaded onto a Biotage SNAP Ultra cartridge for purification. Purification (6–50% ethyl acetate/hexanes over 15 CVs) afforded 101 mg (70%) of **S5** as a pale yellow solid. This procedure was repeated as needed to generate more **S5**. ^{1}H NMR (400 MHz, chloroform-*d*) δ 3.28 (t, *J* = 6.7 Hz, 2H), 2.84 (s, 4H), 2.77 (t, *J* = 7.2 Hz, 2H), 2.24 (p, *J* = 6.9 Hz, 2H). ^{13}C NMR (101 MHz, chloroform-*d*) δ 169.13, 167.69, 31.93, 28.25, 25.71, 4.01. HRMS (ESI) calculated for $C_8H_{10}NO_4INa$ ($[M+Na]^+$) 333.9552, found 333.9546 (Δ = -1.8 ppm).

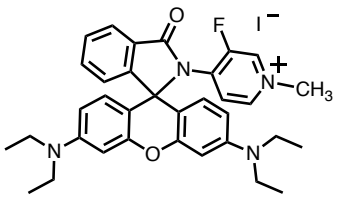

Rhodamine spirolactam (**7**): A flame-dried 2-neck (14/20) 25 mL round bottom flask was charged with rhodamine **S4** (100 mg, 0.186 mmol, 1.0 eq) and PTFE stir bar. Acetonitrile (10 mL) was added to the flask and methyl iodide (23.2 µL, 0.373 mmol, 2.0 eq) was subsequently added. The flask was quickly attached to a reflux condenser and refluxed at 92 °C for 3 h. TLC (2% v/v methanol in methylene chloride) was used to monitor the reaction and indicated the presence of starting material. Methyl iodide (23.2 µL, 0.373 mmol, 2.0 eq) was added to the refluxing solution after 2 h. After an additional 1 h, TLC indicated the starting material had not been completely consumed. Another 2.0 eq of methyl iodide (23.2 µL, 0.373 mmol) was added to the solution. Over the next 6 h, methyl iodide (23.2 µL, 0.373 mmol, 2.0 eq) was added every 2 h. After a total of 14 h, the amount of starting material did not decrease further, as indicated by TLC. The reaction mixture was

cooled to room temperature and concentrated *in vacuo*. Flash chromatography (Biotage SNAP Ultra, 1–2% v/v methanol/methylene chloride over 15 CVs) afforded 88.4 mg (70%) of rhodamine spirolactam **7** as a brilliant red powder. ^{1}H NMR (400 MHz, DMSO-d_6) δ 9.36 (d, J = 5.8 Hz, 1H), 8.72 (dd, J = 6.8, 1.5 Hz, 1H), 8.04 – 7.97 (m, 1H), 7.69 (td, J = 7.4, 1.4 Hz, 1H), 7.63 (td, J = 7.4, 1.2 Hz, 1H), 7.13 (d, J = 7.5 Hz, 1H), 6.93 (t, J = 6.9 Hz, 1H), 6.60 (d, J = 8.9 Hz, 2H), 6.44 (dd, J = 9.0, 2.6 Hz, 2H), 6.36 (d, J = 2.6 Hz, 2H), 4.16 (s, 3H), 3.34 – 3.22 (m, 8H), 1.08 (t, J = 6.9 Hz, 12H). ^{13}C NMR (101 MHz, DMSO-d_6) δ 165.89, 154.86, 154.24, 152.29, 152.08, 151.95, 148.91, 143.86, 143.82, 139.93, 139.83, 137.38, 137.00, 135.25, 129.32, 128.02, 126.70, 124.18, 123.71, 121.27, 108.79, 103.67, 97.13, 68.29, 48.03, 43.66, 12.38. ^{19}F NMR (282 MHz, DMSO-d_6) δ -118.19. HRMS (ESI) calculated for $C_{34}H_{36}N_4O_2F$ ($[M]^+$) 551.2822, found 551.2831 (Δ = 1.6 ppm).

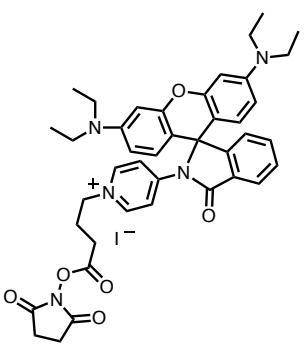

Rhodamine spirolactam NHS ester (**S6**): A flame-dried 2-neck (14/20) 25 mL round bottom flask was charged with rhodamine **S3** (250 mg, 0.482 mmol, 1.0 eq), NHS ester **S5** (300 mg, 0.964 mmol, 2.0 eq), and PTFE stir bar. Acetonitrile (12 mL) was added and the flask was quickly attached to a reflux condenser. The solution was heated to 90 °C and allowed to stir under refluxing conditions for 48 h, after which the solution was cooled to room temperature and solvent was removed *in vacuo*, resulting in a tan precipitate. Ethyl acetate (10 mL) was added to the flask, and the solution was allowed to gently stir for 12 h, after which the solid was collected by filtration. The solid was washed with ethyl acetate (3 x 10 mL) and dried under vacuum to afford 300 mg (75%) rhodamine spirolactam NHS ester **S6** as a tan powder. ^{1}H NMR (400 MHz, DMSO-d_6) δ 8.74 (d, J = 7.6 Hz, 2H), 8.08 (d, J = 7.6 Hz, 2H), 8.03 – 8.01 (m, 1H), 7.67 (td, J = 7.5, 1.2 Hz, 1H), 7.59 (td, J = 7.4, 1.0 Hz, 1H), 7.05 (d, J = 7.8 Hz, 1H), 6.57 (d, J = 8.9 Hz, 2H), 6.48 (d, J = 2.6 Hz, 2H), 6.31 (dd, J = 9.0, 2.6 Hz, 2H), 4.36 (t, J = 7.2 Hz, 2H), 3.33 – 3.22 (m, 8H), 2.80 (s, 4H), 2.79 – 2.74 (m, 2H), 2.17 (q, J = 7.5 Hz, 2H), 1.07 (t, J = 7.0 Hz, 12H). ^{13}C NMR (101 MHz, DMSO-d_6) δ 170.15, 169.13, 168.17, 154.07, 151.61, 149.87, 148.91, 144.85, 136.05, 129.23, 127.38, 125.47, 124.07,

123.69, 115.09, 108.60, 103.98, 97.41, 66.85, 58.04, 43.63, 27.12, 25.45, 24.89, 12.39. HRMS (ESI) calculated for $C_{41}H_{44}N_5O_6$ ($[M]^+$) 702.3292, found 702.3267 (Δ = -3.6 ppm).

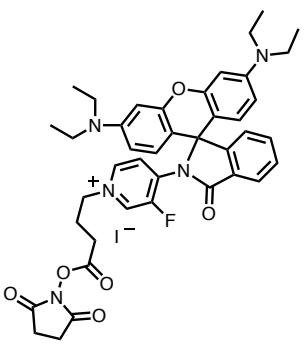

Rhodamine spirolactam NHS ester (**S7**): To a flame-dried 2-neck (14/20) 50 mL round bottom flask was added rhodamine **S4** (125 mg, 0.233 mmol, 1.0 eq), NHS ester **S5** (181.2 mg, 0.582 mmol, 2.5 eq), and PTFE stir bar. Acetonitrile (15 mL) was added to the flask and the flask was quickly attached to a reflux condenser. The solution was heated to 95 °C and allowed to reflux for 48 h, after which the solvent was removed *in vacuo*, resulting in a red oil with a purple hue. Ethyl acetate (5 mL) was added to the flask, and the solution was allowed to stir for 24 h at room temperature, resulting in a purple solid. The solid was collected by filtration, washed with ethyl acetate (3 x 5 mL), and dried under vacuum to afford 126 mg (64%) of rhodamine spirolactam NHS ester **S7** as a purple powder. ^{1}H NMR (400 MHz, DMSO-d_6) δ 9.41 (d, J = 5.8 Hz, 1H), 8.79 (d, J = 6.9 Hz, 1H), 8.04 – 8.00 (m, 1H), 7.69 (td, J = 7.5, 1.3 Hz, 1H), 7.63 (td, J = 7.4, 1.1 Hz, 1H), 7.13 (d, J = 7.7 Hz, 1H), 6.99 (t, J = 6.9 Hz, 1H), 6.60 (d, J = 8.9 Hz, 2H), 6.44 (dd, J = 9.0, 2.6 Hz, 2H), 6.37 (d, J = 2.6 Hz, 2H), 4.48 (t, J = 7.1 Hz, 2H), 3.33 – 3.25 (m, 8H), 2.81 (s, 4H), 2.80 – 2.77 (m, 2H), 2.23 (p, J = 7.4 Hz, 2H), 1.08 (t, J = 6.9 Hz, 12H). ^{13}C NMR (101 MHz, DMSO-d_6) δ 170.14, 168.15, 165.90, 155.02, 154.27, 152.45, 152.05, 148.91, 142.96, 140.41, 140.31, 136.67, 136.29, 135.32, 129.31, 127.96, 126.54, 124.16, 123.75, 121.12, 108.81, 103.78, 97.16, 68.38, 43.65, 40.15, 39.94, 39.73, 39.52, 39.31, 39.10, 38.89, 27.07, 25.45, 24.65, 12.37. HRMS (ESI) calculated for $C_{41}H_{43}N_5O_6F$ ($[M]^+$) 720.3197, found 720.3178 (Δ = -2.6 ppm).

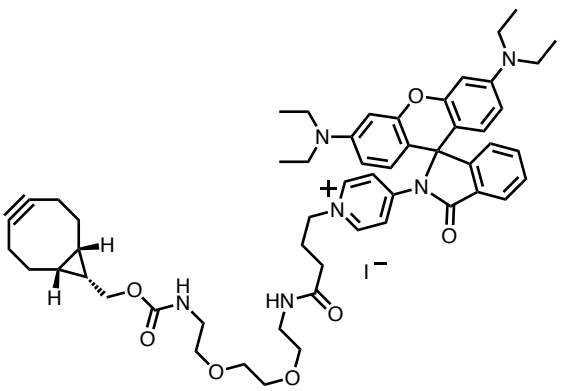

Bicyclononyne rhodamine conjugate (**4**): To a 20 mL scintillation vial was added ester **S6** (15 mg, 18.1 μmol, 1.0 eq), 0.5 mL dimethylformamide, and a PTFE stir bar. BCN-NH_2 (see **Scheme S4.3**) (7.62 mg, 23.5 μmol, 1.3 eq, dissolved in 1.0 mL dimethylformamide) was added to the solution; N,N-diisopropylethylamine (5.6 μL, 32.01 μmol, 1.8 eq) was added subsequently. The reaction mixture was allowed to stir for 2 h at room temperature, after which the crude mixture was directly dry loaded onto Celite. Flash chromatography (Biotage SNAP KP-NH, 0–20% methanol/ethyl acetate over 15 CVs) afforded 11.1 mg (59%) of **4** as a pale yellow film. ^{1}H NMR (400 MHz, chloroform-*d*) δ 8.70 (d, *J* = 7.0 Hz, 2H), 8.25 (d, *J* = 7.3 Hz, 2H), 8.01 – 7.98 (m, 1H), 7.57 (td, *J* = 7.5, 1.2 Hz, 1H), 7.49 (td, *J* = 7.5, 1.0 Hz, 1H), 7.08 – 7.06 (m, 1H), 6.46 (d, *J* = 2.6 Hz, 2H), 6.43 (d, *J* = 8.9 Hz, 2H), 6.22 (dd, *J* = 9.0, 2.6 Hz, 2H), 5.47 (br s, 1H), 4.75 (t, *J* = 7.8 Hz, 2H), 4.17 – 4.07 (m, 3H), 3.62 – 3.59 (m, 4H), 3.58 – 3.53 (m, 3H), 3.54 – 3.48 (m, 2H), 3.39 – 3.29 (m, 12H), 2.51 (t, *J* = 6.8 Hz, 2H), 2.26 – 2.20 (m, 7H), 1.64 – 1.52 (m, 3H), 1.38 – 1.31 (m, 1H), 1.17 (t, *J* = 7.1 Hz, 12H), 0.92 (t, *J* = 10.0 Hz, 2H). ^{13}C NMR (101 MHz, chloroform-*d*) δ 171.85, 171.74, 170.12, 157.06, 154.46, 152.49, 152.15, 151.11, 149.66, 143.70, 136.07, 129.08, 127.02, 125.71, 124.42, 124.06, 115.93, 108.77, 108.07, 103.77, 99.00, 98.38, 98.00, 70.41, 70.33, 70.26, 69.59, 68.05, 62.75, 60.55, 58.90, 44.53, 40.85, 40.73, 39.29, 39.16, 32.35, 29.21, 28.10, 21.59, 21.21, 20.23, 17.94, 14.34, 12.74. HRMS (ESI) calculated for $C_{54}H_{67}N_6O_7$ ($[M]^+$) 911.5071, found 911.5060 (Δ = -1.2 ppm).

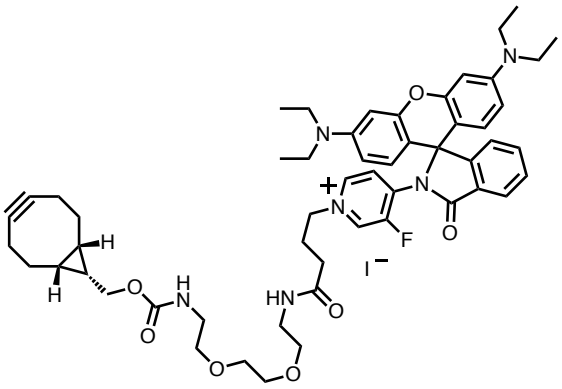

Bicyclononyne rhodamine conjugate (**5**): To a 20 mL scintillation vial was added ester **S7** (12 mg, 14.2 μmol, 1.0 eq), 0.5 mL dimethylformamide, and a PTFE stir bar. BCN-NH_2 (see **Scheme S4.3**) (9.19 mg, 28.3 μmol, 2.0 eq, dissolved in 1.0 mL dimethylformamide) was added to the solution; N,N-diisopropylethylamine (3.71 μL, 21.3 μmol, 1.5 eq) was added subsequently. The reaction mixture was allowed to stir for 2 h at room temperature, after which the crude mixture was directly dry loaded onto Celite. Flash chromatography (Biotage SNAP KP-NH, 0–20% methanol/ethyl acetate over 15 CVs) afforded 1.4 mg (9.6%) of **5** as a purple film. ^{1}H NMR (400 MHz, chloroform-*d*) δ 9.02 – 8.97 (m, 1H), 8.02 (d, *J* = 7.4 Hz, 1H), 7.65 – 7.46 (m, 3H), 7.14 – 7.08 (m, 1H), 6.58 (d, *J* = 8.9 Hz, 2H), 6.36 (d, *J* = 2.5 Hz, 2H), 6.31 (dd, *J* = 9.1, 2.7 Hz, 2H), 6.23 – 6.20 (m, 1H), 5.45 (s, 1H), 4.96 (s, 1H), 4.21 – 4.07 (m, 3H), 3.69 – 3.53 (m, 9H), 3.43 – 3.29 (m, 12H), 2.55 – 2.41 (m, 2H), 2.34 – 2.15 (m, 7H), 1.41 – 1.30 (m, 4H), 1.18 (t, *J* = 7.1 Hz, 12H), 1.00 – 0.90 (m, 2H). ^{13}C NMR (101 MHz, chloroform-*d*) δ 173.03, 168.44, 166.70, 157.12, 156.37, 154.54, 153.14, 152.71, 149.67, 144.47, 136.75, 135.20, 134.68, 128.00, 124.41, 124.35, 108.99, 108.27, 108.10, 103.89, 101.60, 99.00, 97.94, 70.41, 70.36, 70.24, 69.62, 68.10, 62.82, 60.56, 57.62, 44.55, 40.90, 40.84, 39.37, 39.10, 31.98, 29.20, 27.95, 21.59, 21.22, 20.25, 17.93, 14.35, 12.75. ^{19}F NMR (376 MHz, chloroform-*d*) δ -111.36. HRMS (ESI) calculated for $C_{54}H_{66}N_6O_7F$ ($[M]^+$) 929.4977, found 929.4978 (Δ = 0.1 ppm).

4.8 Supplementary Figures

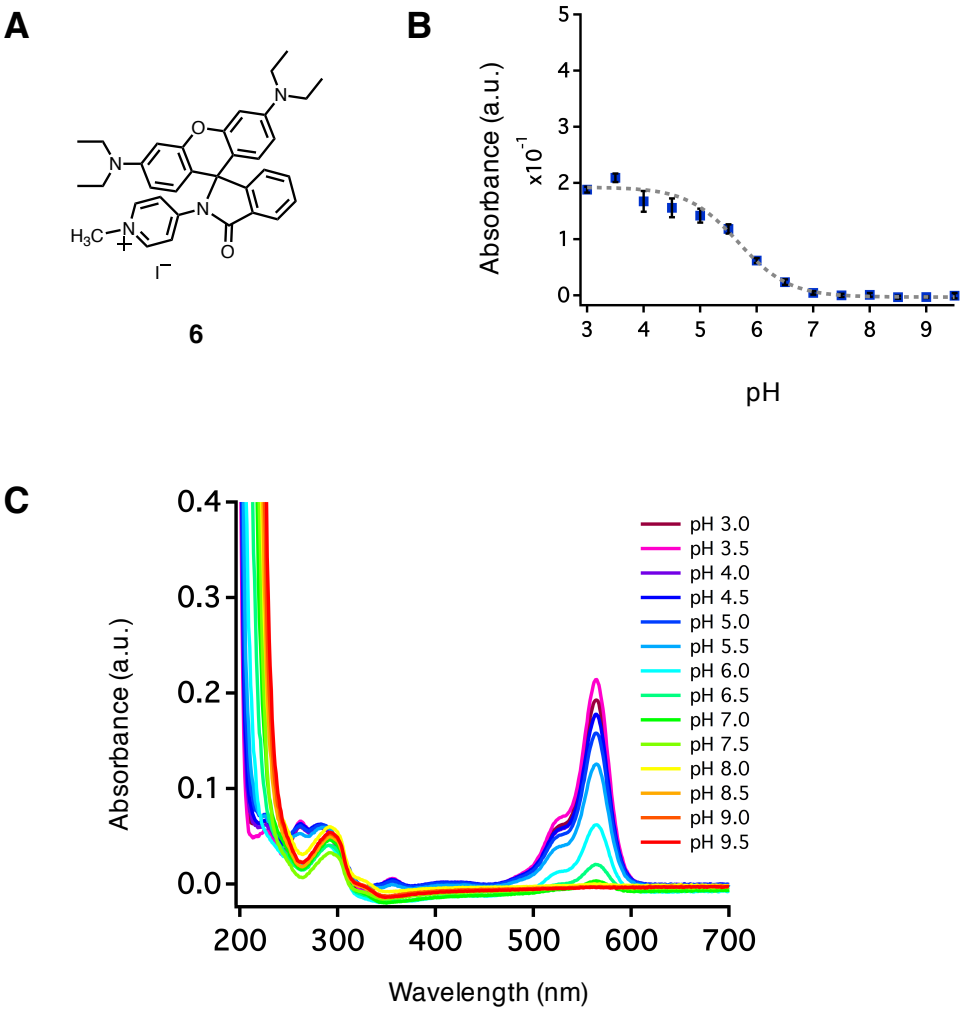

Figure S4.1. Absorption spectra of rhodamine **6** in bis-tris propane at different pH values. (**A**) Structure of **6**. (**B**) Absorbance at 561 nm as a function of pH. (**C**) Absorption spectra of **6** across different pH ranges. Error bars denote the standard deviation from three independent experiments.

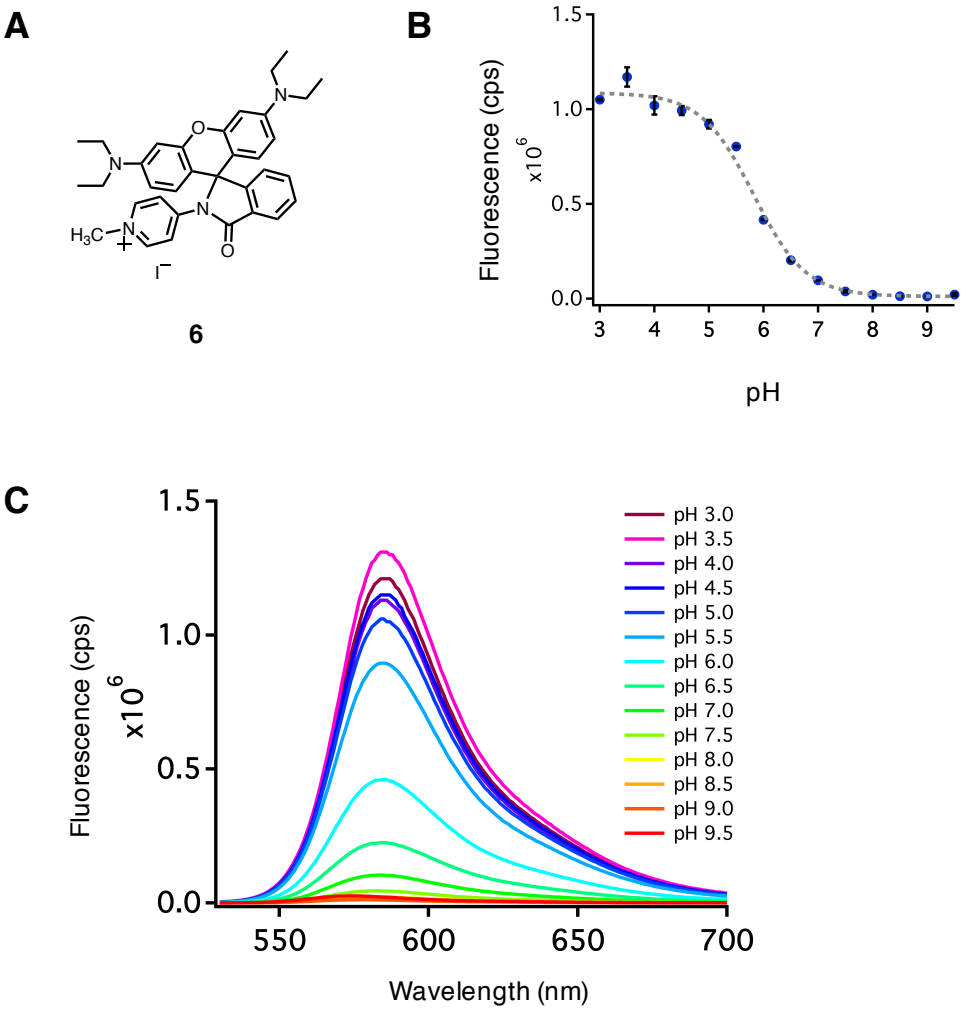

Figure S4.2. Fluorescence emission of rhodamine **6** in bis-tris propane at different pH values. (**A**) Structure of **6**. (**B**) Fluorescence emission at 577 nm as a function of pH. (**C**) Fluorescence emission spectra of **6** across different pH ranges. Error bars denote the standard deviation from three independent experiments.

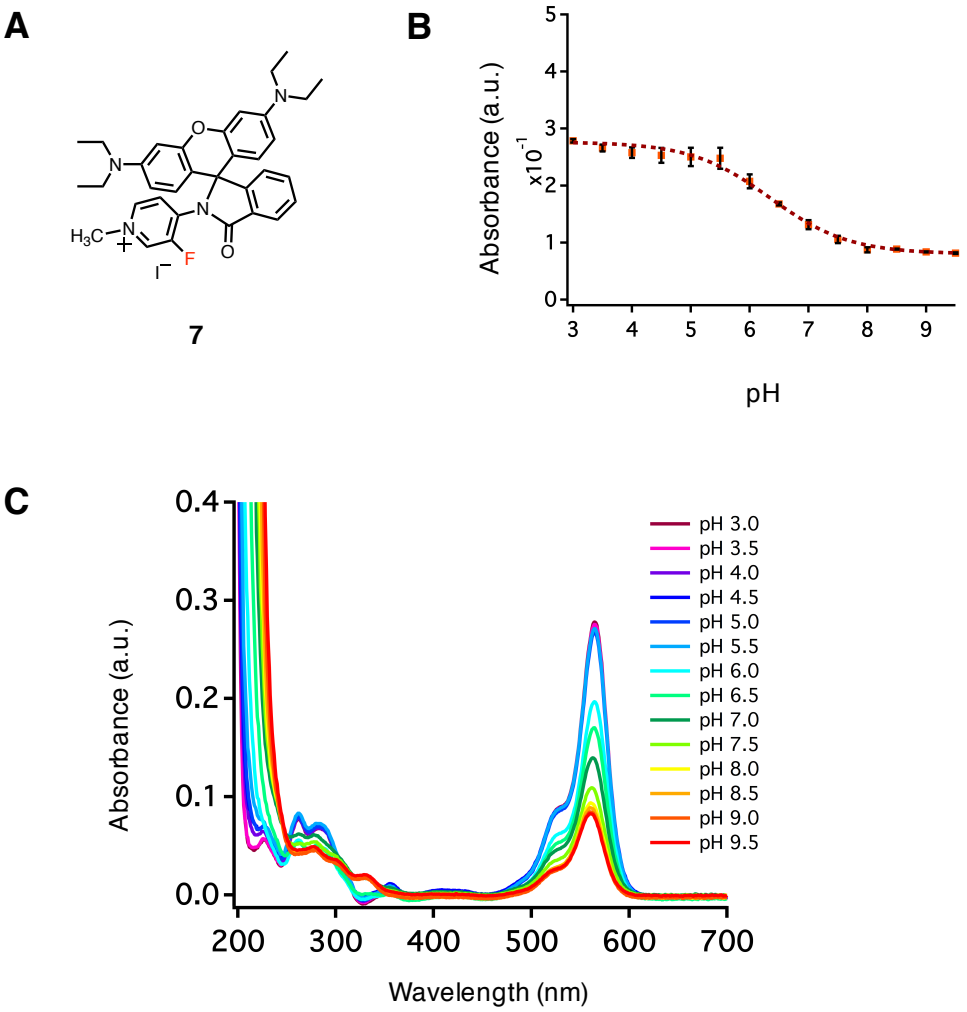

Figure S4.3. Spectroscopic characterization of rhodamine **7** in bis-tris propane at different pH values. (**A**) Structure of **7**. (**B**) Absorption spectra at 563 nm as a function of pH. (**C**) Absorption spectra of **7** across different pH ranges. Error bars denote the standard deviation from three independent experiments.

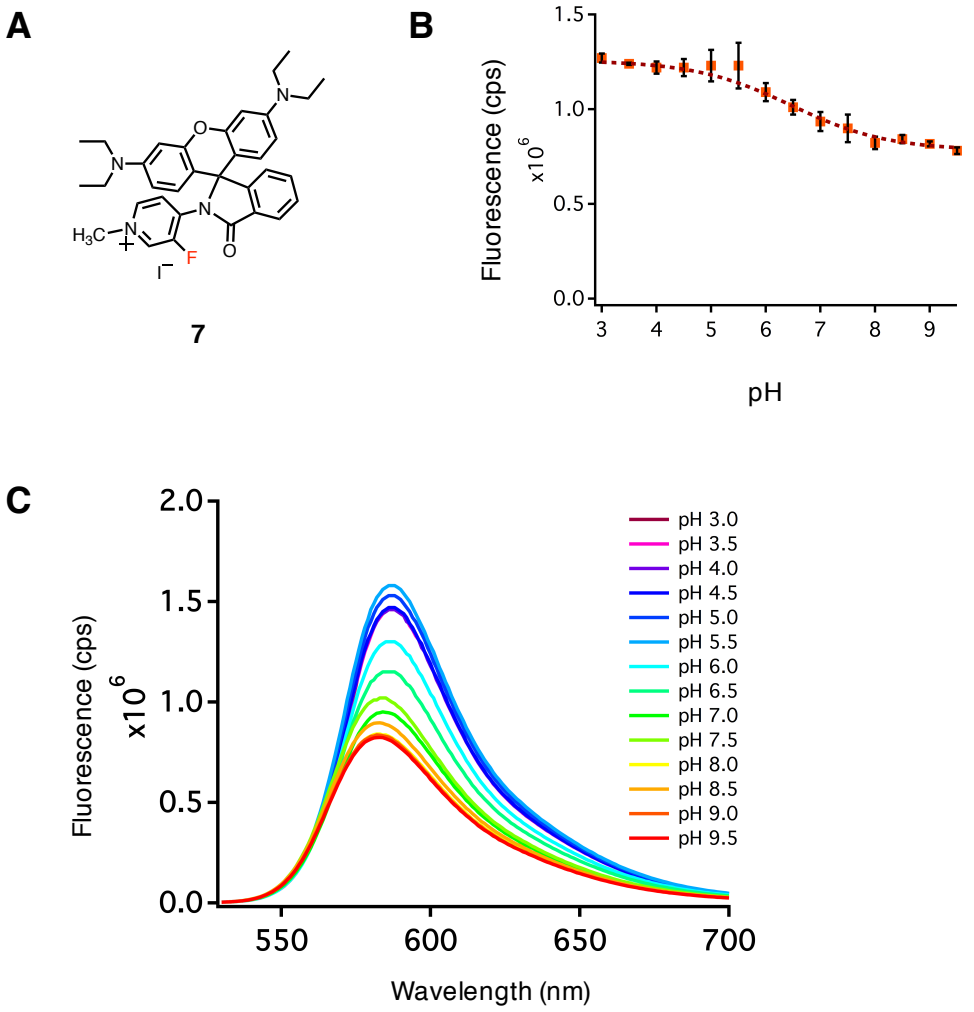

Figure S4.4. Spectroscopic characterization of rhodamine **7** in bis-tris propane at different pH values. (**A**) Structure of **7**. (**B**) Fluorescence emission at 578 nm as a function of pH. (**C**) Fluorescence emission spectra of **7** across different pH ranges. Error bars denote the standard deviation from three independent experiments.

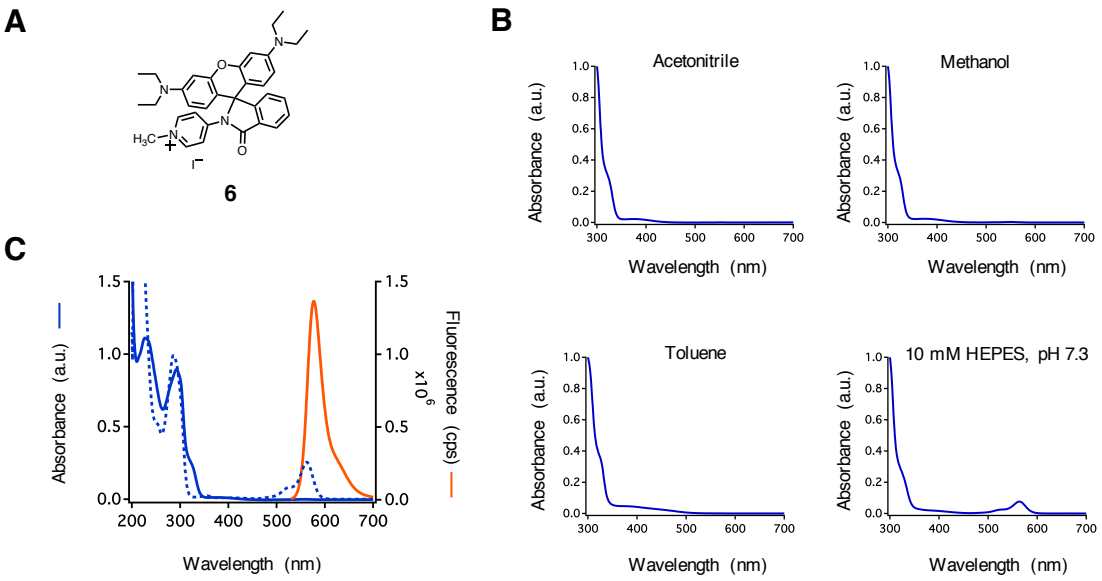

Figure S4.5. Spectroscopic characterization of rhodamine **6** in different solvents. (**A**) Structure of **6**. (**B**) Absorption spectra of **6** in different solvents. (**C**) Absorption and fluorescence emission spectra of **6**. Absorption spectrum was taken in 1:1 water: acetonitrile (solid blue line) or 1:1 water: acetonitrile with addition of 1 M HCl (dashed blue line). Emission spectrum was taken in acidic ethanol (orange line).

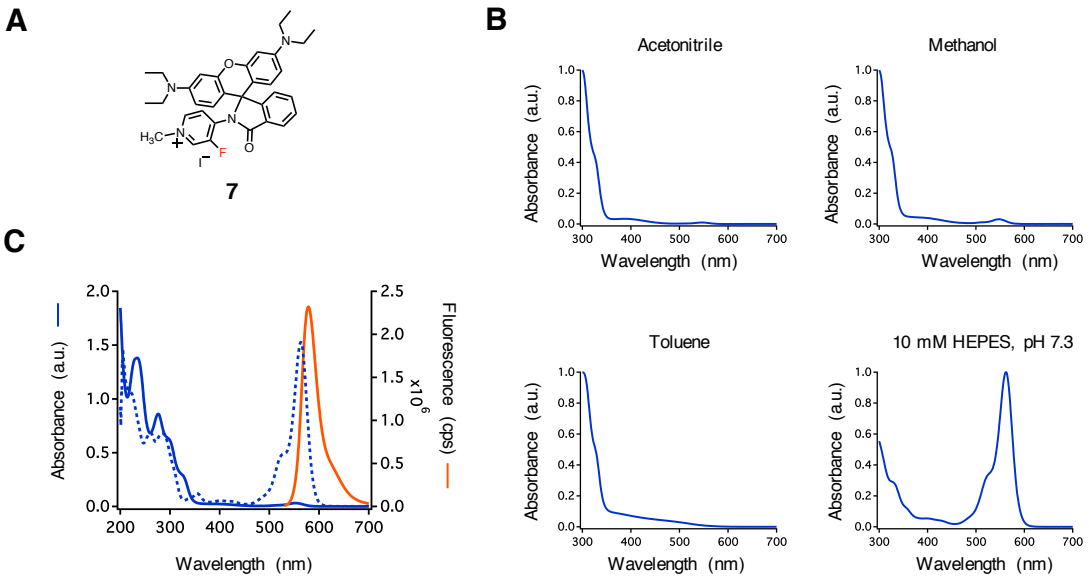

Figure S4.6. Spectroscopic characterization of rhodamine **7** in different solvents. (**A**) Structure of **7**. (**B**) Absorption spectra of **7** in different solvents. (**C**) Absorption and fluorescence emission spectra of **7**. Absorption spectrum was taken in 1:1 water: acetonitrile (solid blue line) or 1:1 water: acetonitrile with addition of 1 M HCl (dashed blue line). Emission spectrum was taken in acidic ethanol (orange line).

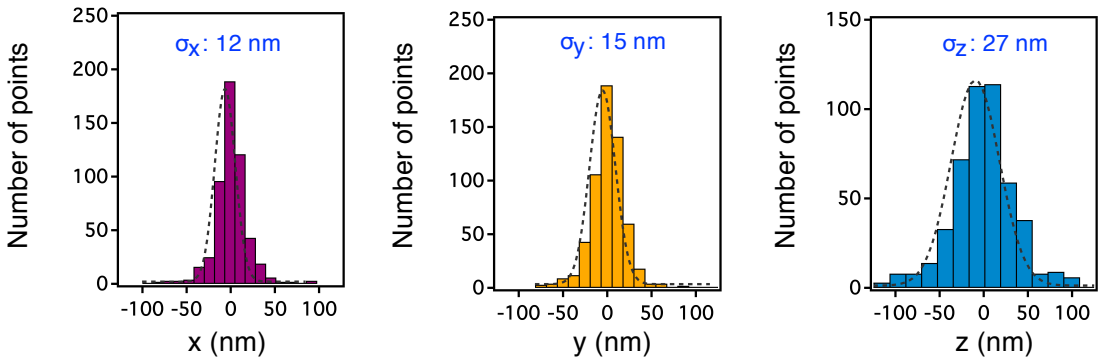

Figure S4.7. Radial and axial resolutions for *E. coli* cells expressing Tar and labeled with **4**. Precision was calculated with 50 clusters that had ≥5 localizations. Histogram for the X-resolution gave a deviation of 12 nm in the *x* direction (gray dash line represents Gaussian fit) and a FWHM of 28 nm. Histogram for the Y-resolution gave a deviation of 15 nm in the *y* direction (gray dash line represents Gaussian fit) and a FWHM of 35 nm. Histogram for the Z-resolution gave a deviation of 27 nm in the *z* direction (gray dash line represents Gaussian fit) and a FWHM of 64 nm.

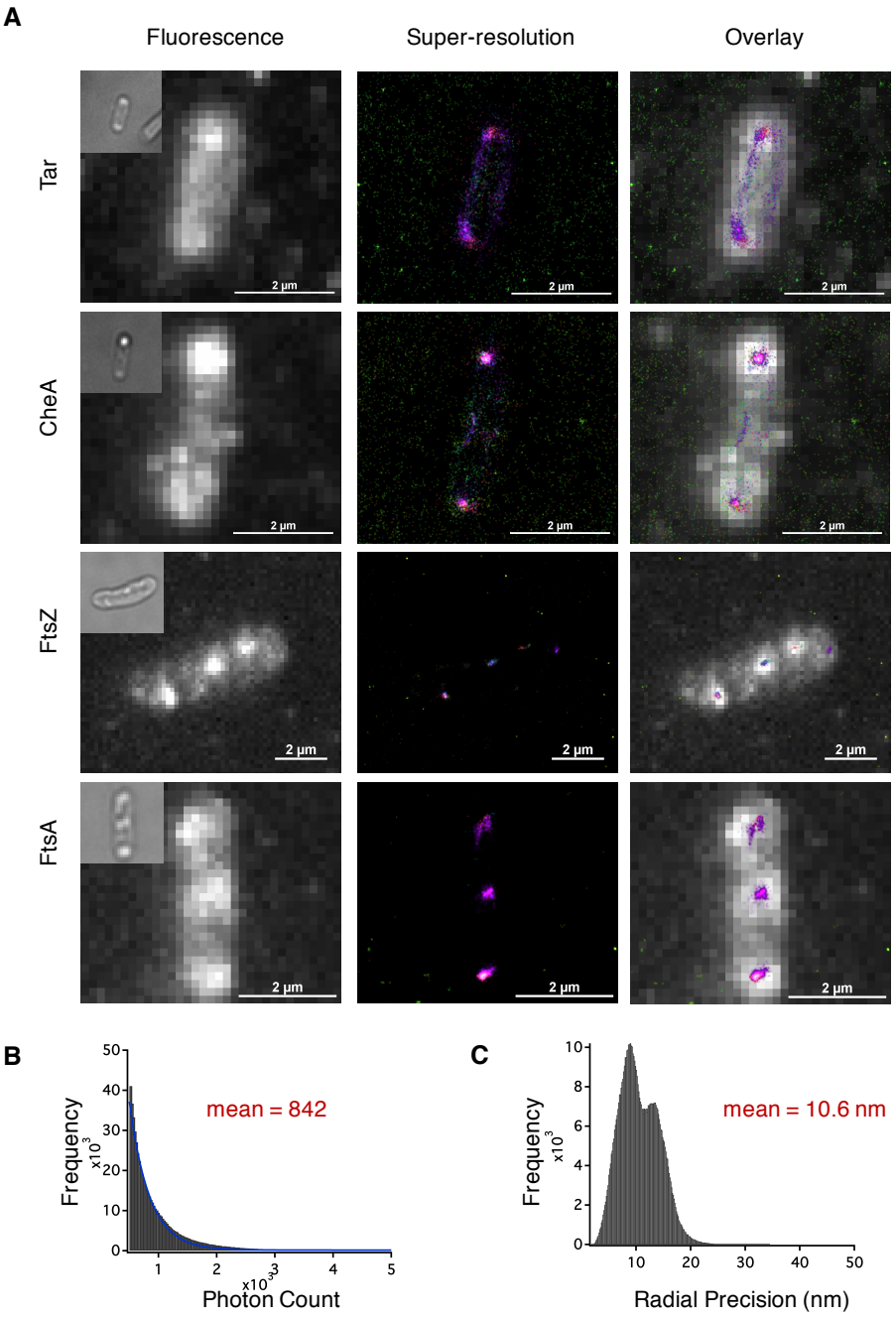

Figure S4.8. Super-resolution imaging of bacterial proteins in live cells. Cells expressing one of four bacterial proteins were labeled with **1** and **5**. (**A**) STORM images of bacterial proteins with polar localization (Tar and CheA) or septal localization (FtsZ and FtsA) expressed in *E. coli*. Brightfield images of cells are shown in the top left corner of fluorescence images. (**B**) Histogram indicating number of detected photons during image acquisition with fit to single exponential. The mean number of photons was calculated from the exponential fit (blue curve). (**C**) Mean radial precision for imaging in live bacterial cells.

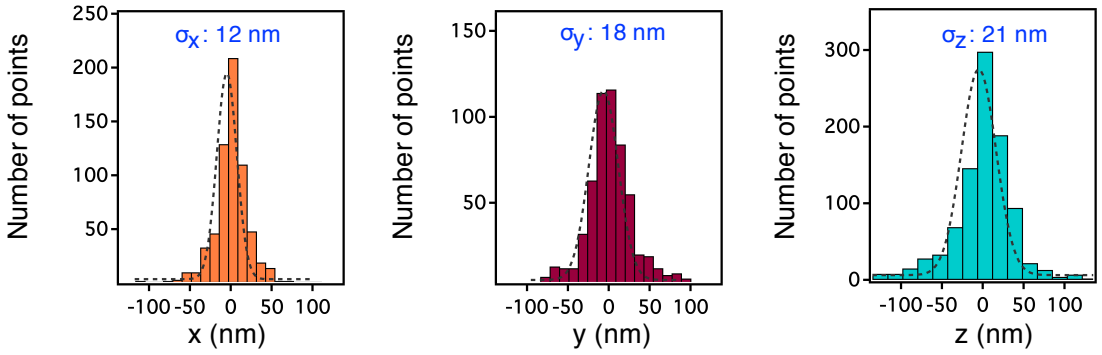

Figure S4.9. Radial and axial resolution for *E. coli* cells expressing Tar and labeled with **5**. Precision was calculated with 50 clusters that had ≥5 localizations. Histogram for the X-resolution gave a deviation of 12 nm in the *x* direction (gray dash line represents Gaussian fit) and a FWHM of 28 nm. Histogram for the Y-resolution gave a deviation of 18 nm in the *y* direction (gray dash line represents Gaussian fit) and a FWHM of 42 nm. Histogram for the Z-resolution gave a deviation of 21 nm in the *z* direction (gray dash line represents Gaussian fit) and a FWHM of 49 nm.

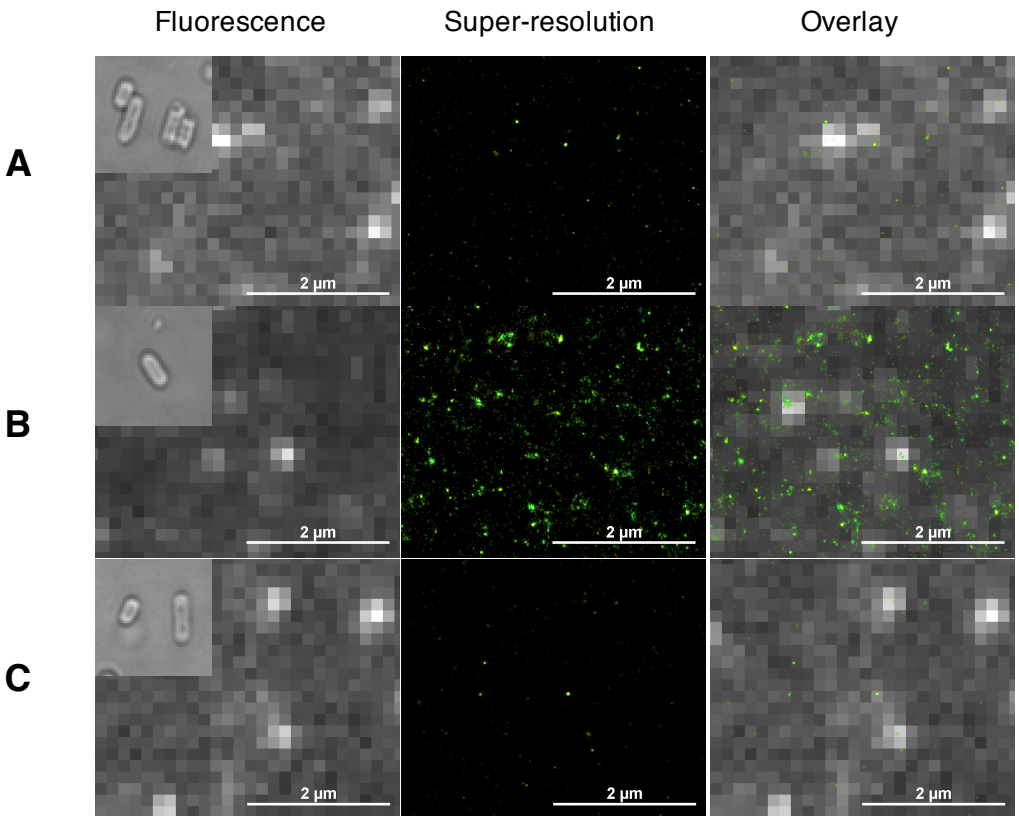

Figure S4.10. Representative live-cell super-resolution imaging in control experiments. (**A**) Cells that did not express the protein of interest (Tar), labeled only with **4** (no added **1**). (**B**) Cells that did not express the protein of interest (Tar), treated with **1** and **4**. (**C**) Cells that expressed Tar, labeled only with **4** (no added **1**). None of these controls shows any distinct localization pattern. For all images, brightfield images of cells are shown in the top left corner of the fluorescence image.

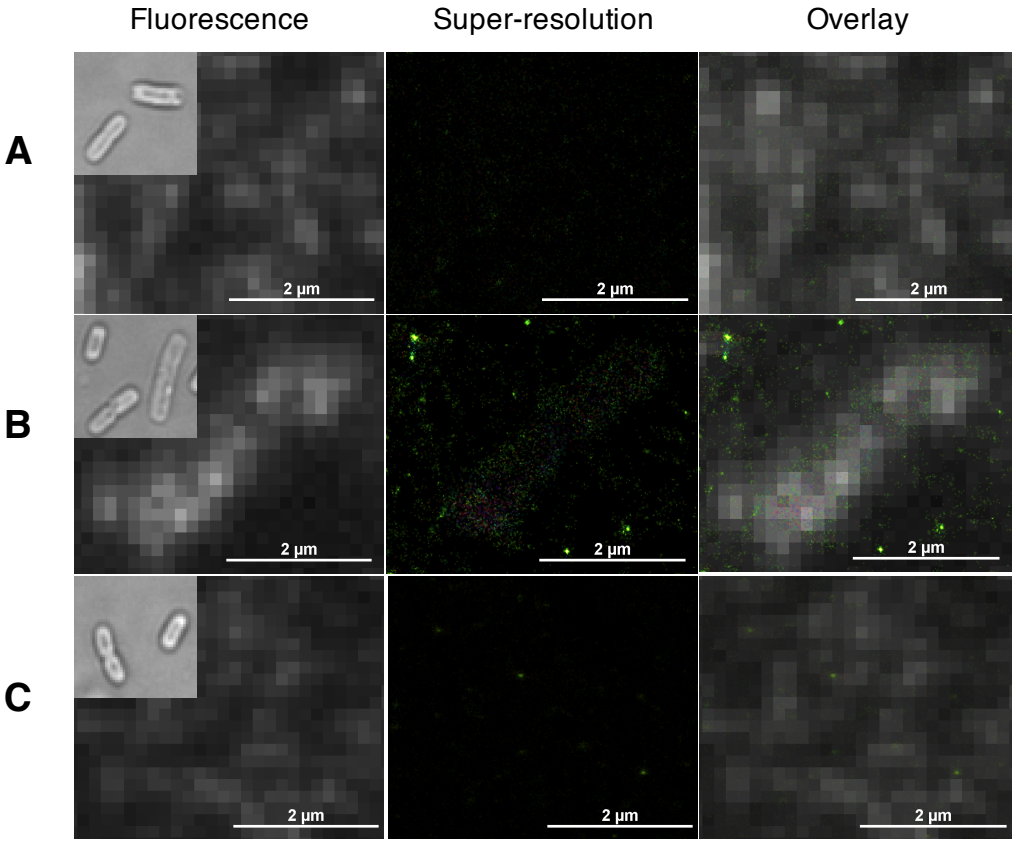

Figure S4.11. Representative live-cell super-resolution imaging in control experiments. (**A**) Cells that do not express the protein of interest (Tar) and not been treated with **1** but labeled with **5** show no distinct localization patterns. (**B**) Cells that do not express the protein of interest (Tar) but have been treated with **1** and **5** show no distinct localization patterns. (**C**) Cells that express Tar but are not treated with **1** and are labeled with **5** show no distinct localization patterns. For all images, brightfield images of cells are shown in the top left corner of the fluorescence image.

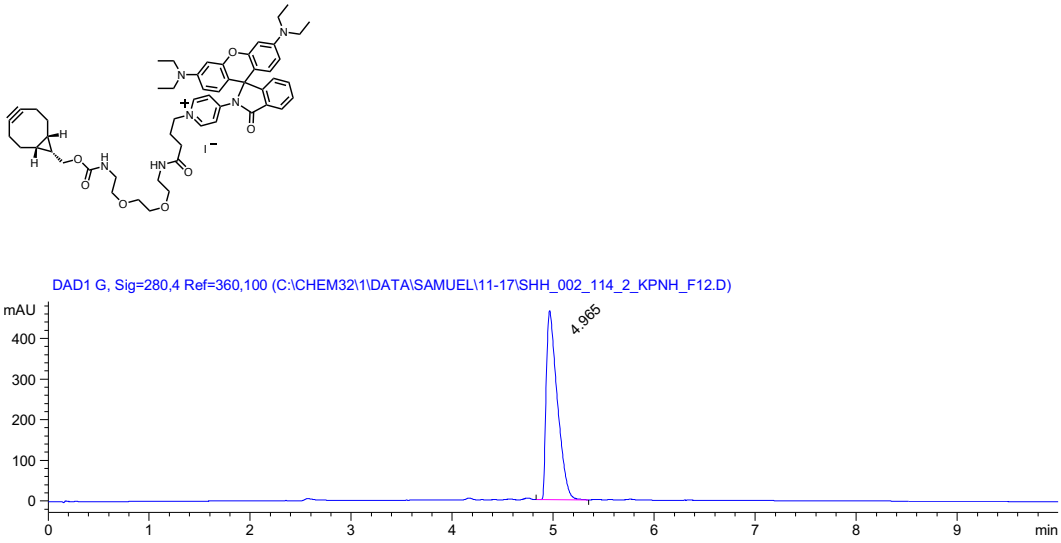

Figure S4.12. LC–MS trace of compound **4** (0–95% acetonitrile in water buffered with 0.1% v/v acetic acid).

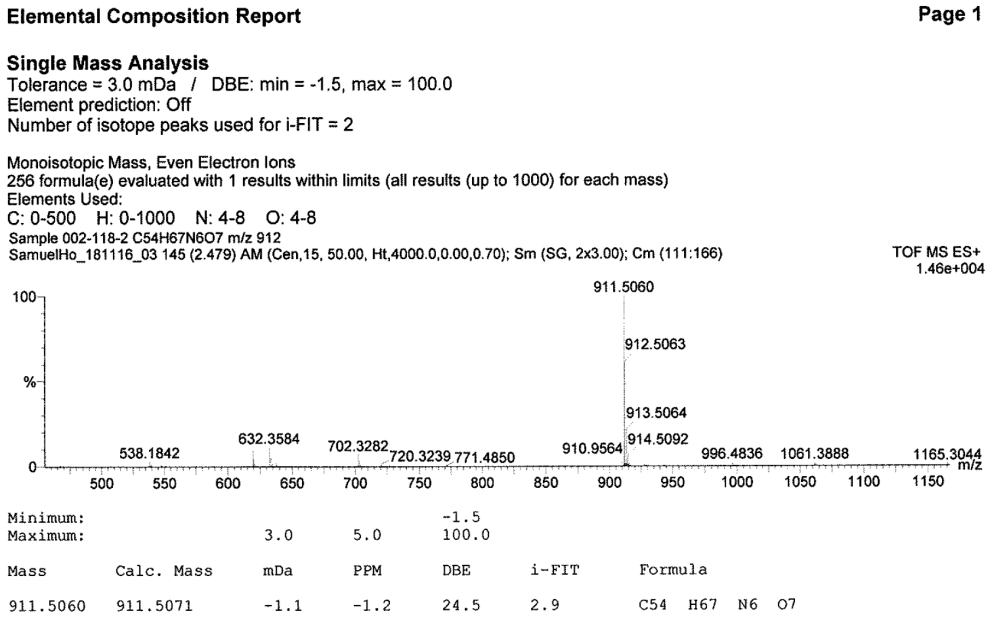

Figure S4.13. High-resolution mass spectrum of compound **4**.

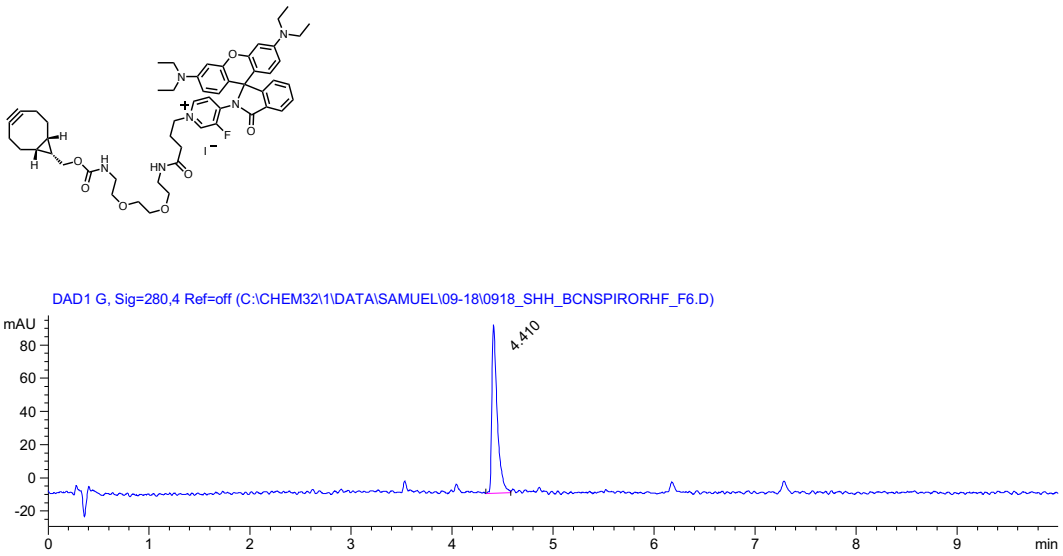

Figure S4.14. LC–MS trace of compound **5** (0–95% acetonitrile in water buffered with 0.1% v/v acetic acid).

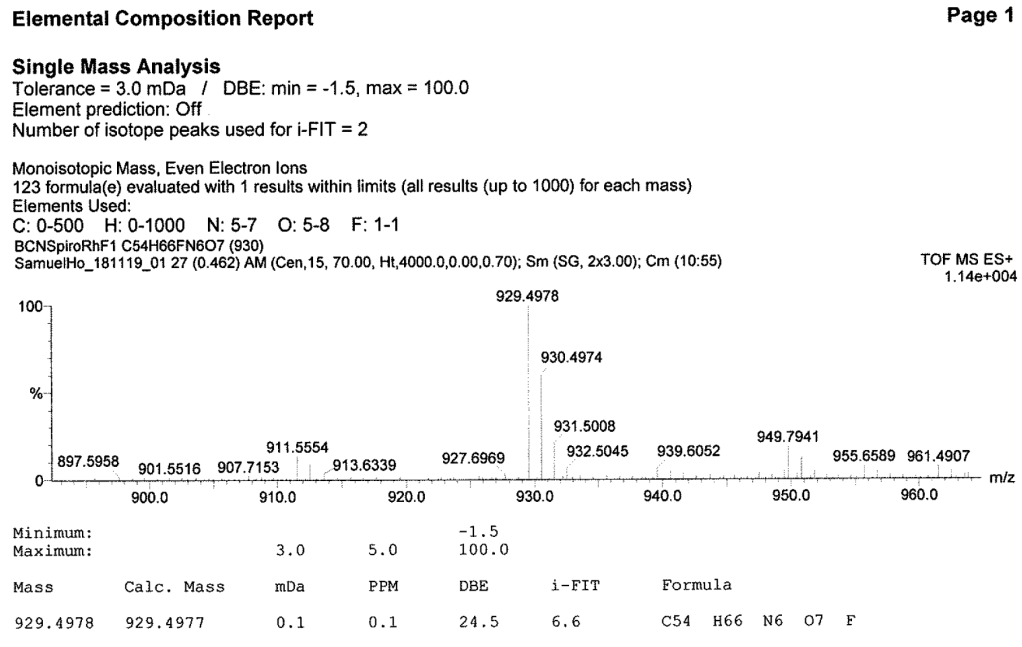

Figure S4.15. High-resolution mass spectrum of compound **5**.

4.9 NMR Spectra

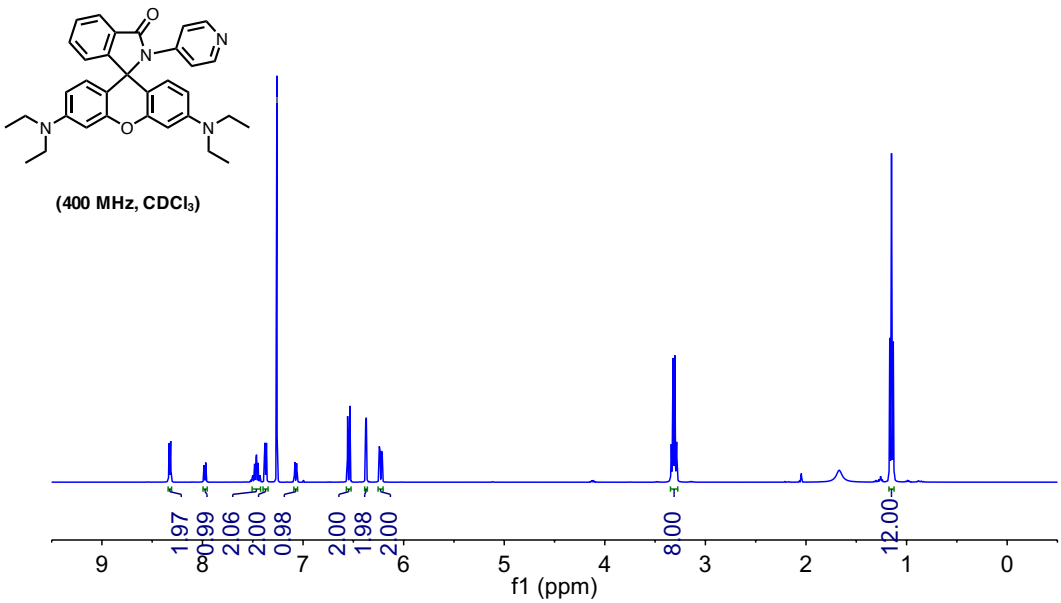

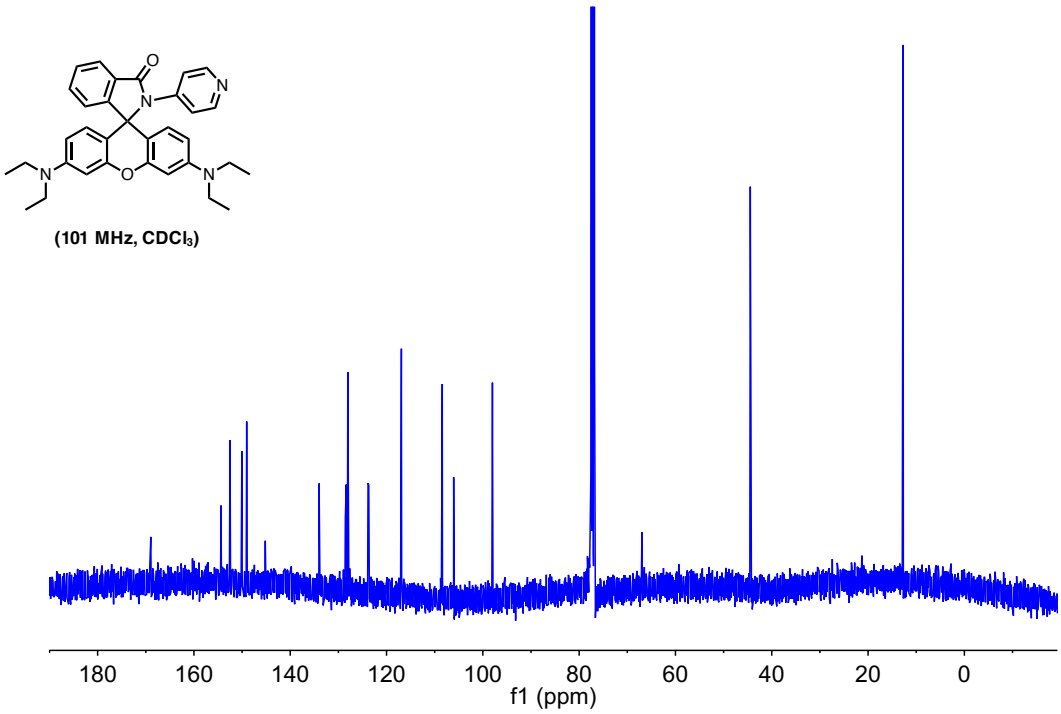

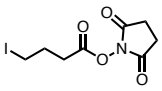

(400 MHz, $CDCl_3$)

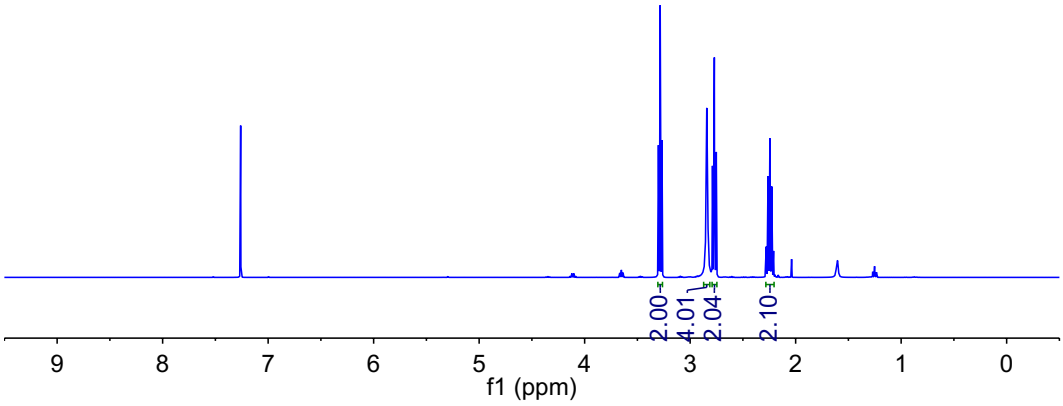

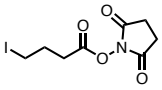

(101 MHz, $CDCl_3$)

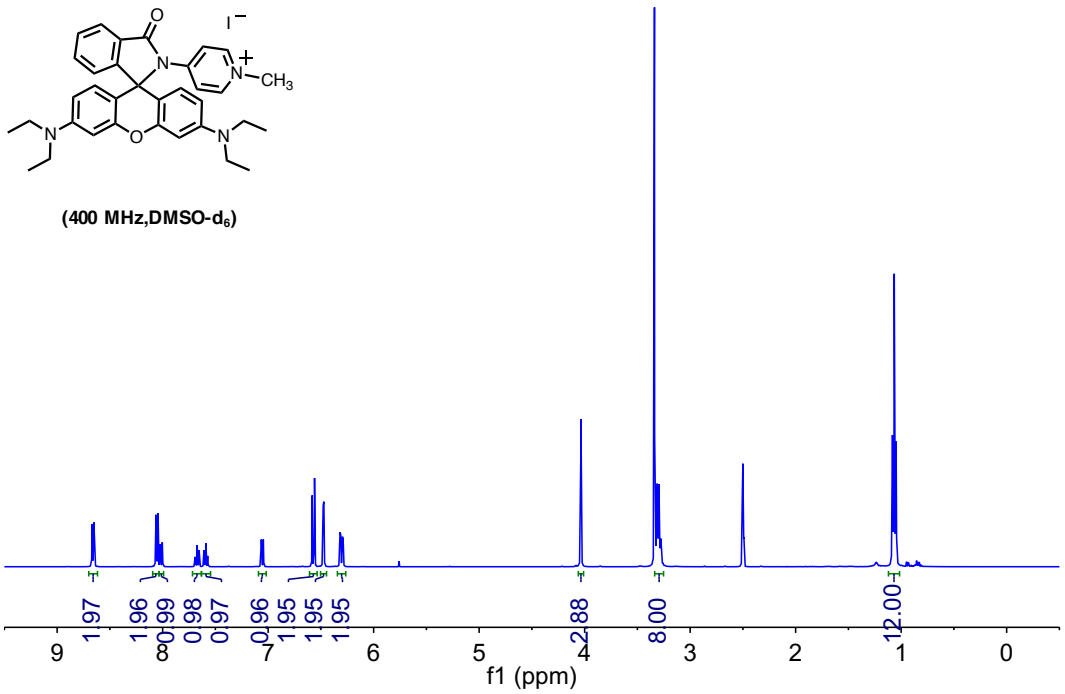
(400 MHz,DMSO-d6)
1.97
1.96
0.99
0.98
0.97
0.96
1.95
1.95
1.95
2.88
8.00
12.00
9
8
7
6
5
4
3
2
1
0
f1 (ppm)

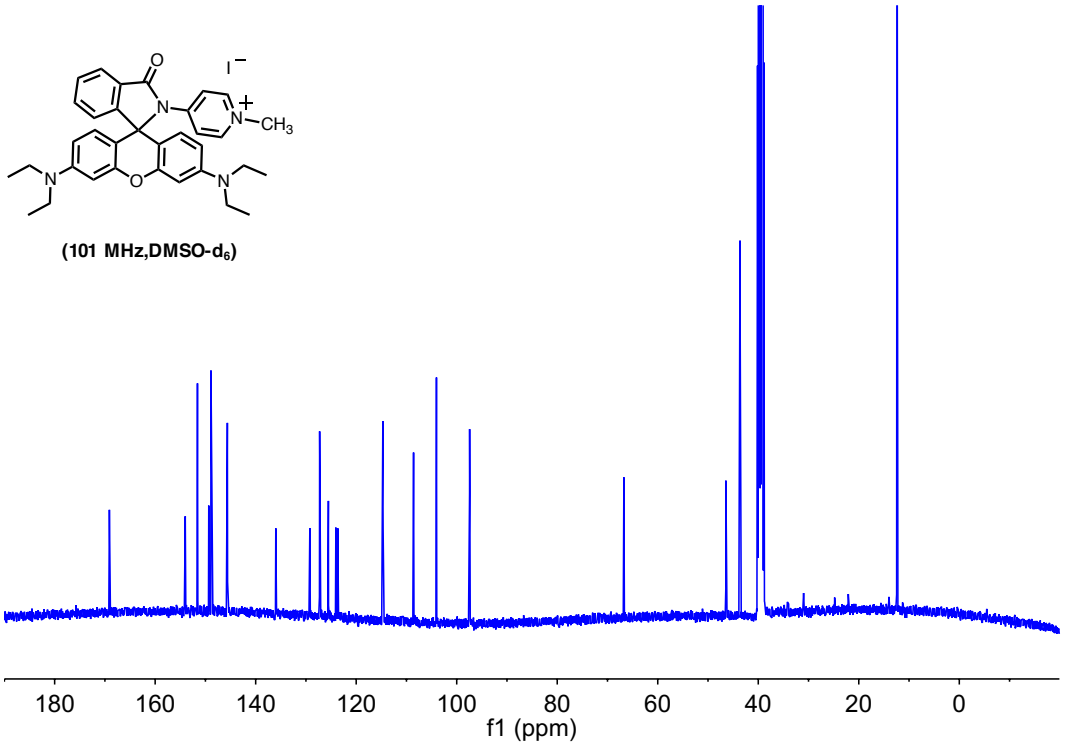
(101 MHz,DMSO-d6)
180
160
140
120
100
80
60
40
20
0
f1 (ppm)

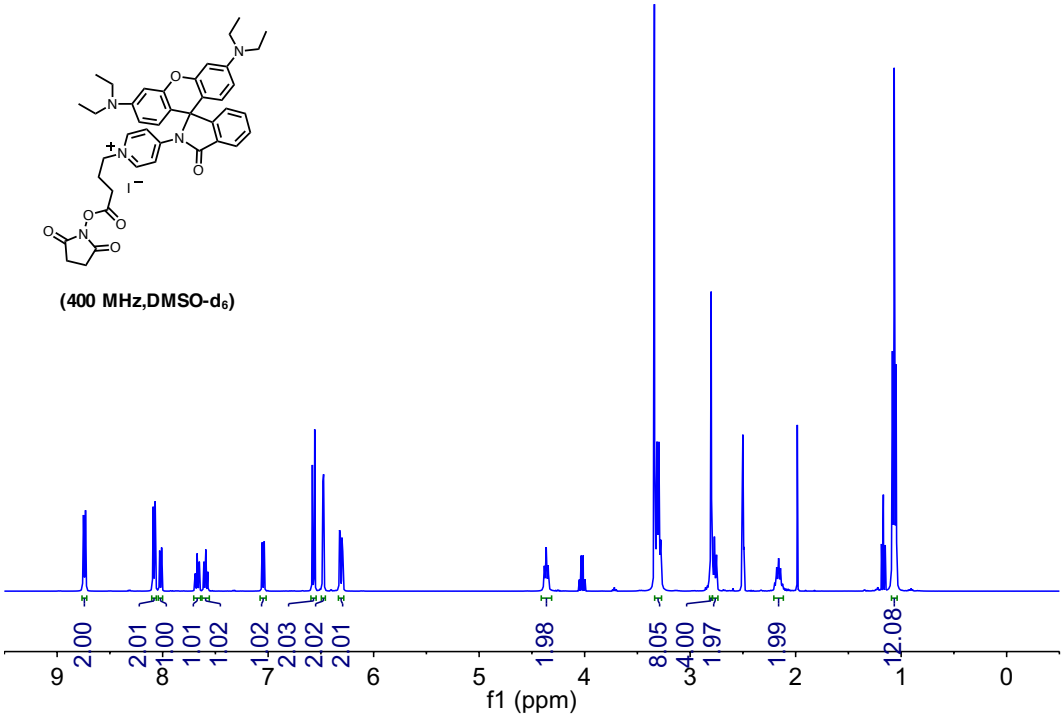
(400 MHz,DMSO-d6)
2.00
2.01
1.00
1.01
1.02
1.02
2.03
2.02
2.01
1.98
8.05
4.00
1.97
1.99
12.08
9
8
7
6
5
4
3
2
1
0
f1 (ppm)

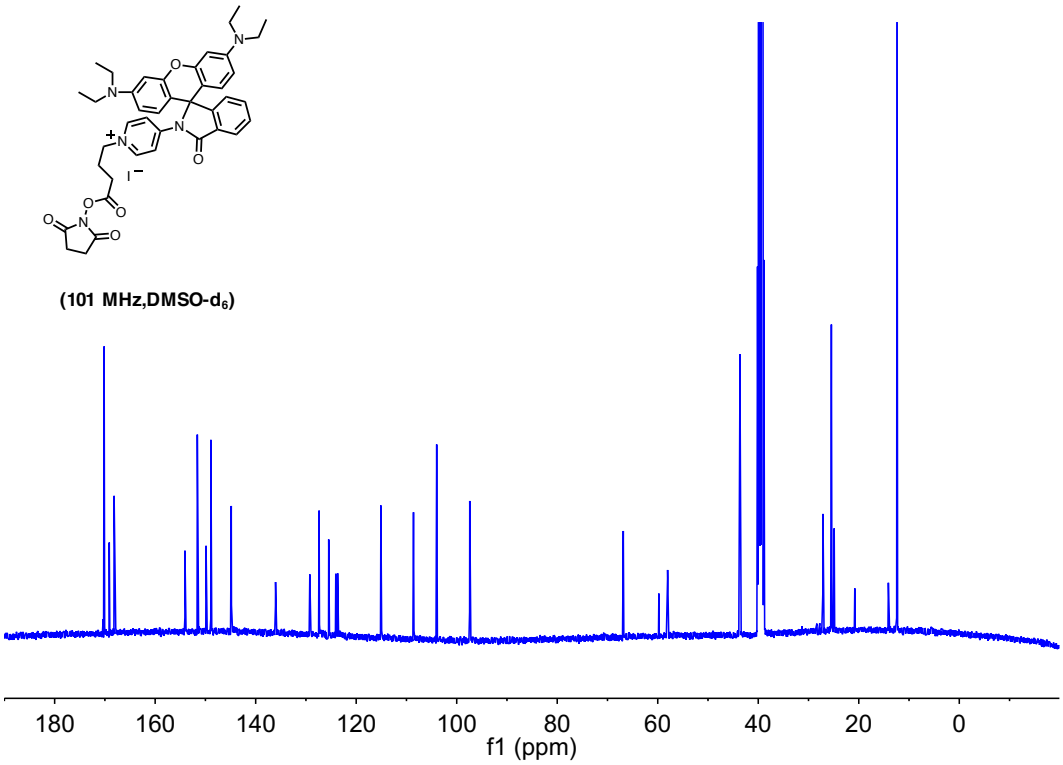
(101 MHz,DMSO-d6)
180
160
140
120
100
80
60
40
20
0
f1 (ppm)

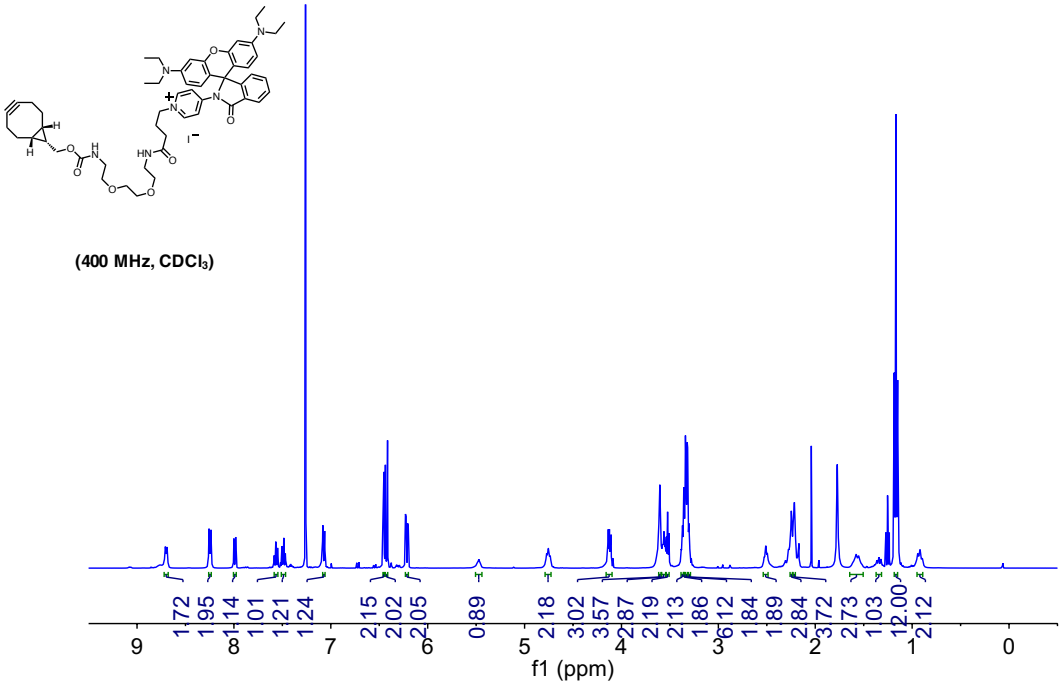
(400 MHz, CDCl3)
1.72
1.95
1.14
1.01
1.21
1.24
2.15
2.02
2.05
0.89
2.18
3.02
3.57
2.87
2.19
2.13
1.86
6.12
1.84
1.89
2.84
3.72
2.73
1.03
12.00
2.12
9
8
7
6
5
4
3
2
1
0
f1 (ppm)

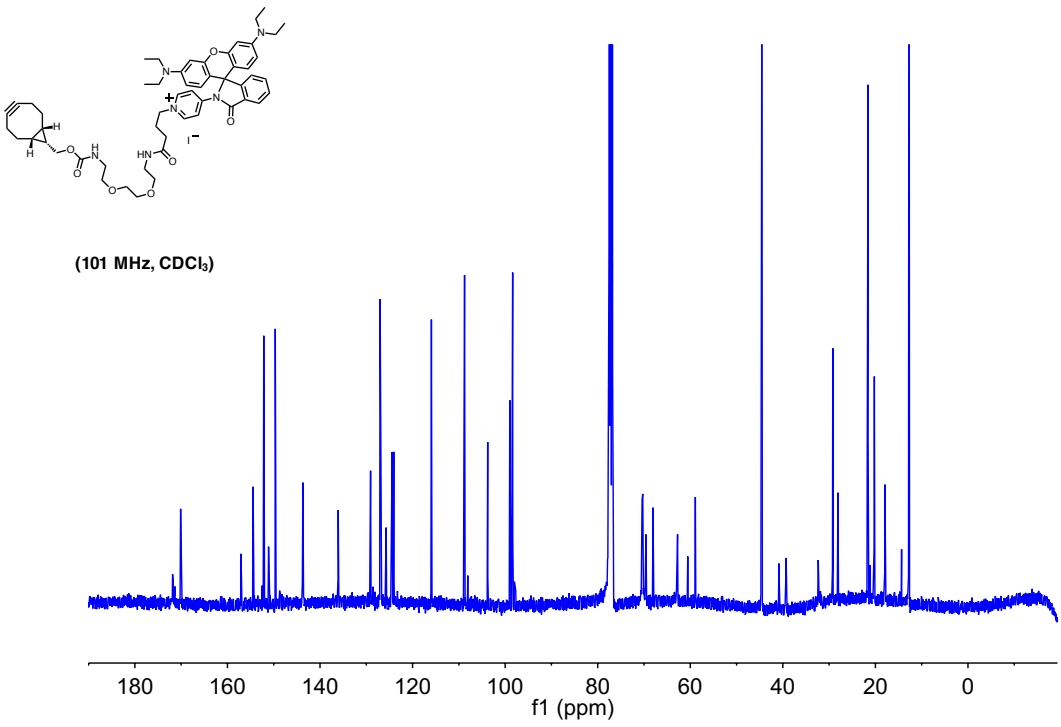
(101 MHz, CDCl3)
180
160
140
120
100
80
60
40
20
0
f1 (ppm)

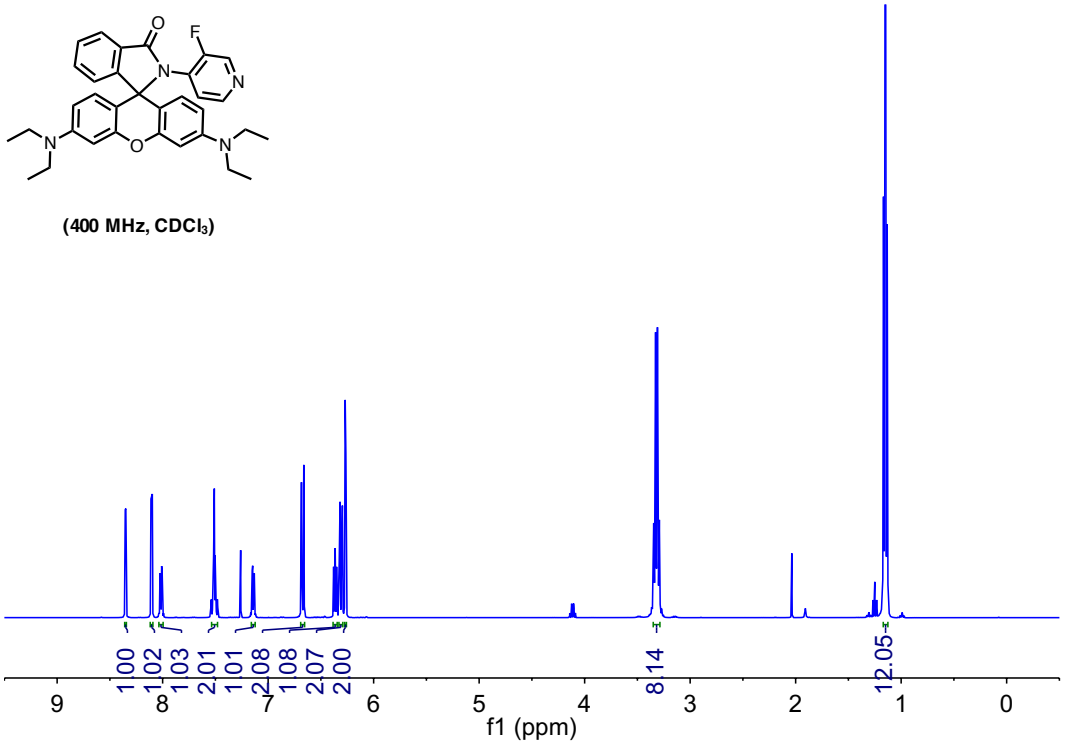
(400 MHz, CDCl3)
1.00
1.02
1.03
2.01
1.01
2.08
1.08
2.07
2.00
8.14
12.05
9
8
7
6
5
4
3
2
1
0
f1 (ppm)

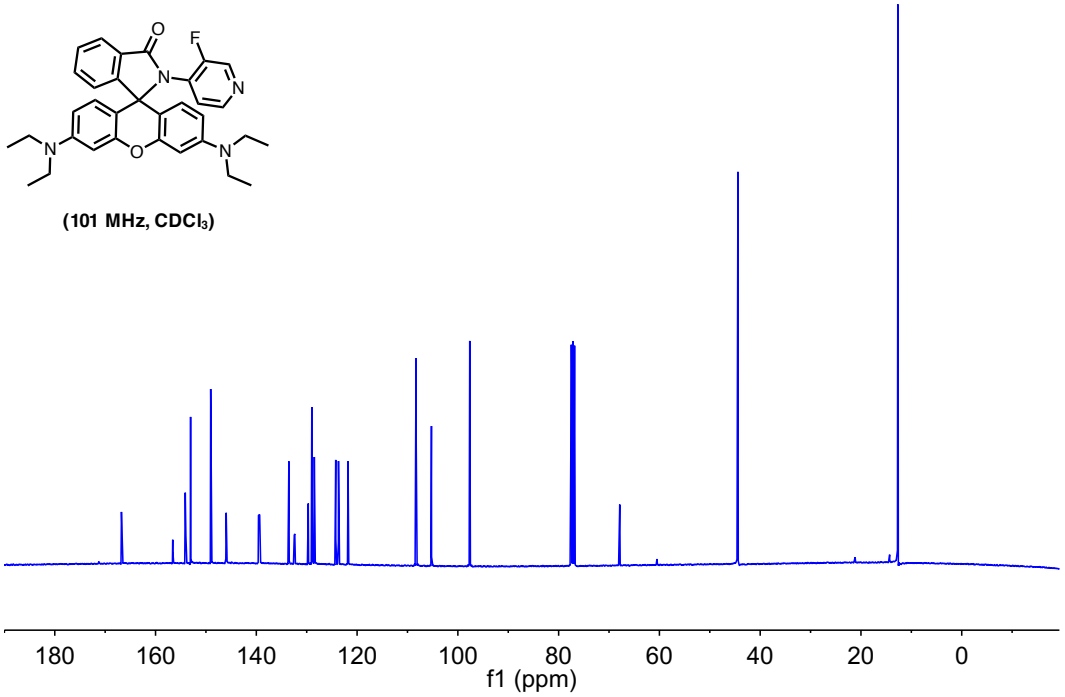
(101 MHz, CDCl3)
180
160
140
120
100
80
60
40
20
0
f1 (ppm)

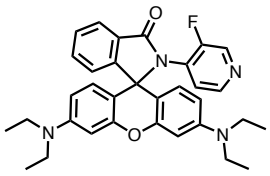

(282 MHz, $CDCl_3$)

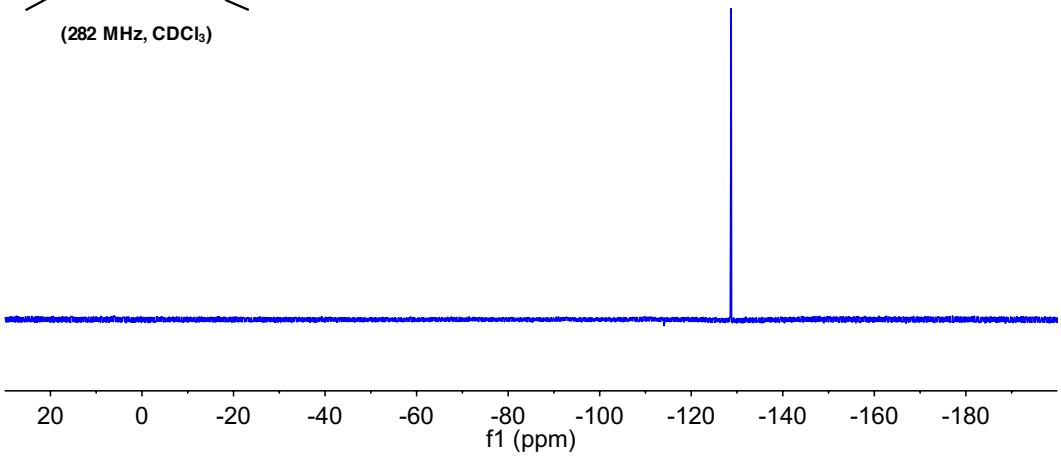

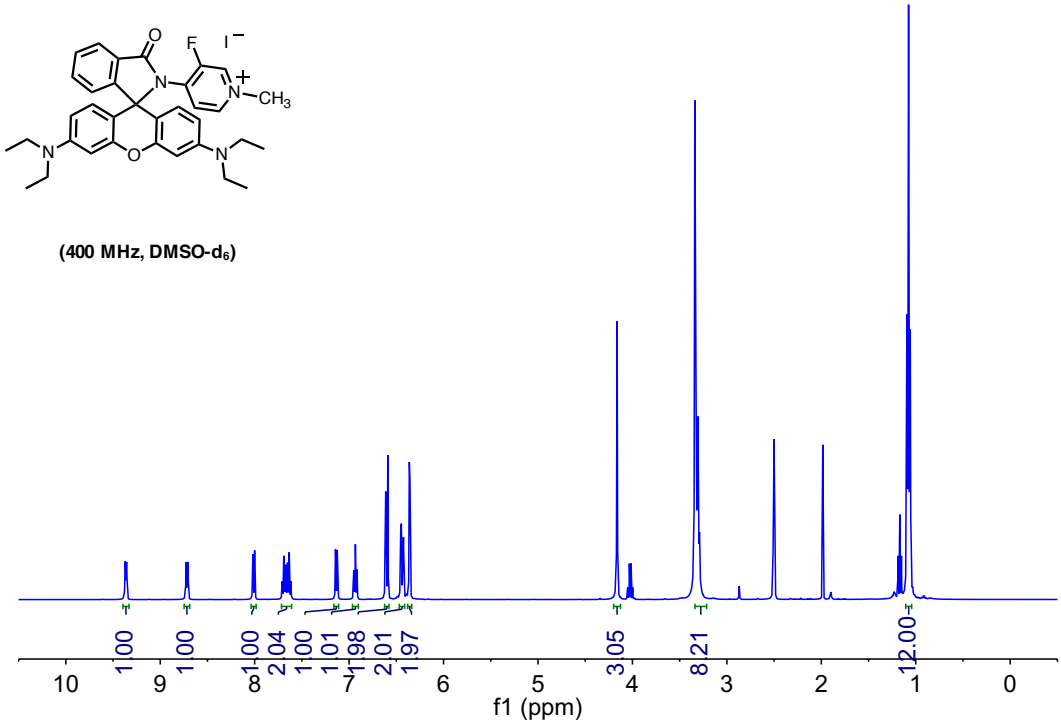
(400 MHz, DMSO-d6)
1.00
1.00
1.00
2.04
1.00
1.01
1.98
2.01
1.97
3.05
8.21
12.00
10
9
8
7
6
5
4
3
2
1
0
f1 (ppm)

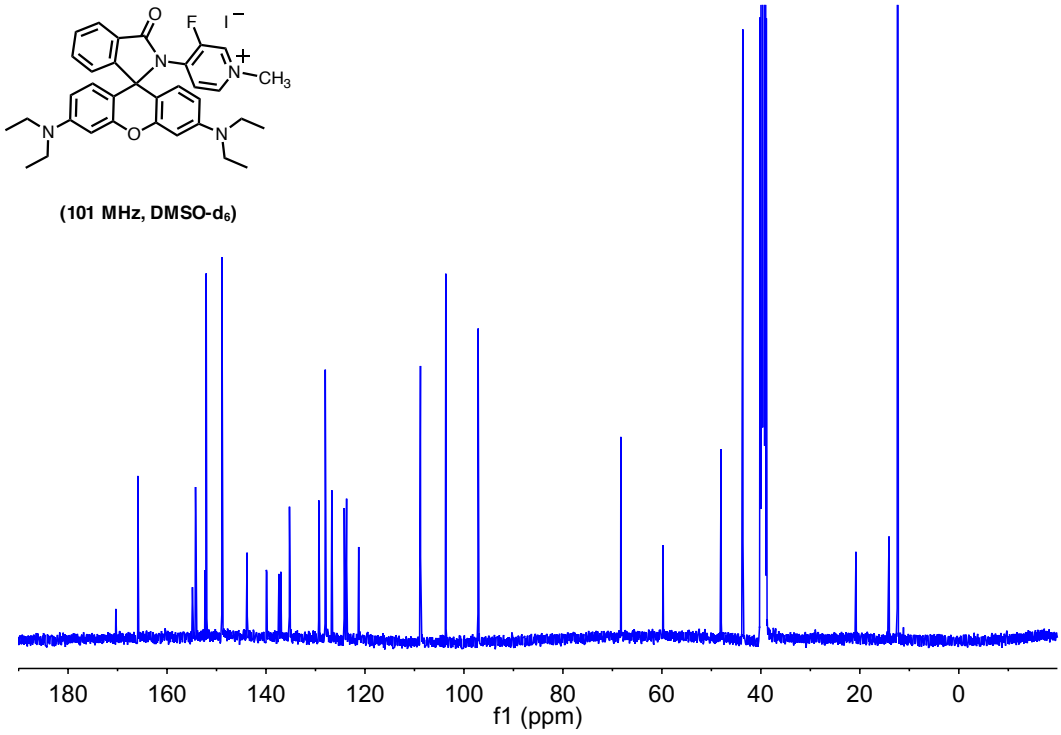
(101 MHz, DMSO-d6)
180
160
140
120
100
80
60
40
20
0
f1 (ppm)

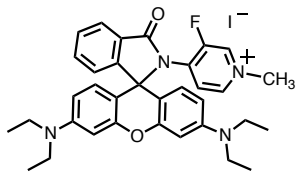

(282 MHz, DMSO-d_6)

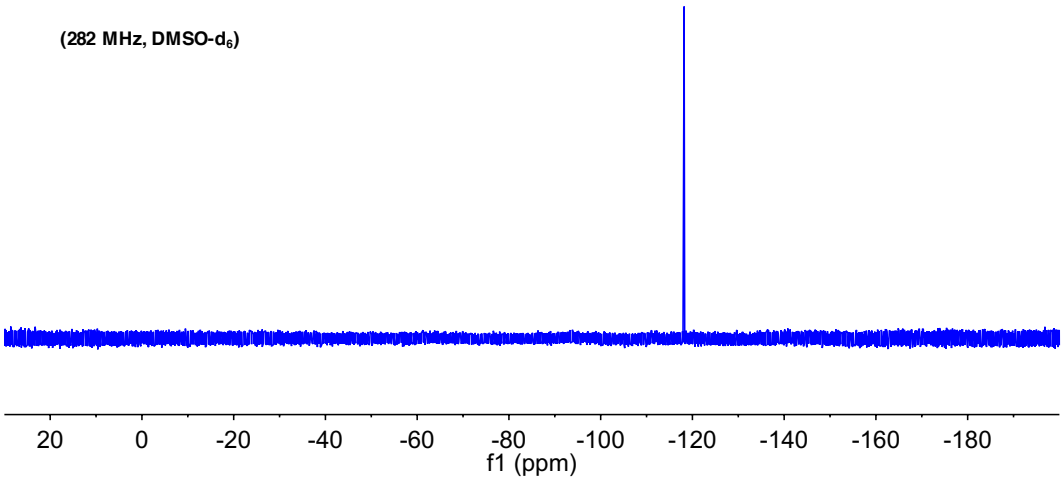

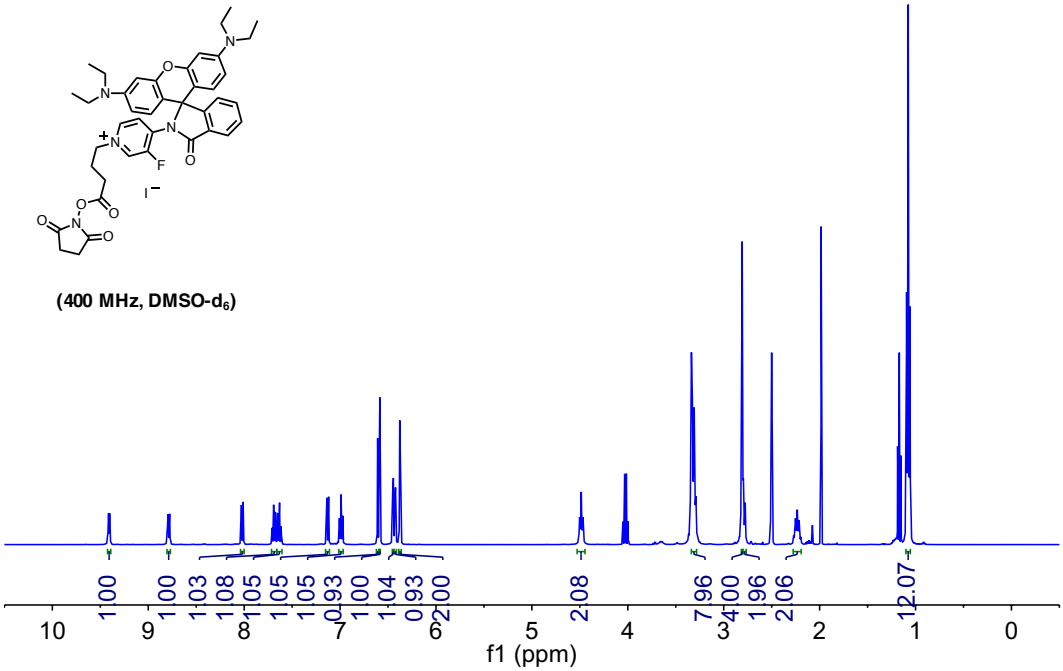
(400 MHz, DMSO-d6)
1.00
1.00
1.03
1.08
1.05
1.05
1.05
0.93
1.00
1.04
0.93
2.00
2.08
7.96
4.00
1.96
2.06
12.07
10
9
8
7
6
5
4
3
2
1
0
f1 (ppm)

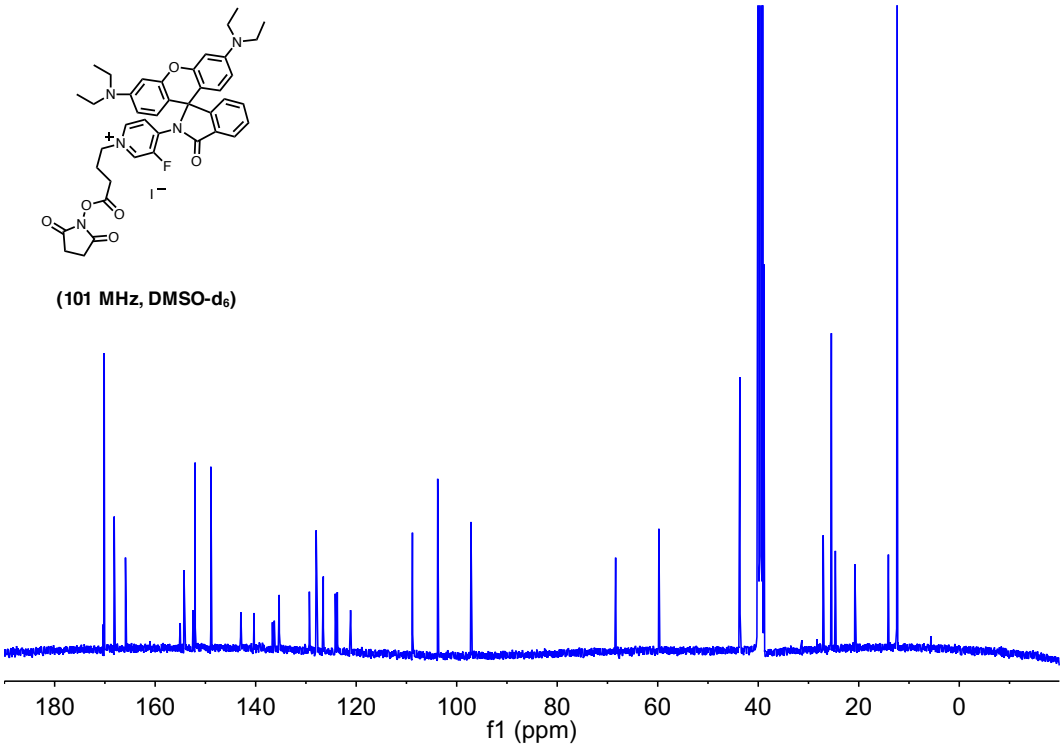
(101 MHz, DMSO-d6)
180
160
140
120
100
80
60
40
20
0
f1 (ppm)

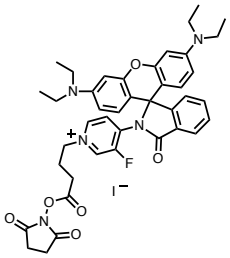

(282 MHz, DMSO-d_6)

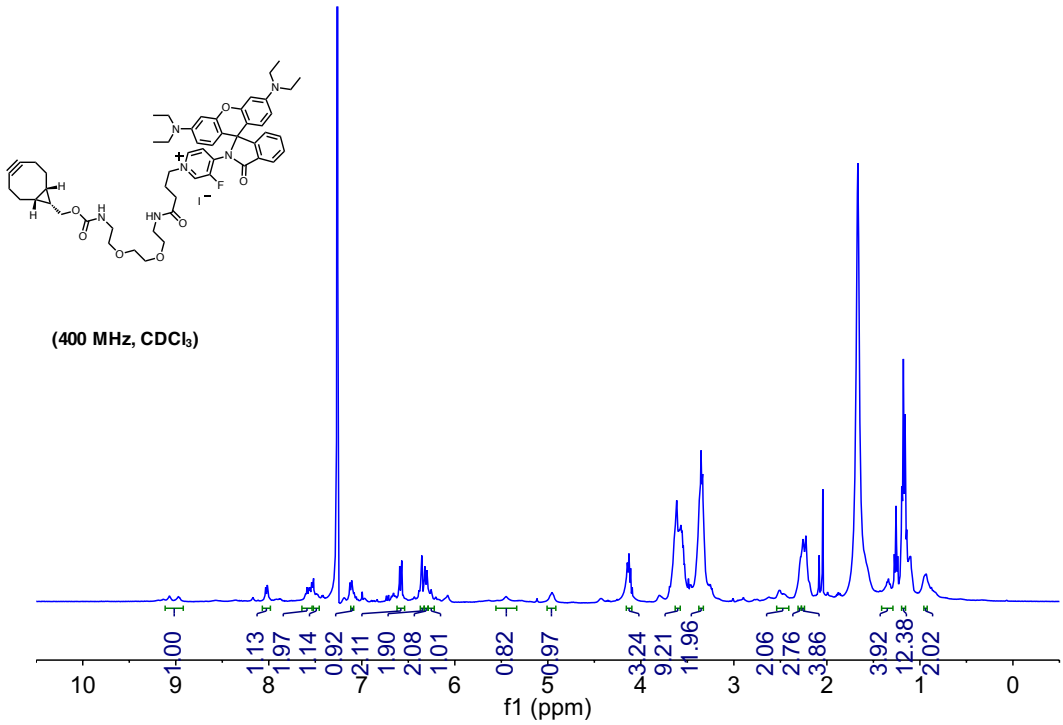
(400 MHz, CDCl3)
1.00
1.13
1.97
1.14
0.92
2.11
1.90
2.08
1.01
0.82
0.97
3.24
9.21
11.96
2.06
2.76
3.86
3.92
12.38
2.02
10
9
8
7
6
5
4
3
2
1
0
f1 (ppm)

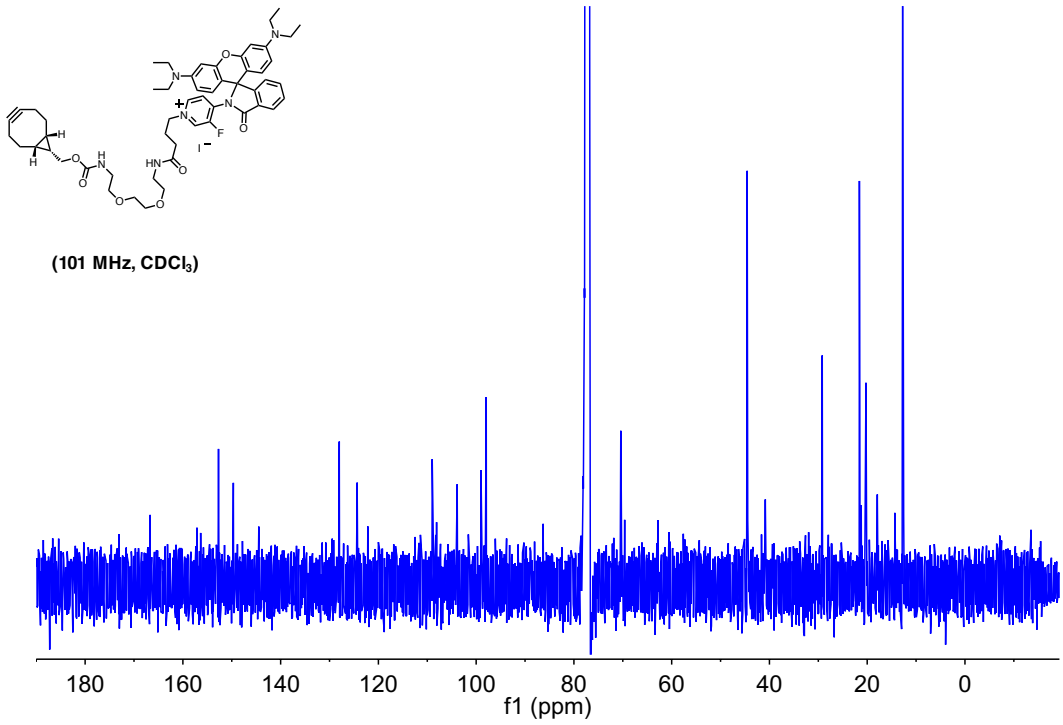
(101 MHz, CDCl3)
180
160
140
120
100
80
60
40
20
0
f1 (ppm)

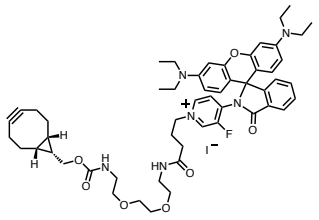

(376 MHz, $CDCl_3$)

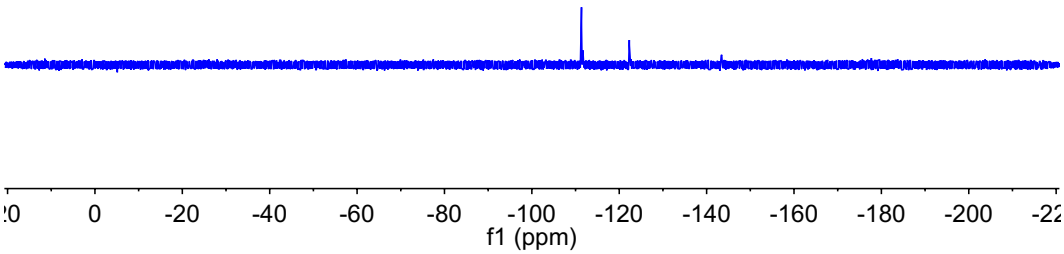

4.10 References

(1) Klar, T. A.; Jakobs, S.; Dyba, M.; Egner, A.; Hell, S. W. Fluorescence Microscopy with Diffraction Resolution Barrier Broken by Stimulated Emission. *Proc. Natl. Acad. Sci. U.S.A.* **2000**, *97* (15), 8206–8210.

(2) Betzig, E.; Patterson, G. H.; Sougrat, R.; Lindwasser, O. W.; Olenych, S.; Bonifacino, J. S.; Davidson, M. W.; Lippincott-Schwartz, J.; Hess, H. F. Imaging Intracellular Fluorescent Proteins at Nanometer Resolution. *Science* **2006**, *313* (5793), 1642–1645. https://doi.org/10.1126/science.1127344.

(3) Gahlmann, A.; Moerner, W. E. Exploring Bacterial Cell Biology with Single-Molecule Tracking and Super-Resolution Imaging. *Nat Rev Microbiol* **2014**, *12* (1), 9–22. https://doi.org/10.1038/nrmicro3154.

(4) Bates, M.; Huang, B.; Dempsey, G. T.; Zhuang, X. Multicolor Super-Resolution Imaging with Photo-Switchable Fluorescent Probes. *Science* **2007**, *317* (5845), 1749–1753. https://doi.org/10.1126/science.1146598.

(5) Huang, B.; Wang, W.; Bates, M.; Zhuang, X. Three-Dimensional Super-Resolution Imaging by Stochastic Optical Reconstruction Microscopy. *Science* **2008**, *319* (5864), 810–813. https://doi.org/10.1126/science.1153529.

(6) Xu, K.; Zhong, G.; Zhuang, X. Actin, Spectrin, and Associated Proteins Form a Periodic Cytoskeletal Structure in Axons. *Science* **2013**, *339* (6118), 452–456. https://doi.org/10.1126/science.1232251.

(7) Jans, D. C.; Wurm, C. A.; Riedel, D.; Wenzel, D.; Stagge, F.; Deckers, M.; Rehling, P.; Jakobs, S. STED Super-Resolution Microscopy Reveals an Array of MINOS Clusters along Human Mitochondria. *Proc. Natl. Acad. Sci. U.S.A.* **2013**, *110* (22), 8936–8941. https://doi.org/10.1073/pnas.1301820110.

(8) Hess, S. T.; Girirajan, T. P. K.; Mason, M. D. Ultra-High Resolution Imaging by Fluorescence Photoactivation Localization Microscopy. *Biophys J* **2006**, *91* (11), 4258–4272. https://doi.org/10.1529/biophysj.106.091116.

(9) Rust, M. J.; Bates, M.; Zhuang, X. Sub-Diffraction-Limit Imaging by Stochastic Optical Reconstruction Microscopy (STORM). *Nature Methods* **2006**, *3* (10), 793–796. https://doi.org/10.1038/nmeth929.

(10) Heilemann, M.; van de Linde, S.; Schüttpelz, M.; Kasper, R.; Seefeldt, B.; Mukherjee, A.; Tinnefeld, P.; Sauer, M. Subdiffraction-Resolution Fluorescence Imaging with Conventional Fluorescent Probes. *Angew. Chem. Int. Ed. Engl.* **2008**, *47* (33), 6172–6176. https://doi.org/10.1002/anie.200802376.

(11) Abbe, E. Beiträge zur Theorie des Mikroskops und der mikroskopischen Wahrnehmung. *Archiv f. mikrosk. Anatomie* **1873**, *9* (1), 413–418. https://doi.org/10.1007/BF02956173.

(12) Dempsey, G. T.; Bates, M.; Kowtoniuk, W. E.; Liu, D. R.; Tsien, R. Y.; Zhuang, X. Photoswitching Mechanism of Cyanine Dyes. *J Am Chem Soc* **2009**, *131* (51), 18192–18193. https://doi.org/10.1021/ja904588g.

(13) Vogelsang, J.; Kasper, R.; Steinhauer, C.; Person, B.; Heilemann, M.; Sauer, M.; Tinnefeld, P. A Reducing and Oxidizing System Minimizes Photobleaching and Blinking of Fluorescent Dyes. *Angew. Chem. Int. Ed. Engl.* **2008**, *47* (29), 5465–5469. https://doi.org/10.1002/anie.200801518.

(14) Heilemann, M.; Margeat, E.; Kasper, R.; Sauer, M.; Tinnefeld, P. Carbocyanine Dyes as Efficient Reversible Single-Molecule Optical Switch. *J. Am. Chem. Soc.* **2005**, *127* (11), 3801–3806. https://doi.org/10.1021/ja044686x.

(15) Deniz, E.; Tomasulo, M.; Cusido, J.; Yildiz, I.; Petriella, M.; Bossi, M. L.; Sortino, S.; Raymo, F. M. Photoactivatable Fluorophores for Super-Resolution Imaging Based on Oxazine Auxochromes. *The Journal of Physical Chemistry C* **2012**, *116* (10), 6058–6068. https://doi.org/10.1021/jp211796p.

(16) Biteen, J. S.; Thompson, M. A.; Tselentis, N. K.; Bowman, G. R.; Shapiro, L.; Moerner, W. E. Super-Resolution Imaging in Live Caulobacter Crescentus Cells Using Photoswitchable EYFP. *Nat. Methods* **2008**, *5* (11), 947–949. https://doi.org/10.1038/nmeth.1258.

(17) Andresen, M.; Stiel, A. C.; Trowitzsch, S.; Weber, G.; Eggeling, C.; Wahl, M. C.; Hell, S. W.; Jakobs, S. Structural Basis for Reversible Photoswitching in Dronpa. *Proc. Natl. Acad. Sci. U.S.A.* **2007**, *104* (32), 13005–13009. https://doi.org/10.1073/pnas.0700629104.

(18) Patterson, G. H.; Lippincott-Schwartz, J. A Photoactivatable GFP for Selective Photolabeling of Proteins and Cells. *Science* **2002**, *297* (5588), 1873–1877. https://doi.org/10.1126/science.1074952.

(19) Lord, S. J.; Conley, N. R.; Lee, H. D.; Samuel, R.; Liu, N.; Twieg, R. J.; Moerner, W. E. A Photoactivatable Push-Pull Fluorophore for Single-Molecule Imaging in Live Cells. *J. Am. Chem. Soc.* **2008**, *130* (29), 9204–9205. https://doi.org/10.1021/ja802883k.

(20) Bossi, M.; Fölling, J.; Belov, V. N.; Boyarskiy, V. P.; Medda, R.; Egner, A.; Eggeling, C.; Schönle, A.; Hell, S. W. Multicolor Far-Field Fluorescence Nanoscopy through Isolated Detection of Distinct Molecular Species. *Nano Lett.* **2008**, *8* (8), 2463–2468. https://doi.org/10.1021/nl801471d.

(21) Belov, V. N.; Wurm, C. A.; Boyarskiy, V. P.; Jakobs, S.; Hell, S. W. Rhodamines NN: A Novel Class of Caged Fluorescent Dyes. *Angewandte Chemie International Edition* **2010**, *49* (20), 3520–3523. https://doi.org/10.1002/anie.201000150.

(22) Chudakov, D. M.; Verkhusha, V. V.; Staroverov, D. B.; Souslova, E. A.; Lukyanov, S.; Lukyanov, K. A. Photoswitchable Cyan Fluorescent Protein for Protein Tracking. *Nat. Biotechnol.* **2004**, *22* (11), 1435–1439. https://doi.org/10.1038/nbt1025.

(23) Subach, F. V.; Patterson, G. H.; Manley, S.; Gillette, J. M.; Lippincott-Schwartz, J.; Verkhusha, V. V. Photoactivatable MCherry for High-Resolution Two-Color Fluorescence Microscopy. *Nature Methods* **2009**, *6* (2), 153–159. https://doi.org/10.1038/nmeth.1298.

(24) McKinney, S. A.; Murphy, C. S.; Hazelwood, K. L.; Davidson, M. W.; Looger, L. L. A Bright and Photostable Photoconvertible Fluorescent Protein for Fusion Tags. *Nat Methods* **2009**, *6* (2), 131–133. https://doi.org/10.1038/nmeth.1296.

(25) Gurskaya, N. G.; Verkhusha, V. V.; Shcheglov, A. S.; Staroverov, D. B.; Chepurnykh, T. V.; Fradkov, A. F.; Lukyanov, S.; Lukyanov, K. A. Engineering of a Monomeric Green-to-Red Photoactivatable Fluorescent Protein Induced by Blue Light. *Nat. Biotechnol.* **2006**, *24* (4), 461–465. https://doi.org/10.1038/nbt1191.

(26) Baddeley, D.; Bewersdorf, J. Biological Insight from Super-Resolution Microscopy: What We Can Learn from Localization-Based Images. *Annu. Rev. Biochem.* **2018**, *87*, 965–989. https://doi.org/10.1146/annurev-biochem-060815-014801.

(27) Dempsey, G. T.; Vaughan, J. C.; Chen, K. H.; Bates, M.; Zhuang, X. Evaluation of Fluorophores for Optimal Performance in Localization-Based Super-Resolution Imaging. *Nature Methods* **2011**, *8* (12), 1027–1036. https://doi.org/10.1038/nmeth.1768.

(28) Ulrich, G.; Ziessel, R.; Harriman, A. The Chemistry of Fluorescent Bodipy Dyes: Versatility Unsurpassed. *Angewandte Chemie International Edition* **2008**, *47* (7), 1184–1201. https://doi.org/10.1002/anie.200702070.

(29) Nahidiazar, L.; Agronskaia, A. V.; Broertjes, J.; van den Broek, B.; Jalink, K. Optimizing Imaging Conditions for Demanding Multi-Color Super Resolution Localization Microscopy. *PLoS ONE* **2016**, *11* (7), e0158884. https://doi.org/10.1371/journal.pone.0158884.

(30) Bates, M.; Jones, S. A.; Zhuang, X. Preparation of Photoswitchable Labeled Antibodies for STORM Imaging. *Cold Spring Harb Protoc* **2013**, *2013* (6), 540–541. https://doi.org/10.1101/pdb.prot075168.

(31) Huang, B.; Babcock, H.; Zhuang, X. Breaking the Diffraction Barrier: Super-Resolution Imaging of Cells. *Cell* **2010**, *143* (7), 1047–1058. https://doi.org/10.1016/j.cell.2010.12.002.

(32) Whelan, D. R.; Bell, T. D. M. Image Artifacts in Single Molecule Localization Microscopy: Why Optimization of Sample Preparation Protocols Matters. *Sci Rep* **2015**, *5*, 7924. https://doi.org/10.1038/srep07924.

(33) Los, G. V.; Encell, L. P.; McDougall, M. G.; Hartzell, D. D.; Karassina, N.; Zimprich, C.; Wood, M. G.; Learish, R.; Ohana, R. F.; Urh, M.; et al. HaloTag: A Novel Protein Labeling Technology for Cell Imaging and Protein Analysis. *ACS Chem. Biol.* **2008**, *3* (6), 373–382. https://doi.org/10.1021/cb800025k.

(34) Lee, H. D.; Lord, S. J.; Iwanaga, S.; Zhan, K.; Xie, H.; Williams, J. C.; Wang, H.; Bowman, G. R.; Goley, E. D.; Shapiro, L.; et al. Superresolution Imaging of Targeted Proteins in Fixed and Living Cells Using Photoactivatable Organic Fluorophores. *J Am Chem Soc* **2010**, *132* (43), 15099–15101. https://doi.org/10.1021/ja1044192.

(35) Grimm, J. B.; English, B. P.; Choi, H.; Muthusamy, A. K.; Mehl, B. P.; Dong, P.; Brown, T. A.; Lippincott-Schwartz, J.; Liu, Z.; Lionnet, T.; et al. Bright Photoactivatable Fluorophores for Single-Molecule Imaging. *Nature Methods* **2016**, *13* (12), 985–988. https://doi.org/10.1038/nmeth.4034.

(36) Ho, S. H.; Tirrell, D. A. Chemoenzymatic Labeling of Proteins for Imaging in Bacterial Cells. *Journal of the American Chemical Society* **2016**, *138* (46), 15098–15101. https://doi.org/10.1021/jacs.6b07067.

(37) Kulkarni, C.; Kinzer-Ursem, T. L.; Tirrell, D. A. Selective Functionalization of the Protein N Terminus with N-Myristoyl Transferase for Bioconjugation in Cell Lysate. *ChemBioChem* **2013**, *14* (15), 1958–1962. https://doi.org/10.1002/cbic.201300453.

(38) Aitken, A.; Cohen, P.; Santikarn, S.; Williams, D. H.; Calder, A. G.; Smith, A.; Klee, C. B. Identification of the NH2-Terminal Blocking Group of Calcineurin B as Myristic Acid. *FEBS Lett.* **1982**, *150* (2), 314–318.

(39) Lee, M. K.; Rai, P.; Williams, J.; Twieg, R. J.; Moerner, W. E. Small-Molecule Labeling of Live Cell Surfaces for Three-Dimensional Super-Resolution Microscopy. *Journal of the American Chemical Society* **2014**, *136* (40), 14003–14006. https://doi.org/10.1021/ja508028h.

(40) Knauer, K.-H.; Gleiter, R. Photochromism of Rhodamine Derivatives. *Angewandte Chemie International Edition in English* **1977**, *16* (2), 113–113. https://doi.org/10.1002/anie.197701131.

(41) Willwohl, H.; Wolfrum, J.; Gleiter, R. Kinetics and Mechanism of the Photochromism of N-Phenyl-Rhodaminelactame. *Laser Chemistry* **1989**, *10* (2), 63–72. https://doi.org/10.1155/1989/69709.

(42) Shiomi, D.; Banno, S.; Homma, M.; Kawagishi, I. Stabilization of Polar Localization of a Chemoreceptor via Its Covalent Modifications and Its Communication with a Different Chemoreceptor. *Journal of Bacteriology* **2005**, *187* (22), 7647–7654. https://doi.org/10.1128/JB.187.22.7647-7654.2005.

(43) Maddock, J. R.; Shapiro, L. Polar Location of the Chemoreceptor Complex in the Escherichia Coli Cell. *Science* **1993**, *259* (5102), 1717–1723.

(44) Sun, Q.; Margolin, W. FtsZ Dynamics during the Division Cycle of Live Escherichia Coli Cells. *J Bacteriol* **1998**, *180* (8), 2050–2056.

(45) Addinall, S. G.; Lutkenhaus, J. FtsA Is Localized to the Septum in an FtsZ-Dependent Manner. *Journal of Bacteriology* **1996**, *178* (24), 7167–7172. https://doi.org/10.1128/jb.178.24.7167-7172.1996.

(46) Belov, V. N.; Bossi, M. L.; Fölling, J.; Boyarskiy, V. P.; Hell, S. W. Rhodamine Spiroamides for Multicolor Single-Molecule Switching Fluorescent Nanoscopy. *Chemistry* **2009**, *15* (41), 10762–10776. https://doi.org/10.1002/chem.200901333.

(47) Dickson, R. M.; Cubitt, A. B.; Tsien, R. Y.; Moerner, W. E. On/off Blinking and Switching Behaviour of Single Molecules of Green Fluorescent Protein. *Nature* **1997**, *388* (6640), 355–358. https://doi.org/10.1038/41048.

(48) Wang, S.; Moffitt, J. R.; Dempsey, G. T.; Xie, X. S.; Zhuang, X. Characterization and Development of Photoactivatable Fluorescent Proteins for Single-Molecule-Based Superresolution Imaging. *Proc. Natl. Acad. Sci. U.S.A.* **2014**, *111* (23), 8452–8457. https://doi.org/10.1073/pnas.1406593111.

(49) Van Valkenburgh, H. A.; Kahn, R. A. Coexpression of Proteins with Methionine Aminopeptidase/or N-Myristoyltransferase in Escherichia Coli to Increase Acylation Homogeneity of Protein Preparations. In *Methods in Enzymology*; Elsevier, 2002; Vol. 344, pp 186–193. https://doi.org/10.1016/S0076-6879(02)44715-5.

(50) Guzman, L. M.; Belin, D.; Carson, M. J.; Beckwith, J. Tight Regulation, Modulation, and High-Level Expression by Vectors Containing the Arabinose PBAD Promoter. *Journal of Bacteriology* **1995**, *177* (14), 4121–4130. https://doi.org/10.1128/jb.177.14.4121-4130.1995.

(51) Shiomi, D.; Yoshimoto, M.; Homma, M.; Kawagishi, I. Helical Distribution of the Bacterial Chemoreceptor via Colocalization with the Sec Protein Translocation Machinery. *Mol. Microbiol.* **2006**, *60* (4), 894–906. https://doi.org/10.1111/j.1365-2958.2006.05145.x.

(52) Greenfield, D.; McEvoy, A. L.; Shroff, H.; Crooks, G. E.; Wingreen, N. S.; Betzig, E.; Liphardt, J. Self-Organization of the Escherichia Coli Chemotaxis Network Imaged with Super-Resolution Light Microscopy. *PLoS Biol.* **2009**, *7* (6), e1000137. https://doi.org/10.1371/journal.pbio.1000137.

(53) Yang, X.; Lyu, Z.; Miguel, A.; McQuillen, R.; Huang, K. C.; Xiao, J. GTPase Activity-Coupled Treadmilling of the Bacterial Tubulin FtsZ Organizes Septal Cell Wall Synthesis. *Science* **2017**, *355* (6326), 744–747. https://doi.org/10.1126/science.aak9995.

(54) Bisson-Filho, A. W.; Hsu, Y.-P.; Squyres, G. R.; Kuru, E.; Wu, F.; Jukes, C.; Sun, Y.; Dekker, C.; Holden, S.; VanNieuwenhze, M. S.; et al. Treadmilling by FtsZ Filaments Drives Peptidoglycan Synthesis and Bacterial Cell Division. *Science* **2017**, *355* (6326), 739–743. https://doi.org/10.1126/science.aak9973.

(55) Rowlett, V. W.; Margolin, W. 3D-SIM Super-Resolution of FtsZ and Its Membrane Tethers in Escherichia Coli Cells. *Biophys. J.* **2014**, *107* (8), L17–L20. https://doi.org/10.1016/j.bpj.2014.08.024.

(56) Fu, G.; Huang, T.; Buss, J.; Coltharp, C.; Hensel, Z.; Xiao, J. In Vivo Structure of the E. Coli FtsZ-Ring Revealed by Photoactivated Localization Microscopy (PALM). *PLoS ONE* **2010**, *5* (9), e12682. https://doi.org/10.1371/journal.pone.0012680.

(57) Wang, L.; Frei, M. S.; Salim, A.; Johnsson, K. Small-Molecule Fluorescent Probes for Live-Cell Super-Resolution Microscopy. *J. Am. Chem. Soc.* **2019**, *141* (7), 2770–2781. https://doi.org/10.1021/jacs.8b11134.

(58) Grimm, J. B.; English, B. P.; Chen, J.; Slaughter, J. P.; Zhang, Z.; Revyakin, A.; Patel, R.; Macklin, J. J.; Normanno, D.; Singer, R. H.; et al. A General Method to Improve Fluorophores for Live-Cell and Single-Molecule Microscopy. *Nat. Methods* **2015**, *12* (3), 244–250, 3 p following 250. https://doi.org/10.1038/nmeth.3256.

(59) Godin, A. G.; Lounis, B.; Cognet, L. Super-Resolution Microscopy Approaches for Live Cell Imaging. *Biophys J* **2014**, *107* (8), 1777–1784. https://doi.org/10.1016/j.bpj.2014.08.028.

(60) Ivankov, D. N.; Payne, S. H.; Galperin, M. Y.; Bonissone, S.; Pevzner, P. A.; Frishman, D. How Many Signal Peptides Are There in Bacteria? *Environmental Microbiology* **2013**, *15* (4), 983–990. https://doi.org/10.1111/1462-2920.12105.

(61) Butkevich, A. N.; Bossi, M. L.; Lukinavicius, G.; Hell, S. W. Triarylmethane Fluorophores Resistant to Oxidative Photobluing. *J. Am. Chem. Soc.* **2018**. https://doi.org/10.1021/jacs.8b11036.

(62) Chang, Y.-W.; Chen, S.; Tocheva, E. I.; Treuner-Lange, A.; Löbach, S.; Søgaard-Andersen, L.; Jensen, G. J. Correlated Cryogenic Photoactivated Localization Microscopy and Cryo-Electron Tomography. *Nature Methods* **2014**, *11* (7), 737–739. https://doi.org/10.1038/nmeth.2961.

(63) Dahlberg, P. D.; Sartor, A. M.; Wang, J.; Saurabh, S.; Shapiro, L.; Moerner, W. E. Identification of PAmKate as a Red Photoactivatable Fluorescent Protein for Cryogenic Super-Resolution Imaging. *Journal of the American Chemical Society* **2018**, *140* (39), 12310–12313. https://doi.org/10.1021/jacs.8b05960.

(64) Arbeloa, F. L.; Ojeda, P. R.; Arbeloa, I. L. Flourescence Self-Quenching of the Molecular Forms of Rhodamine B in Aqueous and Ethanolic Solutions. *Journal of Luminescence* **1989**, *44* (1), 105–112. https://doi.org/10.1016/0022-2313(89)90027-6.